STUDIES ON REACTIVE OXO INTERMEDIATES GENERATED DURING SELECTIVE HYDROCARBON OXIDATIONS OVER METALLOSILICATE AND MIXED METAL OXIDE CATALYSTS

A THESIS

SUBMITTED TO THE

UNIVERSITY OF PUNE

FOR THE DEGREE OF

DOCTOR OF PHILOSOPHY

IN

CHEMISTRY

BY

VASUDEV NAGESH SHETTI

CATALYSIS DIVISION

NATIONAL CHEMICAL LABORATORY

PUNE - 411 008, INDIA

JANUARY 2006

Dr. D. Srinivas
Catalysis Division
Tel: +91-20-2590 2018
Fax: +91-20-2589 3761
e-mail: d.srinivas@ncl.res.in

National Chemical Laboratory
Dr Homi Bhabha Road
Pune – 411 008, INDIA

CERTIFICATE

It is certified that the work incorporated in the thesis entitled "**Studies on Reactive Oxo Intermediates Generated During Selective Hydrocarbon Oxidations over Metallosilicate and Mixed Metal Oxide Catalysts**", submitted by **Mr. Vasudev Nagesh Shetti,** for the degree of **Doctor of Philosophy in Chemistry**, was carried out by the candidate under my supervision in the Catalysis Division, National Chemical Laboratory, Pune – 411 008, India. Materials obtained from other sources have been duly acknowledged in the thesis.

Dr. D. Srinivas
Research Guide

DECLARATION

I here by declare that the thesis entitled "**Studies on Reactive Oxo Intermediates Generated During Selective Hydrocarbon Oxidations over Metallosilicate and Mixed Metal Oxide Catalysts**", submitted for the Degree of **Doctor of Philosophy in Chemistry** to the University of Pune, has been carried out by me at the Catalysis Division, National Chemical Laboratory, Pune - 411 008, India, under the supervision of **Dr. D. Srinivas**. The work is original and has not been submitted in part or full by me for any other degree or diploma to this or any other University.

Vasudev Nagesh Shetti
Research Scholar

Acknowledgments

I express my profound gratitude to my research guide Dr. D. Srinivas for suggesting the problem; giving invaluable guidance, constant encouragement, having numerous discussions and suggesting the right way, throughout the course of this investigation.

I take this opportunity to express my deepest sense of gratitude and reverence towards Dr.Paul Ratnasamy for his equally valuable discussions and suggestions during my research work.

My heartfelt thanks to Dr. S. Sivasanker who has been there as a huge green shadowy tree under whom I started enjoying my research life.

It is my privilege to thank Dr. S.G. Hegde for his kindness and consideration throughout this remarkable journey.

I would like to express my profound gratitude to Dr. A.V. Ramaswamy, the then Head of Catalysis Division, NCL and Dr. Rajiv Kumar Chaturvedi, the Head of Catalysis Division for providing all facilities required for my work.

It gives me a great pleasure to express my deep sense of gratitude and indebtedness to all the scientific and non-scientific staff of Catalysis Division and Catalysis Pilot Plant especially Drs. S.B. Halligudi,C.V.V. Satyanarayana, P.N. Joshi, P. Manikandan, C.S. Gopinath, A.J. Chandwadkar, V. Ramaswamy, S.A. Pardhy, N.E. Jacobs, S. Deshpande, S.P. Mirajkar, M. Agashe, A.A. Belhekar, S. Sheikh, S.V. Awte, T. Raja, Ms. S. Violet, Mr. R.K. Jha, Mr. Purushottaman, Mr. Katti, Mr. Madhu and Mr. Milind for their help in one or the other way, during my research work.

I thank all my friends especially, Bennur, Suhas, Suresh, Raja, Rajendra, Lakshi, Venkatathri, Rohit, Ganapati, Girish, Sanju, Sharanu, Santosh, Abhimanyu, Murugan, Vijayraj, Maitri, Prashant, Sangam, Swamy, Pai, Smitha, Surekha, Dhanashree, JP, Sachin ,Shiju, Ankur, Kumbar, Raghu, Sunil and Nagaraj for being literally up to the proverbial "friend in need is friend indeed".

It gives me great pleasure to acknowledge my parents, my brothers Bhaskar, Ramakrishna and sister Vasudha for the love, unfailing support, patience, trust and encouragement during many years of my studies that they have shown to me in their own special way.

It is indeed my privilege to thank the Director, NCL, for allowing me this opportunity and extending all possible infrastructural facilities at NCL. Financial assistance from CSIR-India is greatly acknowledged

Vasudev Nagesh Shetti

Isaac Newton's admonition:

"To explain all nature is too difficult a task for any man or even for any one age. 'Tis much better to do a little with certainty, and leave the rest for others that come after you than to explain all things"

Chapter – 1
General Introduction

1.1. Historical Background

Selective oxidation of hydrocarbons is one of the most important and challenging organic transformations producing value-added chemicals [1 - 8]. About one quarter of all the organic compounds produced worldwide is synthesized *via* selective oxidation of the hydrocarbons [9]. While molecular oxygen and hydrogen peroxide are preferred in industrial applications, other oxidants including organic peroxides, iodosylbenzene, persulphates, *meta*-chloroperbenzoic acid, hypochlorites etc., are also used in producing oxygenated compounds [10 - 12]. Some of the large scale industrial catalytic oxidation processes include: oxidation of (a) *para*-xylene to terephthalic acid (oxidant – oxygen, liquid phase process), (b) methanol to formaldehyde (oxygen, gas phase), (c) ethene to ethene oxide (oxygen, gas phase), (d) propene to propene oxide (organic hydroperoxide, liquid phase), (e) ethene to vinyl acetate (oxygen, liquid & gas phase), (f) toluene to benzoic acid (oxygen, liquid phase), (g) benzene to adipic acid (oxygen, liquid phase), (h) *n*-butane to maleic anhydride (oxygen, gas phase) etc [1, 2]. In all these processes, reactions are conducted at high temperatures and pressures.

Nature performs the task of biological oxidations at ambient conditions, employing metalloenzyme and protein catalysts, which are remarkably more efficient, specific and particularly, selective for producing a specific oxygenated compound [13-15]. In a majority of industrial practices, over man-made catalysts, significant amounts of undesired side-products are usually produced. In order to make the process more economical and green one of the major challenges in catalysis research is to develop solid, highly efficient and selective oxidation catalysts for reactions at ambient conditions.

In a pursuit to design enzyme mimic oxidation catalysts, catalysis researchers have, in the past, immobilized or encapsulated homogeneous metal complexes in the cavities and pores of zeolites and zeolitic materials [16 - 19]. The discovery of metallosilicate molecular sieves in the early 1980s is a major breakthrough in heterogeneous catalysis research [20, 21]. Metallosilicates especially those of Ti and V analogs exhibit very high activity in selective oxidation of a variety of organic compounds, at mild conditions, using H_2O_2 or *tert.*-butyl hydroperoxide (TBHP) as oxidant [22 - 29]. In order to achieve transformation of bulkier organic molecules of pharmaceutical interest, a range of mesoporous molecular sieves have been developed

[30 - 45]. Surface modification and hydrophobization enabled some success in improving selectivity for the desired products [46 - 55]. Studies have revealed that a variety of factors including method of catalyst preparation, solvent, oxidant, temperature etc., influence the reactivity and selectivity of solid catalysts in oxidation reactions [56 - 60]. It is known that during oxidations, different types of active metal-oxo species (metal-peroxo, hydroperoxo and superoxo) are generated [61 - 68]. A fundamental understanding of their composition, reactivity, factors affecting their formation, mode of O-O bond cleavage (homolytic *vs* heterolytic) and mechanism of O-atom transfer would, possibly, enable developing more *efficient* and *selective*, mesoporous oxidation catalysts.

Metal supported ceria-based materials are another important class of oxidation catalysts that have attracted considerable attention in recent times [69 - 72]. They are used in a variety of applications including automotive pollution control, fuel cell electrodes, hydrogen gas generation by hydrocarbon steam reforming, water-gas shift reaction, CO oxidation and several other oxidation reactions [73 - 80]. The superiority of these catalysts was corresponded to a facile $Ce^{4+} \leftrightarrow Ce^{3+}$ redox couple, oxygen storage capacity (OSC) and strong metal-support interactions [81 - 85]. Since the beginning of 1980, CeO_2 has been used in the automotive pollution control as a three-way catalyst (TWC) to convert simultaneously, the toxic flue gases in effluents *viz.*, hydrocarbons (HCs), CO and NOx to less harmful materials like H_2O, CO_2 and N_2, respectively [86, 87]. Structural doping of CeO_2 with ZrO_2 has proved to be an efficient route to stabilize and enhance the oxygen storage and hence, the catalytic activity [88]. Zirconia doping has also prevented sintering of the catalysts. Noble metal supported CeO_2-based catalysts are commonly used in TWC and preferential CO oxidation reactions. One of the issues in this area is to develop efficient, cheaper base metal-modified CeO_2 materials for the above applications. Further, the catalysts should be active for oxidation of CO at *low-temperatures* and *in presence of H_2O and sulfur-containing compounds* in the feed. An understanding of the influence of composition and support-metal interactions on metal ion speciation and redox behavior could help developing efficient, oxidation catalysts. In this thesis, a detailed investigation is made on the redox behavior and reactive oxygen species generated during oxidation reactions in metallosilicates (titano and vanadosilicates, for example) and CuO-containing CeO_2-based materials.

1.2. Zeolites and Molecular Sieves

Traditionally, zeolites are defined as (natural or synthetic) crystalline aluminosilicates with a three-dimensional, microporous framework, which is constructed by an infinitely extending connected network of AlO_4 and SiO_4 tetrahedron linked by shared oxygen atoms at the corner points of the tetrahedrons [89]. Since AlO_2^- tetrahedron bears a net negative charge, they are balanced by cations like alkaline (Li^+, Na^+, K^+) and alkaline earth (Mg^{2+}, Ca^{2+}, Ba^{2+}) ions, quaternary ammonium ions, protons (in the acid form of zeolites), and rare earth and noble metal ions. The connection of two AlO_4 tetrahedra is not encountered restricting zeolites to Si/Al ratios of ≥ 1 (Löwenstein rule). Si/Al ratio determines a number of important properties useful for catalysis, ion-exchange and adsorption. Zeolite with Si/Al value of infinity can be prepared by dealumination or direct synthesis procedures. Silicalite-1 and its titanium modification (TS-1) belong to the category of zeolites with infinite Si/Al ratios. Due to the missing AlO_2 tetrahedron these materials have no ion-exchange capacity and after calcination they exhibit hydrophobic character, at least, as long as the number of lattice defects (silanol groups) is low. Strictly speaking zeolites with infinite Si/Al ratio do not meet the definition of a zeolite and should be referred only as molecular sieves. However, especially, the metallosilicates are often referred to as zeolites and frequently both terms are used interchangeably. Since all tetrahedron of the zeolite framework are exposed to the pore volume, zeolites possess a very high surface area compared to non-porous inorganic solids. While the zeolites have pores in the range of 0.3 to 1.4 nm, the recently developed mesoporous materials (MCM-41 and SBA-15, for example) have pores up to 10 nm in diameter.

1.3. Titano- and Vanadosilicate Molecular Sieves

Taramasso et al [20] in 1983 discovered a microporous, crystalline, titanium-containing silicate-1 molecular sieve (TS-1), which exhibited remarkable, enzyme-mimic, catalytic activity in stereo-, regio- and chemoselective catalytic hydrocarbon oxidations, at ambient temperatures, using H_2O_2 as oxidant [22, 90 - 93]. TS-1 catalyzed a wide range of oxidation reactions including, epoxidations, hydroxylation of aromatic and aliphatic compounds and oxidation of nitrogen, sulfur and oxygen-containing compounds (Fig. 1.1) [94 - 98] and acid catalyzed reactions including Beckmann rearrangement, transesterification, synthesis of polycarbonate precursors, C-C bond formation reactions, formation of pinacols and oxidative dehydrogenation of ethylbenzene.

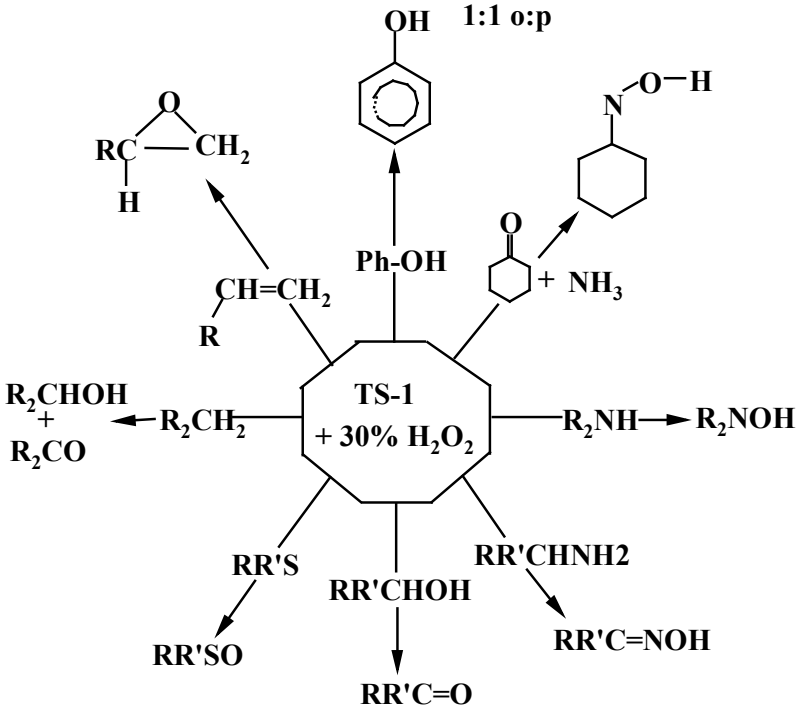

Fig. 1.1. Reactions catalyzed by titanium silicalite-1 (TS-1).

Titanium in these silicates occupies the framework site of Si and possesses a pseudo-tetrahedral structure (Fig. 1.2) [99]. Ti in most of the natural minerals (titanium oxide, titanite, bentoite, ramsayte, pyroxene, for example) is in an octahedral geometry. Squrepyramidal structure is found in the mineral fresnoite. Tetra-coordinated titanium is hardly found except in one of the rare examples Ba_2TiO_4. The unique catalytic activity of

TS-1 has been attributed to the unusual tetrahedral Ti structure, framework substitution, isolation of Ti ions and capability to expand its coordination number from 4 to 5 or 6 during catalytic oxidations. One of the drawbacks of TS-1 is, because of its microporous nature the reactions are confined only to molecules of smaller dimensions. Since the discovery of TS-1, many titanium silicate molecular sieves in various structural and geometric locations have been synthesized and their physical, chemical and catalytic properties investigated (TS-2 (*100*, *91*), Ti-ZSM-48 (*102*), Ti-beta (*103 - 109*), Ti-ZSM-12 (*110*), Ti-MCM-41 (*30 - 32*), Ti-HMS (*32 - 34*), Ti-MCM-48 (*35*), Ti-MSU (*36*, *37*), Ti-SBA-15 (*38 - 40*), Ti-MMM (*40-43*), Ti-MWW (*44*) and Ti-TUD-1 (*45*)).

Fig. 1.2. The structure of the orthorhombic form of silicalite-1 (MFI-type) showing the 12

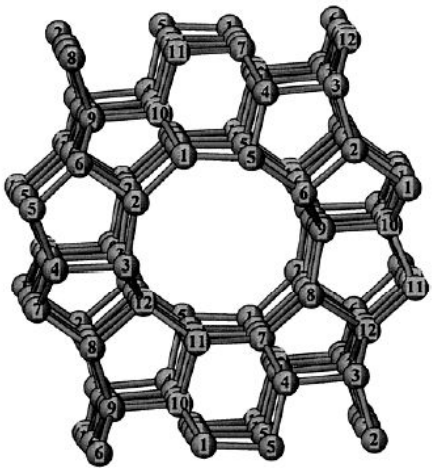

crystallographically distinct T sites. Oxygen atoms are omitted for clarity [99].

In spite of the significant progress that has been made in the structural and scientific investigations of TS-1 during the past two decades, and, not withstanding the enormous potential of such a novel class of selective oxidation catalysts in the chemical and petrochemical industry, their commercial utilization in industrial plants has been rather disappointing. Only two processes (phenol to dihydroxybenzenes and cyclohexanone to cyclohexanone oxime) have been commercialized so far. Based on the ENIchem Technology, DOW and BASF are jointly starting a propene oxide manufacturing plant from propene [20, 94, 111].

High-valued fine chemicals (used in the pharmaceutical, agrochemical, flavors, and perfumery industries) are, however, usually complex molecules too large to enter the pores of the MFI structure in TS-1. This was one of the driving forces for attempts, worldwide, to synthesize titanosilicate molecular sieves with large and mesoporous structures. Such materials (such as Ti-beta, Ti-MCM-41, and Ti-SBA-15, for example) do not have the geometric constraints of TS-1. Unfortunately, even though significant success has been attained in the synthesis of such materials, they are not found to be as chemoselective as TS-1 in oxidation reactions using aqueous H_2O_2 as the oxidant. Their structural stability is also less (especially with regard to leaching of the Ti ions). They are more suitable when alkyl hydroperoxides are used as oxidant, there by lacking the advantages of inherent process simplicity and environmental advantages that ensue when aqueous H_2O_2 is used. Apart from the higher cost of manufacture of TS-1 (the current price is about U.S. $100/kg), another major constraint has been the necessity to use H_2O_2 in stoichiometric quantities, rather than molecular oxygen, as the oxidant. Because H_2O_2 itself is rather expensive, its use can be commercially justified only for the manufacture of high-value products (say, those costing more than U.S. $2/kg), thereby excluding the majority of bulk and petrochemicals. Some of the issues that have yet to be resolved include: (1) why is TS-1 more chemoselective than Ti-beta and Ti-MCM-41 [*30, 32*] even though Ti^{4+} ions are isolated and in near-tetrahedral locations in all of them? (2) Are differences in hydrophobicity/hydrophilicity between TS-1 and the large/mesoporous material the only factors responsible for the lower chemoselectivity of the latter?

In situ EXAFS studies have revealed presence of at least 2 to 3 types of tetrahedral Ti structures in titanosilicate molecular sieves. These include the tetrapodal, tripodal and bipodal-Ti structures (Fig. 1.3). While the tetrapodal-Ti structures are more prevalent in well-prepared and dehydrated TS-1 samples, tripodal and bipodal-Ti were observed in abundance in mesoporous materials. On the basis of XANES data, Gleeson et al. [*64*] inferred two types of tetrapodal structures, one having three 140° Ti–O–Si angles and one 160° Ti–O–Si angle and the other having only two 140° Ti–O–Si angles but two 160° Ti–O–Si angles in TS-1 samples. Which of these Ti structures are active and what kind of oxo-Ti species are generated and how they influence the product selectivity? A

detailed understanding of these issues will enable designing more efficient and selective titanosilicate molecular sieves.

Fig. 1.3. Tetrahedral Ti-structures in titanosilicates. I - tetrapodal, II – tripodal and III-bipodal Ti species.

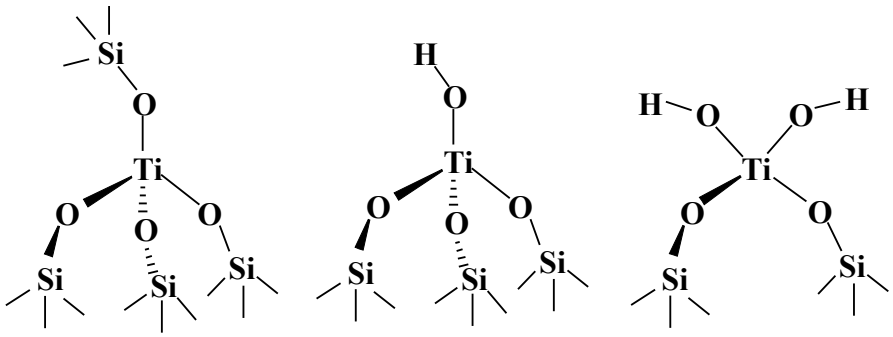

I II III

Vanadosilicate molecular sieves also exhibited efficient catalytic activity in selective oxidation of hydrocarbons [42, 112 - 122]. More interestingly, they catalyze the terminal, primary C-H bond oxidation of *n*-alkanes, which their titanium analogs cannot [122, 123]. Vanadosilicates also exhibit higher efficiency in the photocatalytic decomposition of NO [124, 125]. While there have been a large number of studies on the reactive oxygen species generated over Ti-silicates using a range of spectroscopic techniques [61, 63, 68, 99, 126, 127], similar studies on V-silicates are scarce [128, 129].

1.4. $CeO_2/ZrO_2/TiO_2$-based Catalysts – Oxygen Storage Capacity

Ceria (CeO_2) is a peculiar substance among many oxides of the lanthanide series and is an inevitable catalyst component for automobile exhaust purification [82, 130]. Among various functions of CeO_2, oxygen storage action and its facile transformation between $Ce^{4+} \leftrightarrow Ce^{3+}$ forms in its fluorite structure are notable ones. It acts as support as well as promoter in many oxidation reactions [131, 132]. When mixed with other reducible (TiO_2) or non-reducible (ZrO_2) oxides, ceria shows synergistic effect in its redox behavior. When a transition metal oxide like CuO is dispersed on it, there is a strong metal-support interaction (SMSI).

The support that works the best in three-way catalysts (TWCs) and CO oxidations is ceria. The most crucial role of ceria is its ability to exchange oxygen with the

environment. Ceria is a non-stoichiometric compound, which exhibits two valence states, +3 and +4, with low redox potential.

$$CeO_2 \leftrightarrow CeO_{2-x} + x/2O_2$$

The oxygen storage on the catalyst is simply described as cyclic reduction and oxidation of CeO_2. The process of oxygen storage and transport in ceria can be described by the defect mechanism. There are two types of defects: intrinsic and extrinsic [133]. The former is due to oxygen anion vacancies created upon reduction of ceria. Accordingly, the reduction process involved in ceria is written as

$$CeO_2 + \delta R \rightarrow CeO_{2-\delta} + \delta RO + \delta V_0$$

where, R is a reductant, RO is a gaseous product and V_0 is oxygen anion vacancy which may be charged singly or doubly [134]. The extrinsic defects are due to oxygen anion vacancies created by charge compensation effect of foreign cations, which have a valence, lower than that of host Ce ions they substitute. For example, the doping reaction of ceria with bi- or trivalent cations can be written as

$$2MO + Ce_{Ce} \rightarrow 2M_{Ce} + CeO_2 + 2V_0$$

$$2M_2O_3 + 3Ce_{Ce} \rightarrow 4M_{Ce} + 3CeO_2 + 2V_0$$

where, M is bi- or trivalent cation, Ce_{Ce} is the Ce cation on the Ce site of the ceria lattice, M_{Ce} is foreign cation on the Ce cation site [134]. Trivalent dopants generally produce a higher ionic conductivity (i.e. oxygen mobility) than divalent ones [134]. Both of these vacancies were believed to provide a practical way to increase oxygen storage capacity (OSC) in ceria. The CeO_2 and ZrO_2 combination has imparted several beneficial effects to three-way catalysts [88].

- It prevents the chain growth of CeO_2 crystallites at high temperatures and improves thermal stability of CeO_2. When the exhaust temperatures exceed 1123 K pure CeO_2 catalyst suffers irreversible losses in its ability to store oxygen. The "sintering effect" at higher temperature, that causes smaller particles to bond to each other and form larger particles, decreases the surface area and hence, lowers the number of active sites available for catalytic reactions. The ceria is stabilized when zirconia is incorporated to enable the oxide to withstand high temperatures [88].

- The oxygen storage capacity (OSC) increases by improving the homogeneity of Ce and Zr atoms and modification of oxygen environment. The improved OSC is due to higher lability of oxygen atoms compared to that in pure CeO_2. In effect, the ceria/zirconia relationship is symbiotic because zirconia provides better access to oxygen for most of the ceria particles.
- Pure ceria reacts only on the surface, whereas zirconia-stabilized ceria enables oxygen liberation-absorption throughout the material.
- Some oxygen atoms are located at long distances from the Zr atoms, providing higher mobility and hence, enhanced catalytic activity.
- A remarkable property of CeO_2–ZrO_2 mixed oxides compared to CeO_2 is their ability to easily remove bulk oxygen species at moderate temperatures even in highly sintered samples. ZrO_2 has the ability to modify the oxygen sub-lattice in CeO_2–ZrO_2 mixed oxides, generating defective structures at moderate temperatures [135, 136]. Thus increased OSC property can be achieved by using CeO_2–ZrO_2 mixed oxides instead of CeO_2 since, even if the sample sinters under high temperature reaction conditions, it should be more effective than CeO_2 due to the high oxygen mobility in the bulk; lattice oxygen species could effectively participate in redox processes even under fluctuating exhaust feed-stream conditions.
- It improves the dispersion of noble metals and metal oxides and increases resistance to their sintering.
- These catalysts favor catalytic activity at the interfacial metal-support sites.
- The CeO_2-ZrO_2 catalysts are tolerant to sulfur compounds like SO_2 and water vapour and hence, can be used in diesel-based engines and steam reforming.
- The CeO_2-ZrO_2 catalysts exhibited enhanced activities compared to CeO_2 catalysts in the water-gas shift reaction

$$CO + H_2O \rightarrow CO_2 + H_2$$

and the steam reforming reaction

$$C_3H_8 + 3H_2O \rightarrow 3CO + 7H_2$$

Since 1995, CeO_2-ZrO_2 mixed oxides have gradually replaced pure CeO_2 as oxygen storage material in the TWCs [137], even though some low purity CeO_2 materials may be employed for less demanding TWC technologies [138].

The ideal fuel for PEM fuel cells is pure hydrogen with CO levels lower than 10 ppm (CO is a poison to the Pt-fuel cell catalyst). Hence, efforts are in progress to selectively remove CO (0.5 – 1% composition) from the H_2-rich reformate. The methods include (a) CO preferential oxidation (PROX), (b) catalytic methanation and (c) Pd-membrane separation. Among these, PROX is the most effective and a low cost method for trace CO clean-up from the reformate stream prior to its introduction in the PEM cell. High CO oxidation activities coupled with low hydrogen oxidation activities (at the desired operating temperatures) are the essential requirements of the PROX catalysts.

Oh and Sinketvitch [77] compared the efficiency of several noble metals for the PROX reaction. The CO conversion was found to decrease in the following order: $Ru/Al_2O_3 > Rh/Al_2O_3 > Pt/Al_2O_3 > Pd/Al_2O_3$ (metal loading: 0.5 wt.% for all catalysts). While Pd showed a similar CO oxidation activity to Ru and Rh at lower temperatures, it showed significantly inferior activity at higher temperatures. This effect was attributed to the change in oxidation state (from a highly active reduced form to a less active oxidized form) of Pd with increasing reaction temperature. Nano-gold catalysts are extremely promising for the PROX reaction at low temperatures; while larger Au particles show higher oxidation activity for H_2 as compared to CO, the situation is entirely reversed for supported nano-gold catalysts [78, 139 - 144]. In spite of the superior activities, the high cost and low availability of the noble metals have led way to alternative, cheaper metal oxide and bimetallic systems [145 - 148].

Copper on ceria, ceria–samaria, or other ceria-promoted supports have been investigated for the CO oxidation. $CuO\text{-}CeO_2$ catalysts exhibited excellent activity [149]. Among Pt/Al_2O_3, Au/Fe_2O_3 and $CuO\text{-}CeO_2$, the Au formulation was the most active at low temperature, while the selectivity of $CuO–CeO_2$ was remarkably higher than that of both Au and Pt formulations.

1.5. Reactive Oxo-Intermediate Species and Mechanism of Oxygen Transfer

The tetrahedral Ti in titanosilicates generates reactive oxygen species on contact

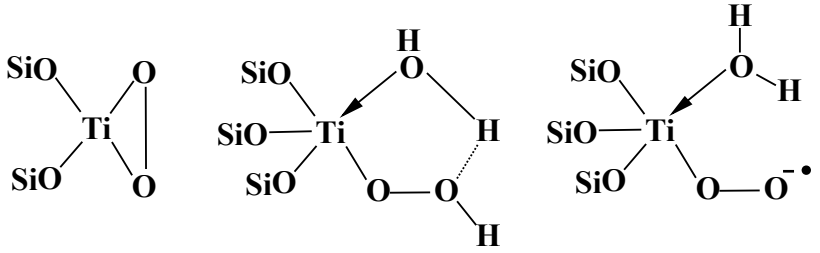

Peroxide **Hydroperoxide** **Superoxide**

with H_2O_2 or alkyl hydroperoxides. Mainly three types of oxo-titanium species *viz.*, hydroperoxo-, peroxo- and superoxo-Ti, have been identified so far (Fig. 1.4) [63, 64, 126] Concentration of these oxo-species depends on the structure and electronic properties of the active sites. These species differ in their reactivities.

Fig. 1.4. Possible oxo-titanium species in titanosilicate molecular sieves.

Upon contact with H_2O_2 the color of titanosilicates changes from white to yellow. The yellow color is a clear indication of the generation of oxo-titanium species. These species showed a characteristic broad band at 300 – 500 nm in diffuse reflectance UV-visible spectrum. The origin of this band was attributed to peroxo oxygen to titanium (ligand to metal) charge transfer transition. IR and Resonance Raman spectroscopies of titanosilicates contacted with H_2O_2 showed characteristic peaks at 886 and 837 cm^{-1} corresponding to the O-O stretching modes of end-on Ti-OOH (at neutral pH) and anionic triangular Ti-peroxo species (at alkaline pH) [150]. Lin and Frei [61] claimed the formation of η^2-TiOOH species absorbing at 837 and 3400 cm^{-1}. Thomas and co-workers [126] proposed the formation of a bidentate side-on (η^2-) peroxo-Ti species based on EXAFS measurements, which were also substantiated by DFT calculations. Based on EPR spectroscopy measurements, Srinivas and co-workers [67, 68] reported formation of end-on superoxo-Ti species in different titanosilicates. They also reported that the superoxo-Ti undergoes interconversion into a hydroperoxo-Ti species in TS-1 + H_2O_2 systems. The O-O bond in oxo species cleaves either homolytically (yielding oxygen-centered free radicals) or heterolytically (yielding ionic species). It was proposed that the oxo-Ti species participate in various oxidation reactions *via* radical or non-radical mechanism. However, which of these oxo-Ti species are active in which type of oxidation reactions have not been conclusively identified.

Assuming that the active Ti species is titanyl, Huybrechts et al. [151, 152] suggested a radical mechanism wherein initially a Ti-peroxo biradical is formed which

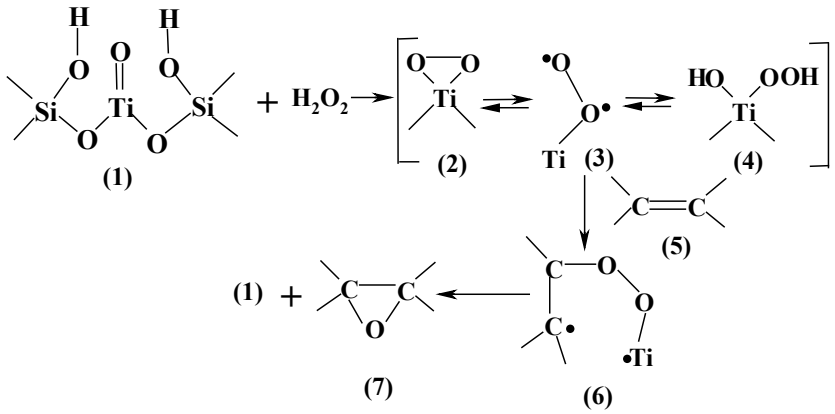

can abstract a H-atom from alkane or alcohol or can add to the double bond of the alkene or an arene producing new C-centered radicals. These C-radicals abstract OH group or one of the O atoms from the Ti-peroxo group and a subsequent fast recombination leads to the formation of the corresponding products of oxidation and restoration of the titanyl group. In a non-radical mechanism, intramolecular rearrangement takes place inside the coordination sphere of the Ti center (Fig. 1.5).

Fig. 1.5. Radical (top) and non-radical (bottom) mechanism of the oxidation on TS-1 [152].

Since alkanes contain no nucleophilic groups that can coordinate to Ti center. Huybrechts et al. [151, 152] supposed that the paraffin oxidation is realized through radical mechanism while oxidation of alcohols, olefins and aromatics can be accomplished by both the mechanisms.

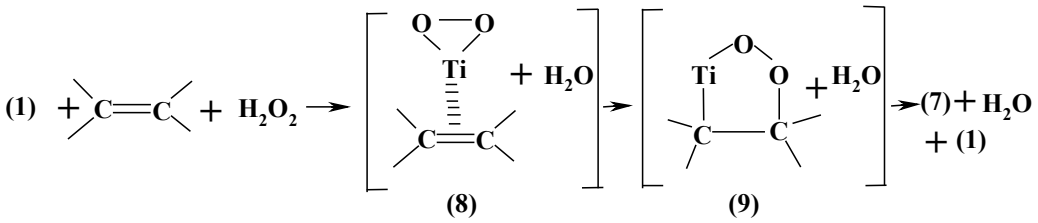

Van Santen and co-workers [153, 154] proposed a mechanism for the epoxidation of olefins, which involves only a change in coordination number of the Ti atoms while its valence state does not change during the catalytic reactions. There is no formation of catalytic intermediate titanyl groups. Based on density functional theory calculations, the

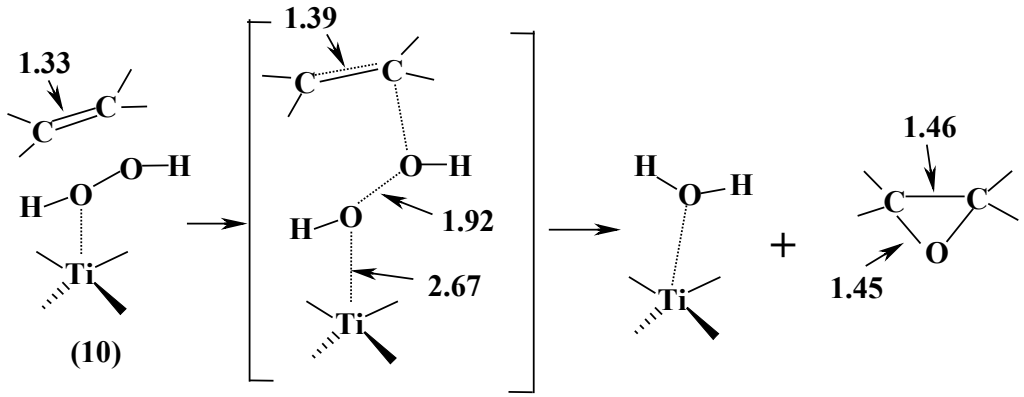

C-C bond of the olefin is elongated from 0.133 nm to 0.139 nm in the transition state due to interaction with one of the OH groups of the activated hydrogen peroxide The binding of the alkane to the peroxide is realized by a π-electron pair partially shared with the Ti-hydroperoxo complex. As a consequence of this, the bond between the two peroxo oxygens is much stretched such that one of the oxygen atoms can migrate to the organic molecule forming an epoxide.

Fig. 1.6. Mechanism of olefin epoxidation suggested by Vayssilov and van Santen [154].

Clerici et al. [155] suggested two ways of olefin oxidation (Fig. 1.7). In this mechanism, together with hydrogen peroxide, a solvent molecule is also coordinated to the Ti center forming an extended Ti-hydroperoxo complex. In one case the substrate molecule reacts with the oxygen atom in second position. According to Clerici et al.

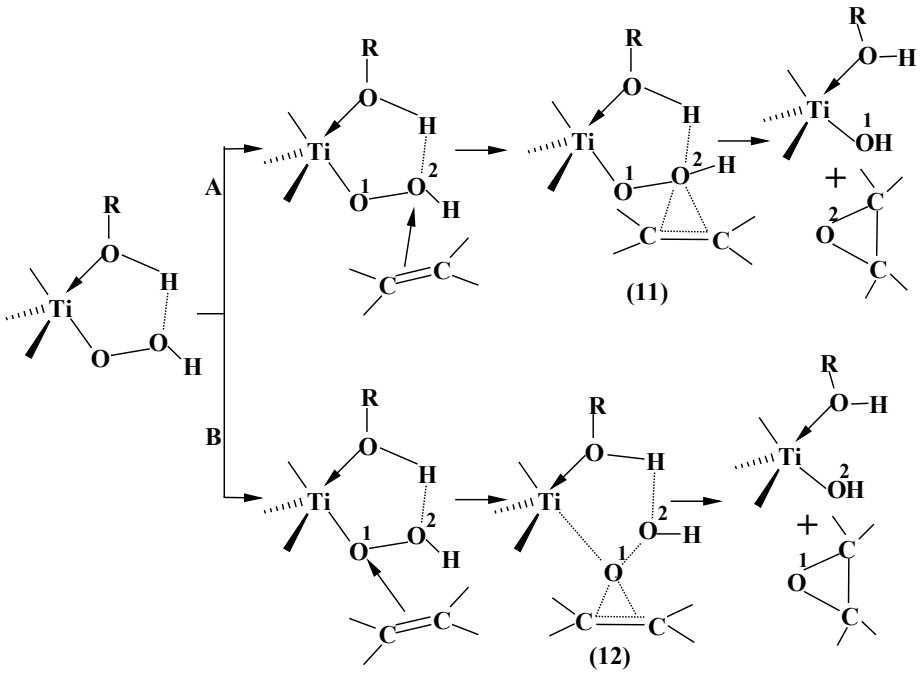

[155] this mechanism is more consistent with lower olefins. In the second mechanism, the substrate molecule reacts with oxygen atom at the first position and the same products are formed as in the first version. However, this attack is disfavored due to steric reasons. However, it is still a debatable that which of the transition states are really favored and formed and what is the mode of O-O bond cleavage in the oxo-species and how does it affect the product selectivity?

Fig. 1.7. Two possible ways of oxidation of olefins proposed by Clerici et al. [155].

1.6. Spectroscopic Methods for Detection of Reactive Oxo Species

The oxo-species formed on Ti and V surfaces are very transient and can best be studied by *in situ* spectroscopic techniques. EPR spectroscopy is very helpful in the identification and quantification of paramagnetic species such as superoxo-Ti and V species. Further, it is a sensitive tool in distinguishing the superoxo species having different structural and magnetic environments. While EPR spectroscopy can identify only the paramagnetic oxo species, diffuse reflectance UV-visible (DRUV-visible) spectroscopy can detect both paramagnetic (superoxo-, for example) and diamagnetic (hydroperoxo- and peroxo, for example) species.

The O-centered free radicals that are formed by homolytic cleavage of O-O bond in oxo-Ti/V species are very short lived (*ca.* 10^{-9} sec. for $HO^{\bullet}$). Their identification can be made possible by forming stable adducts with spin traps. The half-life of these adducts is thus increased to about half a minute, which is sufficient to detect by conventional EPR spectroscopic techniques.

1.6.1. Electron Paramagnetic Resonance (EPR) Spectroscopy

EPR spectroscopy provides information about the oxidation state of metal ions as well as presence of paramagnetic intermediates, such as $O_2^{-\bullet}$, $O^{-\bullet}$ etc. The paramagnetic species are characterized by the Hamiltonian parameters like g and A-values. The g-value for a free electron is isotropic and has a value of 2.0023. But, when this electron is in an orbital having non-zero orbital angular momentum, the g becomes anisotropic and deviates from the free-electron value. The extent of deviation of g-value from g_e depends on the type of orbital it is associated with. In general, the components of the g-matrix are given by

$$\mathbf{g}_{ij} = \mathbf{g}_{\beta}\delta_{ij} + 2\sum_{K}\sum_{\mathbf{m}\,\tau\,\beta}\frac{\zeta_K\langle m|l_{ki}|O\rangle\langle O|l_{kj}|m\rangle}{E_0 - E_m}$$

where, the indices i and j refer to molecular coordinate axes (x, y and z), K sums over atoms with unpaired electron density, and m sums over filled and empty molecular orbitals with energy E_m (E_0 is the energy of the semi-occupied molecular orbital

(SOMO); ζ_k is the spin-orbit coupling constant for atom k, and l_{ki} is the i-component orbital angular momentum operator for the atom k. The integrals $\langle m | l_{ki} | n \rangle$ are easily computed if the MO's are written as linear combination of atomic orbitals. Spin orbit coupling to empty MO's (E_0-E_m<0) gives a negative contribution to g_{ij} whereas coupling to the filled MO's has the opposite effect. Thus the EPR spectra of d^1 systems (Ti^{3+} and V^{4+}, for example) generally have g-values smaller than g_e whereas for d^9 (Cu^{2+} system, for example) the g values are greater than the free-spin value (g_e).

The free ($O_2^{-\bullet}$) has the electronic configuration of $(1\sigma_g)^2\ (1\sigma_u)^2\ (2\sigma_g)^2\ (2\sigma_u)^2\ (3\sigma_g)^2\ (1\pi_u)^4\ (1\pi_g)^3$ with a $^2\pi$ ground state. Interaction with Ti or V centers, for example removes the degeneracy of the HOMO π_g into π_g^x and π_g^y orbitals with energy separation being Δ. The g-value expressions for the ($O_2^{-\bullet}$) radicals when $\lambda < \Delta \ll E$ and neglecting the second terms can be written as

$$g_x \approx g_e$$

$$g_y = g_e + 2\lambda/ E$$

$$g_z = g_e + 2\ \lambda/ \Delta$$

where, λ is the spin-orbit coupling constant (λ = 135 cm^{-1} for oxygen) and E is the energy separation between $3\sigma_g$ and the $1\ \pi_g^x$ orbitals.

Further, EPR-spin trapping experiments are efficient techniques for the identification and quantification of the highly short-lived reactive oxo species (ROS) like $O_2^{-\bullet}$, $HO^{\bullet}$, $HOO^{\bullet}$.

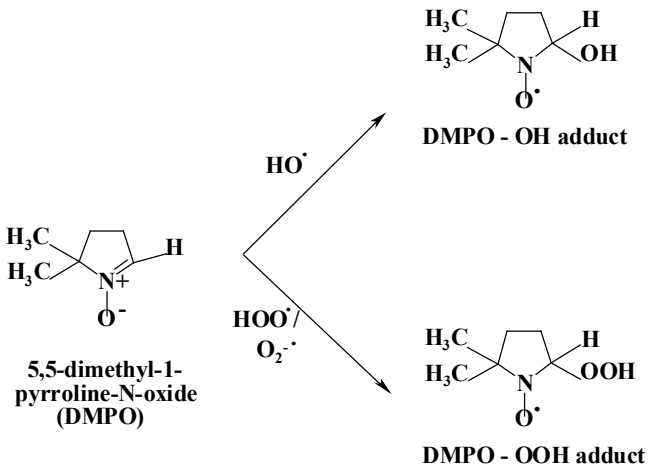

Fig. 1.9. DMPO-spin adducts

All these spin-adducts are paramagnetic and can be distinguished by EPR since they differ in their Hamiltonian parameters. The unpaired electron on nitroxyl group interacts with the nuclear spin of N (I = 1), causing three hyperfine features (with hyperfine coupling constant (hfc) being a_N). Each of these split further into two lines by the β-hydrogen coupling (a_H) (I = 1/2). The γ-H interaction is also often felt. The splitting pattern is governed by the selection rule (2I +1) as shown below.

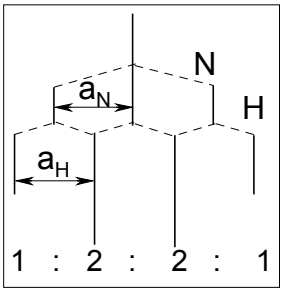

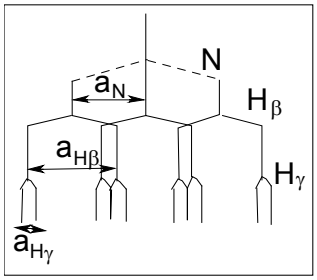

Ex: DMPO-OH ($a_N = a_H$) Ex: DMPO-OOH ($a_N \neq a_{H\beta} \neq a_{H\gamma}$)

However, the Hamiltonian parameters (g, a_N, $a_{H\beta}$ and $a_{H\gamma}$) of superoxo- and hydroperoxo-DMPO adducts are almost identical and hence, these species cannot be differentiated by EPR spectroscopy. The typical ESR spectra of different O-centered radical adducts are shown in Fig.1.9.

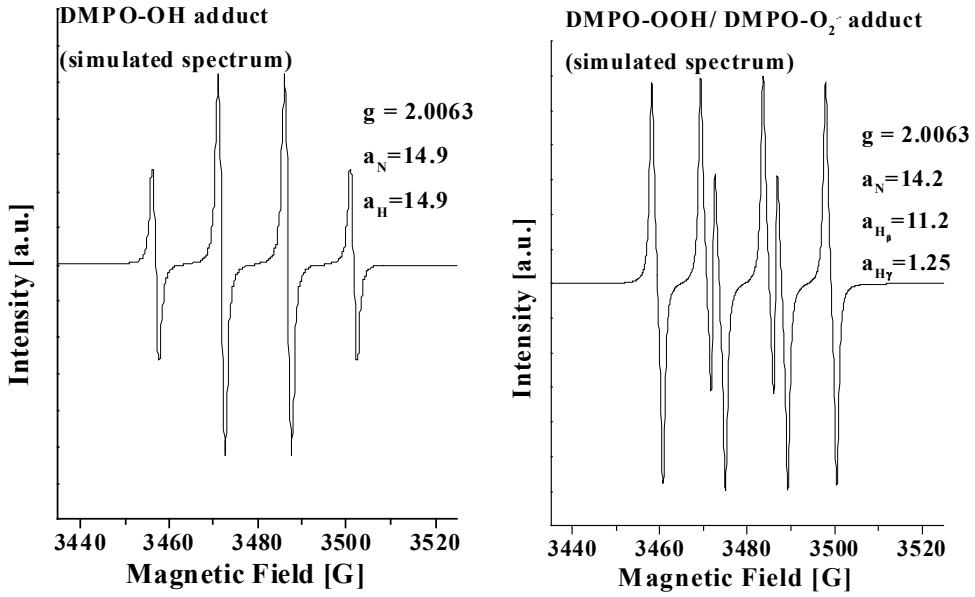

Fig. 1.9. Typical EPR spectra of O-centered radical adducts.

Cu^{2+} has an electron spin of ½ and nuclear spin of 3/2. At a particular sample orientation in a condensed matter one observed four hyperfine features. Since there are two isotopes for copper (^{63}Cu and ^{65}Cu), in ideal cases one should be able to distinguish the two sets of quartets corresponding to ^{63}Cu and ^{65}Cu, respectively. The g and A values are highly sensitive to the location and environment of the Cu^{2+} ion. In the case of a dimeric Cu^{2+}-Cu^{2+} system, one observes a seven-line hyperfine pattern with intensities of signals in the ratio of 1:6:15:20:15:6:1. In other words, EPR spectroscopy is a powerful tool to differentiate different types of copper species.

1.6.2. Diffuse Reflectance UV-Visible (DRUV-Visible) Spectroscopy

DRUV-visible spectroscopy is an ideal technique to study solids, particularly dispersed oxides and metal ions in constrained environments such as those in zeolitic or molecular sieve materials. It gives the information about the coordination and oxidation state of the transition and rare earth metal ions. One of the advantages of DRUV-visible spectroscopy is that, the obtained information is directly chemical since the outer shell electrons are probed. Further, this technique provides quantitative information.

In the diffuse reflectance spectrum, the ratio of light scattered from an infinitely thick layer and the scattered light from an ideal non-absorbing reference sample is measured as a function of wavelength λ. The incident light is partially absorbed and partially scattered. The scattered radiation, emanating from the sample is collected in an integration sphere and detected. The basic equation for the phenomenological description of diffuse reflection is the radiation transfer equation:

$$-dI/(\kappa\rho\, dS) = I - j/\kappa'$$

where I is the incident light intensity of a given wavelength; dI/ dS is the change of the intensity with the path length dS; ρ is the density of the medium; κ an attenuation coefficient corresponding with the total radiation loss due to absorption and scattering; j is the scattering function.

In this theory, the incident and scattered light flux are approximated by two fluxes I and J perpendicular to the surface of the powdered sample, but in the opposite direction. I is the flux of monochromatic diffuse illumination, and J is the flux of diffusively scattered light. If the sample is infinitely thick, the diffuse reflectance of the sample (R_∞)

is related to an apparent absorption (K) and apparent scattering coefficient (S) via the Kubelka-Munk (K.M.) function:

$$f(R) = (1-R^2)/ 2R = k/s$$

where R is the absolute reflectance of the sampled layer, k is the molar absorption coefficient and s is the scattering coefficient.

1.7. Scope and Objectives

The major limitation of titanosilicate (TS-1) molecular sieves is their application only to substrates of smaller dimensions. Although there has been a significant progress in developing large and mesopore metallosilicate molecular sieves (Ti-beta, Ti-HMS, Ti-MCM-41, Ti-SBA-15 etc., for example), the intrinsic activity of Ti in those mesoporous materials is lower than that in TS-1. Further, selectivity for epoxides is also lower in the case of mesoporous than in microporous materials. A systematic and detailed understanding of the factors affecting oxo species generation and O-O bond cleavage in metallosilicate molecular sieves would help developing efficient, large and mesoporous metallosilicate molecular sieves for oxidation of bulkier organic molecules for pharmaceutical applications.

The oxygen storage-release capacity of the ceria-based materials chiefly depends on the composition of support oxide material and the method of preparation. The support composition influences the nature, type and dispersion of the supported metal. A detailed study would enable designing efficient metal-ceria-based catalysts for application in selective oxidations at mild conditions. Electron paramagnetic resonance (EPR) spectroscopy together with diffuse reflectance UV-visible (DRUV-vis) and vibrational spectroscopy and magnetic susceptibility is an ideal combination for the study of active sites and transient reactive oxo-species formed during the reactions. Accordingly, the objectives of the present work are as follows:

(1) To synthesize and characterize micro and mesoporous titano- and vanadosilicates and copper supported CeO_2/ TiO_2/ ZrO_2 catalysts. To investigate their catalytic activities for various selective oxidations.

(2) To generate oxo species *in situ* in these catalyst systems by contacting with hydrogen peroxide or (H_2 + O_2) and study using EPR/ magnetic susceptibility/DRUV-visible techniques.

(3) To examine the influence of surface modification (with noble metal ions and alkali/alkaline earth metal ions) of titanosilicates on the nature and type of oxo-species formation and chemoselectivity in oxidation reactions.

(4) To study the factors influencing O-O bond cleavage of oxo-titano and vanado species.

(5) To investigate the support composition in $CeO_2/ZrO_2/TiO_2$–based catalysts on metal (Cu) speciation, oxygen storage-release capacity and catalytic activity in oxidative dehydrogenation of ethylbenzene and preferential CO oxidations in hydrogen-rich-fuels.

(6) Finally, to understand the structure-activity correlations and factors governing the selectivity of metallosilicates and mixed oxide catalysts in hydrocarbon oxidation reactions.

1.8. Outline of the Thesis

Accordingly, the thesis is divided into eight chapters including the present Chapter-1 on general introduction.

Chapter-2 describes the synthesis methodologies of various catalyst systems investigated in the present work. The various catalysts investigated in the present work include:

Titanosilicates- TS-1, Ti-MCM-41, Ti-SBA-15;

Metal modified titanosilicates- M-TS-1, where M = Pt and Pd;

Alkali modified titanosilicates- M'-TS-1 and M'-Ti-MCM-41, where M'= Li, Na, K, Cs, Mg and Ca;

Vanadosilicates- VS-1 and V-MCM-41;

CuO incorporated CeO_2-based catalysts – CuO-CeO_2, CuO-ZrO_2, CuO-TiO_2, CuO-CeO_2-ZrO_2 and CuO-CeO_2-TiO_2.

Detailed experimental procedures for the catalytic activity tests (epoxidation of allyl alcohol, allyl chloride, styrene and cyclohexene, oxidative dehydrogenation of ethylbenzene and preferential CO oxidation) and product analysis procedures are also presented in this chapter.

Chapter-3 deals with the study of oxo-species and chemoselective epoxidation of ally alcohol and allyl chloride over noble metal (Pd and Pt) modified TS-1

catalysts. The oxo species are produced by contacting the molecular sieves with (H_2 + O_2) or aqueous H_2O_2. For comparison, studies were also made on unmodified microporous TS-1 and mesoporous Ti-MCM-41 and Ti-SBA-15 molecular sieves.

Chapter-4 reports the effect of alkali and alkaline earth metal ion modification of TS-1 and Ti-MCM-41 on the chemoselective epoxidation activity with aqueous H_2O_2.

Chapter-5 describes studies on the mode of O-O bond cleavage (homolysis *vs* heterolysis) in oxo-Ti species and the factors influencing the cleavage. The consequences of O-O cleavage in product selectivity in the oxidation of cyclohexene were investigated. Influence on the addition of radical quenchers to the reaction medium was examined.

Chapter-6 reports the oxo species generated on vanadosilicate molecular sieves (VS-1 and V-MCM-41). The influence of silicate structure, oxidant and solvent on the type of oxo-species formed and the mode of O-O bond cleavage is investigated.

Chapter-7 deals with the spectroscopic and catalytic activity studies of CuO containing CeO_2, ZrO_2, TiO_2, CeO_2-ZrO_2 and CeO_2-TiO_2. The influence of support structure on oxygen storage capacity, metal speciation and metal redox behavior is investigated. Catalytic activities of the catalysts in oxidative dehydrogenation of ethylbenzene with N_2O and preferential CO oxidation in H_2-rich fuels have been examined.

Chapter-8 provides an executive summary and conclusions of the work presented in the thesis.

By and large, the thesis explores the ways and means of improving chemoselectivity in selective oxidations over titano- and vanadosilicate molecular sieves and ceria-based catalysts. The objective is achieved by logically examining the types of reactive oxygen species formed during oxidation reactions and factors affecting their concentration and reactivity. The work presented in the thesis is expected to help developing more efficient, solid, oxidation catalysts. It throws light on the fundamental understanding of reaction mechanisms in organic oxidation reactions.

1.9. References

[1] R.A. Sheldon, J.K. Kochi, "Metal-Catalyzed Oxidations of Organic Compounds" Academic Press, New York, 1981.

[2] R.A. Sheldon, Heterogeneous Catalytic Oxidation and Fine Chemicals, Stud.

Surf. Sci. Catal. 66 (1991) 33.

[3] R.A. Sheldon, I.W.C.E. Arends, H.E.B. Lempers, Catal. Today 41 (1998) 387.

[4] R.A. Sheldon, CHEMTECH, (1991) 566.

[5] R.A. Sheldon, J. Mol. Catal. A: Chemical, 107 (1996) 75.

[6] P.Gallezot, Selective Oxidation with Air on Metal Catalysts, Catal. Today 37 (1997) 405.

[7] K. Shimizu, T. Kaneko, T. Fujishima, T. Kodama, H. Yoshida, Y. Kitayama, Appl. Catal. A: General 225 (2002) 185.

[8] Y. Moro-oka, M. Akita, Catal. Today 41 (1998) 327.

[9] R.K. Graselli, Catal. Today 49 (1999) 141.

[10] T. Katsuki, J. Mol. Catal. A: Chemical 113 (1996) 87.

[11] T. Katsuki, Coord. Chem. Rev. 140 (1995) 189.

[12] A.R. Silva, C. Freire, B. de Castro, New. J. Chem. 28 (2004) 253.

[13] C. Piovezan, K.A.D.F. de Castro, S.M. Drechsel, S. Nakagaki, Appl. Catal. A 293 (2005) 97.

[14] A.C. Rosenzwieg, C.A. Frederick, S.J. Lippard, P. Nordlund, Nature 366 (1993) 537.

[15] J. Green, H. Dalton, J. Biol. Chem. 264 (1998) 17696.

[16] R. Parton, D. De Vos, P.A. Jacobs, Zeolite Microporous Solids: Synthesis, Structure and Reactivity, in: E.G. Derouane et al. (Ed.), Kluwer, Dordrecht, The Netherlands, (1992), 555.

[17] J.M. Thomas, J. Mol. Catal. A: Chemical 115 (1997) 371.

[18] R.A. Sheldon, J. Mol. Catal. A: Chemical, 7 (1980) 107.

[19] R.A. Sheldon, J.D. Chen, J. Dakka, E. Neelemen, Stud. Surf. Sci. Catal., 82 (1994) 515; ibid. 83 (1994) 107; R.A. Sheldon, J. Dakka, Catal. Today, 19 (1994) 215.

[20] M. Taramasso, G. Perego, B. Notari, US Patent 4,410,501 (1993) to SNAM Progetti.

[21] B. Notari, Stud. Surf. Sci. Catal., 37 (1987) 413.

[22] B. Notari, Adv. Catal. 41 (1996) 253.

[23] P. Kumar, R. Kumar, B. Pandey, Synlett (1995) 289.

[24] M. Ramaswamy, H.W. Roesky, Angew. Chem. Int. Ed. Engl. 36 (1997) 477.

[25] R.A. Sheldon, I.W.C.E. Arends, H.E.B. Lempers, Heterogeneous catalysts for liquid phase oxidations (supported reagents and catalysis in chemistry). Spec. Publ. R. Soc. Chem. 216 (1998) 37.

[26] R.A. Sheldon, I.W.C.E. Arends, H.E.B. Lempers, Collect. Czech. Chem. Commun. 63 (1998) 1724.

[27] M.G. Clerici, in Fine Chemicals through Heterogeneous Catalysis (2001) 538.

[28] J. Patarin, H. Kessler, J. Guth, Zeolites 10 (1990) 674.

[29] M.S. Rigutto, H. van Bekkum, Appl. Catal. 68 (1991) L1.

[30] A. Corma, M.T. Navarro, J. Perezpariente, J. Chem. Soc., Chem. Commun. (1994) 147.

[31] T. Blasco, A. Corma, M.T. Navarro, J. Perezpariente, J. Catal. 156 (1995) 65.

[32] P.T. Tanev, M. Chibwe, T.J. Pinnavaia, Nature 368 (1994) 321.

[33] S. Gontier, A. Tuel, Zeolites 15 (1995) 601.

[34] J.S. Reddy, A. Dicko, A. Sayari, in "Synthesis of Porous Materials: Zeolites, Clays and Nanostructures" (M. Occelli and H. Kessler, Eds.) p. 405-415. Marcel Dekker, New York, 1997.

[35] K.A. Koyano, T. Tatsumi, Chem. Commun. (1996) 145.

[36] S.A. Bagshaw, E. Prouzet, T.J. Pinnavaia, Science 269 (1995) 1242.

[37] S.A. Bagshaw, F. Di Renzo, F. Fajula, Chem. Commun.(1996) 2209.

[38] M.S. Morey, S. O'Brien, S. Schwarz, G.D. Stucky, Chem. Mater. 12 (2000) 898.

[39] Z. Luan, L. Kevan, Micropor. Mesopor. Mater. 44/45 (2001) 337.

[40] B.L. Newalkar, J. Olanrewaju, S. Komarneni, Chem. Mater. 13 (2001) 552.

[41] O.A. Kholdeeva, A. Yu Derevyankin, A.N. Shmakov, N.N. Trukhan, E.A. Paukshtis, A. Tuel, V.N. Romannikov, J. Mol. Catal. A: Chemical 158 (2000) 417.

[42] N.N. Trukhan, A. Yu Derevyankin, A.N. Shmakov, E.A. Paukshtis, O.A. Kholdeeva, V.N. Romannikov, Micropor. Mesopor. Mater. 44/45 (2001) 603.

[43] N.N. Trukhan, V.N. Romannikov, E.A. Paukshtis, A.N. Shmakov, O.A.

Kholdeeva, J. Catal. 202 (2001) 110.

[44] P. Wu, T. Tatsumi, T. Komatsu, T. Yashima, J. Phys. Chem. B 105 (2001) 2897.

[45] Z. Shan, J.C. Jansen, L. Marchese, Th Maschmeyer, Micropor. Mesopor. Mater. 48 (2001) 181.

[46] L. Zhao, G. Zhu, D. Zhang, Y. Chen, S. Qiu, J. Solid State Chem. 178 (2005) 2980

[47] X. Feng, G.E. Fryxell, L.Q. Wang, A.Y. Kim, J. Liu, K.M. Kemner, Science 276 (1997) 923.

[48] A.M. Liu, K. Hidajat, S. Kawi, D.Y. Zhao, Chem. Commun. (2000) 1145.

[49] Q.H. Yang, H. Liu, H. Yang, L. Zhang, Z.C. Feng, J. Zhang, C. Li, Micropor. Mesopor. Mater. 77 (2005) 257.

[50] W.M. Van Rhijn, D.E. De Vos, B.F. Sels, W.D. Bossaert, P.A. Jacobs, Chem. Commun. (1998) 317.

[51] D. Das, J.F. Lee, S.F. Cheng, Chem. Commun. (2001) 2178.

[52] I.K. Mbaraka, D.R. Radu, V.S.Y. Lin, B.H. Shanks, J. Catal. 219 (2003) 329.

[53] S. Hamoudi, S. Kaliaguine, Micropor. Mesopor. Mater. 59 (2003) 195.

[54] S. Hamoudi, S. Royer, S. Kaliaguine, Micropor. Mesopor. Mater. 71 (2004) 17.

[55] T. Tatsumi, K.A. Koyano, N. Igarashi, Chem. Commun. (1998) 325.

[56] F. Maspero, U. Romano, J. Catal. 146 (1994) 476.

[57] G. Bellussi, A. Carati, M.G. Clerici, G. Maddinelli, R. Millini, J. Catal. 133 (1992) 220.

[58] A. Thangaraj, L. Puthoor, S. Sivasanker, Ind. J. Chem. 33A (1994) 255.

[59] M.A. Uguina, D.P. Serrano, G. Ovejero, R.V. Grieken, M. Camacho, Appl. Catal. A 124 (1995) 391.

[60] N.K. Mal, A.V. Ramaswamy, J. Mol. Catal. A: Chemical 105 (1996) 149.

[61] W. Lin, H. Frei, J. Am. Chem. Soc. 124 (2002) 9292.

[62] S. Bordiga, A. Damin, F. Bonino, G. Ricchiardi, A. Zecchina, R. Tagliapietra, C. Lamberti, Phys. Chem. Chem. Phys. 5 (2003) 4390.

[63] G. Sankar, J.M. Thomas, C.R.A. Catlow, C.M. Barker, D. Gleeson, N.

Kaltsoyannis, J. Phys. Chem. B 105 (2001) 9028.

[64] D. Gleeson, G. Sankar, C.R.A. Catlow, J.M. Thomas, G. Spanò, S. Bordiga, A. Zecchina, C. Lamberti, Phys. Chem. Chem. Phys. 2 (2000) 4812.

[65] A. Carati, C. Flego, E.P. Massara, R. Millini, L. Carluccio, W. Jr. Parker, G. Bellussi, Micropor. Mesopor. Mater. 30 (1999) 137.

[66] S. Krijenen, P. Sánchez, B.T.F. Jakobs, J.H.C. van Hooff, Micropor. Mesopor. Mater. 31 (1999) 163.

[67] K. Chaudhari, D. Srinivas, P. Ratnasamy, J. Catal. 203 (2001) 25.

[68] D. Srinivas, P. Manikandan, S.C. Laha, R. Kumar, P. Ratnasamy, J. Catal. 217 (2003) 160.

[69] L. Bonoldi, C. Busetto, A. Congiu, G. Marra, G. Ranghino, M. Salvalaggio, G. Spanò, E. Giamello, Spectrochim. Acta 58A (2002) 1143.

[70] H. He, H.X. Dai, L.H. Ng, K.W. Wang, C.T. Au, J. Catal. 206 (2002) 1.

[71] L. Li, G. Li, Y. Che, W. Su, Chem. Mater. 12 (2000) 2567.

[72] Y. Liu, T. Hayakawa, K. Suzuki, S. Hamakawa, T. Tsunoda, T. Ishii, M. Kumagai, Appl. Catal. A: General 223 (2002) 137.

[73] J.R. Ladebeck, J.P. Wagner, in: W. Vielstich, et al. (Eds.), Handbook of Fuel Cell Technology—Fundamentals, Technology, and Applications, Wiley, 2003 Ch. 17.

[74] R.J. Gorte, S. Zhao, Catal. Today 104 (2005) 18.

[75] T. Shido, Y. Iwasawa, J. Catal. 136 (1992) 493.

[76] T. Shido, Y. Iwasawa, J. Catal. 141 (1993) 71.

[77] S.H. Oh, R.M. Sinkevitch, J. Catal. 142 (1993) 254.

[78] M. Haruta, Catal. Today 36 (1997) 153.

[79] P.P. Silva, A.F. Silva, H.P. Souza, A.G. Lobo, L.V. Mattos, F.B. Noronha, C.E. Hori, Catal. Today 101 (2005) 31.

[80] Y.F. Yu Yao, J. Catal. 87 (1984) 152.

[81] A. Holmgren, B. Andersson, J. Catal. 178 (1998) 14.

[82] H.C. Yao, Y.F. Yu Yao, J. Catal. 86 (1984) 254.

[83] T. Miki, T. Ogawa, M. Haneda, N. Kakuta, A. Ueno, S. Tateishi, S. Matsuura, M. Sato, J. Phys. Chem. 94 (1990) 6464.

[84] A. Martìnez-Arias, M. Fernández-García, O. Gálvez, J. M. Coronado, J. A. Anderson, J. C. Conesa, J. Soria, G. Munuera, J. Catal. 195 (2000) 207.

[85] S.J. Tauster, S.C. Fung, R.L. Garten, J. Am. Chem. Soc. 100 (1978) 170.

[86] G. Djéga-Mariadassou, F. Fajardie, J.-F. Tempeŕe, J.-M. Manoli, O. Touret, G. Blanchard, J. Mol. Catal. A: Chem. 161 (2000) 179.

[87] A. Trovarelli, *Catal. Rev.-Sci. Eng.* 38 (1996) 439, and references therein.

[88] M. Fernández-García, A. Martìnez-Arias, A. Iglesias-Juez, C. Belver, A.B. Hungria, J.C. Conesa, J. Soria, J. Catal. 194 (2000) 385.

[89] R. Szostak, Molecular Sieves, Principles of Synthesis and Identification, Blackie Academic and Professional, London, 1998.

[90] I. Schmidt, A. Krogh, K. Wienberg, A. Carlsson, M. Brorson, C.J.H. Jacobsen, Chem. Commun. (2000) 2157.

[91] A.J.H.P. Van der Pol, A.J. Verduyn, J.H.C. van Hooff, Appl. Catal. A: Gen. 92 (1992) 113.

[92] U. Romano, A. Esposito, F. Maspero, C. Neri, M.G. Clerici, Chim. Ind. 72 (1990) 610.

[93] T. Tatsumi, M. Yako, M. Nakamura, Y. Yuhara, H. Tominaga, J. Mol. Catal. 78 (1993) L41.

[94] M.G. Clerici, G. Bellussi, U. Romano, J. Catal. 129 (1991) 159.

[95] J.A. Martens, Ph. Buskens, P.A. Jacobs, A. van der Pol, J.H.C. van Hooff, C. Ferrini, H.W. Kouwenhoven, P.J. Kooyman, H. van Bekkum, Appl. Catal. A: Gen. 99 (1993) 71.

[96] Z. Tvaruzkova, N. Zilkova, Appl. Catal. A: Gen. 103 (1993) L1.

[97] F. Maspero, U. Romano, J. Catal. 146 (1994) 476.

[98] M.G. Clerici, Appl. Catal. 68 (1991) 394.

[99] P. Ratnasamy, D. Srinivas, H. Knözinger, Adv. Catal. 48 (2004) 1.

[100] G. Belussi, A. Carati, M.G. Clerici, A. Esposito, R. Millini, F. Buonomo, Belg, Patent No. 1,001,038 (1989) to ENIricerche, S.p.A., Snamprogetti S.p.A., ENIchem S.p.A.

[101] J.S. Reddy, R. Kumar, P. Ratnasamy, Appl. Catal. 58 (1990) L1.

[102] D.P. Serrano, L. Hong-Xin, M.E. Davis, J. Chem. Soc. Chem. Commun.

(1992) 745.

[103] M.A. Camblor, A. Corma, A. Martinez, J. Pérezpariente, J. Chem. Soc. Chem. Commun. (1992) 589.

[104] M.A. Camblor, A. Martinez, J. Pérezpariente, Zeolites 13 (1993) 82.

[105] A. Corma, M.A. Camblor, P. Esteve, A. Martinez, J. Pérezpariente, J. Catal. 145 (1994) 151.

[106] M.A. Camblor, M. Costantini, A. Corma, L. Gilbert, P. Esteve, A. Martinez, S. Valencia, Chem. Commun. (1996) 1339.

[107] T. Blasco, M.A. Camblor, A. Corma, P. Esteve, J.M. Guil, A. Martinez, J.A. Perdigon-Melon, S. Valencia, J. Phys. Chem. B 102 (1998) 75.

[108] R.J. Davis, Z. Liu, J.E. Tabora, W.S. Wieland, Catal. Lett. 34 (1995) 101.

[109] J.C. van der Waal, P.J. Kooyman, J.C. Jansen, H. van Bekkum, Micropor. Mesopor. Mater. 25 (1998) 43.

[110] A. Tuel, Zeolites 15 (1995) 236.

[111] M.G. Clerici, U. Romano, US Patent 4,824,976 (1989) to Eniricerche S.p.A. and ENIchem Sintesi S.p.A.

[112] P.R. Hari Prasad Rao, A.V. Ramaswamy, P. Ratnasamy, J. Catal. 137 (1992) 225.

[113] P.R. Hari Prasad Rao, A.A. Belhekar, S.G. Hedge, A.V. Ramaswamy, P. Ratnasamy, J. Catal. 141 (1993) 595.

[114] P.R. Hari Prasad Rao, A.V. Ramaswamy, P. Ratnasamy, J. Catal. 141 (1993) 604.

[115] K.R. Reddy, A.V. Ramaswamy, P. Ratnasamy, J. Catal. 143 (1993) 275.

[116] A.V. Ramaswamy, S. Sivasanker, Catal. Lett. 22 (1993) 239.

[117] A.V. Ramaswamy, S. Sivasanker, P. Ratnasamy, Microporous Mater. 2 (1994) 451.

[118] P. Kumar, R. Kumar, B. Pandey, Synlett (1995) 289.

[119] A.P. Singh, T. Selvam, Appl. Catal. A: Gen. 143 (1996) 111.

[120] A.P. Singh, T. Selvam, J. Mol. Catal. A: Chem. 113 (1996) 489.

[121] S. Kannan, T. Sen, S. Sivasanker, J. Catal. 170 (1997) 304.

[122] S.C. Laha, R. Kumar, Microporous Mesoporous Mater. 53 (2002) 163.

[123] N.K. Mal, A.V. Ramaswamy, Appl. Catal A: Gen. 143 (1996) 75.

[124] M. Anpo, S.G. Zhang, S. Higashimoto, M. Matsuoka, H. Yamashita, J. Phys. Chem. B 103 (1999) 9295.

[125] S. Higashimoto, M. Matsuoka, S.G. Zhang, H. Yamashita, O. Kitao, H. Hidaka, M. Anpo, Micropor. Mesopor. Mater. 48 (2001) 329.

[126] J.M. Thomas, G. Sankar, Acc. Chem. Res. 34 (2001) 571.

[127] S. Bordiga, A. Damin, F. Bonino, G. Ricchiardi, C. Lamberti, A. Zecchiana, Angew. Chem Int. Ed. 41 (2002) 4734.

[128] T. Tatsumi, Y. Watanabe, Y. Himasawa, J. Tsuchiya, Res. Chem. Intermed. 24 (1998) 529.

[129] A.M. Gasymov, L.K. Przheval'skaya, V.A. Shvets, V.B. Kazanski, Kinet. Katal. 25 (1984) 358.

[130] K.C. Taylor, "Catalysis, Science and Technology" (J.R. Anderson and M. Boudart, Eds.) Springer-Verlag, Berlin, 1984.

[131] P. Larsson, A. Andersson, Appl. Catal. B: Environ. 24 (2000) 175.

[132] J. Kašpar, P. Fornasiero, M. Graziani, Catal. Today 50 (1995) 285.

[133] J. Soria, J. C. Conesa, A. Martínez-Arias, Colloids and Surf. A 158 (1999) 67.

[134] B.K. Cho, *J. Catal.,* 131 (1991) 74.

[135] P. Fornasiero, R. Di Monte, G. Ranga Rao, J. Kaspar, S. Meriani, A. Trovarelli, M. Graziani, J. Catal. 151 (1995) 168.

[136] G. Vlaic, P. Fornasiero, S. Geremia, J. Kaspar, M. Graziani, J. Catal. 168 (1997) 386.

[137] J. Kaspar, P. Fornasiero, M. Graziani, Catal. Today 50 (1999) 285.

[138] R.W. McCabe, H.W. Jen, W. Chun, G.W. Graham, L.P. Haack, A. Straccia, D. Benson, Appl. Catal. A: General 184 (1999) 265.

[139] S.D. Gardner, G.B. Hoflund, B.T. Upchurch, D.R. Schryer, E.J. Kielin, J.Schryer, J. Catal. 129 (1991) 114.

[140] M. Haruta, S. Tsubota, T. Kobayashi, H. Kageyama, M.J. Genet, B. Delmon, J. Catal. 144 (1993) 175.

[141] S.-J. Lee, A. Gavrilidis, J. Catal. 206 (2002) 305.

[142] R.J.H. Grisel, B.E. Nieuwenhuys, J. Catal. 199 (2001) 48.

[143] S.-J. Lee, A. Gavriilidis, Q. A. Pankhusrst, A. Kyek, F.E. Wagner, P.C.L. Wong, K.L. Yeung, J. Catal. 200 (2001) 298.

[144] H. Liu, A.I. Kozlov, A.P. Kozlova, T. Shido, Y. Iwasawa, Phys. Chem. Chem. Phys. 1 (1999) 2851.

[145] J.G.E. Cohn, US Patent No. 3,216,783 (Nov 9, 1965).

[146] K. Takamura, H. Yasushi, US Pat. Apppln. 20010004453 A1 (June 21, 2001).

[147] J. Xiaoyuan, L. Guanglie, Z. Renxian, M. Jianxin, C. Yu, Z. Xiaoming, Appl. Surf. Sci. 173 (2001) 208.

[148] R.J. Bellows, J.L. Robbins, US Patent No. 5,955,214 (Sep 21, 1999).

[149] G. Avgouropoulas, T. Joannides, Ch. Papadopoulou, J. Batista, S. Hicevar, H.K. Matralis, Catal. Today, 75 (2002) 157.

[150] G. Tozzola, M.A. Mantegazza, G. Ranghino, G. Petrini, S. Bordiga, G. Ricchiardi, C. Lamberti, R. Zulian, A. Zecchina, J. Catal. 179 (1998) 64.

[151] D.R.C. Huybrechts, G. Valsen, P.A. Jacobs, Catal. Lett. 8 (1991) 231.

[152] D.R.C. Huybrechts, P.L. Buskens, P.A. Jacobs, J. Mol. Catal. 71 (1992) 129.

[153] R.A. van Santen, Theoretical Heterogeneous Catalysis, World Scientific, Singapore, Ch. 4, (1991).

[154] G.N. Vayssilov, R.A. van Santen, J. Catal. 175 (1998) 170.

[155] M.G. Clerici, P. Ingallina, J. Catal. 140 (1993) 71.

Chapter - 2
Experimental Methodology

2.1. Introduction

This chapter describes the syntheses of various catalyst materials used in the present work. It also presents the methodologies adopted for characterizing the materials and the procedures for catalytic activity experiments. The materials investigated may be classified, broadly, into two categories: (1) Metallosilicate molecular sieves, and (2) Nanocrystalline CuO-containing CeO_2-based mixed oxides. Among the first category of catalysts, several titanosilicates (mesoporous Ti-MCM-41 and Ti-SBA-15 and microporous TS-1) and vanadosilicates (VS-1 and V-MCM-41) have been investigated. The second-category of catalysts consists of varying compositions of CuO-containing CeO_2, ZrO_2, TiO_2, CeO_2-ZrO_2 and CeO_2-TiO_2. The generalized synthesis methodologies that are adopted in the present work include, hydrothermal synthesis, co-precipitation and sol-gel method.

Formation, purity, structural integrity and textural properties of the materials were determined using a range of physicochemical techniques *viz*., chemical analysis (atomic absorption spectroscopy (AAS) and X-ray fluorescence spectroscopy (XRF)), X-ray diffraction (XRD), N_2 adsorption measurements, temperature-programmed reduction (TPR), Fourier transform infrared spectroscopy (FT-IR), diffuse reflectance UV-visible (DRUV-visible), electron paramagnetic resonance (EPR), X-ray photoelectron spectroscopy (XPS), magnetic susceptibility and cyclic voltammetry. The catalytic oxidation reactions investigated include: (1) chemoselective liquid-phase oxidations (allyl alcohol, allyl chloride, styrene, cyclohexene and *n*-hexane), (2) vapor-phase oxidative dehydrogenation of ethylbenzene (EB), and (3) preferential CO oxidation in hydrogen-rich fuels. While this chapter presents only the general procedures, specific details are given in the respective chapters.

The chemicals used in the synthesis and their sources are listed in Table 2.1. Solvents were purified and dried according to the standard procedures [1]. Methanol was purified as follows. First, 50 - 75 ml of previously dried methanol and 5 g of magnesium turnings were taken in a round bottom flask. To it, 0.5 g of iodine was added and the contents were refluxed till the color of iodine disappeared. To it, 1 L of methanol was added and refluxed for half an hour. Then, the solvent was distilled off and preserved under nitrogen atmosphere over activated 4Å molecular sieves.

Acetone was purified by refluxing it over 10 g of $KMnO_4$ for 5 h followed by distillation. The distillate was once again refluxed over 10 g of anhydrous K_2CO_3 for 1 h. Acetonitrile was dried by distilling over anhydrous P_2O_5.

Table 2.1. Chemicals and Starting Materials used in the Present Work

No.	Chemical	Grade	Catalogue No.	Remarks
1	Acetone "dry"	AR, 99%	20868	S.D. Fine-Chem. Ltd., India
2	Acetonitrile	GR, 99%	015	Loba Chemie, Pvt. Ltd. India
3	Allyl alcohol	99%	875	Loba Chemie, Pvt. Ltd. India
4	Allyl chloride	>98%	877	Loba Chemie, Pvt. Ltd. India
5	*tert.*-Butyl hydroperoxide (TBHP)	~ 5.5 M in decane, over molecular sieve 4Å	19997	Fluka Chemika, Switzerland
6	*tert*.-Butyl hydroperoxide (TBHP)	~70% in water	19995	Fluka Chemika, Switzerland
7	Cerous nitrate	GR	2644	Loba Chemie Pvt. Ltd. India
8	Cupric nitrate trihydrate	GR	3075	Loba Chemie Pvt. Ltd. India
9	Cetyltrimethylammonium bromide	98%	37665	S.D. Fine-Chem. Ltd., India
10	Cyclohexene	99%	37873	S.D. Fine-Chem. Ltd., India
11	5,5-Dimethyl-*1*-pyrroline-*N*-oxide	97%	19,458-1	Aldrich Chem. Comp. Inc. USA

12	Ethanol absolute "Omnis"	99.9%	58051	S.D. Fine-Chem. Ltd., India
13	Ethylbenzene	99%	3719-D	Loba Chemie Pvt. Ltd. India (Distilled)
14	*n*-Hexane	AR 99%	20387	S.D. Fine-Chem. Ltd., India
15	Hydrogen peroxide solution 30%	GR	182	Loba Chemie Pvt. Ltd. India
16	Hydrogen peroxide 50%		4099	Loba Chemie Pvt. Ltd. India
17	Methanol extra pure	99%	20158	Loba Chemie Pvt. Ltd. India
18	Palladium(II) acetate	98%	20,586-9	Aldrich Chem. Comp. Inc. USA
19	Poly(ethylene glycol)-block-poly(propylene glycol)-block-poly(ethylene glycol)	Avg. M_n *ca.* 5,800	43,546-5	Sigma-Aldrich, Germany
20	2-Propanol	GR, 99.7%	0963425001046	Merck Ltd., India
21	Styrene monomer	99%	0901	Encore Chemicals
22	Tetraammine palladium(II) chloride monohydrate	99.99+%	32,343-8	Aldrich Chem. Comp. Inc. USA
23	Tetraammine platinum(II) chloride hydrate	99.99%	32,333-0	Aldrich Chem. Comp. Inc. USA
24	Tetrabutyl orthotitanate (TBOT)	99%		Acros Organics, USA
25	Tetraethyl	99%	157810010	Acros Organics,

	orthosilicate (TEOS)			USA
26	Tetramethyl ammonium hydroxide, (25 wt% aqueous TMAOH)		33163-5	S.D. Fine-Chem. Ltd., India
27	Tetrapropyl ammonium hydroxide, (20 wt% aqueous TPAOH)	< 10 ppm Na^+		Catalysis Pilot Plant, NCL, Pune
28	Vanadyl sulfate trihydrate		23,370-6	Aldrich Chem. Comp. Inc. USA
29	Zirconium Oxychloride	GR	6569	Loba Chemie Pvt. Ltd. India

2.2. Materials Preparation

2.2.1. Syntheses of Metallosilicate Molecular Sieves

2.2.1.1. Titanium-containing Molecular Sieves

2.2.1.1.1. Ti-MCM-41

Mesoporous titanium-containing silicate molecular sieve, Ti-MCM-41 (Si/Ti = 33), was prepared by direct hydrothermal synthesis method [2] using a gel of the following molar composition:

SiO_2: 0.03 TiO_2: 0.40 TMAOH: 0.20 CTMABr: 96 H_2O

In a typical preparation, 3.5 g of cetyltrimethylammonium bromide (CTMABr) was dissolved in 70 g of water, under vigorous stirring. To this, tetramethylammonium hydroxide (TMAOH; 1.75 g) was added and stirred for 30 min. To this basic solution, tetraethylorthosilicate (TEOS; 10 g) was added drop-wise (for 30 min) and the slurry was stirred for 30 min. Tetrabutylorthotitanate (TBOT, 0.49 g) dissolved in 10 ml of *iso*-propanol was added to it slowly with vigorous stirring. The resultant mixture was stirred for further 30 min and 12 g of water was added to it. It was then heated at 353 K, under stirring, for 4 h, to remove *iso*-propanol and ethanol produced during the hydrolysis of TEOS. The synthesis gel was then transferred to a Teflon-lined steel

autoclave (100 ml capacity) after adjusting the amount of water lost during the heating treatment. The crystallization was carried out hydrothermally under static conditions at 373 K, for 72 h. The solid obtained was filtered, washed with water and dried at 393 K, for 12 h. It was then calcined at 823 K, for 8 h.

2.2.1.1.2. Ti-SBA-15

In the first step, mesoporous silica SBA-15 was synthesized hydrothermally according to the reported procedure [3]. In a typical synthesis, 4 g of amphiphilic tri-block copolymer, poly(ethylene glycol)-block-poly(propylene glycol)-block-poly(ethylene glycol) ($EO_{20}PO_{70}EO_{20}$; average molecular weight = 5800), was dispersed in 30 g of water and 120 g of 2 M HCl solution with stirring followed by the addition of 8.4 g of TEOS to the homogeneous mixture. The gel was continuously stirred for 24 h, and finally, crystallilzed in a Teflon-lined steel autoclave at 373 K, for 48 h. The solid product was filtered, washed with distilled water and dried in air, at 298 K, for 12 h. It was then calcined at 823 K for 6 h to decompose the tri-block copolymer.

In the second step, Ti was impregnated on SBA-15 by the post-synthesis method [4]. For that, first, TBOT (0.05 g) was taken in 15 ml of glycerol and hydrolyzed with tetrapropylammonium hydroxide (20 wt% TPAOH) while stirring for 4 h. Calcined SBA-15 (200 mg) was added and stirred at 373 K for 72 h. The contents were filtered under vacuum and the solid obtained was dried at 393 K and calcined at 773 K, for 6 h. Si/Ti (mol/mol, input) = 20.

2.2.1.1.3. Titanium Silicalite-1 (TS-1)

Authentic TS-1 samples with Si/Ti = 30, 60 and 80 were obtained as gift from the Catalysis Pilot Plant, National Chemical Laboratory, Pune and at certain times, the samples were prepared according to the procedure of Thangaraj et al. [5] by the hydrothermal synthesis method.

In a typical TS-1 synthesis (Si/Ti = 33), 9.0 g of TEOS was slowly added to 10.5 g of 20% aqueous TPAOH solution (3/4 of the total requirement) while stirring for 30 min. Next, to it, was added a solution containing 0.44 g of TBOT in *iso*-propanol (2 g) over 10 min. It was stirred for another 30 min, to complete hydrolysis. Then, the remaining TPAOH (3.5 g) dissolved in 14 ml of double-distilled water was

added slowly to the above solution in 50 min. The final composition of the clear gel was as follows.

SiO_2: 0.32 TPAOH: 0.03 TiO_2: 36 H_2O

It was stirred at 343 K for 2 h to remove the alcohol liberated during TEOS hydrolysis. Then, 12 ml of water was added to compensate the losses during the heating treatment. The final, clear gel was transferred to a Teflon-lined autoclave (100 ml capacity) and aged for 24 h, at 443 K, under static condition. The solid obtained was washed with distilled water and dried at 393 K, for 12 h, in static air. Later, the solid (as-synthesized material) was calcined at 813 K for 12 h.

2.2.1.1.4. Noble Metal Modified-Titanosilicates : M-TS-1 where M= Pt or Pd

Modified TS-1 samples were prepared by impregnation technique using noble metal salt solutions and TS-1. In the preparation of Pd(n)-TS-1 (n refers to Pd content, 0.5 – 4.5 wt.%) [6], an aqueous solution (15 ml) containing required amount of $[Pd(NH_3)_4]Cl_2.H_2O$ or $Pd(CH_3COO)_2$ was added to TS-1 (3 g) taken in a 50 ml round bottom flask. The slurry was stirred at 353 K, for 20 – 24 h, under N_2 atmosphere. The contents were then dried over a rotavapor (338 K) and then in an oven at 348 K for 15 h. The resultant solid was heated in nitrogen-flow at 423 K for 2 h to accomplish autoreduction of Pd(II) to Pd(0).

Pt(0.015)-TS-1 was prepared similarly, except that $[Pt(NH_3)_4]Cl_2.H_2O$ was used. In the preparation of Pt(0.015)-Pd(1)-TS-1, required amounts of Pd and Pt sources were taken in aqueous solution and the samples were prepared as described above. All the noble metal impregnated samples were grayish in color.

2.2.1.1.5. Alkali and Alkaline Earth Metal Ion Modified-Titanosilicates: M'-TS-1 and M'-Ti-MCM-41, where M' = Li, Na, K, Cs, Mg and Ca

TS-1 and Ti-MCM-41 (40 mg) were initially activated in air, at 673 K. It was then suspended in 10 ml of CH_3OH; pH was adjusted to a desired value using NaOH (for pH above 7) or oxalic acid (for pH of 4.5 and 5.5). The suspension was stirred for 10 – 30 min, and the solid catalyst was separated by centrifugation and air-dried.

TS-1 modified with other alkali and alkaline earth ions (pH = 8) were prepared in a similar manner using the compounds Li_2CO_3, KOH, CsOH, NH_4OH, MgO, CaO and $Ba(OH)_2$.

2.2.1.2. Vanadium-containing Molecular Sieves

2.2.1.2.1. VS-1

VS-1 samples were prepared hydrothermally according to known procedure [7]. In a typical preparation, to 18 g of TEOS (86.4 mmol), 21 g of 20% TPAOH (three fourth of the total amount) was added drop-wise over a period of 30 min with vigorous stirring. To the resultant mixture, 0.728 g of $VOSO_4.5H_2O$ (2.88 mmol for Si/V= 30) in 2.5 g of distilled water was added drop-wise under stirring over 30 min. Remaining TPAOH (7 g) in 20 g of distilled water was added slowly to the above mixture with vigorous stirring for 50 min. The resultant greenish gel was stirred for one hour at 298 K. The pH of the synthesis gel was adjusted to 11.1 with TPAOH. It was then stirred at 353 K for 2.5 h to remove alcohol formed during the hydrolysis of TEOS. 16 ml of water was added to compensate the mass loss while the heating treatment. The composition of the final gel was as follows.

$$SiO_2: 0.32\ TPAOH: 0.033\ VO^{2+}: 28\ H_2O$$

Crystallization was carried out in a Teflon-lined autoclave at 443 K, for 48 h. The crystalline white solid was filtered, washed with distilled water until neutrality, dried at 373 K, for 12 h and calcined at 823 K, in air, for 6 h. The calcined VS-1 material was white in color. However, it turned to orange color upon contact with atmosphere.

2.2.1.2.2. V-MCM-41

V-MCM-41 was prepared by direct hydrothermal synthesis method [8] using the gel of following molar composition:

$$SiO_2: x\ VO^{2+}: 0.20\ CTMABr : 96\ H_2O\ (x = 0.0067, 0.02)$$

In a typical synthesis, 3.5 g of CTMABr was dissolved in 70 g of water under vigorous stirring. In a separate beaker a required amount of $VOSO_4.5H_2O$ (x = 0.08098 and 0.2429 for Si/ V = 150 and 50, respectively) was added to 10 g of TEOS (48 mmol) and 13 g of water under stirring. Later, to this blue slurry was added CTMABr solution drop-wise over 50 min. Aq. solution of NH_4OH was used to adjust the pH to 10.7. This pale blue colored mixture was stirred further for 6 h. It was then

transferred to an autoclave and crystallization was done under static conditions at 373 K for 3 days. The white solid obtained was filtered, washed with distilled water and dried at 373 K for 12 h. It was then calcined at 823 K for 6 h. The calcined V-MCM-41 was white in color and it became yellow upon contact with air.

2.2.2. Syntheses of CuO-incorporated CeO_2-based Materials

2.2.2.1. CeO_2

Ceria was prepared by two different precipitation synthesis methods: (A) aqueous precipitation method [9] and (B) using an ethanolic solution of cerous nitrate.

In the first method (A) (for 5 g batch), $Ce(NO_3)_3.6H_2O$ (12.62 g) was dissolved in 290 ml of distilled water. This solution was added drop-wise to the continuously stirred solution of 0.1 M KOH in water (1 L) taken in a 2 L round bottom flask, placed in a heating mantle, and fitted with a pH electrode, water-cooled condenser and burette containing additional 0.1 M KOH solution. During addition, the temperature of the flask was maintained at 353 K and pH at 10. The cations were precipitated in the form of their hydroxides. The mixture was digested at 353 K for another 3 h and then cooled to 298 K. The precipitate was separated, washed copiously with distilled water until all the potassium ions were removed. It was then air-dried in an oven at 393 K for 8 h. Later, the dried material was crushed into powder and calcined in air at 773 K, for 5 h, to get the final product.

In the second method (B) (for 5 g batch), $Ce(NO_3)_3.6H_2O$ (10 g) was dissolved in absolute ethanol (30 ml). To this, dilute aqueous NH_4OH solution (about 2 %) was added drop-wise with stirring, till the pH of the solution was 7. The hydroxide gel formed was then stirred at 353 K, for 3 h. The solution was evaporated while heating and the yellow colored solid was calcined at 723 K, for 4 h.

2.2.2.2. *ZrO_2*

ZrO_2 was prepared by precipitation route (method A) in the same way as mentioned above except that, $ZrO(NO_3)_2.xH_2O$ (9.42 g) was used as the Zr source.

2.2.2.3. TiO_2

TiO_2 was synthesized by method B using TBOT as the Ti source.

2.2.2.4. CeO_2-ZrO_2

Ce : Zr ratio in the catalysts was 1:1 wt%. The samples (5 g batch) were prepared by co-precipitation method. $Ce(NO_3)_3.6H_2O$ (7.35 g) and $ZrO(NO_3)_2.xH_2O$ (2.80 g) were dissolved separately in distilled water (168 and 120 ml respectively). These solutions were mixed together and added drop-wise to a continuously stirred 0.1 M aq. solution (1 L) of KOH taken in a 2 L round bottom flask, placed in a heating mantle. The rest of the procedure was the same as that in case of CeO_2 synthesis following method A.

2.2.2.5. CeO_2-TiO_2

Ceria-titania materials of varying Ce : Ti ratios (5 : 95, 10 : 90, 20 : 80, 50 : 50 and 95 : 5 mol%) were prepared by the sol-gel technique [10]. In a typical preparation of CeO_2 (5 mol%)-TiO_2 (95 mol%) (5 g batch), TBOT (20.2 g) was dissolved in absolute ethanol (15 ml). To this, $Ce(NO_3)_3.6H_2O$ (1.36 g) dissolved in ethanol (20 ml) was added and kept for stirring at room temperature. 5 ml of water was added to it drop-wise. To the resultant gel, dilute NH_4OH solution (about 2 %) was added drop-wise till the pH was 7. The hydroxide gel formed was stirred at 353 K for 3 h. The gel was evaporated while heating and the solid obtained was dried at 393 K for 12 h and then calcined at 723 K for 4 h.

2.2.2.6. CuO-CeO_2

CuO-CeO_2 was synthesized by two methods: (A) aqueous precipitation method and (B) by using ethanolic solution of cerous nitrate.

In the typical preparation of CuO(1 wt%)-CeO_2 (99 wt%) from the method A (5 g batch), $Ce(NO_3)_3.6H_2O$ (12.48 g) was dissolved in 288 ml of distilled water. $Cu(NO_3)_2.3H_2O$ (0.152 g) was dissolved in 6.3 ml of distilled water separately. The solutions were mixed together and added drop-wise to the continuously stirred solution of 0.1 M KOH in water (1 L) taken in a 2 L round bottom flask, placed in a heating mantle. During the addition, the temperature of the flask was maintained at 353 K and pH at 10. The mixture was digested at 353 K for another 3 h and then cooled to 298 K. The precipitate was separated, washed copiously with distilled water until all the potassium ions were removed. It was then air-dried in an oven at 393 K for 8 h. Later, the dried material was crushed into powder and calcined in air, at 773 K, for 5 h to get the final product. CeO_2 containing varying amounts of CuO (1, 2 and

5 wt.%), hereafter designated as CuO(n)-CeO_2(100 – n), were prepared; n refers to wt% of CuO in the sample.

In the second method (B) (5 g batch), $Ce(NO_3)_3.6H_2O$ and $Cu(NO_3)_2.3H_2O$ were dissolved separately in absolute ethanol and mixed together. To this, dilute aqueous NH_4OH solution (about 2 %) was added drop-wise with stirring till the pH was 7. The hydroxide gel formed was then stirred at 353 K for 3 h. The gel was dried while heating and the solid obtained was calcined at 723 K for 4 h. CeO_2 samples containing 1, 2, 3, 5, 10 and 20 mol% of CuO, hereafter designated as CuO(n')-CeO_2 (100-n'), were prepared; n' refers to mol% of CuO.

2.2.2.7. CuO-ZrO_2

CuO-ZrO_2 was prepared by method A. In a typical preparation of CuO (1 wt%)-ZrO_2 (99 wt%) (5 g batch), 9.28 g of $ZrO(NO_3)_2.xH_2O$ dissolved in 400 ml distilled water and 0.152 g of $Cu(NO_3)_2.3H_2O$ dissolved in 6.3 ml distilled water were used. The samples were designated as CuO(n)-ZrO_2(100-n) where n refers to the wt% of CuO.

2.2.2.8. CuO-TiO_2

CuO-TiO_2 was prepared by the sol-gel method. In a typical synthesis of CuO(5 mol%)-TiO_2 (95 mol%) (5 g batch), TBOT (20.2 g) was first dissolved in ethanol (15 ml). An ethanolic solution of $Cu(NO_3)_2.3H_2O$ (0.76 g in 10 ml) was added to it and kept for stirring at 298 K. To it, 2 ml of water was added drop-wise to make the emulsion. Then, dilute NH_4OH was added to adjust the pH to 7 while stirring. The hydroxide gel formed was then stirred at 353 K for 3 h. The gel was dried while heating and the solid obtained was calcined at 723 K for 4 h. TiO_2 samples containing 1, 2, 3, 5, 10 and 20 mol% of CuO, designated as CuO(n')-TiO_2(100-n'); n' refers to mol% of CuO.

2.2.2.9. CuO-CeO_2-ZrO_2

CuO-CeO_2-ZrO_2 was prepared by method A. Ce:Zr in these materials was 1:1 wt%. In the preparation of CuO (1 wt%)-CeO_2 (49.5 wt%)-ZrO_2 (49.5 wt%) (5 g batch), 6.24 g of $Ce(NO_3)_3.6H_2O$ dissolved in 144 ml of distilled water, 4.64 g of $ZrO(NO_3)_2.xH_2O$ dissolved in 200 ml of distilled water, and 0.152 g of $Cu(NO_3)_2.3H_2O$ dissolved in 6.3 ml of distilled water were used. The catalysts were

prepared in a similar manner as described above. The samples were designated as CuO(n)-CeO_2 (50-n/2)-ZrO_2(50-n/2), where n refers to wt% of CuO in the sample.

2.2.2.10. CuO-CeO_2-TiO_2

CuO-CeO_2-TiO_2 was prepared by the sol-gel method. In a typical synthesis of Cu (5 mol%)-CeO_2 (4.75 mol%)-TiO_2 (90.25 mol%), $Cu(NO_3)_2.3H_2O$ (0.76 g), $Ce(NO_3)_3.6H_2O$(1.29 g) and TBOT (19.19 g) were dissolved separately in ethanol (10, 20 and 15 ml, respectively) and mixed together and kept for stirring at 298 K. To this, 5 ml of water was added drop-wise to make the emulsion. Then dilute NH_4OH solution (about 2%) was added drop-wise to adjust the pH to 7 while stirring. The hydroxide gel formed was then stirred at 353 K for 3 h. The gel was dried while heating and the solid obtained was calcined at 723 K for 4 h. The samples containing 1, 2, 3, 5, 10 and 20 mol% of CuO and 5, 10, 20 and 50 mol% of CeO_2, designated as CuO(n')-CeO_2(m(100-n')/100)-TiO_2((100-m)(100-n')/100); n' refers to mol% of CuO and m refers to mol% of CeO_2..

2.3. Characterization Procedures

The materials were characterized by a variety of physicochemical and spectroscopic techniques.

2.3.1. Powder X-ray Diffraction (XRD)

XRD studies enabled determination of phase purity, crystallinity and crystal structure of various catalyst systems investigated in the present work [11]. The mesoporous materials (Ti-MCM-41, Ti-SBA-15, V-MCM-41) were analyzed using an X'Pert Pro (Philips) diffractometer with Cu-Kα radiation (λ = 0.15406 nm) and a proportional counter as detector. A divergent slit of 1/32◦ on the primary optics and an antiscatter slit of 1/16◦ on the secondary optics were used to measure the data in the low-angle region. The microporous solids were analyzed using a Rigaku Geigerflex X-ray diffractometer with Ni-filtered Cu-Kα radiation (40 kV, 30 mA). The XRD patterns were measured in the 2θ range of 5 – 50º in the case of microporous metallosilicates and 10 – 90° in the case of CeO_2-based oxide solids at a scan rate of 2 º/min. For mesoporous metallosilicates the XRD patterns were recorded in the 2θ range of 0.5-10º at a scan speed of 0.12 º/ min. Crystallite size of the materials was determined using the Scherrer equation, $L = K\lambda/\beta\cos\theta$, where θ and λ

have their usual meanings. K is a constant approximately taken as 0.9. β is the line width on 2θ scale in radians. Unit cell parameter (a) for cubic systems was found using the equation $a = d_{(111)}\sqrt{3}$. Here d is the interplanar distance obtained from Bragg's equation $n\lambda = 2d \sin\theta$, n is taken as unity.

2.3.2. Diffuse Reflectance UV-Visible (DRUV-Visible)

DRUV-visible spectroscopy is a highly sensitive and useful technique for identification and characterization of metal ions' coordination and location (framework or extra-framework) in metal-containing solid catalysts [12]. The measurements were conducted on a Shimadzu UV-2550 spectrophotometer equipped with an integrating sphere attachment (ISR 2200). In general spectral grade $BaSO_4$ was used as the reference material.

About 2 g of solid catalyst was taken in the sample holder and the measurements were done at 298 K. In certain experiments with metallosilicates the samples were contacted with aqueous H_2O_2 or *tert*.-butyl hydroperoxide (TBHP) and the metal-oxo species were generated *in situ*. The spectra were immediately recorded. Spectral bands were deconvoluted using the Bruker WIN-EPR software package.

2.3.3. Fourier Transform Infrared (FT-IR)

Formation of silicate framework and metal ion incorporation was determined using FT-IR spectroscopy [13]. The spectra were recorded on a Shimadzu FTIR-8201 PC spectrophotometer in the wavenumber range of 400 – 4000 cm^{-1}. The samples were mixed with Nujol mull forming a paste which was then placed in between KBr plates. It was mounted on the sample holder and the spectra were recorded.

2.3.4. Electron Paramagnetic Resonance (EPR)

EPR spectroscopy provided evidence for the formation of oxo-species and the structure and reducibility of metal ions in various catalysts systems studied in the present work [14, 15]. The spectra were recorded on a Bruker EMX spectrometer operating at X-band frequency (ν ≈ 9.4 GHz) and 100 kHz field modulation. The samples were taken the specially designed Suprasil quartz tubes (~ 4 mm o.d.) and activated at elevated temperatures, in air, and the spectra were recorded. Metal oxo species in metallosilicate molecular sieves were generated *in situ* contacting a known amount of metallosilicate (40 mg) with aqueous H_2O_2 or TBHP (~0.1 ml). In certain

cases, the samples were initially soaked with solvents in EPR tubes and then the oxo species were generated contacting peroxides. The redox behavior of the catalysts was investigated by reacting the activated catalysts with dry-hydrogen at elevated temperatures and then dosing with molecular oxygen or air at ambient temperatures. EPR spectra were deconvoluted using the Bruker Simfonia software package. Concentrations of different species were estimated by double integration of the first-derivative EPR plots. Diphenylpicrylhydrazine (DPPH) was used as a standard. Spectral calculations and manipulations were done using the Bruker WIN-EPR software package.

2.3.5. Cyclic Voltammetry (CV)

Cyclic voltammetry enabled determination of the redox behavior of metal ions in solid catalysts investigated in the present study [16]. Cyclic voltammetric measurements were performed using a CHI 660 A (USA) electrochemical instrument. A conventional three-electrode cell assembly was used. Saturated Ag/AgCl as reference and Pt as auxiliary electrodes were used for this purpose. Zeolite-modified graphite electrode was used as working electrode. In the preparation of this electrode, powder samples of zeolite and graphite were mixed together by gentle grinding in a weight ratio of 60:40. It was then made into a pellet (diameter = 10 mm and thickness ~ 1mm) and fixed to a polished silver wire. Silver paint was diluted with *iso*-amyl acetate and a small drop of it was used for making electrical contact between the pellet and wire. It was dried under an IR lamp for 30 min. An adhesive, Araldite gum was applied to hold the pellet and the wire covering the silver paint. The modified electrode was kept for 16 h for drying before it was used in the experiment. 0.1 M KNO_3 solutions were used as electrolyte. Prior to the CV measurements, dissolved oxygen in the electrolyte solution was removed by purging with argon for 30 min. The CV scans were made in the potential range of +1 to –1 V with a scan rate of 50 mV/sec.

2.3.6. Magnetic Susceptibility

Magnetic susceptibility measurements revealed the magnetic properties and provided information about dispersion and the type of active metal species in the catalyst samples [17]. The measurements were conducted with a Lewis-coil force

magnetometer (Series 300, George Associates, USA) coupled with a high vacuum system (10^{-6} torr) with provision for *in situ* treatment in desired gases at elevated temperatures. The measurements were made at 298 K on 10 – 15 mg of catalyst samples. Corrections for sample holder and ferromagnetic impurities, if any were made. Magnetic moment (μ) was calculated by the equation, $\mu = 2.83\sqrt{\chi_g MT}$, where, χ_g is the gram magnetic susceptibility obtained from the instrument, M is molecular weight and T is temperature.

2.3.7. Temperature-Programmed Reduction (TPR)

Reduction behavior and the type of metal species present in the solid catalysts were estimated also by TPR experiments [18]. The measurements were conducted on a Micromeritics AutoChem 2910 instrument using 5% hydrogen-helium (50 ml/min). Ceria based samples (200 mg) were placed in a U-shaped quartz cell and treated under helium at 373 K, for 1 h, under a helium flow of 50 ml/min. The gas composition was then changed to 5% H_2-He (50 ml/min) and the temperature was raised at 5º/ min. H_2 consumption was then measured using a TCD detector.

2.3.8. X-ray Photoemission Spectroscopy (XPS)

The nature, oxidation state and dispersion of surface metal species were estimated by XPS [19]. The spectra were acquired on a VG Microtech Multilab ESCA 3000 instrument with a non-monochromatized Mg Kα X-ray radiation (hν = 1253.6 eV) on calcined powder samples. Base pressure in the analysis chamber was maintained at 3 - 6 × 10^{-10} mbar range. The energy resolution of the spectrometer was set at 0.8 eV at a pass energy of 20 eV. Binding energy (BE) was calibrated with respect to Au $4f_{7/2}$ core level at 83.9 eV. The error in BE values was ±0.1 eV.

2.3.9. Adsorption Measurements

The adsorption studies reveal the pore volume, pore size distribution and surface area of the sample [20]. Adsorption of nitrogen measured by Brunauer-Emmett-Teller (BET) equation at low pressure (10^{-4} Torr) and liquification temperature of N_2 (77 K) is the standard method for the determination of surface area, pore volumes and pore size distribution of molecular sieves. All these measurements were conducted on a Coulter (Omnisorb 100 CX) instrument.

2.3.10. Atomic Absorption Spectroscopy (AAS) and X-ray Fluorescence (XRF)

The metal ion content in the catalyst samples was determined by AAS and XRF techniques. The sample solution required for AAS analysis was prepared by dissolving 200 mg of catalyst in conc. H_2SO_4 and HF (about 2-3 drops) and diluting it to 100 ml with deionized water. The sample solutions, thus, prepared were injected into the sample port of the spectrometer. The metal ion content (in ppm) was estimated from the optical absorption values and calibration plot (made using standard solutions of different concentrations).

The concentration of the Ti-atoms present in titanosilicates, for example, was estimated by XRF based on the intensity of the emitted X-rays [21]. For that, calibration of the instrument was done using reference samples with known Ti content.

2.4. Catalytic Activity Studies – Reaction Procedures

2.4.1. Chemoselective Liquid-Phase Oxidations

2.4.1.1. Oxidation of Allyl Alcohol (AA)

2.4.1.1.1. With Aqueous H_2O_2 as Oxidant

In a typical batch reaction, 100 mg of titanosilicate catalyst (TS-1, Ti-MCM-41, Pd-/Pt-modified TS-1, alkali or alkaline earth metal ion-modified TS-1 and Ti-MCM-41), 10 g of solvent (methanol, acetonitrile or acetone) and 0.5 g of allyl alcohol (AA) were taken in a 50 ml double-necked round-bottom, glass flask fitted with a water-cooled condenser and placed in a temperature-controlled oil bath. To this, a known quantity aqueous H_2O_2 (30 or 50%) was added. The reaction was carried out at 333 K, while stirring for 8 h. The products were analyzed by gas chromatography (CHROMPACK CP 9001; 50 m long, 0.32 mm i.d., and 0.3 μ film thickness Hewlett Packard fused silica capillary column) and identified by GC-MS (Shimadzu, QP-5000; 30 m long, 0.25 mm i.d., and 0.25 μ film thickness capillary column DB-1).

2.4.1.1.2. With (H_2 + O_2) as Oxidant

In reactions with H_2+O_2, 100 mg of the reduced noble metal-modified TS-1 catalyst, 5 g of acetone, 5 g of *iso*-propanol and 0.5 g of AA were taken in a double-

necked round-bottom flask. The reactions were conducted at 333 K, for 8 h, while contacting with O_2 (20 ml/min).

2.4.1.1.3. Influence of pH and Alkali Addition

With alkali-modified titanosilicate catalysts, reactions were carried out in a rotating hydrothermal synthesis reactor unit (Hiro Company, Japan, Model KH-02) maintained at 333 K (FC-410 ADVANTEC Forced Convection Oven) and rotation speed of 30 rpm. The reactions were carried out at different pH conditions and in different solvents (e.g., CH_3OH, CH_3OH + CH_3CN and CH_3COCH_3). In a 100 ml Teflon-lined steel autoclave, 100 mg of unmodified TS-1 or Ti-MCM-41 was taken in a solvent (10 g); pH of the slurry was adjusted to a desired value using NaOH (for pH > 6.8) or oxalic acid (for pH < 6.8). Allyl alcohol (8.62 mmol) and aqueous H_2O_2 (50%, 0.9 ml) were then added. The autoclave was sealed, placed in the reactor and the reaction was carried out for 8 h. At the end of the reaction, the catalyst was separated by centrifugation. Liquid samples were analyzed by gas chromatography as above. The pH of the solution at the end of the reaction was determined. H_2O_2 left out at the end of the reaction was estimated by iodometric titrations.

Epoxidation of allyl alcohol was carried out also in the presence of different alkali metal and alkaline compounds (Li_2CO_3, NaOH, KOH, CsOH, MgO, CaO, $Ba(OH)_2$ and NH_4OH) in a similar manner at pH = 8.0.

2.4.1.2. Oxidation of Allyl Chloride (AC)

The reactions were carried out in a rotating hydrothermal synthesis reactor (Hiro Company, Japan, Model KH-02) at different pH conditions and in different solvents (e.g., CH_3OH, CH_3OH + CH_3CN and CH_3COCH_3). In a 100 ml Teflon-lined steel autoclave, 100 mg of unmodified TS-1 or Ti-MCM-41 and 10 g of solvent were taken. The pH of the slurry was then adjusted to a desired value using NaOH (for pH > 6.8) and oxalic acid (for pH < 6.8). Allyl chloride (8.62 mmol) and aqueous H_2O_2 (50%, 0.9 ml) were then added. The autoclave was sealed, placed in the reactor and the reaction was carried out at 333 K, for 8 h. The products were analyzed by gas chromatography as described above.

2.4.1.3. Oxidation of Styrene

The reactions were carried out in Teflon-lined hydrothermal reactor as described in Section 2.4.1.2 using styrene as substrate.

2.4.1.4. Oxidation of Cyclohexene

In a typical reaction, 0.1 g of titanosilicate (TS-1, Ti-MCM-41 or Ti-SBA-15), 0.82 g of cyclohexene and 5 ml of solvent were taken in a round bottom glass flask fitted with a water-cooled condenser and placed in a constant temperature (333 K) oil bath. H_2O_2 ([cyclohexene]/[H_2O_2] = 3 mol/mol) was added drop-wise over a period of 10 min and then the reaction was carried out for 4 h. The products were analyzed by gas chromatography (CHROMPACK CP9001; 50 m-long x 0.32 mm-i.d. x 0.3 μm thick Hewlett-Packard fused silica capillary column) and identified by GC-MS (Shimadzu QP-5000; 30 m-long x 0.25 mm-i.d. x 0.25 mm-thick capillary DB-1 column).

2.4.1.5. Oxidation of Styrene and Cyclohexene in the Presence of Radical Scavengers

In certain oxidations with cyclohexene and styrene as substrates, the reactions were conducted in the presence of radical scavengers such as mannitol, catechol, thiourea, sodium acetate, sodium salicylate, *p*-benzoquinone, hydroquinone and sodium formate. In those experiments a known quantity of radical scavenger (0 – 0.018 mmol) was added to the reaction mixture and the reaction conducted in a similar manner as described above.

2.4.2. Vapor-Phase Oxidative Dehydrogenation of Ethylbenzene

Oxidative dehydrogenation (ODH) of ethylbenzene was carried out in fixed-bed down-flow glass reactor operated at atmospheric pressure and 673 K. CuO-CeO_2, CuO-TiO_2 and CuO-CeO_2-TiO_2 were used as catalysts. A catalyst sample (1.5 g) was placed at the center of the glass reactor using glass wool plugs. Ethylbenzene was fed with a syringe pump (WHSV = 1) together with N_2O oxidant (50 ml/ min). The products were collected at different time intervals and analyzed by a HP gas chromatograph equipped with a FID detector and SGE BPX 5 column (50 m long and 0.32 mm i.d.).

2.4.3. Preferential CO Oxidation (PROX) in H_2-rich Fuels

PROX reactions were carried out in a fixed-bed, down-flow, glass-reactor (i.d. = 15 mm), using 1.5 g of the calcined catalyst. The sample was made into a pellet (without any binder), crushed and sized (10 – 20 mesh). Then, it was activated at 573 K, for 3 h, in flowing hydrogen and, then cooled to 403 – 473 K. A synthetic feed gas mixture of volume composition H_2 (74.17%) + CO (0.49%) + CO_2 (23.26%) + CH_4 (2.08%) was passed through a mass-flow controller at a specified flow rate (2.5 – 10 l/h; GHSV = 5000 – 20000) along with a required amount of oxygen in air (O_2/CO = 0.5 – 1.5).

Experiments were also conducted with a stream containing added water (1.25 ml/h; $p(H_2O)$ = 200 torr) or an actual effluent from a steam reformer-*cum*-water gas shift reactor processing LPG. The products were analyzed online using a CHEMITO 8610 gas chromatograph equipped with a methanator. A Spherocarb column (1/8 inch diameter x 8 feet length) was used for analysis. A calibrated gas was used as a reference to estimate the concentrations of gases.

2.4.4. H_2O_2 Decomposition over Cu-containing CeO_2-based Materials

In a typical study, 100 mg of catalyst and 50 ml of water were taken in a double-necked, glass, round-bottom flask which was placed in a thermostat. To this, aqueous H_2O_2 (30 %, 1.2 g) was added at a stretch while stirring. The concentration of H_2O_2 in the reaction mixture was estimated by titrating 5 ml of the reaction mixture with standard $KMnO_4$ solution at regular intervals of time. The decomposition reaction was carried out at four different temperatures (300, 306, 312, 318 and 323 K). Since H_2O_2 decomposition follows first-order kinetics, the slope of the straight line from the graph of $\ln(A^o/A)$ *vs*. time (t) gives rate constant (k) for H_2O_2 decomposition. Here, A^o and A are the concentrations of H_2O_2 at 0 h and at time t. Activation energy of the reaction was calculated by multiplying the negative value of the slope (from the graph of ln(k) *vs.* 1/T) with gas constant (R).

2.5. References

[1] A.I. Vogel, A.R. Tatchell, B.S. Furnis, A.J. Hannaford, P.W.G. Smith, "Vogel's Textbook of Practical Organic Chemistry" Eds. Prentice Hall, 1996.

[2] K. A. Koyona, T. Tatsumi, Micropor. Mesopor. Mater.10 (1997) 259.

[3] D. Zhao, J. Feng, Q. Huo, N. Melosh, G. H. Fredrickson, B. F. Chmelka, G. D. Stucky, Science 279 (1998) 548.

[4] M.S.Morey, S.O'Brien, S. Schwarz, G.D. Stucky, Chem. Mater. 12 (2000) 898.

[5] A. Thangaraj, R. Kumar, S.P. Mirajkar, P. Ratnasamy, J. Catal. 130 (1991) 1.

[6] W. Laufer, R. Meiers, W. Hölderich, J. Mol. Catal. A: Chem. 141 (1999) 215.

[7] T. Sen, V. Ramaswamy, S. Ganapathy, R. Rajamohanan, S. Sivasanker, J. Phys. Chem. 100 (1996) 3809.

[8] V.Pârvulescu, C.Anastasscu, B.L.Su, J.Mol.Catal.A: Chemical 198 (2003) 249.

[9] Y. Li, D. He, Q. Zhu, X. Zhang, B. Xu, J. Catal. 221 (2004) 584.

[10] G. Neri, G. Rizzo, S. Galvagno, G. Loiacono, A. Donato, M.G. Musolino, R. Pietropaolo, E. Rombi, Appl. Catal. A: General 274 (2004) 243.

[11] D.L. Bish, J.E. Post, "Structures and Structure determination" Eds. H.G. Karge and J. Weitkamp, Springer 1999. Modern Powder Diffraction.

[12] C.N. Banwell, "Fundamentals of Molecular Spectroscopy" Tata McGraw-Hill Pub. Co. Ltd. New Delhi, 1979.

[13] V.B. Kartha, "Spectroscopic Methods in Heterogeneous Catalysis" Eds N.M. Gupta, V.B. Kartha and R.A. Rajadhyaksha, Tata McGraw Hill, 1991, p.1.

[14] J.E.Wertz, J.R.Bolton, "Electron Spin Resonance," McGraw-Hill, NY, 1972.

[15] A. Abragam, B. Bleaney, "Electron Paramagnetic Resonance of Transition Ions" Clarendon, Oxford, 1970.

[16] D.K. Gosser, "Cyclic Voltammetry Simulation and Analysis of Reaction Mechanisms" Wiley-VCH, Germany, 1993.

[17] S. Chikazumi, "Physics of Magnetism" Wiley, New York, 1964.

[18] J.M. Thomas, R.M. Lambert, "Characterization of Catalysts" John Wiley, New York, 1980.

[19] J. Wolstenholme, "An Introduction to Surface Analysis by XPS and AES" John Wiley & Sons, New York, 2003.

[20] S. Brunauer, P.H. Emmett, E.J. Teller, J. Am. Chem. Soc. 60 (1938) 309.

[21] B. Viswanathan, S. Sivasanker, A.V. Ramaswamy, "Principles and Applications of Catalysis" Narosa Publication, New Delhi, 2001.

Chapter – 3
Oxo-Titanium Species on Noble Metal Modified Titanosilicate Molecular Sieves

3.1. Introduction

Titanosilicate molecular sieves, especially titanium silicalite-1 (TS-1), have been widely studied, for their remarkable catalytic properties in selective oxidation of organic compounds with aqueous H_2O_2 at mild conditions [1 – 3]. They are one of the earliest classes of molecular sieves containing a transition metal cation, Ti^{4+}, in framework position and possessing remarkable activity and selectivity for partial hydrocarbon oxidation by H_2O_2. Isolation, isomorphous substitution in the silicate framework, tetrahedral geometry and capability to expand geometry from tetra- to penta- or hexa-coordination of Ti^{4+} ions in TS-1 during oxidation reactions have been attributed to be the characteristic features for their unique catalytic activity. At present there are two commercial processes that utilize TS-1 as the oxidation catalyst – (1) the production of hydroquinone and catechol from hydrogen peroxide and phenol (10 kilo tons/y plant built in 1986 in Ravenna, Italy), and (2) the production of cyclohexanone oxime from hydrogen peroxide, cyclohexanone and ammonia (12 kilo tonns/y plant in Marghera, Italy; the same process is being applied by Sumitomo in combination with the rearrangement of the cyclohexanone oxime for the industrial production of caprolactam [4, 5]. Production of propylene oxide (PO) from propylene by oxidation with aqueous H_2O_2 over TS-1 (ENIchem Technology) [6 – 8] is a "greener" alternative to the conventional chlorohydrin route (that generates lots of chlorinated by-products, mainly dichloropropane and $CaCl_2$) [9, 10] and Halcon-ARCO and Shell processes using organic hydroperoxides (that needs great equipments investment) [11]. In the Halcon method, the sales fluctuations of the stoichiometrically produced by-products *viz.*, tert-butyl alcohol or styrene greatly affect the economy of PO. The ENIchem Technology produces no by-products and achieves PO selectivity as high as 98% (at H_2O_2 conversion of 97%; methanol solvent; hydrophobized TS-1 catalyst). However, it incurs the cost associated with the use of aqueous H_2O_2 [12]. The hydrogen peroxide-based PO process (HPPO) of capacity ~ 200,000 mt/yr is expected to be commercialized by around 2006 by a joint venture of DOW and BASF [13, 14].

In situ production of H_2O_2 directly from O_2 in the presence of H_2 and using it in the oxidations over noble metal modified titanosilicates has been reported [13 – 28].

The yield and selectivity of PO depended on the precursor used for noble metal, method of deposition, pretreatment conditions and framework structure of the support – titanosilicate. A small amount of Pt addition enhanced significantly the catalytic activity of Pd/TS-1 catalysts [17, 19]. Presence of Pt in small amounts enhanced the dispersion of palladium and the fraction of Pd(II) species favoring the formation of propylene oxide [17]. When the catalysts were prepared using $[Pd(NH_3)_4](NO_3)_2$ and $[Pt(NH_3)_4]Cl_2$ as precursors for Pd and Pt, respectively, auto-reduction by the amine ligands under a flow of N_2 at 423 K led to maximum PO selectivities, whereas those catalysts that were hydrogen reduced and calcined prior to reduction were less effective [17].

Molecular sieves containing a redox metal cation in framework positions have an enormous potential in shape-selective oxidation-reduction reactions similar to the predominant role of their aluminosilicate analogs. However, compared to the enormous amount of literature on the structure and dynamics of the acidic, active sites (both Brönsted and Lewis type) in aluminosilicate zeolites, our knowledge of the reactive oxo intermediates over these titanosilicates is inadequate. IR spectroscopic studies [31] of TS-1 had identified TiOOH (η^1 and η^2) species in the presence of H_2O_2. Sankar et al. [32 - 34] have, using EXAFS measurements and DFT calculations, claimed the existence of a bidentate (side-on) peroxo species on Ti-grafted MCM-41. On the other hand, a bidentate hydroperoxo species (Ti-OOH (η^2)) had also been claimed earlier [35] to be the reactive intermediate. Clarification and confirmation of the identity and role of oxo species generated on the surface of these interesting class of materials will hopefully, enable the design and synthesis of tailor-made oxidation catalysts. As had happened in the case of acidic aluminosilicate molecular sieves, oxidation reactions can then, be investigated and put on more quantitative lines.

In spite of two decades of significant progress there are still many unresolved issues and challenges in this field. For example, why is TS-1 more chemoselective than Ti-beta and Ti-MCM-41 [36, 37] even though Ti^{4+} ions are isolated and in tetrahedral locations in all of them? An understanding of this problem might lead to

the development of efficient large-pore titanium silicate molecular sieves more active than the medium-pore TS-1 in the selective oxidation of large molecules of interest to the fine chemicals industry. Again, even though attempts have been made to substitute aqueous H_2O_2 by a mixture of H_2 and O_2 in the presence of metals like Pd, Pt, Au etc. [13 – 28], the observed catalytic activities are much lower. But, selectivities of 99% for PO formation from propylene were observed by Haruta and co-workers [28] over Au-containing catalysts. Srinivas and co-workers [38 – 40] had, earlier, shown that reactive oxygen species (superoxides, hydroperoxide and peroxides of Ti) generated during the oxidation process may influence the activity and selectivity of the titanosilicate molecular sieves.

In this chapter a comprehensive investigation of such species formed in the presence of aqueous H_2O_2 (HP), H_2O_2-urea adduct (UHP) and (H_2+O_2) over TS-1, Ti-MCM-41, Ti-SBA-15 and Pt-/Pd-TS-1 during the selective oxidation of allyl alcohol has been investigated. Electron Paramagnetic Resonance (EPR) and diffuse reflectance UV-visible (DRUV-visible) spectroscopic techniques have been utilized to probe the structure and estimate the surface concentration of these oxygen species. The results lead to a better understanding and control of the catalytic behavior of these redox molecular sieves of great potential in the fine chemicals industry.

3.2. Experimental

The syntheses of titanosilicate molecular sieves TS-1, Ti-MCM-41, Ti-SBA-15 and Pd- and Pt-Pt modified TS-1 are described in Chapter 2. The samples were characterized by chemical analysis (AAS and XRF), XRD, N_2 adsorption measurements, FT-IR and diffuse reflectance UV-visible spectroscopy.

3.2.1. Sample Treatments

3.2.1.1. EPR Spectroscopy

Titanosilicates Contacted with Aq. H_2O_2 (HP). A known quantity of titanosilicate (40 mg) was taken in 4.5 mm o.d. Suprasil quartz EPR tube. H_2O_2 (50%, 0.1 ml) was added to it in amounts adequate enough to wet the solid completely. In the experiments on solvent effects, the titanosilicate samples were initially activated at

373 K in static air, cooled to 298 K and then soaked in a desired solvent (0.4 ml). H_2O_2 was next, added and EPR spectra were recorded.

Titanosilicates Contacted with Urea-H_2O_2 Adducts (UHP). In the experiments with UHP, 50 mg of titanosilicate sample was physically mixed (without grinding) with 100 mg of UHP. In the experiments involving solvents, this mixture was then exposed to solvent vapor (water, methanol, acetone and acetonitrile) for 5 – 15 min before recording the spectra. UHP was prepared by mixing equimolar quantities of urea and H_2O_2 (30%).

Titanosilicates Contacted with (H_2 + O_2). Titanosilicates (40 mg) were initially evacuated at 423 K, for 2 h. Then the samples were reacted with dry hydrogen (20 ml/min), at 323 – 343 K, for 4 h and subsequently with molecular oxygen (20 ml/min) for 15 min. The sample temperature was quenched to 80 K and EPR spectra were recorded.

3.2.1.2. Diffuse Reflectance UV-Visible (DRUV-Visible)

A known quantity of activated titanosilicate (~ 2 g) was taken in a sample holder. To it, a known quantity of aqueous H_2O_2 (30%) was added drop-wise till the solid became completely wet. Spectral grade $BaSO_4$ was used as a reference material.

3.2.2. Catalytic Activity – Epoxidation of Allyl Alcohol (AA)

In a typical batch reaction, 100 mg of catalyst, 10 g of acetone and 0.5 g of AA were taken in a 50 ml double-necked, glass, round bottom flask fitted with a water-cooled condenser. To this, HP (0.9 ml) was added. The reaction was carried out at 333 K, while stirring for 8 h. The products were analyzed by gas chromatography (CHROMPACK CP 9001; Hewlett Packard fused-silica capillary column, 50 m long x 0.32 mm i.d. x 0.3 μ film thickness) and GC-MS (Shimadzu, QP-5000; 30 m long, 0.25 mm i.d., and 0.25 μ film thickness capillary column DB-1).

In the reactions with (H_2+O_2), 100 mg of the pre-reduced catalyst (with H_2), 5 g of acetone, 5 g of iso-propanol and 0.5 g of AA were taken in a double-necked,

round bottom flask. The reactions were conducted at 333 K, for 8 h, while contacting with O_2 (20 ml/min).

3.3. Results and Discussion

3.3.1. Characterization of Materials

3.3.1.1 XRD

The crystallinity (in the case of TS-1) and phase purity of the titanosilicates were confirmed from the XRD patterns (Fig. 3.1). The XRD pattern can be described based on an orthorhombic symmetry for TS-1 [6]. It may be mentioned that in the absence of Ti, the parent silicalite-1 sample showed a XRD pattern corresponding to a monoclinic symmetry [41, 42]. The absence of splitting in the reflection at around 24.5º (for TS-1) is a clear indication of a structural transition from a monoclinic to an orthorhombic space group as a consequence of Ti incorporation in the framework of silicalite-1 [41].

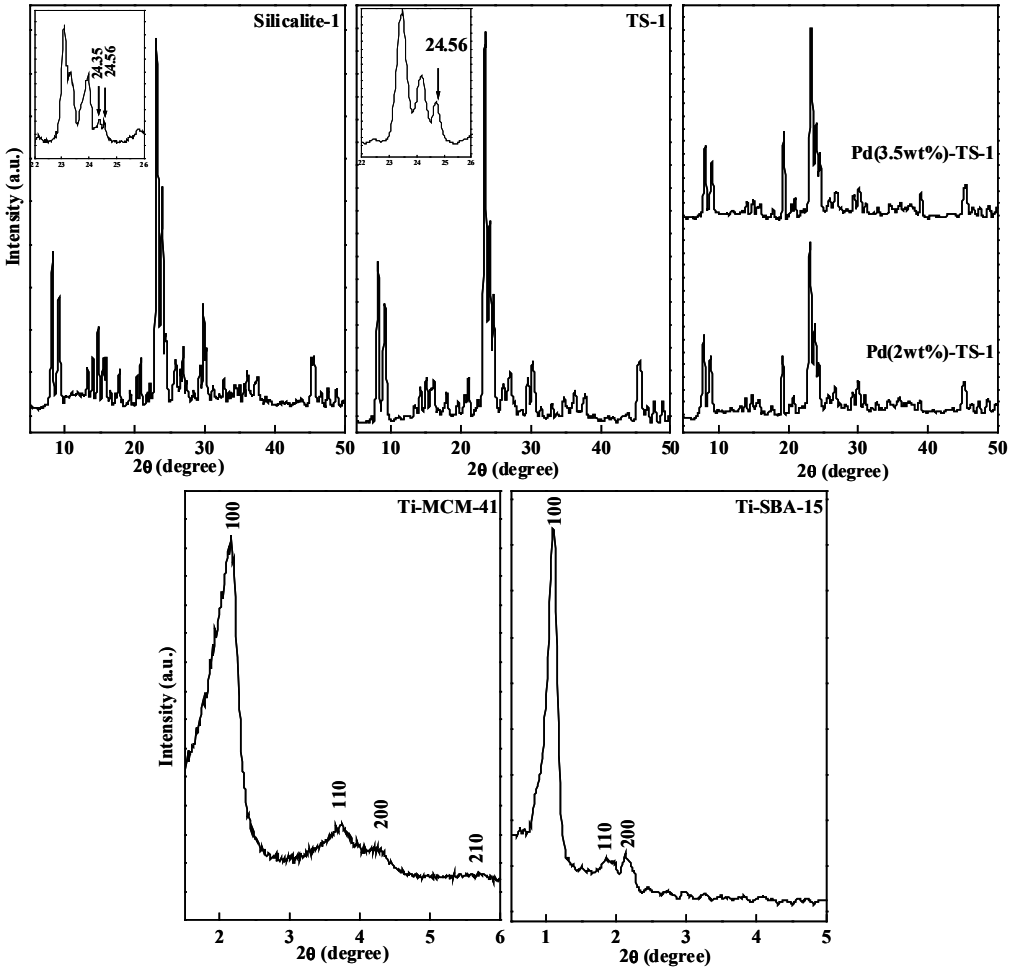

Fig. 3.1. XRD pattern of silicalite-1 and different titanosilicates.

The low-angle (100) reflection and well resolved (110) and (200) reflections of Ti-MCM-41 and Ti-SBA-15 indicate that Ti incorporation did not alter the long-range order and hexagonal symmetry of the mesoporous materials. The d spacing (d_{100}), estimated from the position of the low-angle peak is 4.1 nm (for Ti-MCM-41) and 8.1 nm (for Ti-SBA-15). The unit cell parameters calculated using the equation $a = 2d_{100}/\sqrt{3}$ (4.7 nm for Ti-MCM-41 and 9.3 nm for Ti-SBA-15) are in good agreement with the values reported by others [43, 44]. Post-impregnation of Pd and Pt and reduction treatments did not alter the structure of titanosilicates (Fig. 3.1, compare XRD pattern of Pd-TS-1 with that of TS-1).

3.3.1.2. FT-IR

The weak band at 966 cm^{-1} in the FT-IR spectra for TS-1 (Fig. 3.2) is characteristic of Ti incorporation in the silicalite-1 framework [45-47]. This band corresponding to the stretching of Si-O bonds in Ti-O-Si group appears at 960 cm^{-1} for Ti-MCM-41 (Fig. 3.2). In the case of TS-1, the band at 543 cm^{-1} indicates the formation of zeolitic structure. Palladium impregnation on TS-1 did not alter the spectral characteristics. Ti-SBA-15 showed similar spectral characteristics as that of Ti-MCM-41.

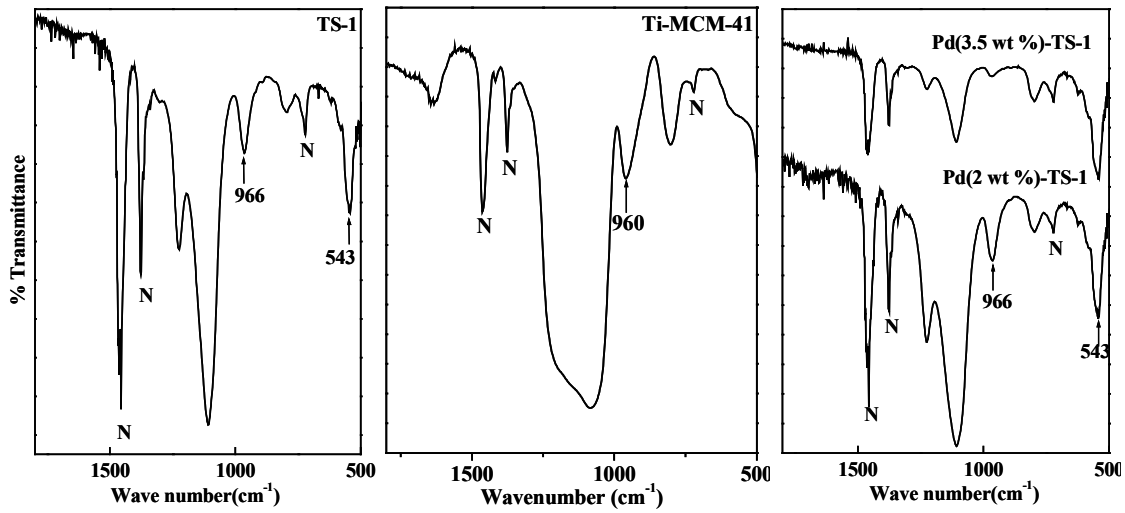

Fig. 3.2. FT-IR spectra (in Nujol mull) of TS-1, Ti-MCM-41 and Pd-modified TS-1. The bands marked by N correspond to that of Nujol mull.

3.3.1.3. DRUV-Visible

DRUV-visible spectra (Fig. 3.3) also confirmed the structure formation and Ti incorporation in the silicate framework structure. The O → Ti charge transfer band at 208 and 215 nm in TS-1 and Ti-MCM-41 / Ti-SBA-15, respectively indicate that the Ti^{4+} ions are isolated and possess tetrahedral framework geometry [39, 40, 45, 48, 49]. TiO_2 (anatase-like phase) was negligible (< 0.01%; 335 nm). However, some amount of penta- and/or octa-coordinated Ti^{4+} species is observed in the case of Ti-MCM-41 and Ti-SBA-15 (see the UV band at around 290 nm) [39,40].

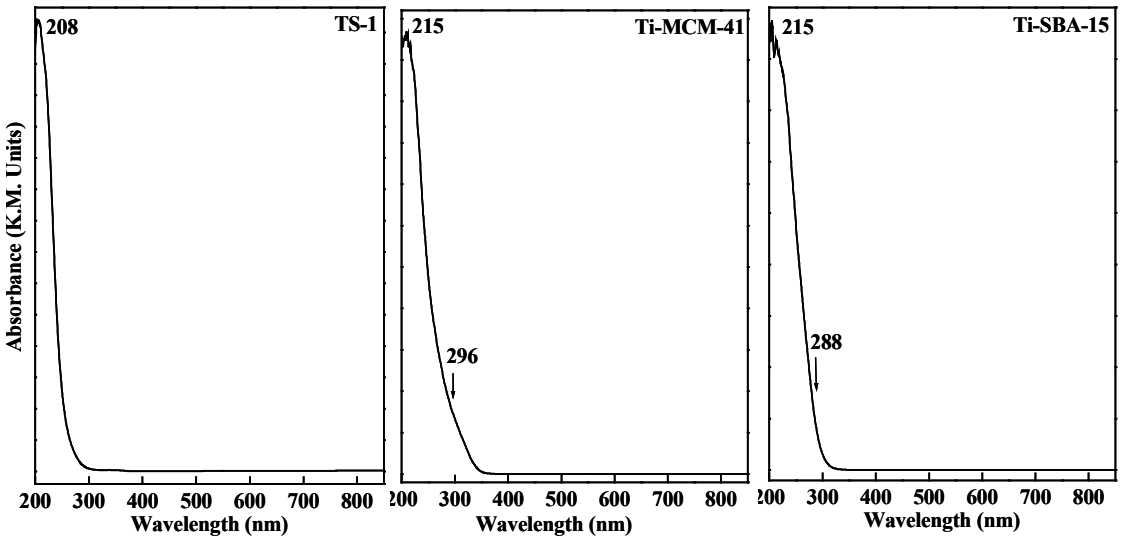

Fig. 3.3. DRUV-visible spectra of TS-1, Ti-MCM-41 and Ti-SBA-15. The bands corresponding to tetrahedral (208 and 215 nm) and penta-/octacoordinated (288 and 296 nm) Ti^{4+} species are indicated.

In addition to the characteristic TS-1 band at 204 nm, the palladium impregnated TS-1 samples showed charge transfer bands at 275, 350 and 390 nm attributable to PdO_xCl_y or $PdO_x(OAc)_y$ species (Fig. 3.4). The broad background absorption in the region 450 – 850 nm is due to metallic Pd species. Samples with high Pd loadings showed an additional band at 460 nm due to the palladium oxide phase. In Pd(n)-TS-1, part of the Pd is in +2 oxidation state and the remaining in zero oxidation state. A similar observation was made also by Meiers et al. [19, 20] in the XPS of Pd-TS-1 samples.

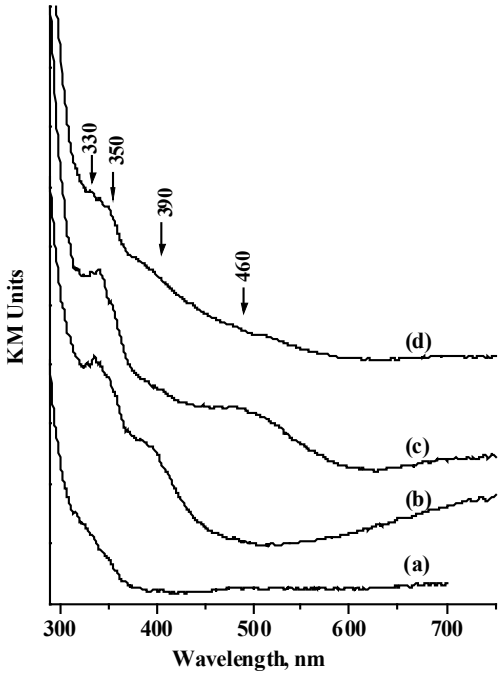

Fig. 3.4. DRUV-visible spectra (in Kubelka-Munk units): (a) TS-1, (b) Pd(0.5)-TS-1 (before reduction), (c) Pd(2)-TS-1 (before reduction) and (d) Pd(2)-TS-1 (after reduction).

3.3.1.4. Chemical Composition and Surface Area

From XRF analyses, the Si/Ti molar ratios in TS-1 and Ti-MCM-41 were estimated to be 36 and 46, respectively. By AAS analysis, the value of Si/Ti in Ti-SBA-15 was determined to be 150. The BET surface areas of TS-1 and Ti-MCM-41 were 400 and 963 m^2/g, respectively. The pore diameter of Ti-MCM-41 was 3 nm.

3.3.2. Reactive Oxo Species and Spectroscopic Characterization

The samples were EPR inactive consistent with the +4 ($3d^0$) oxidation state of Ti in titanosilicates. On contact with aqueous H_2O_2 (HP) or urea-H_2O_2 adduct (UHP), the color of the samples changed from white to yellow. The samples became paramagnetic, showing sharp EPR signals (Fig. 3.5) attributable to Ti(IV)-superoxo radical species $Ti(O_2^{-\bullet})$ with one unpaired electron (S = ½) [40, 50]. The signals (Fig. 3.5) of TS-1 were narrower, while those of Ti-MCM-41 and Ti-SBA-15, as expected, were relatively broader. This is due to the highly crystalline nature of the former-type molecular sieves. Spectral simulations (performed using Bruker Simfonia software

package) revealed that TS-1 contains two types of Ti($O_2^{-\bullet}$) species – A and B; species A being more abundant in TS-1. Ti-MCM-41 and Ti-SBA-15 contain mainly the B-type Ti($O_2^{-\bullet}$) species. Thus, the silicate structure has a definite influence on the type of Ti-oxo species formed and their concentration. These species differ, mainly in their g_{zz} value (2.0275(7) for A and 2.0243(8) for B, respectively); g_{xx} and g_{yy} are almost the same for all samples (Table 3.1). The line width of the g_{zz} signal is different for different Ti($O_2^{-\bullet}$) species. Species B has a larger line width (~3.8 G) than species A (1.8 G). The intensity of these signals increased with Ti-content confirming their origin from Ti-containing species (TS-1 samples with Si/Ti = 30, 60 and 80 were prepared in a similar manner as described in Chapter 2 by varying the input Ti content). It may be mentioned here that these paramagnetic oxo-titanium species were not observed in the interactions of H_2O_2 with either silicalite-1 or anatase TiO_2 in agreement with the results of Zhao et al. [50]. Thus the superoxo Ti species are generated only from the isolated, tetrahedral Ti sites.

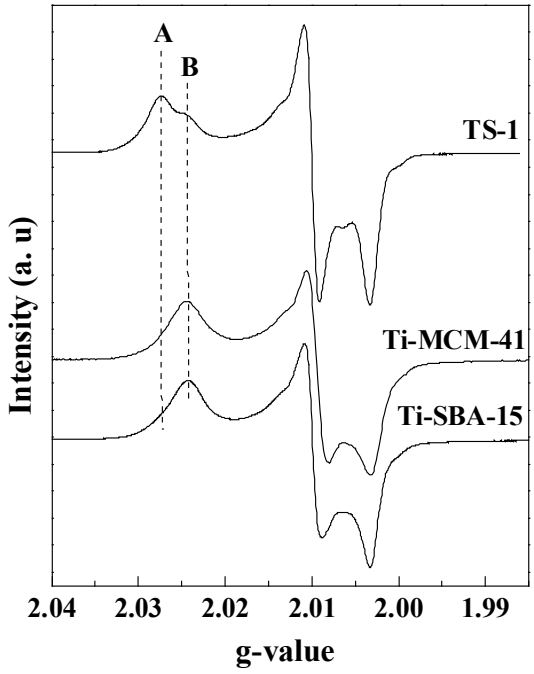

Fig. 3.5. EPR spectra of Ti($O_2^{-\bullet}$) in different titanosilicates contacted with aq. H_2O_2. The oxo-titanium species were generated at 298 K and the spectra were recorded at 80 K. The g_{zz} signals corresponding to different Ti($O_2^{-\bullet}$) species (A and B) are indicated.

Fig. 3.6 shows the EPR spectra of titanosilicate molecular sieves contacted with urea-H_2O_2 adduct (UHP). Marked changes in the spectra may be noticed compared to those observed with aq. H_2O_2 (compare Fig. 3.6 and Fig. 3.5). Only in the case of Ti-MCM-41 some resemblance is evident. Four types of superoxo-Ti species, with their concentrations varying in the order: A > B > A' > C, were generated on TS-1 samples contacted with UHP. Only species B was detected in Ti-MCM-41 + UHP system. The g-values of the various $Ti(O_2^{-\bullet})$ species generated with UHP are also reported in Table 3.1.

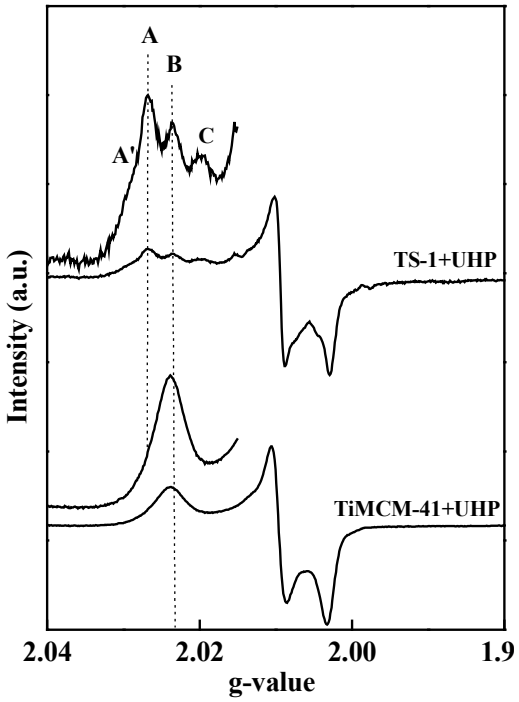

Fig. 3.6. EPR spectra of $Ti(O_2^{-\bullet})$ in TS-1 and Ti-MCM-41 contacted with urea-H_2O_2 adduct (UHP). The oxo-titanium species were generated at 298 K and spectra were recorded at 80 K. The g_{zz} signals corresponding to different $Ti(O_2^{-\bullet})$ species (A', A, B and C) are indicated.

Upon reduction with dry hydrogen at elevated temperatures Ti^{4+} ($3d^0$) in titanosilicates (TS-1 and Ti-MCM-41) reduced to paramagnetic Ti^{3+} ($3d^1$) ions which showed characteristic EPR signals below g = 2. The intensity of the Ti^{3+} signals increased when the reduction was carried out at 873 K instead of 673 K. Ti-MCM-41

was relatively easier to reduce than TS-1. Exposing of the reduced samples to molecular oxygen/air generated oxo-titanium species. A representative spectrum of TS-1 reacted with H_2 + O_2 at 673 K is shown in Fig. 3.7 (a). Appearance of signals due to both Ti^{3+} ions and oxo-titanium species may be noted in the figure. In the absence of H_2, exposure of titanosilicates to oxygen alone did not generate the superoxo species. But when Pd(Pt)-TS-1 samples were contacted with H_2 + O_2, Ti^{4+} was reduced to Ti^{3+} by H_2. The Ti^{3+} ion generates $Ti(O_2^{-\bullet})$ species on interaction with O_2. The EPR signals due to Ti^{3+} and $Ti(O_2^{-\bullet})$ were well separated and could be differentiated. This reduction and reoxidation of Ti ions, which required 673 K and above in case of TS-1 and Ti-MCM-41, was facilitated by Pd or Pt even at 323 K (Fig. 3.7 (b)). The superoxo species generated over Pd-modified TS-1 were more of A and A'-type. The extent of Ti reduction and $Ti(O_2^{-\bullet})$ formation depended on the Pd content, with the concentration of the paramagnetic Ti-oxo species reaching maximal values at 2 wt.% Pd (Fig. 3.8).

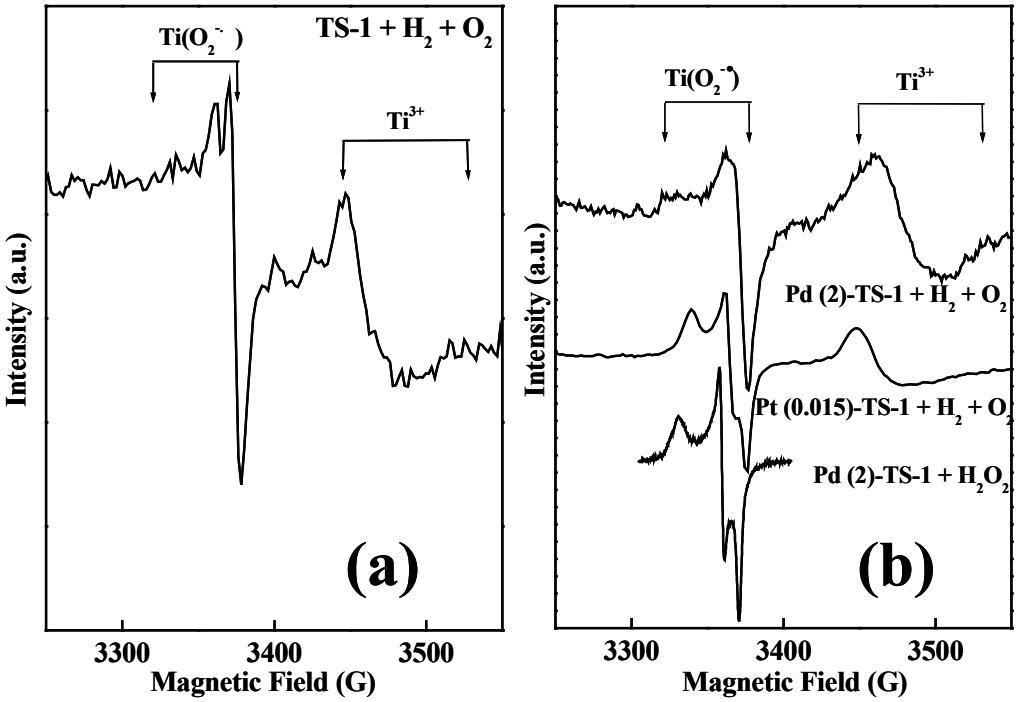

Fig. 3.7. (a) EPR spectrum of TS-1 reacted with H_2 + O_2 at 673 K. (b) The spectra of Pd(2)-TS-1 + H_2O_2, Pt(0.015)-TS-1 + H_2 + O_2 (treated at 673 K) and Pd(2)-TS-1 + H_2 +O_2 (treated at 323 K). The spectra were recorded at 80 K and the signals due to Ti^{3+} and $Ti(O_2^{-\bullet})$ are indicated.

At least six different $Ti(O_2^{-\bullet})$ species (A", A', A, B', B and C) were detected in Pd(n)-TS-1 contacted with aq. H_2O_2. The Ti sites adjacent to Pd ions are magnetically different than the other Ti ions, accounting for the greater variety of $Ti(O_2^{-\bullet})$ species (Table 3.1).

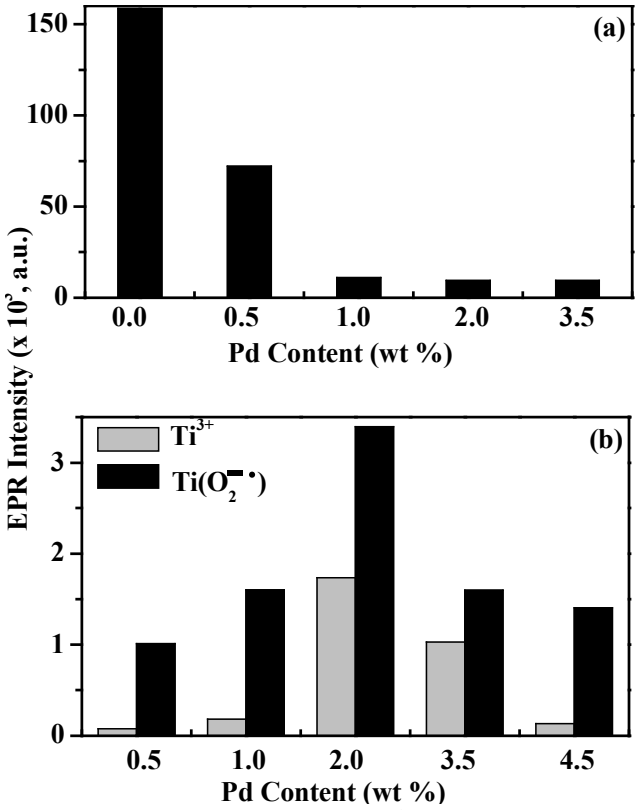

Fig. 3.8. (a) EPR spectral intensity of $Ti(O_2^{-\bullet})$ ions as a function of Pd content in Pd(n)-TS-1 samples on reaction with H_2O_2. (b) EPR spectral intensity of Ti^{3+} and $Ti(O_2^{-\bullet})$ ions as a function of Pd content in Pd(n)-TS-1 reacted with $H_2 + O_2$.

Fig. 3.9 shows the variation of the relative spectral intensity per mole of Ti, (ln(I(T)/I(220))), in TS-1 and Ti-MCM-41 + H_2O_2 systems as a function of temperature. Here, I(220) is the total EPR signal intensity at 220 K and I(T) is that at temperature T. This value increased steeply with a decrease in the temperature. Below ~175 K, the increase was less marked. The total spectral intensity at 80 K for TS-1 is lower than that for Ti-MCM-41. The line width of the individual signals A and B increased at lower temperatures. This broadening was more significant for A (2.2 to

3.0 G in TS-1) than for B-type Ti($O_2^{-\bullet}$) species. A marginal shift in the signals to a higher g value and a reduction in the intensity of A-type signal were also noted at lower temperatures.

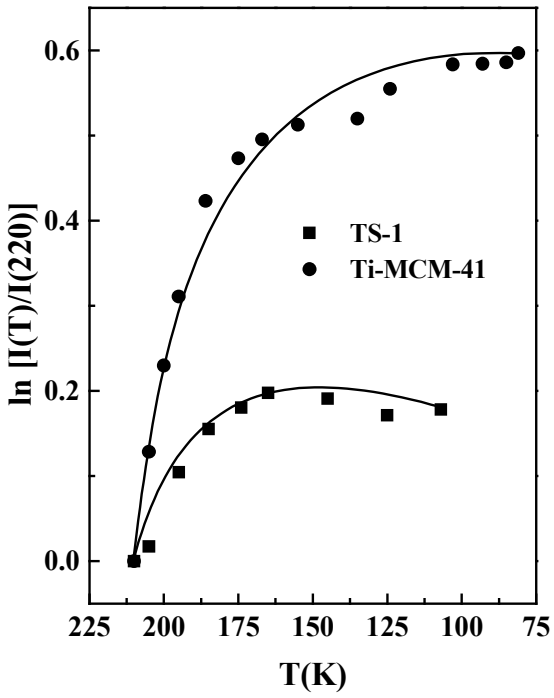

Fig. 3.9. Variation of total EPR intensity per mole of Ti as a function of temperature (ln[I(T)/I(220)] *vs* T) in TS-1 and Ti-MCM-41 contacted with aqueous H_2O_2.

The intensity of the EPR signal of a paramagnetic sample should vary linearly with 1/T [51]. The total spectral intensity of titanosilicates exhibited a different behavior below 175 K (Fig. 3.9); the rise in intensity was marginal below 175 K. This can happen if a part of the EPR-active Ti($O_2^{-\bullet}$) is converted into an EPR-inactive oxo-titanium species, such as hydroperoxides/peroxides, below 175 K. The onset of antiferromagnetic resonance may be an alternative explanation for the phenomenon observed in Fig. 3.9. However, in view of the very low concentration of Ti ions in the sample, antiferromagnetic coupling between two adjacent $O_2^{-\bullet}$ on two neighboring Ti sites is considered unlikely. It may be recalled that the UV-visible spectra of our TS-1 sample confirm the predominant concentration of *isolated*, tetrahedrally coordinated,

Ti ions in titanosilicates. The hydroperoxo-/peroxo-titanium species are more stable at low temperatures and the superoxo species are stable at higher temperatures. The stabilization of the EPR-inactive hydroperoxo/peroxo-titanium species at lower temperatures is also in agreement with the DFT calculations of Sankar et al. [32]. It may be noted from Fig. 3.9 that the overall spectral intensity per mole of Ti decreased among titanosilicates in the order: Ti-MCM-41 > TS-1 suggesting that a larger amount of oxo-titanium species is in the form of EPR-inactive hydroperoxo/peroxo-titanium in TS-1, while the EPR-active superoxo-titanium predominates in Ti-MCM-41.

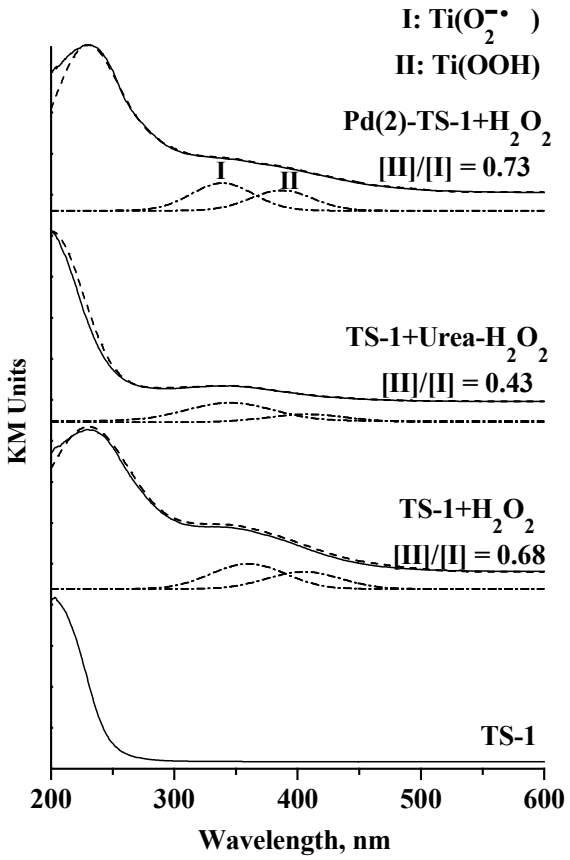

Fig. 3.10. DRUV-visible spectra of oxo-titanium species in TS-1 samples. Experimental (——), simulated (– – – –) and deconvoluted (– · – · –) oxo-titanium bands.

It was found earlier [39] that solvent also influences the superoxo–hydroperoxo conversion and their concentration. Weakly polar CH_3CN stabilizes the

hydroperoxo/peroxo-titanium species, while the more polar CH_3OH stabilizes the superoxo-titanium species [39]. The overall signal intensity variation with

Table 3.1. EPR Parameters of the Oxo-Titanium(IV) Species

System	Species	g_{zz}	g_{yy}	g_{xx}	Δ (cm^{-1})
TS-1 + HP	A	2.0264	2.0090	2.0023	11203
	B	2.0238	2.0090	2.0023	12558
Ti-MCM-41 + HP	B	2.0244	2.0095	2.0031	12217
Ti-SBA-15 + HP	B	2.0236	2.0100	2.0031	12217
Pd(2)-TS-1 + HP	A’	2.0309	2.0100	2.0350	9440
	A	2.0276	2.0100	2.0350	10672
	A”	2.0265	2.0100	2.0350	11157
	B’	2.0255	2.0100	2.0350	11638
	B	2.0245	2.0100	2.0350	12162
	C	2.0220	2.0100	2.0350	13705
TS-1 + UHP	A’	2.0300	2.0101	2.0035	9747
	A	2.0275	2.0101	2.0035	10715
	B	2.0242	2.0101	2.0035	12329
	C	2.0206	2.0101	2.0035	14754
Ti-MCM-41 + UHP	B	2.0232	2.0096	2.0046	12919
TS-1 + H_2 + O_2	A	2.0265	2.0080	2.0010	11157
	Ti^{3+}	1.930	1.956	1.956	
Pd(2)-TS-1+H_2+O_2	A’	2.0340	2.0092	2.0022	8517
	A”	2.0295	2.0092	2.0022	9926
	B	2.0241	2.0092	2.0022	12385
	Ti^{3+}	1.928	1.953	1.953	
Pt(0.015)-TS-1 + H_2 + O_2	A’	2.0300	2.0080	2.0012	9747
	A”’	2.0295	2.0080	2.0012	9890
	B	2.0241	2.0080	2.0012	12385
	Ti^{3+}	1.931	1.955	1.955	

temperature was different in urea-H_2O_2 adducts of TS-1 and Ti-MCM-41. In the case of TS-1-UHP, the conversion of the superoxo to the hydroperoxo/peroxo species takes place at still lower temperatures (110 K) as against 175 K observed in the case of TS-1-HP system. In Ti-MCM-41-UHP the spectral intensity increased with lowering of temperature even up to 80 K. Thus, urea promotes the stability of the superoxo-titanium species.

To establish further the nature of oxo-titanium species formed on contact with peroxides and H_2+O_2, the samples were subjected to *in situ* DRUV-visible studies. On reaction with HP or UHP, an asymmetric, broad band was observed for TS-1 and Pd-TS-1 (Fig. 3.10). This could be deconvoluted into two bands – I and II. These are attributed to the charge transfer transitions associated with Ti(IV)-superoxo ($Ti(O_2^{-\bullet})$) and Ti(IV)-hydroperoxo (Ti(OOH)) species, respectively. The position and relative intensity of these bands are different in HP- and UHP-TS-1 systems and in Pd-containing samples (Fig. 3.10). For TS-1+HP, these bands occur at 360 and 405 nm. For Pd(2)-TS-1+HP, they occur at 339 and 387 nm and for TS-1+UHP at 345 and 408 nm, respectively. The bandwidth at half maximum of I and II, in TS-1+HP/UHP systems, is 70 and 75 nm, respectively and it is 60 nm in Pd(2)-TS-1+HP. The intensity ratio [II]/[I] decreases in the following order: Pd(2)-TS-1+HP (0.73) > TS-1+HP (0.68) > TS-1+UHP (0.43). In Ti-MCM-41+HP these bands overlap with the Ti-MCM-41 bands. These results, in agreement with the *in situ* EPR studies, reveal that UHP generates predominantly, the superoxo species while HP stabilizes the hydroperoxo species.

Conversion energy for hydropero ↔ superoxo transformation was estimated, from the DRUV-visible band positions of II and I, in TS-1+HP, Pd(2)-TS-1+HP and TS-1+UHP to be 9.7, 11.5 and 14.1 kcal/mol, respectively. This energy correlates with the energy of the reaction:

$$\text{Ti-OOH} \leftrightarrow \text{Ti}(O_2^{-\bullet}) + H^+$$

and supports the assignments of the UV-visible bands. This is the first report on the identification and estimation of Ti(IV)-hydroperoxo and superoxo species by DRUV-

visible spectroscopy. Most of the earlier works [52] had reported only a broad unresolved band in the region 300 – 500 nm.

An attempt was made to compare the relative concentrations of the hydroperoxo-/peroxo and superoxo-titanium species obtained from EPR and UV-visible spectroscopies. The "theoretical" line passing through the origin in Fig. 3.11 was computed on the assumption that all the Ti ions in the sample react with H_2O_2 forming only the paramagnetic superoxo species. For the "experimental" line in Fig. 3.11, the intensity of the EPR signal varies linearly with the Ti content in the various TS-1 samples. This line, however, does not pass through the origin (Fig. 3.11). If all the Ti in TS-1 had formed the paramagnetic Ti-superoxo species the "experimental" line would have passed through the origin and coincided with the "theoretical" line. It may be recalled that all the Ti ions in the chosen samples (Si/Ti = 30, 60 and 80) are isolated and in framework positions (XRD, FT-IR and UV-visible analyses). Thus, they are expected to interact with H_2O_2 and form either paramagnetic superoxo or diamagnetic peroxo-Ti species. Thus, only a part of the Ti ions form paramagnetic superoxo-Ti species and the rest form diamagnetic hydroperoxo/peroxo-Ti species. From the difference in the "theoretical" and "experimental" EPR intensity values (Fig. 3.11) the amounts of Ti-hydroperoxo and Ti-superoxo species were estimated to be 45 and 55%, respectively, at 80 K. In the absence of a suitable reference standard, this method of estimation of oxo-titanium species is more reliable. Thus, the Ti(OOH)/Ti($O_2^{-\bullet}$) ratio is found to be 0.82 at 80 K. At 298 K this ratio is lower. The comparative value from DRUV-visible experiments, at 298 K for TS-1+HP is 0.66. This independent EPR estimation of the concentration of the oxo-titanium also supports the assignments of the DRUV-visible bands to the Ti-hydroperoxo and superoxo species.

The conversion of hydroperoxide/peroxide to superoxide is a one-electron redox reaction and requires the presence of transition metals having accessible multiple oxidation states as in biological Fe or Mn clusters (e.g., Fe(II, III, IV) clusters of monooxygenase or the Mn(II, III, IV) clusters of photosystems. Ti is

usually not reduced at ambient temperatures. The various possibilities that could facilitate the transformation of hydroperoxo/peroxo to superoxo species are:

(1) Homolysis of H_2O_2 to $HO^{\bullet}$ radicals, which react with hydroperoxo-Ti species to form superoxo-Ti and H_2O.

$$H_2O_2 \rightarrow 2HO^{\bullet}$$

$$Ti\text{-}OOH + HO^{\bullet} \rightarrow Ti(O_2^{-\bullet}) + H_2O$$

Formation of $HO^{\bullet}$ radicals by decomposition of H_2O_2 on contact with titanium silicates increases with temperature. At 77 K, this decomposition is less probable.

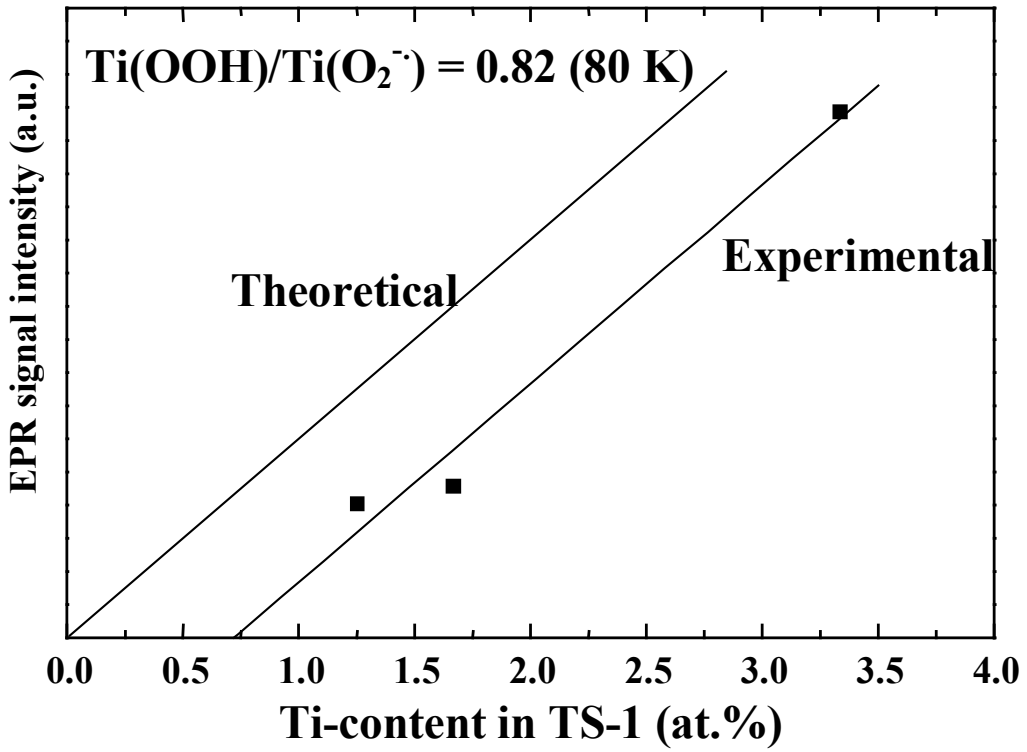

Fig. 3.11. Total EPR signal intensity *vs* Ti content in TS-1 samples.

(2) The second possibility is the dismutation of two superoxo ions to yield the peroxo species.

$$O_2^{-\bullet} + O_2^{-\bullet} \rightarrow O_2^{2-} + O_2$$

Again, even if mobile superoxide ions were present in the sieve, they would not be able to diffuse at the low temperatures used for the EPR experiments (190 – 77 K).

(3) The third possibility for the conversion of the superoxide to the peroxide is the homolytic opening of a cyclic peroxo species (more precisely $Ti^{4+}(O_2^{2-})$ to $Ti^{3+}(O_2^{-\bullet})$) as proposed by Notari [1]. Formation of Ti^{3+} species was indeed observed in the presence of a base, like NaOH (details will be repored in Chapter-4), but in the neutral or acidic pH conditions, the Ti^{3+} species were not observed. Either their concentration, if formed, is very low or they are short-lived.

(4) The concentration of the $Ti(O_2^{-\bullet})$ species is solvent dependent. Thus solvent (or H_2O) may play the role of a redox partner.

The $HO^{\bullet}$ radicals, generated from the decomposition of H_2O_2, cause, perhaps, the hydroperoxo/peroxo to superoxo conversion. The superoxo species (the O-O stretching absorption near 1120 – 1150 cm^{-1}) could not be seen in the FT-IR spectrum [13] perhaps due to the dominant stretching and bending modes of water in the same region.

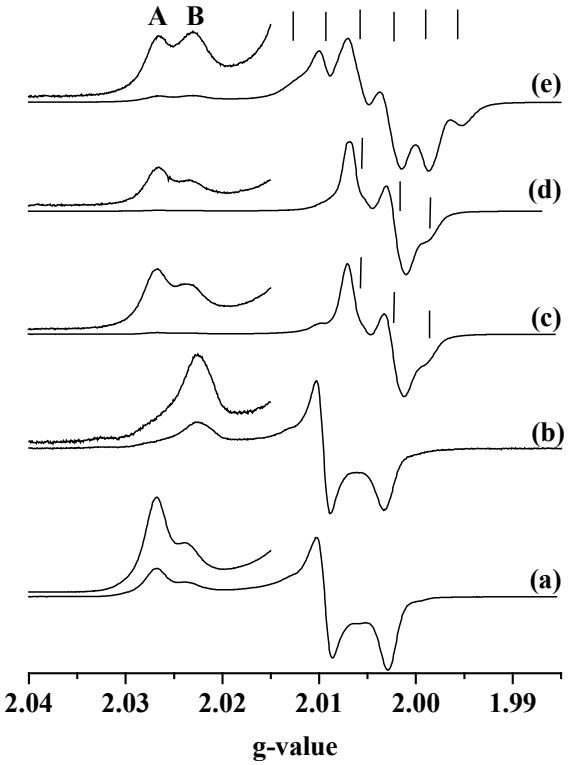

Fig. 3.12. EPR spectra at 180 K of TS-1+HP in the presence of substrate. (a) no substrate, (b) allyl alcohol, (c) phenol, (d) benzene and (e) toluene. Signals indicated

by the vertical lines are due to the substrate-based radicals formed during the oxidation reaction.

3.3.3. Reactivity of Oxo-Titanium Species – In situ EPR Study

The oxo-titanium species were generated in the EPR cells by contacting TS-1 (40 mg) with 50% aqueous H_2O_2 (0.1 ml). On further contact with substrate molecules (allyl alcohol, benzene, phenol or toluene; 0.1 ml), the intensity of the $Ti(O_2^{-\bullet})$ species decreased. In the absence of the substrate the intensity of type A species in TS-1 was more than that of type B (Fig. 3.5). On adding allyl alcohol, the reaction was highly exothermic and the concentration of the type A species decreased faster than that of B (Fig. 3.12), indicating the faster consumption of the former. The spectrum after 10 min of the reaction at 318 K, contained only the unreacted species B (Fig. 3.12).

Table 3.2. Catalytic Activity Data in the Epoxidation of Allyl Alcohol over TS-1 and Pd(n)-TS-1 Catalysts[a]

Catalyst	Oxidant	TOF[b]	H_2O_2 Efficiency (%)	Conversion (wt%)	Epoxide Selectivity (wt%)
TS-1	H_2O_2	15.3	42.8	77.0	96.1
Pd(0.5)-TS-1	H_2O_2	12.3	34.2	61.5	95.6
Pd(2)-TS-1	H_2O_2	10.5	28.8	51.7	90.4
Pd(3.5)-TS-1	H_2O_2	7.6	20.7	37.1	82.8
Pd(4.5)-TS-1	H_2O_2	6.2	16.7	30.0	74.0
Pd(2)-TS-1	$H_2 + O_2$	2.1	-	10.5	99.0

[a]Reaction medium: catalyst (100 mg) + allyl alcohol (0.5 g) + acetone (10 g) + H_2O_2 (50%, 0.9 ml); temperature = 333 K; run time = 8 h.

[b]Turnover frequency (TOF) = moles of allyl alcohol converted per mole of Ti per hour.

When the TS-1+HP slurry was contacted with toluene, benzene or phenol, the color of the solution changed initially to orange and then dark blackish green. In the

case of phenol or benzene the initially generated species B, was consumed faster than A (Fig. 3.12, curves b and c). Species B are, apparently, more active than A in ring hydroxylation reactions. In the case of toluene oxidation, the intensity of both A and B are altered on addition of the substrate (curve d) revealing that both species A and B are probably involved in the oxidation of toluene. Comparison of the toluene results with those of phenol/benzene suggests that while species B is involved in ring hydroxylations, A may be involved in the side chain oxidation. In reactions with benzene/phenol/toluene, at least two types of radicals were formed (Fig. 3.12; denoted by vertical lines). Their identity is not clear at present. These radicals were not formed in the presence of allyl alcohol. The catalytic activity data using (H_2+O_2) as the oxidant, over Pd(2)-TS-1 (Table 3.2) also confirm the correlation between the epoxidation selectivity and the concentration of type A species. Higher epoxide selectivities were observed also in the TS-1+UHP system [53] where species A' was predominant. The in situ studies, suggest that the different oxo species lead to different products.

3.3.4. Catalytic Activity of Pd(n)-TS-1 in the Epoxidation of Allyl Alcohol

Controlled experiments revealed that in the absence of titanosilicate catalysts no reaction took place between allyl alcohol and H_2O_2. Epoxide is the major product while glycidol, diol and methylated products (only in case of methanol solvent) formed as minor products. In a typical liquid phase, batch reaction, allyl alchol (AA) conversions of 77% (theoretical value) and epoxide selectivities of 96% were obtained over TS-1 at 333 K when aq. H_2O_2 was used as oxidant. Over Pd(n)-TS-1 catalysts, the conversion and selectivity decreased with increasing Pd-content (Table 3.2) consistent with the lower Ti($O_2^{-\bullet}$) signal intensities at higher Pd content (Fig. 3.8(a)). Pd catalyzes the decomposition H_2O_2 into H_2O and O_2 and leads to lowered H_2O_2 efficiency for epoxidation. In addition to epoxidation, the acid catalyzed condensation of epoxide with solvent acetone also takes place over the Pd-containing TS-1 catalysts. When the reactions were conducted with H_2+O_2 instead of aq. H_2O_2, the epoxide selectivities were significantly higher (99%). In this case the epoxide conversion was only 10.5%. The lower epoxide conversions are possibly due to lower

amounts of in situ formed H_2O_2 and decomposition of H_2O_2 over the noble metal. Enhancement of epoxide selectivity in the presence of Pd ions and when used H_2+O_2 instead of H_2O_2 is, however, gratifying to note.

3.3.5. Structure-Reactivity Correlations

The XRD, DRUV-visible and FT-IR spectroscopic studies confirm that most of the Ti in TS-1, Ti-MCM-41 and Ti-SBA-15 are in framework tetrahedral positions [39]. No extraframework anatase was detected. During the reaction with alkyl hydroperoxides, EXAFS studies had indicated [32, 54, 55] that Ti expands its coordination number from 4 to 5 or 6 depending on their location and the nature of the titanoslicate.

The free $O_2^{-\bullet}$ radical with a $^2\Pi$ ground state has a $(1\sigma_g)^2(1\sigma_u)^2(2\sigma_g)^2(2\sigma_u)^2(3\sigma_g)^2\ (1\pi_u)^4(1\pi_g)^3$ electronic configuration. Interaction with Ti removes the degeneracy of the HOMO π_g into π_g^x and π_g^y orbitals with an energy gap of Δ. Neglecting the second order terms, the g value expressions (when $\lambda < \Delta << E$) are written as [56, 57]:

$$g_{zz} = g_e + 2\lambda/\Delta,$$

$$g_{yy} = g_e + 2\lambda/E, \text{ and}$$

$$g_{xx} \approx g_e = 2.0023,$$

where λ is the spin orbit coupling constant (135 cm^{-1} for oxygen) and E is the energy separation between $3\sigma_g$ and $1\pi_g^x$ orbital. The g_z value of the superoxo anion is sensitive to the oxidation state, coordinating number and local geometry of the cation to which it is coordinated (Ti in the present case). Ti— ($O_2^{-\bullet}$) bond distance also influences the g_{zz} parameter. Stronger the Ti—O bond, lower will be the g_{zz} value of the superoxo anion. Using the above expressions and the experimental g_{zz} value, the separation between the π_g^x and π_g^y orbitals (Δ), was estimated (Table 3.1). The g_{zz} value of different Ti($O_2^{-\bullet}$) species decrease in the order: A-type (A, A' and A") > B-type (B, B') > C. The Δ values vary in the reverse order. Hence, the strength of the Ti-O bond increases in the order: A-type < B-type < C. The O-O bond strength, on the other hand, will follow the reverse order since a stronger binding of the O-atoms to the Ti ion weakens the intramolecular O-O bonding. As the lability of the O-O

bonds influences its reactivity, the different Ti($O_2^{-\bullet}$) species are expected to exhibit different reactivities. The observed differences in the activity and chemoselectivity of the different titanosilicates probably arises from such differences in the strength of the O-O bond in the Ti-oxo species formed over them in the presence of oxidants like H_2O_2, urea-H_2O_2 or H_2+O_2. Although the calculation of Δ values is based on a purely ionic model, they are also relevant for the metal superoxide complexes. Interestingly, they also correlate well with the catalytic activity data.

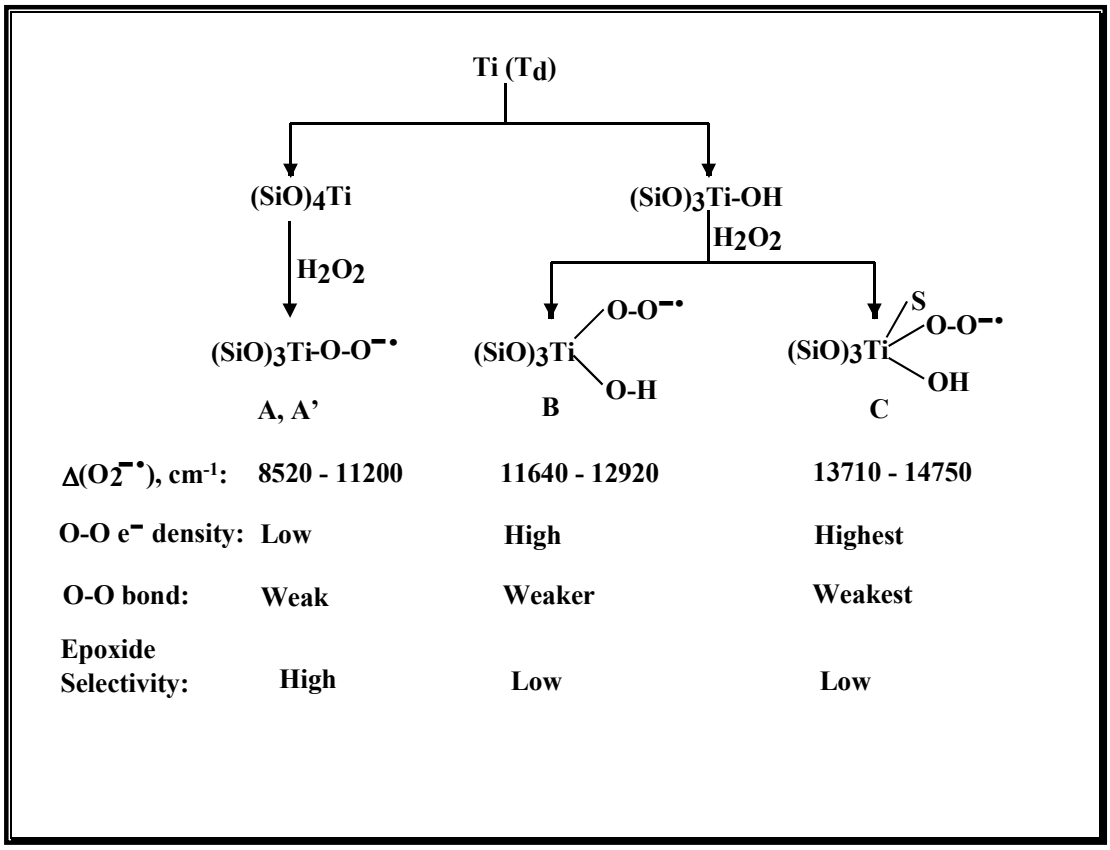

Fig. 3.13. Schematic diagram of different Ti($O_2^{-\bullet}$) species generated by H_2O_2.

The EXAFS studies [54] on TS-1 catalysts had revealed a tetrapodal coordination for Ti. Gleeson et al [54] have divided the $(SiO)_4Ti$ units into two groups, one group with three Ti-O-Si bond angles at 140° and one Ti-O-Si at 160° and the other with two Ti-O-Si bond angles at 140° and the remaining two at 160°. In the case of Ti-MCM-41, prepared by a grafting method, a tripodally coordinated Ti species with coordinated hydroxyl group was also observed [32, 55]. Such a structure cannot be ruled out even in other titanosilicates (like TS-1) with high Ti-content or

surface defects. The different Ti($O_2^{-\bullet}$) species, perhaps, correspond to oxo species formed over these different Ti sites. Depending on the coordination number (5 or 6) of Ti in the Ti($O_2^{-\bullet}$) species, different types of (A", A', A), (B', B) and C species will be formed. The A and B species, revealed by EPR studies are probably formed by reaction of H_2O_2 with the tetra- and tripodal Ti ions indicated by EXAFS [32, 33, 54]. Zhao et al. [50] had also observed the two types of Ti($O_2^{-\bullet}$) species A and B in TS-1+H_2O_2 system. The former (A) was attributed to framework Ti and the latter (B) to extraframework species. Since in the present samples (Si/Ti = 30 – 80), the ratio of A and B was independent of the Ti content, the A and B signals are attributed to the oxo species formed on tetrapodal and tripodal Ti ions, respectively, in framework positions [32, 33]. Bonoldi et al. [58] have also arrived at the same conclusions. Tentative structures of the superoxo-titanium species (A, B and C), arising from the tetrahedral TiO_4 unit upon interaction with H_2O_2, are shown in Fig. 3.13.

The type A species is, probably, the active intermediate in epoxidations while B and C lead to non-selective oxidations (Fig. 3.13). TS-1 generates type A species in greater abundance than Ti-MCM-41 and Ti-SBA-15, which generates mostly the type B species from H_2O_2. The greater epoxidation selectivity of TS-1 (compared to Ti-MCM-41) probably arises from this crucial difference. The present work also provides, for the first time, experimental evidence for the formation of reactive oxo species in the interaction of H_2+O_2 over Pd(n)-TS-1 catalysts. Even though, similar oxo species are formed over all the titanosilicates in the presence of either H_2O_2 or H_2+O_2, their relative concentration determines the catalytic activity and selectivity. A schematic representation of the possible role of Pd is shown in Fig. 3.14.

Haruta and other workers [23 – 26] have postulated that the role of noble metal is to generate H_2O_2 in situ from H_2 + O_2, which is then used up by the isolated, tetrahedral Ti sites in titanosilicates in the oxidation reactions. It is, however, found in this study that Ti can be reduced from +4 to +3 state in the presence of H_2. The reduced ions of Ti, subsequently react with O_2 forming the reactive oxo-titanium species. Presence of noble metals facilitates the reduction of Ti and formation of reactive oxo-titanium species. In other words, H_2O_2 is generated at the site of

modified Ti itself. However, still more detailed studies are required to resolve the issue of site where H_2O_2 is generated in situ from H_2+O_2. It is also quite likely that H_2O_2 is generated at both the noble metal and modified Ti sites.

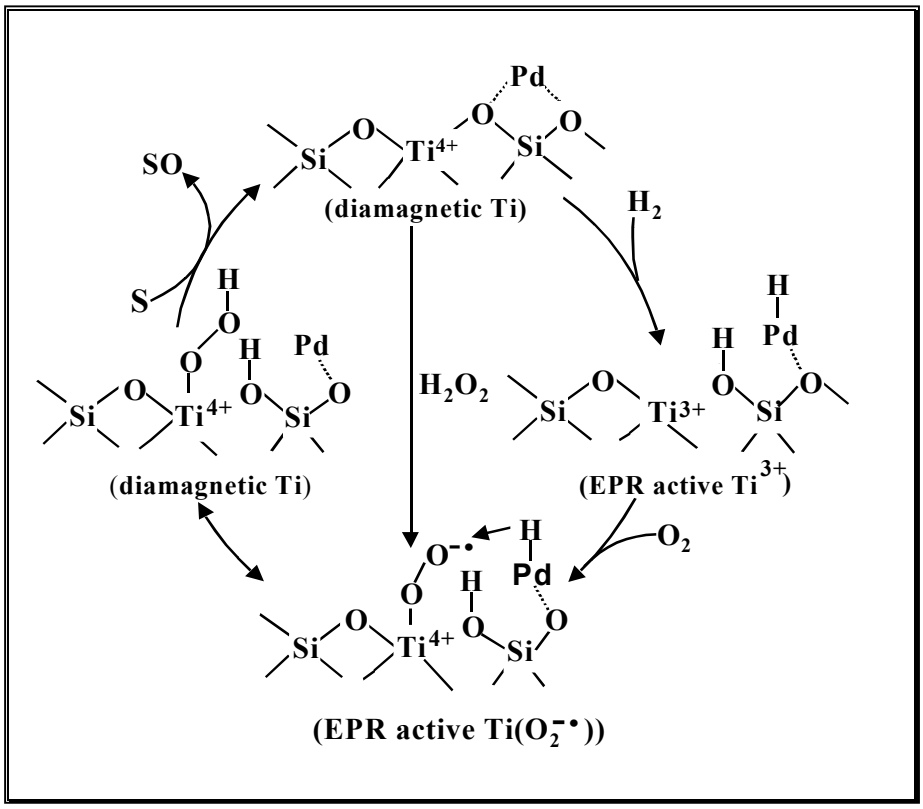

Fig. 3.14. Role of Pd in the in situ generation of H_2O_2 from H_2+O_2 over Pd(n)-TS-1 catalysts. S denotes the substrate and SO the oxygenated product.

Conclusions

Interaction of titanoslilicates (TS-1, Ti-MCM-41, Ti-SBA-15 and Pd(n)-TS-1) with H_2O_2, urea-H_2O_2 and (H_2+O_2) generates reactive Ti(IV)-superoxo and hydroperoxo/peroxo species. These could be identified and quantified, for the first time, by DRUV-visible and EPR spectroscopies. Two types of Ti(IV)-superoxo species, A and B (A being preponderant), were detected in TS-1. Ti-MCM-41 contained mainly the B-type species. Pd-TS-1 generated six types of Ti-oxo species. Epoxidation selectivities were correlated to the relative concentration of these various oxo species during the reaction. Type A species was mainly responsible for

epoxidation of olefins while aromatic ring hydroxylations were promoted by type B species. The greater selectivity of TS-1 (over Ti-MCM-41) in epoxidations is, probably, due to the formation of type A species in greater quantities over the former. Pd enhances the reducibility of Ti^{4+} ions to Ti^{3+} by H_2 at lower temperatures (323 K) thereby facilitating the formation of similar reactive Ti-oxo species from H_2+O_2. The oxo species generated from H_2+O_2 are mainly of the A-type species. The study reveals that the chemoselectivity in oxidations can be enhanced either by modifying the Ti environment (by impregnation with Pd ions) or by employing a suitable oxidant (H_2+O_2 instead of aqueous H_2O_2, for example).

3.4. References

[1] B. Notari, Adv. Catal. 41 (1996) 253.

[2] G.N. Vayssilov, Catal. Rev. Sci.-Eng. 39 (1997) 209.

[3] P. Ratnasamy, D. Srinivas, H. Knozinger, Adv. Catal. 48 (2004) 1.

[4] G. Petrini, G. Leofanti, M.A. Mantegazza, F. Pignataro, in "Green Chemistry: Designing Chemistry for the Environment," (P.T. Anastas and T.C. Williamson, Eds.), ACS Symp. Ser. No. 626, p. 33. Am. Chem. Soc., Washington DC., 1996.

[5] (a) C. Perego, A. Carati, P. Ingallina, M.A. Mantegazza, G. Bellussi, Appl. Catal. A: Chem. 221 (2001) 63. (b) T. Suzuki "Active Site Model of a High Silica MFI Zeolite for the Vapor Phase Rearrangement of Cyclohexanone Oxime to Caprolactam" Proceedings 5th International Symposium on Acid Base Catalysis, July 1st, 2005, Puerta Vallarte, Mexico Paper O-14.

[6] M. Taramasso, G. Perego, B. Notari, US Patent 4,410,501 (1993) to SNAM Progetti.

[7] M.G. Clerici, U. Romano, US Patent 4,824,976 (1989) to Eniricerche S.p.A. and ENIchem Sintesi S.p.A.

[8] M.G. Clerici, G. Bellussi, U. Romano, J. Catal. 129 (1991) 159.

[9] R.A. Sheldon, R.A. van Santen (Eds.), "Catalytic Oxidation: Principals and Applications," World Scientific, Singapore, 1995.

[10] "Industrial Organic Chemicals: Starting Materials and Intermediates," An

Ullmann's Encyclopedia, Vol. 7, p. 4135, Wiley-VCH, 1995.

[11] K. Weissermel, H.J. Arpe, Industrial Organic Chemistry, VCH, New York, 1993.

[12] Chem. Eng. News 80 (2002) 14.

[13] G. Wang, X. Guo, X. Wang, R. Wang, J. Hao, Catal. Lett. 96 (2004) 79.

[14] Press Release, The Catalyst Group Resources, Spring House, PA, USA, September 03, 2002.

[15] R.G. Bowman, J.L. Womack, H.W. Clark, J.L. Joseph, G.E. Hartwell, US Patent 6,031,116 (2000) to The Dow Chemical Co. Midland, MI.

[16] J.C. Jubin, Jr., R.A. Grey, US Patent 6,867,312 (2005) to Arco Chem. Tech., L.P. Greenville, DE.

[17] J.D. Jewson, C.A. Jones, R.M. Dessau, PCT Int. Appl. WO 2001062380 A1 (2001) to Arco Chem. Tech., L.P. Greenville, DE.

[18] T. Tatsumi, K. Yuasa, H.Tominaga, J. Chem. Soc. Chem. Commun. (1992) 1446.

[19] R. Meiers, U. Dingerdissen, W.F. Hölderich, J. Catal. 176 (1998) 376.

[20] R. Meiers, W.F. Hölderich, Catal. Lett. 59 (1999) 161.

[21] G. Jenzer, T. Mallat, M. Maciejewski, F. Eigenmann, A. Baiker, Appl. Catal. A: Gen. 208 (2001) 125.

[22] T. Hayashi, K. Tanaka, M. Haruta, J. Catal. 178 (1998) 566.

[23] Y. A. Kalvachev, T. Hayashi, S. Tsubota, M. Haruta, J. Catal. 186 (1999) 228.

[24] B.S. Uphade, M. Okumura, S. Tsubota, M. Haruta, Appl. Catal. A: Gen. 190 (2000) 43.

[25] C. Qi, T. Akita, M. Okumura, M. Haruta, Appl. Catal. A: Gen. 218 (2001) 81.

[26] B.S. Uphade, T. Akita, T. Nakamura, M. Haruta, J. Catal. 209 (2002) 331.

[27] N. Yap, R.P. Andres, W.N. Delgass, J. Catal. 226 (2004) 156.

[28] A.K. Sinha, S. Seelan, S. Tsubota, M. Haruta, Topics Catal. 29 (2004) 95.

[29] A.K. Sinha, S. Seelan, M. Okumura, T. Akita, S. Tsubota, M. Haruta, J. Phys. Chem. B 109 (2005) 3956.

[30] E.E. Stangland, B. Taylor, R.P. Andres, W.N. Delgass, J. Phys. Chem. B 109 (2005) 2321.

[31] G. Tozzola, M.A. Mantegazza, G. Ranghino, G. Petrini, S. Bordiga, G. Ricchiardi, C. Lamberti, R. Zulian, A. Zecchina, J. Catal. 179 (1998) 64.

[32] G. Sankar, J.M. Thomas, C.R.A. Catlow, C.M. Barker, D. Gleeson, N. Kaltsoyannis, J. Phys. Chem. B 105 (2001) 9028.

[33] (a) J.M. Thomas, G. Sankar, Acc. Chem. Res. 34 (2001) 571. (b) J.M. Thomas, C.R.A. Catlow, G. Sankar, Chem. Commun. (2002) 2921.

[34] C.M. Barker, D. Gleeson, N. Kaltsoyannis, C.R.A. Catlow, G. Sankar, J.M. Thomas, Phys. Chem. Chem. Phys. 4 (2002) 1228.

[35] E. Karlsen, K. Schoffel, Catal. Today 32 (1996) 107.

[36] A. Corma, M.T. Navarro, J. Perez Pariente, J. Chem. Soc. Chem. Commun. (1994) 147.

[37] P.T. Tanew, M. Chibwe, T.J. Pinnavaia, Nature 368 (1994) 321.

[38] R. Bal, K. Chaudhari, D. Srinivas, S. Sivasanker, P. Ratnasamy, J. Mol. Catal. A: Chemical 162 (2000) 199.

[39] K. Chaudhari, D. Srinivas, P. Ratnasamy, J. Catal. 203 (2001) 25.

[40] D. Srinivas, P. Manikandan, S.C. Laha, R. Kumar, P. Ratnasamy, J. Catal. 217 (2003) 160.

[41] R. Millini, E.P. Massara, G. Perego, G. Bellussi, J. Catal. 133 (1992) 220, and 137 (1992) 497.

[42] R. Millini, G. Perego, Gazz. Chim. Ital. 126 (1996) 133.

[43] T. Blasco, A. Corma, M.T. Navarro, J. P. Pariente, J. Catal. 156 (1995) 65.

[44] R. Srivastava, D. Srinivas, P. Ratnasamy, J. Catal. 233 (2005) 1.

[45] M.R. Boccuti, K.M. Rao, A. Zecchina, G. Leofanti, G. Petrini, Stud. Surf. Sci. Catal. 48 (1989) 133.

[46] G. Bellussi, M.S. Rigutto, Stud. Surf. Sci. Catal. 85 (1994) 177.

[47] D. Scarano, A. Zecchina, S. Bordiga, F. Geobaldo, G. Spato, G. Petrini, G. Leofanti, M. Padovan, G. Tozzola, J. Chem. Soc., Faraday Trans. 89 (1993) 4123.

[48] A. Zecchina, S. Bordiga, C. Lamberti, G. Ricchiardi, D. Scarano, G. Petrini, G. Leofanti, M. Mantegazza, Catal. Today 32 (1996) 97.

[49] S. Bordiga, F. Boscherini, S. Coluccia, F. Genoni, C. Lamberti, G. Leofanti, L. Marchese, G. Petrini, G. Vlaic, A. Zecchina, Catal. Lett. 26 (1994) 195.

[50] Q. Zhao, X. Bao, Y. Wang, L. Lin, G. Li, X. Guo, X. Wang, J. Mol. Catal. A: Chem. 157 (2000) 265.

[51] H.C. Box, Electron Paramagnetic Resonance Spectroscopy, Academic Press, New York, 1997.

[52] S. Bordiga, A. Damin, F. Bonino, G. Ricchiardi, C. Lamberti, A. Zecchina, Angew. Chem., Int. Ed. 41 (2002) 4734.

[53] S.C. Laha, R. Kumar, J. Catal. 204 (2001) 64.

[54] D. Gleeson, G. Sankar, C.R.A. Catlow, J.M. Thomas, G. Spanó, S. Bordiga, A. Zecchina, C. Lamberti, Phys. Chem. Chem. Phys. 2 (2000) 4812.

[55] J.M. Thomas, G. Sankar, Acc. Chem. Res. 34 (2001) 571.

[56] W. Kanzig, M.H. Cohen, Phys. Rev. Lett. 3 (1959) 509.

[57] A.A. Davydov, M.P. Komarova, V.F. Anerfrieneo, N.G. Maksimov, Kinet. Katal. 14 (1973) 1519.

[58] L. Bonaldi, C. Busetto, A. Congiu, G. Marra, G. Ranghino, M. Salvalaggio, G. Spanó, E. Giamello, Spectrochim. Acta 58 A (2002) 1143.

Chapter – 4

Oxo-Titanium Species on Alkali and Alkaline Earth Metal Ion Modified Titanosilicate Molecular Sieves

4.1. Introduction

It is well known that the presence of alkali metal ions such as Na^+ and K^+ *in the synthesis gel of TS-1* results in inactive catalysts for *n*-alkane oxidations [1-7]. Washing these catalysts with acids prior to catalytic activity evaluation could, however, restore their activity [2]. It was postulated [3] that the alkali metal ions present during the synthesis might prevent the incorporation of Ti in the silicalite framework. Clerici and Ingallina [7] reported that basic compounds added, in low concentrations, to TS-1 catalysts during epoxidation of olefins inhibit the ring opening of the epoxide due to solvolysis in methanol and improve the selectivity to the epoxide. Capel-Sanchez et al. [8] have confirmed the enhanced selectivity to epoxide when alkali ions are impregnated on TS-1 samples. They attributed this effect to the neutralization of the surface acidity of TS-1 by the alkali ions and the consequent inhibition of the solvolysis reactions of the epoxide on the acid sites. It may however, be recalled that the presence and type of acid sites on TS-1 has not been unambiguously confirmed so far [9]. In a recent publication, Arca et al. [10] reported the TS-1 activity in the epoxidation reaction of propylene, when it is treated with a metal cation such as zinc. The role of zinc in the first place was thought to be of acidity inhibitor, to reduce and control the propylene oxide solvolysis. Detailed investigations and DFT calculations have, however, revealed a specific zinc role, as direct consequence of its coordination to Ti-site, inducing a peculiar variation in the property of the active center towards the epoxidation reaction. When zinc is present, the donor property of the reaction solvent to Ti-site increases and the Ti-OOH electrophilicity reduces, giving rise to a high propylene oxide selectivity well-evidenced by a lower experimental by-product formation.

In the present work, the influence of pH and added alkali ions on the oxo-titanium species has been explored. It is found that the observed differences in selectivity in the presence of alkali ions can also arise from differences in the type and concentration of the various reactive oxo-titanium species generated in their presence, in addition to the neutralization of surface acidity of TS-1 by the alkali ions.

4.2. Experimental

The synthesis of the alkali and alkaline earth metal ion impregnated titanosilicate molecular sieves (TS-1 and Ti-MCM-41) is described in Chapter 2. The samples were characterized as described using XRD, FT-IR and DRUV-visible spectroscopy techniques.

4.2.1. Sample Treatments

4.2.1.1. EPR

Prior to EPR measurements, the samples (taken in Suprasil quartz tubes; 4 mm o.d.) were activated at 373 K, in air. Oxo-Ti species were generated by contacting the titanosilicates (40 mg) completely soaked in 0.4 ml of CH_3OH, with 0.1 ml of aqueous H_2O_2 (46%).

4.2.1.2. DRUV-Visible

A known quantity of activated titanosilicate (~ 2 g) was taken in a sample holder and to it, a known quantity of aqueous H_2O_2 (30%) was added drop-wise till the solid became completely wet. Spectral grade $BaSO_4$ was used as a reference material.

4.2.2. Catalytic Activity: Epoxidation of Allyl Alcohol, Allyl Chloride and Styrene

Epoxidation of allyl alcohol, allyl chloride and styrene were carried out over alkali and alkaline earth ion impregnated TS-1 and Ti-MCM-41 using aq. H_2O_2 as oxidant. Details of the reaction procedure are given in Chapter 2. The reactions were conducted in a closed stainless-steel autoclaves placed in a rotating hydrothermal synthesis unit.

4.2.3. Estimation of H_2O_2 - Iodometric Titration

After the reaction was over, the unreacted H_2O_2 present in the reaction mixture was estimated by iodometric titration. The preference for iodometric titration to titration with $KMnO_4$, is due to its lesser susceptibility toward interference from the organic substances; the later does not give sharp end point when titrated in the presence of organic compounds.

The principle involved in iodometric titration is that, H_2O_2 oxidizes iodide to iodine in the presence of acid and molybdate catalyst. The iodine formed is titrated with thiosulfate solution, using a starch indicator. The reactions involved are:

$$H_2O_2 + 2KI + H_2SO_4 \rightarrow I_2 + K_2SO_4 + 2H_2O$$

$$I_2 + 2\ Na_2S_2O_3 \rightarrow Na_2S_4O_6 + 2\ NaI$$

The procedure for iodometric titration of unreacted H_2O_2 present in the reaction mixture, is as follows. KI solution (1 % w/v) was prepared by dissolving 5 g of KI in 500 ml of double-deionized water and stored in a capped volumetric flask in cool and in dark place. The light yellow tinge of the air oxidized KI to I_2 was removed by adding 1 - 2 drops of dilute sodium thiosulfate solution to it. Ammonium molybdate solution was prepared by dissolving 9 g of ammonium molybdate in 10 ml of 6 N NH_4OH. To it, 24 g of ammonium nitrate was added and the solution was diluted to 100 ml with double-distilled waster. 5 N H_2SO_4 solution was prepared in a separate volumetric flask. 0.1 N sodium thiosulfate solution was prepared by dissolving 8 g of the salt in 500 ml of water, and standardized by titrating against potassium iodate (0.1 N) solution.

In a typical titration, whole reaction mixture was taken in a 100 ml volumetric flask and diluted up to the mark with deionized water. 10 ml of the diluted solution was pipetted out into the Erlenmeyer flask. To this, 20 ml of double-distilled water, 10 ml of sulfuric acid solution and 10 ml of potassium iodide solution and 2 drops of molybdate solution were added. The liberated iodine was immediately titrated against the 0.1 N sodium thiosulfate solution (taken in a burette) to faint yellow color. At this point, about 2 ml of starch indicator was added and continued the titration until the blue color just disappeared.

4.3. Results and Discussion

4.3.1. Characterization of Materials

4.3.1.1. XRD

Alkali and alkaline earth metal ion modification did not alter the XRD pattern of titanosilicate molecular sieves. Fig. 4.1 shows the XRD pattern of TS-1 modified with NaOH at pH = 10. Also no leaching of Ti from the silicalite framework due to

alkali modification was observed. The reflection at 24.5º indicates that the alkali modified TS-1 also possesses the same space group as that of the unmodified TS-1.

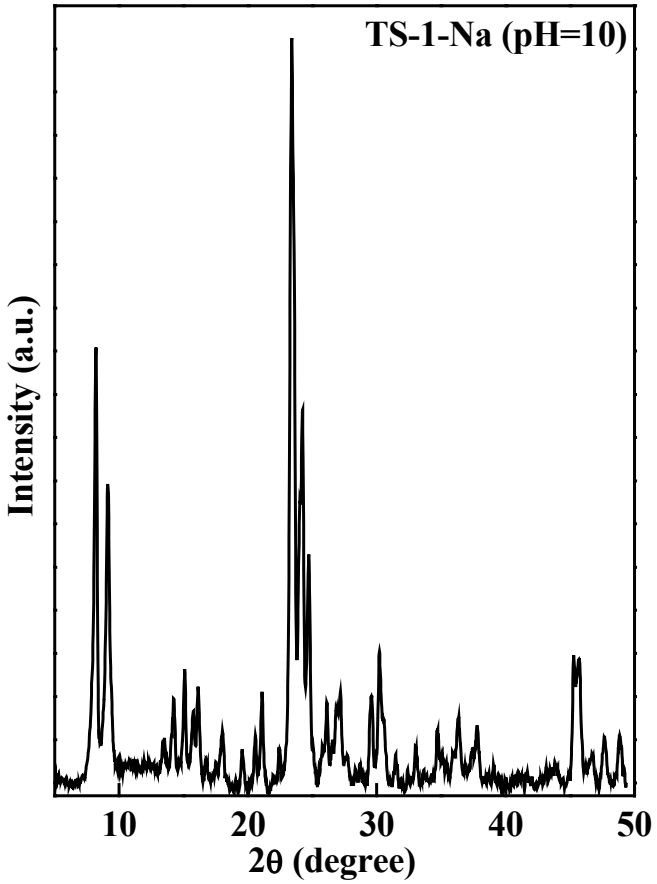

Fig. 4.1. XRD pattern of TS-1 impregnated with Na^+ ions at pH = 10.

4.3.1.2. FT-IR

The weak band at 965 cm^{-1} in the FT-IR spectrum (Fig. 4.2) for TS-1 modified with NaOH at pH = 10 shows the presence of Ti in the silicalite-1 framework [11-13] even after the treatment with alkali. The zeolitic structure is indicated by the band at 544 cm^{-1}. Alkali metal and alkaline earth metal ion impregnation did not alter the spectral characteristics.

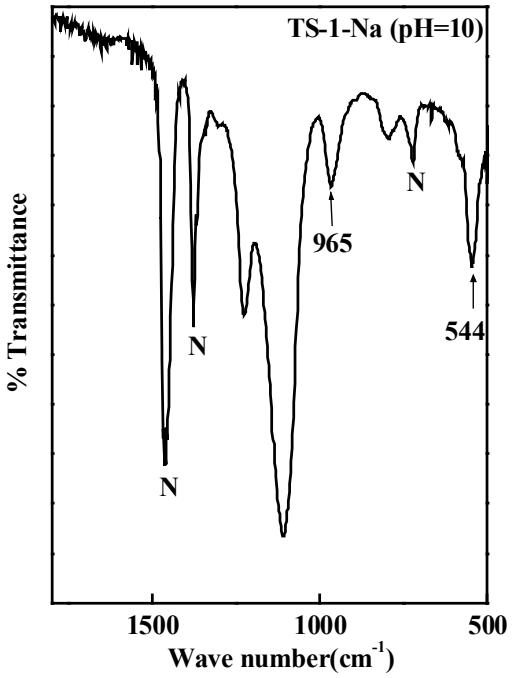

Fig. 4.2. FT-IR (in Nujol mull) of TS-1 impregnated with Na^+ ions (pH = 10).

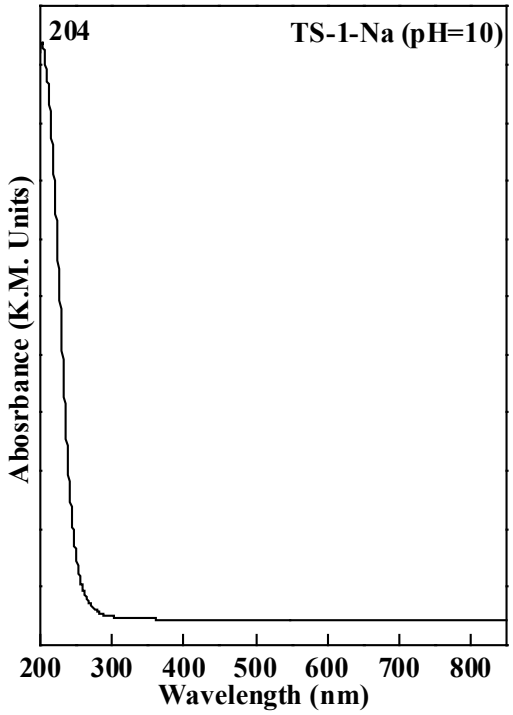

Fig. 4.3. DRUV-visible spectrum of TS-1 impregnated with Na+ ions at pH = 10.

4.3.1.3. DRUV-Visible

DRUV-visible spectrum (Fig. 4.3) of NaOH modified TS-1 at pH = 10 showed a band at 204 nm characteristic of framework Ti. TS-1 samples modified at pH = 8 also showed similar kind of spectrum. No additional band was observed in alkali modified TS-1 compared to the parent TS-1.

4.3.2. Reactive Oxo-Ti Species and Spectroscopic Characterization

4.3.2.1 EPR Spectroscopy

4.3.2.1.1. Influence of pH

Prior to contact with H_2O_2 the titanosilicate samples were EPR inactive consistent with the +4 oxidation state of Ti in those samples. Upon contacting H_2O_2, three types of $Ti(O_2^{-\bullet})$ species, A, B and C were generated on TS-1 [14 - 16]. They were different mainly in their g_{zz} parameter; g_{xx} and g_{yy} values being identical (A-type: g_{zz} = 2.0260, g_{yy} = 2.0090 and g_{xx} = 2.0023; B-type: g_{zz} = 2.0235, g_{yy} = 2.0090 and g_{xx} = 2.0023; C-type: g_{zz} = 2.0220, g_{yy} = 2.0090 and g_{xx} = 2.0023). A and B were more abundant than C [14, 15]. A comparison of the EPR results with the EXAFS analysis [16] suggests that, while the A-type species probably originated from tetrapodally-coordinated Ti sites ($Ti(OSi)_4$), the B-type originated from tripodally-coordinated Ti sites ($(HO)Ti(OSi)_3$) [15]. Ti-MCM-41, in contrast to TS-1, generated, predominantly, the B-type species. Zhao et al. [17] and Bonoldi et al. [18] have also identified the A and B type species in TS-1 catalysts.

Activated samples of TS-1 and Ti-MCM-41 were suspended in 10 ml of CH_3OH and the pH of the slurry was adjusted to a desired value using NaOH (for pH above 7) and oxalic acid (for pH of 4.5 and 5.5). The solid was then removed and dried at 373 K for 8 h and used in the analysis. A new type of $Ti(O_2^{-\bullet})$ species, A', was generated in the presence of alkali metal ions on TS-1 (Fig. 4.4). In acidic and neutral pH conditions, the A and B type $Ti(O_2^{-\bullet})$ species (Fig. 4.4, curves a and b) were observed over TS-1. When the pH was raised to 7 – 9 (using NaOH), an additional species, A', characterized by a signal at g_{zz} = 2.031, was also detected (see curves b – d). Above pH = 9, A' was the predominant species (curves e and f). Integrated EPR signal intensity and, hence, the total concentration of the paramagnetic $Ti(O_2^{-\bullet})$ species, increased by about 3 times when the pH was changed

from 4.5 to 10. At high pH, in addition to the A' species, signals due to Ti^{3+} ions ($g_{\perp}$ = 1.986 and $g_{||}$ = 1.951) [19], were also detected (curves e and f).

The addition of NaOH did not influence, significantly, the spectral features of Ti-MCM-41. The latter generated, mainly, the B-type species in the entire pH range. Ti^{3+} signals were also not detected in Ti-MCM-41. The EPR signal intensity was higher in Ti-MCM-41 than in TS-1 and it did not increase any further at high pH.

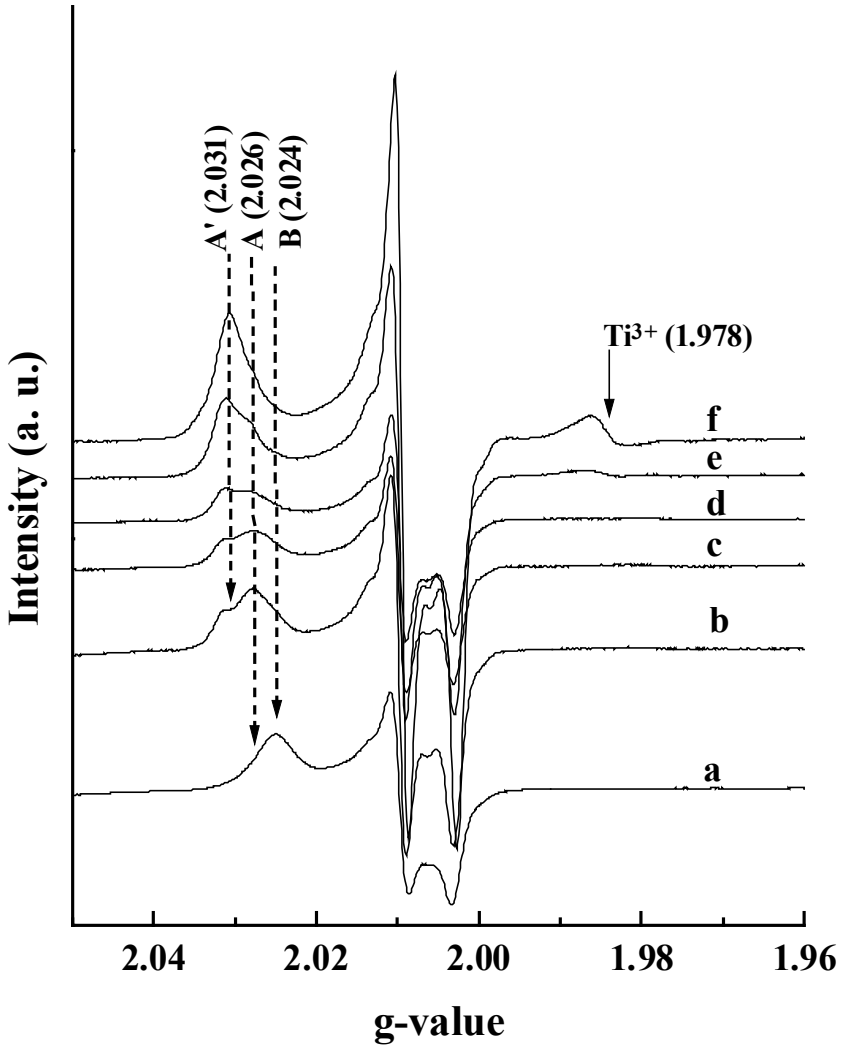

Fig. 4.4. EPR spectra of superoxo-Ti species in TS-1+CH_3OH+H_2O_2 system at 90 K – Influence of pH: pH = 6.8 (a), 7 (b), 8 (c), 9 (d), 10 (e), and 11 (f).

4.3.2.1.2. Influence of Alkali and Alkaline Earth Metal Ions

TS-1 was modified with alkali and alkaline earth metal ions. Li_2CO_3, KOH, CsOH, NH_4OH, MgO, CaO and $Ba(OH)_2$ were used as precursors for impregnation of TS-1. Fig. 4.5 shows the influence of alkali and alkaline earth metal ions on the EPR spectra. Li^+ yielded mainly, the A'-type $Ti(O_2^{-\bullet})$ species. Both A' and A-type species in different proportions were observed in the presence of K^+, Na^+, Cs^+ and NH_4^+ ions. The B-type species were dominant in the presence of Ba^{2+}. The total superoxo-Ti signal intensity was more in the presence of Li^+ than in the presence of NH_4^+, Na^+, K^+, Cs^+ and Ba^{2+}. In addition to $Ti(O_2^{-\bullet})$, signals at 2.078, 2.065 and 2.057 corresponding to the superoxo-species of the alkali and alkaline earth ions and Ti^{3+} ions [20], were also observed.

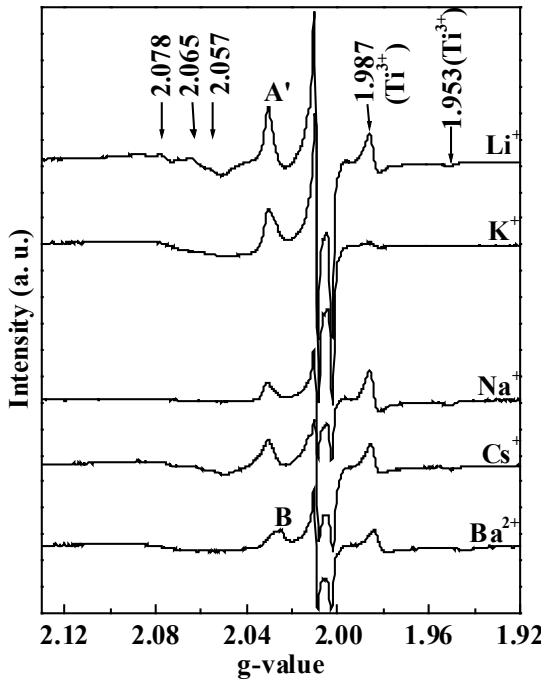

Fig. 4.5. EPR spectra of TS-1 (modified with alkali metal and alkali earth ions)+CH_3OH+H_2O_2 system (pH = 10.3 ± 0.3).

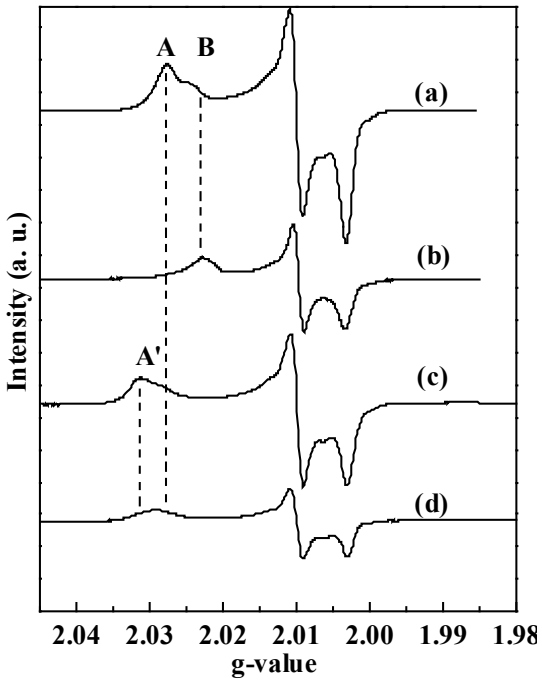

Fig. 4.6. Reactivity of superoxo-Ti species in TS-1. (a) TS-1+H_2O_2, (b) TS-1+H_2O_2+allyl alcohol, (c) TS-1+H_2O_2+CH_3OH+NaOH+H_2O_2 (pH = 9), (d) TS-1+H_2O_2+CH_3OH+NaOH+H_2O_2+allyl alcohol (pH = 9).

Fig. 4.6 shows the EPR spectra of TS-1 samples at controlled experimental conditions. The spectra reveal the differences in the reactivities of oxo-Ti species A', A and B. At neutral pH, on contact with allyl alcohol, the A-type species were consumed faster than the B-type (Fig. 4.6, curves a and b). However, at pH = 9.5, A' species were consumed faster than the A-type species (compare curves c and d). This indicates that the reactivity of the oxo-Ti species increases in the order: B < A < A'.

4.3.2.2. DRUV-Visible Spectroscopy

TS-1 samples showed a charge transfer band at 208 nm in the DRUV-visible spectrum, characteristic of framework Ti species (Fig. 4.7, curve a). On contact with aqueous H_2O_2, this band shifted to 217 nm in neutral condition (curve b) and to 240 nm in basic conditions (curves c and d) due to solvent interactions with the framework Ti [21]. When contacted with H_2O_2, the TS-1 samples showed an additional, broad, asymmetric signal in the range 300 – 500 nm (curves c – d). It was deconvoluted into two bands I (330 nm) and II (395 nm) (Fig. 4.7; dotted curves) attributable to the charge transfer transitions associated with superoxo-Ti ($Ti(O_2^{-\bullet})$)

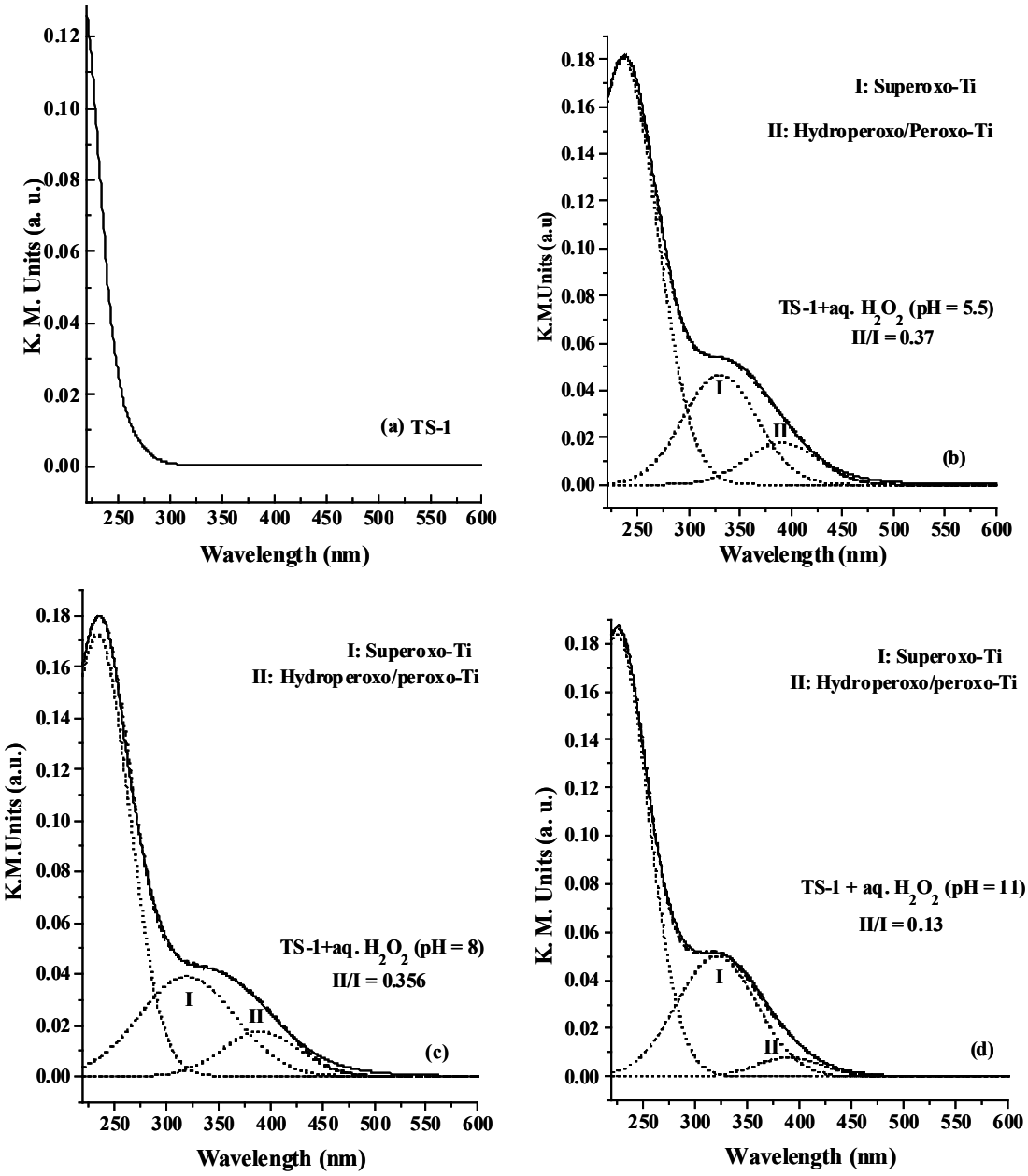

Fig. 4.7. DRUV-visible spectra of TS-1 (a) and TS-1 in CH_3OH reacted with aqueous H_2O_2 at different pH (b – d).

and hydroperoxo/peroxo-Ti ($Ti(OOH)/Ti(O_2^{2-})$) species, respectively [15]. The relative concentration of superoxo-Ti (band I) increases at high pH (Fig. 4.7) in agreement with the EPR results discussed above. Reducing the pH to 7 regenerates curve b from curve d, ruling out the leaching of Ti from the framework under these

conditions. Earlier, Zecchina et al. [22] had attributed similar spectral changes to the formation of η^1-hydroperoxo-Ti in neutral medium and η^2-anionic peroxo-Ti species under basic conditions.

The stability of the oxo-Ti species formed in neutral and basic conditions was determined by recording the DRUV-visible spectra as a function of time (Fig. 4.8, panels I and II, respectively).

As seen from panel I, the intensity of the charge transfer band in the neutral medium was invariant for about 1 h and then decreased with time. This band, under basic conditions (Fig. 4.8, panel II), was however, stable for about 1.5 h and then decreased with time. Hence, the oxo-Ti species formed under basic conditions are somewhat more stable than the ones formed in acidic/neutral conditions.

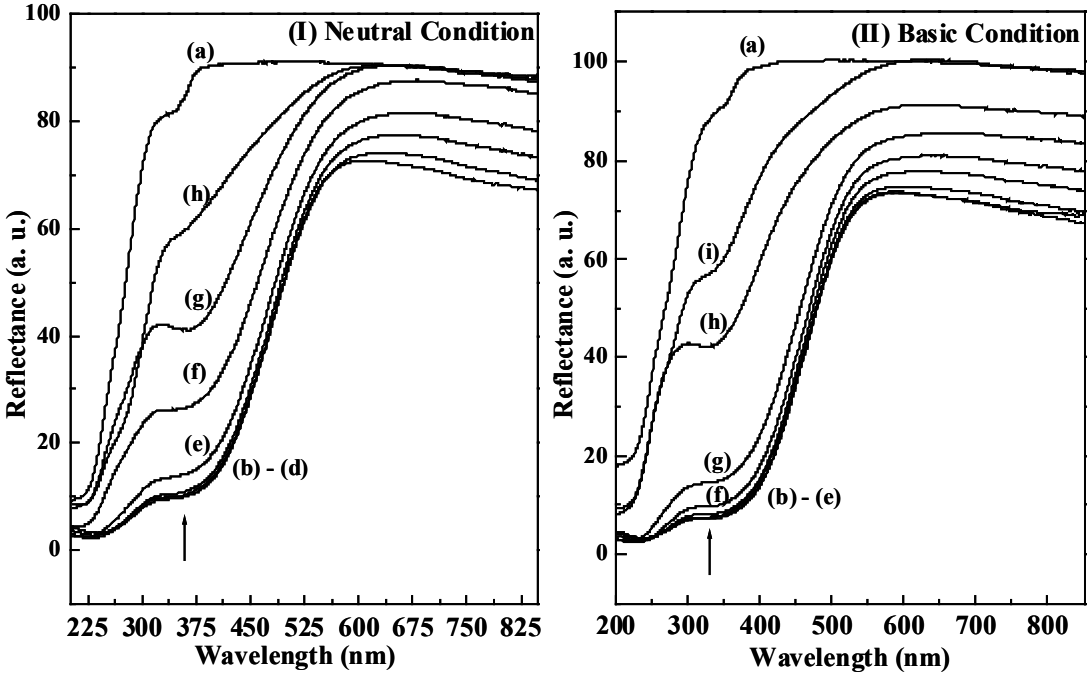

Fig. 4.8. Stability of oxo-titanium species generated on TS-1 in (I) neutral condition (pH = 6.8) and (II) basic condition (pH = 10) – diffuse reflectance UV-visible spectra. (I) – (a) TS-1 + CH_3OH, (b) TS-1 + CH_3OH + H_2O_2, 0 h, (c) 0.5 h, (d) 1 h, (e) 1.5 h, (f) 2.5 h, (g) 4 h and (h) 24 h; (II) – (a) TS-1 + CH_3OH + NaOH, (b) TS-1 + CH_3OH + NaOH + H_2O_2, 0 h, (c) 0.5 h, (d) 1 h, (e) 1.5 h, (f) 2 h (g) 2.5 h, (h) 5.5 h and (i) 24 h.

4.3.3. Catalytic Activity Studies

Table 4.1 reports the effect of pH on the catalytic activities of TS-1 and Ti-MCM-41. Adjustment of pH was done before H_2O_2 addition. As H_2O_2 solutions are acidic, the pH of the reaction mixture decreased from the initially adjusted values after H_2O_2 addition (see Table 4.1). At the end of the reaction (as H_2O_2 was consumed) pH of the solution again increased. The changes in the catalytic activities are correlated with the initial adjusted pH values. It may, however, be noted that the modified pH values are the point of departure, but not the initial adjusted pH values.

With an increase in pH, conversion of allyl alcohol in methanol decreased from 95.3% (at pH = 3.5) to 22.2 mol% (at pH = 8.5) (Run Nos. 1 – 6). However, the epoxide (glycidol) selectivity increased from 86.8 to 100 mol%. The amount of H_2O_2 present in the medium before and after the reaction, was estimated (by iodometric titration) and the H_2O_2 efficiency for epoxide formation was determined from the amount of H_2O_2 consumed. The H_2O_2 efficiency decreased markedly at high pH conditions. Most of the H_2O_2, probably, decomposed into H_2O and O_2 at high pH. Similar observations were made also in the epoxidation of allyl chloride (Run Nos. 12 – 14).

To probe the location of the alkali ions, added during the reaction, the used catalyst samples after Runs 3 and 4 were recovered by centrifugation, combined, air-dried and then, reused *without adding any additional alkali* (Run No. 7). The epoxide selectivity (96.8%), intermediate between runs 3 and 4 (92.8 and 100%, respectively) indicates that, the Na^+ added during Runs 3 and 4 are still located on the surface and were not leached out from the solid catalyst into the medium during the reaction.

Next, the fresh TS-1 samples were impregnated with small amounts of alkali. TS-1-Na(8) and TS-1-Na(10) were thus prepared (initial pH = 8 and 10, respectively, as described in Chapter 2). Catalytic runs with these catalysts (with no further alkali addition) exhibited activities similar to the TS-1 catalysts wherein the alkali was added *in situ* (compare Run Nos. 8 and 9 with 4 and 6, respectively).

Ti-MCM-41 exhibited lower activity compared to TS-1. Significant amounts of formic acid were also formed by oxidation of CH_3OH (negligible over TS-1).

Table 4.1. Epoxidation of Allyl Alcohol and Chloride – Influence of pH[a]

Run No.	Catalyst	Substrate	pH			TOF[b]	Olefin conv. Mol %	H_2O_2 efficiency	Epoxide selectivity (mol%)
			Initial/ before H_2O_2 addition	After H_2O_2 addition	At the end of the reaction				
1	TS-1	Allyl alcohol	4.5	3.5	4.2	18.9	95.3	100	86.8
2	TS-1	Allyl alcohol	5.5	3.5	4.2	18.7	94.4	100	87.4
3	TS-1	Allyl alcohol	7.0	5.5	5.8	17.7	89.2	95	92.8
4	TS-1	Allyl alcohol	8.0	5.7	5.9	16.0	80.7	87	100
5	TS-1	Allyl alcohol	9.0	5.9	6.2	7.1	35.6	46	100
6	TS-1	Allyl alcohol	10.0	8.5	8.0	4.4	22.2	21	100
7	TS-1 in runs 3 & 4 –reused	Allyl alcohol	7.8	5.5	5.7	14.8	74.4	97	96.8
8	TS-1-Na(8)	Allyl alcohol	8.0	5.7	5.9	16.2	81.6	89	100
9	TS-1-Na(10)	Allyl alcohol	10.0	7.8	8.0	5.9	29.7	20	100
10	TiMCM-41	Allyl alcohol	6.8	-	-	2.1	10.4		100
11	TiMCM-41	Allyl alcohol	8.0	-	-	2.3	11.4		100
12	TS-1	Allyl chloride	6.8	3.2	3.0	19.3	97.2	97	73.8
13	TS-1	Allyl chloride	7.0	3.8	3.8	19.8	100	100	79.7
14	TS-1	Allyl chloride	8.0	4.3	4.2	19.8	100	100	81.6

[a]Reaction conditions: catalyst (100 mg) + substrate (0.5 g) + CH_3OH (10 g) + H_2O_2 (50%, 0.9 ml); H_2O_2/substrate = 2.0; temperature = 333 K; run time = 8 h.

[b]TOF = moles of substrate converted per mol of Ti per hr.

Changes in pH did not affect conversions significantly (Run Nos. 10 and 11). It may be recalled that Ti-MCM-41 generated only the B-type of superoxo-Ti species, which are less active than the A- and A'-type species generated on TS-1 catalysts.

The epoxidation of allyl alcohol was carried out at pH = 8 in the presence of different alkali metal and alkaline earth compounds (Li_2CO_3, NaOH, KOH, CsOH, MgO, CaO and $Ba(OH)_2$) and NH_4OH (Table 4.2). Catalytic activity increased in the order: $Li^+ < NH_4^+ < Na^+ < K^+ < Cs^+$ and $Mg^2 < Ca^{2+} < Ba^{2+}$. Epoxide selectivity followed a reverse order; Cs^+ exhibited 100% allyl alcohol conversion, but with lower epoxide selectivity, only 76.7% (Table 4.2, Run No. 4).

Table 4.2. Effect of Alkali and Alkaline Ions on the Epoxidation of Allyl Alcohol[a]

Run No.	Alkali/alkaline earth ion	TOF[b]	Allyl alcohol conversion (mol%)	Epoxide selectivity (mol%)
1	Li^+	2.4	11.9	100
2	NH_4^+	9.7	48.6	100
2	Na^+	17.0	85.8	91.7
3	K^+	18.7	94.4	79.1
4	Cs^+	19.8	100	76.7
5	Mg^{2+}	12.5	63.0	100
6	Ca^{2+}	18.8	94.7	88.5
7	Ba^{2+}	18.6	94.1	75.0

[a]Reaction conditions: catalyst (100 mg) + allyl alcohol (0.5 g) + CH_3OH (10 g) + H_2O_2 (50%, 0.9 ml); H_2O_2/allylalcohol = 2.0; temperature = 333 K; run time = 8 h; pH = 8.0. [b]TOF = moles of allyl alcohol converted per mol of Ti per hr.

Table 4.3. Epoxidation of Styrene over TS-1: Influence of pH[a]

Run No.	pH		Styrene conversion (mol%)	Styrene oxide	Methylated diol	Diol	Benzaldehyde	Phenyl acetaldehyde	Others
	Initial / before H_2O_2 addition	At the end of the reaction							
				Solvent: CH_3OH					
1	6.8	4.0	39.9	35.9	46.0	1.1	13.8	0.3	2.9
2	7.0	4.0	42.3	35.0	45.5	0.8	15.1	0.5	3.1
3	8.0	4.0	35.2	40.9	40.7	1.1	15.5	0.3	1.5
4	9.0	4.5	27.3	45.0	37.4	0.8	16.8	0.0	0.0
5	11.0	5.5	4.4	66.6	5.9	0.0	18.3	9.2	0.0
				Solvent: CH_3OH + CH_3CN (1:1)					
6	7.0	4.0	26.3	29.4	21.8	3.1	35.0	9.2	1.5
7	8.0	4.0	26.1	28.5	20.6	2.3	36.0	11.8	0.8
8	9.0	4.0	28.4	31.8	19.1	2.9	34.7	10.0	1.5
9	10.0	4.5	27.6	32.1	14.1	2.3	40.0	11.2	0.3
10	11.0	5.5	13.3	44.9	4.1	1.0	33.4	16.6	0.0
				Solvent: CH_3CN					
11	6.4	4.0	25.2	20.2	1.0	3.9	65.3	9.1	0.5
				Solvent: CH_3COCH_3					
12	6.0	3.5	25.4	61.4	0.7	2.6	31.9	3.4	0.0

[a]Reaction conditions: TS-1 (100 mg) + styrene (0.898 g) + solvent (10 g)+ H_2O_2 (50%; 0.9 ml); H_2O_2/styrene = 2; temp. = 333 K; run time 8 h.

The epoxidation of styrene is less selective over TS-1 catalysts compared to the epoxidation of allylic compounds. Significant amounts of methylated diols were obtained (Table 4.3). About 15% of benzaldehyde was also observed. Conversion of styrene decreased and styrene oxide selectivity increased marginally at high initial pH values. The solvent has a significant influence on the reactivity (conversion) and product selectivity. In CH_3OH + CH_3CN mixture (1:1 v/v), CH_3CN or CH_3COCH_3, methylated diol was suppressed but benzaldehyde formed in significant amounts.

Fig. 4.9. (a) Variation of allyl alcohol conversion, epoxide selectivity and relative A' signal intensity as a function of pH. (b) Variation of catalytic activity (TOF per hour) as a function of supero-Ti (total EPR signal intensity) and hydroperoxo-Ti/superoxo-Ti (from DRUV-visible).

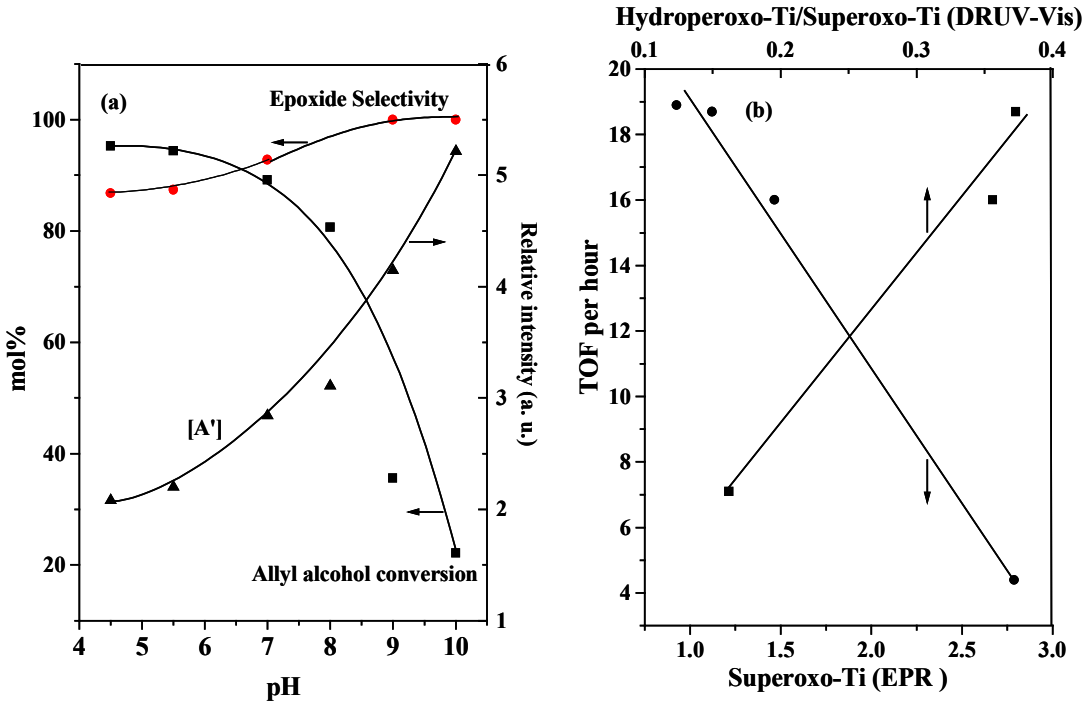

4.3.4. Structure-Reactivity Correlations

A comparison of the spectroscopic results with the catalytic activity data reveals that while specific activity in allyl alcohol conversion (turnover frequency per hour) decreases with increasing *paramagnetic*, *superoxo-Ti species* (Fig. 4.9(a) and (b)), it increases linearly with the *hydroperoxo*/*peroxo content* (estimated from DRUV-visible spectra) (Fig. 4.9(b)). The present study, in agreement with the earlier

results [23, 24], suggests that the diamagnetic hydroperoxo/peroxo-Ti species are, probably, responsible for the selective epoxidation activity. Selectivity for the epoxide increased with the relative A' signal intensity (estimated from EPR spectra) (Fig. 4.9(a)). Similar correlations between total EPR signal intensity (superoxo-Ti concentration) *vs* allyl alcohol conversion and relative A' signal intensity *vs* epoxide selectivity were also observed when the alkali metal ion was changed from Cs^+ to K^+, Na^+ and Li^+ (Fig. 4.10). A' species were generated also when TS-1 was impregnated with Pd^{2+} ions and exposed to (H_2 + O_2) or when urea–H_2O_2 adduct was used in the place of aqueous H_2O_2 (Chapter 3).

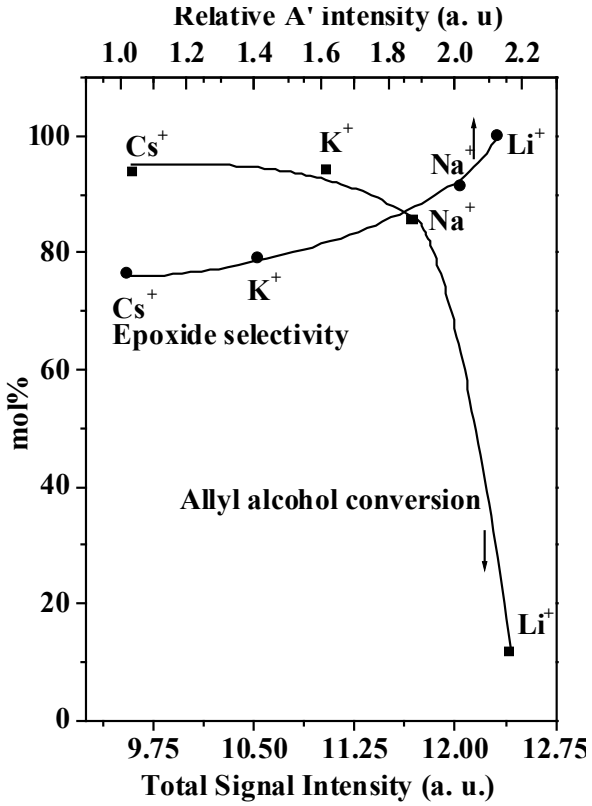

Fig. 4.10. Variations of allyl alcohol conversion with the total EPR signal intensity and epoxide selectivity with the relative A' signal intensity.

Over TS-1, the only primary product is the epoxide. In methanol, the epoxide is opened by the solvent forming monomethylglycol. This ring opening is possibly favored and catalyzed by the acidic sites of TS-1. The added bases neutralize

(deactivate) the acid site of TS-1 and thereby, enhance the chemoselectivity. When the unmodified TS-1 catalyst was reused (see Run 2, Table 1), an improvement in epoxide selectivity (from 88.5 to 93 mol%) was observed, but the product was not exclusively epoxide as was observed in the case of Na^+-modified TS-1 catalyst (initial pH 8, Run 6). It is likely, that the strong Brönsted acid sites that were present in the unmodified TS-1 catalyst are deactivated in the first run or by alkali ion modification. It appears that the deactivation of acid sites as well as the modified Ti sites are responsible for the enhanced chemoselectivity in epoxidation reactions.

4.4. Conclusions

Reactive oxo-Ti species in TS-1 and Ti-MCM-41, generated by interactions with H_2O_2 at different pH values were investigated by EPR and DRUV-visible spectroscopies. Alkali addition enhances epoxide selectivity. A new type of superoxo-Ti species, A' and Ti^{3+} ions were detected under basic conditions by EPR spectroscopy. The concentration of A' during reaction correlates with the selectivity for the epoxide. Neutralization of acid sites on TS-1 by alkali addition as well as formation of new type of reactive oxo-Ti species are the possible reasons for the enhanced selectivity**.**

4.5. References

[1] C.B. Khouw, C.B. Dartt, J.A. Labinger, M.E. Davis, J. Catal. 149 (1994) 195.

[2] C.B. Khouw, M.E. Davis, J. Catal. 151 (1995) 77.

[3] G. Bellussi, V. Fattore, Stud. Surf. Sci. Catal. 69 (1991) 79.

[4] M.G. Clerici, Appl. Catal. 68 (1991) 249.

[5] M.G. Clerici, G. Bellussi, U. Romano, J. Catal. 129 (1991) 159.

[6] G. Bellussi, A. Carati, M.G. Clerici, G. Maddinelli, R. Millini, J. Catal. 133 (1992) 220.

[7] M.G. Clerici, P. Ingallina, J. Catal. 140 (1993) 71.

[8] M.C. Capel-Sanchez, J.M. Campos-Martin, J.L.G. Fierro, Appl. Catal. A: General 246 (2003) 69.

[9] T. Armaroli, F. Milella, B. Notari, R.J. Willey, G. Busca, Top. Catal. 15 (2001) 63.

[10] V. Arca, A.B. Boscoletto, N. Fracasso, L. Meda, G. Ranghino, J. Mol. Catal. A: Chem. 243 (2006) 264.

[11] *M.R. Boccuti, K.M. Rao, A. Zecchina, G. Leofanti, G. Petrini, Stud. Surf. Sci. Catal. 48 (1989) 133.*

[12] *G. Bellussi, M.S. Rigutto, Stud. Surf. Sci. Catal. 85 (1994) 177.*

[13] *D. Scarano, A. Zecchina, S. Bordiga, F. Geobaldo, G. Spato, G. Petrini, G. Leofanti, M. Padovan, G. Tozzola, J. Chem. Soc., Faraday Trans. 89 (1993) 4123.*

[14] K. Chaudhari, D. Srinivas, P. Ratnasamy, J. Catal. 203 (2001) 25.

[15] D. Srinivas, P. Manikandan, S.C. Laha, R. Kumar, P. Ratnasamy, J. Catal. 217 (2003) 160.

[16] D. Gleeson, G. Sankar, R.A. Catlow, J.M. Thomas, G. Spano, S. Bordiga, A. Zecchina, C. Lamberti, C. Phys. Chem. Chem. Phys. 2 (2000) 4812.

[17] Q. Zhao, X.-h. Bao, Y. Wang, L.-w. Lin, G. Li, X.-w. Guo, X.-s. Wang, J. Mol. Catal. A: Chemical 157 (2000) 265.

[18] L. Bonoldi, C. Busetto, A. Congiu, G. Marra, G. Ranghino, M. Salvalaggio, G. Spanó, E. Giamello, Spectrochimica Acta 58A (2002) 1143.

[19] R. Bal, K. Chaudhari, D. Srinivas, S. Sivasanker, P. Ratnasamy, J. Mol. Catal. A: Chem. 162 (2000) 199.

[20] A. Tuel, Y. Ben Taârit, Appl. Catal. A: General 110 (1994) 137.

[21] F. Geobaldo, S. Bordiga, A. Zecchina, E. Giamello, G. Leofanti, G. Petrini, Catal. Lett. 16 (1992) 109.

[22] A. Zecchina, S. Bordiga, C. Lamberti, G. Ricchiardi, D. Scarano, G. Petrini, G. Leofanti, M. Mantegazza, Catal. Today 32 (1996) 97.

[23] B. Notari, Adv. Catal. 41 (1996) 253.

[24] G.N. Vayssilov, Catal. Rev._Sci. Eng. 39 (1997) 209.

Chapter - 5

Mode of O-O Bond Cleavage in Oxo-Titanium Species in Titanosilicate Molecular Sieves and Product Selectivity

5.1. Introduction

The enormous interest in titanosilicate molecular sieves is due to their remarkable catalytic activity in oxidation reactions using the environmentally benign aqueous H_2O_2 as the oxidant [1 - 3]. In the dehydrated state, the surface of a well-prepared titanosilicate molecular sieve like TS-1, is known [4 – 8] to contain mainly two types of Ti^{4+} ions (1) those wherein the Ti^{4+} ions are 4-fold coordinated with lattice (-OSi) groups, $Ti(OSi)_4$, in near tetrahedral symmetry, called the tetrapodal Ti ions, and (2) those wherein they are tripodally coordinated to the surface, $Ti(OSi)_3(OH)$, an extra-lattice OH group forming the fourth ligand. The tetrapodal species dominates in TS-1, TS-2 and Ti-beta while the tripodals are more prevalent in Ti-MCM-41 and other mesoporous materials [4 – 8]. On interaction with H_2O_2, (H_2 + O_2) or alkyl hydroperoxides (ROOH), the Ti ions expand their coordination number to 5 or 6 and form Ti-hydroperoxo/peroxo [9 – 16] and superoxo [17 – 22] complexes, which catalyze the oxidation reactions. What is the influence of the nature and mode of cleavage of the O-O bond (in the oxo-Ti species) on product selectivity? In many oxidations catalyzed by titanosilicates it has been noted [1 - 3] that product selectivity depends on a variety of factors including the type of crystalline structure (TS-1, Ti-beta, Ti-MCM-41), solvent, temperature and oxidant (H_2O_2, alkyl hydroperoxide, (H_2 + O_2), urea-H_2O_2 *etc.*). For example, in olefin oxidations, both epoxidation and allylic oxidations occur, their relative importance varying with the factors mentioned above [1]. In the present work, an attempt is made to explore the relationship between (1) the structure of the Ti-oxo complex, (2) the mode of cleavage of the O-O bond in Ti-oxo species and (3) product selectivity in olefin epoxidation reactions over different titanosilicate molecular sieves. The redox behavior of Ti in TS-1 and Ti-MCM-41 was investigated by cyclic voltammetric (CV) measurements. The stability of the oxo-Ti species was investigated by UV-visible and EPR spectroscopic studies.

The O-centered radical species such as $HO^{\bullet}$, $HOO^{\bullet}$ and $O_2^{-\bullet}$ generated by homolytic O-O cleavage are very short lived (10^{-9} sec for $HO^{\bullet}$, for example). EPR-spin trapping technique is used to detect such free radicals formed during the reaction *via.*, the O-O cleavage. The O-centered radicals were reacted with a spin trap, 5,5-

dimethyl-*1*-pyrroline-*N*-oxide (DMPO), to generate relatively long-lived nitroxide free radicals (spin adducts), easily detected by EPR spectroscopy. The spectral features and the spin Hamiltonian parameters (superhyperfine coupling constant) are highly sensitive to the type of radical adduct (DMPO-OH, DMPO-O_2 and DMPO-OOH). Changes in radical concentrations in different solvents and in the presence of known radical scavengers, like hydroquinone, are also studied. Product selectivities in cyclohexene and styrene oxidations are found to be influenced by the concentration of such radicals.

5.2. Experimental

The procedure for the synthesis of titanosilicate molecular sieves is described in Chapter 2. The experimental methodology of EPR and cyclic voltammetry techniques is also mentioned in Chapter 2.

5.2.1. EPR-Spin Trapping Experiments

In a typical sample preparation procedure, to DMPO solution in water (0.5 mmol; 0.2 ml), 0.5 ml of solvent (DMSO, CH_3CN or C_2H_5OH) was added and the pH was adjusted to 7.4 using 0.1 M phosphate buffer (K_2HPO_4 + KH_2PO_4). Separately, Ti-molecular sieves (8 mg) were treated with dilute H_2O_2 (30% aqueous H_2O_2 was diluted by 10 times; 0.5 ml), warmed for 5 min at 333 K and then centrifuzed. The spin trap solution prepared as above at 298 K was added to the centrifugate. It was immediately taken in an EPR quartz flat cell and its EPR measured at 298 K.

Prior to use, DMPO was purified over activated charcoal. DMPO was diluted to 10 times in double distilled water. The diluted DMPO solution was washed thrice with 10 ml of toluene. The water layer containing DMPO was separated from the toluene layer containing the other organic impurities. Further, the DMPO solution was passed through activated charcoal. The colorless DMPO solution was stored in an amber colored bottle at 280 K. The purity of DMPO was confirmed by the absence of any EPR signal.

5.2.2. Catalytic Activity: Reaction Procedure

5.2.2.1. Epoxidation of Cyclohexene

0.1 g of titanosilicate (TS-1, Ti-MCM-41, Ti-SBA-15 or ETS-10), 0.82 g of cyclohexene, 5 ml of solvent were taken in a glass flask fitted with a water-cooled

condenser and placed in a constant temperature (333 K) oil bath. H_2O_2 ([cyclohexene]/[H_2O_2] = 3 mol/mol) was added drop-wise over a period of 10 min and then the reaction was carried out for 4 h. The products were analyzed by gas chromatography (CHROMPACK CP9001; 50 m-long x 0.32 mm-i.d. x 0.3 μm thick Hewlett-Packard fused silica capillary column) and identified by GC-MS (Shimadzu QP-5000; 30 m-long x 0.25 mm-i.d. x 0.25 mm-thick capillary DB-1 column).

5.2.2.2. Epoxidation of Styrene

In a 100 ml Teflon-lined steel autoclave, 0.1 g of TS-1, 10 g of solvent, 8.63 mmol of styrene and 17.2 mmol of H_2O_2 (aqueous) were taken and the reaction was conducted at 333 K in a rotating hydrothermal synthesis reactor (rotation speed = 30 rpm) for 8 h. The products were analyzed by gas chromatography / mass spectrometry.

5.2.2.3. Epoxidation Reactions in the Presence of Radical Scavengers

Certain oxidations were conducted in the presence of radical scavengers such as mannitol, catechol, thiourea, sodium acetate, sodium salicylate, *p*-benzoquinone, hydroquinone and sodium formate. In those experiments a known quantity of the radical scavenger (0 – 0.018 mmol) was added to the reaction mixture and the reaction conducted in a similar manner.

5.3. Results and Discussion

5.3.1. Structure and Redox Behavior of Ti^{4+} Ions

The titanosilicate samples, TS-1, Ti-MCM-41 and Ti-SBA-15, show an intense UV band at 200 – 230 nm corresponding to a charge transfer transition from O^{2-} to Ti^{4+}. This band was attributed [1 - 3] to dispersed-Ti ions in a pseudo-tetrahedral coordination. Spectral deconvolution studies revealed that this band comprises of two bands with maximum at 206 and 228 nm corresponding to tetrapodal Ti species, $Ti(OSi)_4$ and tripodal Ti species, $Ti(OSi)_3(OH)$, respectively. Intensity of the 206 nm band was more in the case of TS-1. Ti-MCM-41 and Ti-SBA-15 contained mainly the band at 228 nm corresponding to the tripodal Ti. Similar conclusions on the presence of two different tetracoordinated Ti species were drawn earlier [23] from the EPR investigations. The two Ti species differed in their

reducibility in H_2, with the tripodal Ti^{4+} being more easily reducible than the tetrapodal Ti^{4+} ions [23].

Cyclic voltammetry (CV) is a highly sensitive technique for detecting changes in the oxidation state and/or redox potential of ions. TS-1 showed two reduction peaks, A and B (corresponding to $Ti^{4+} + e^- \rightarrow Ti^{3+}$) at –0.51 and –0.27 V (Fig. 5.1; left panel), with the former being more intense than the latter redox peak. They represent Ti^{4+} ions in two different structural environments and, hence, with different reduction potentials. Ti-MCM-41 exhibited (Fig. 5.1, middle panel) four reduction peaks (A, B, C and D) at –0.52, -0.21, -0.22 and –0.05 V, respectively, with intensities A : B : C : D = 1 : 33 : 33 : 33, respectively. The reduction peak A by analogy to TS-1, arises from a tetrapodal Ti while B arises from the tripodal Ti; C and D, originate, perhaps, from penta- and hexa-coordinated defect open structures, respectively. The less negative reduction potential of the tripodal Ti (reduction peak B) compared to the tetrapodal species (reduction peak A) indicates that the former could be reduced more easily. This observation is in agreement with the earlier EPR studies [23] wherein the tripodal Ti^{4+} could be reduced with dry H_2 at 673 K while the tetrapodal Ti were reduced only above 823 K.

Upon contacting TS-1 with H_2O_2, a new reduction peak is observed at –0.69 V (Fig. 5.1, right panel). The original reduction peaks of TS-1 disappeared completely. The new peak is attributed to the reduction of $Ti(O_2^{-\bullet})$ to $Ti(O_2^{2-})$. Molecular oxygen and free superoxide ion are reduced only beyond –0.9 V. Superoxide ions bound to Ti are, hence, more easily reduced than free superoxide ions.

5.3.2. Generation of Oxo-Ti Species with Aqueous H_2O_2 over Titanosilicates

On contact with aqueous H_2O_2, different types of Ti-oxo species (hydroperoxo, peroxo- and superoxo-Ti) were generated in titanosilicates. A detailed spectral characterization of these oxo-Ti species by both EPR and DRUV-visible spectroscopies was discussed in Chapter 3.

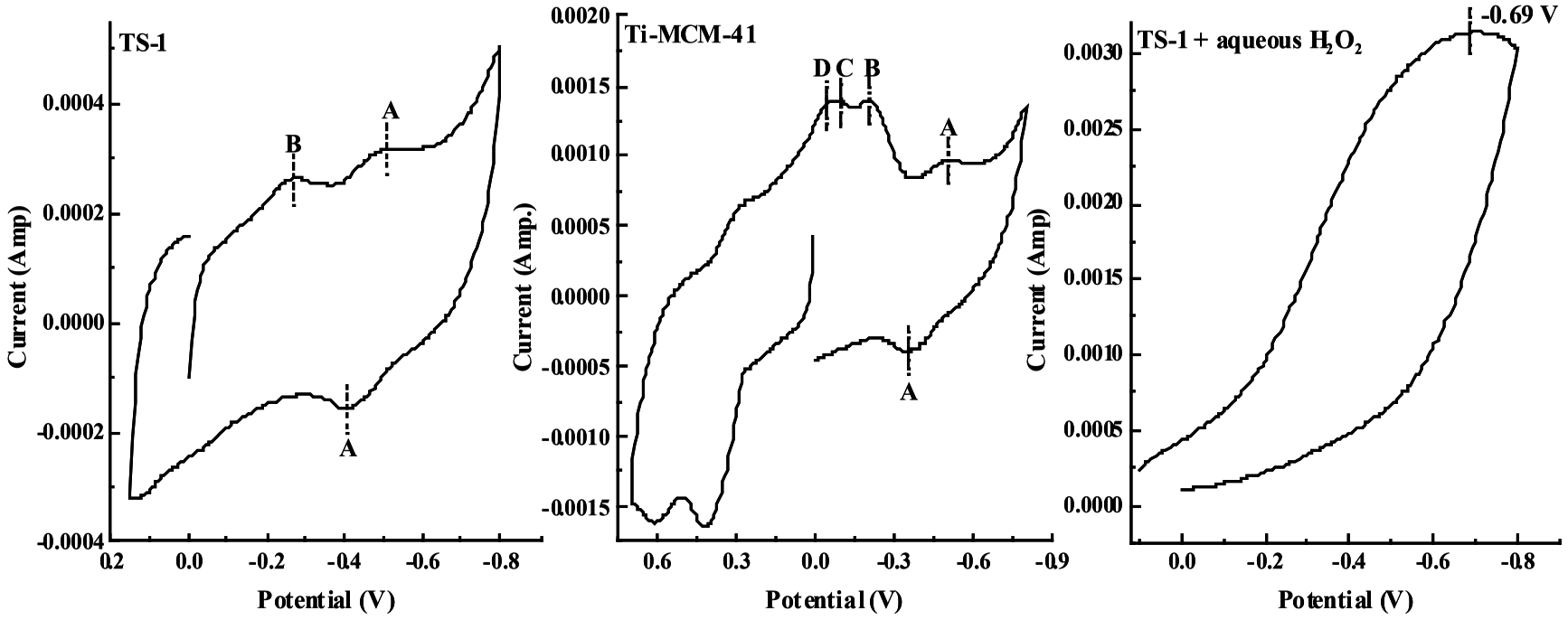

Fig. 5.1. Cyclic voltammographs of TS-1, Ti-MCM-41 and TS-1 contacted with aqueous H_2O_2. Peaks A – D correspond to different types of Ti species in TS-1 and Ti-MCM-41.

5.3.3. Reactivity of Superoxo-Ti Species – *In situ* EPR Studies

In situ EPR studies provided evidence for the participation of these oxo-Ti species in epoxidation reactions (Fig. 5.2). In allyl alcohol epoxidation, the oxo-Ti species (A-type) generated from the tetrapodal Ti were consumed faster than those (**B**-type) generated from the tripodal Ti (Fig. 5.2; left panel). Participation of **A** and **B**-type species was also observed in the epoxidations of cyclohexene and styrene (Fig. 5.2; middle and right panels). In the latter two cases, organic C-centered radicals (multiplet pattern indicated by asterisk; see the 2nd derivative plots; g = 2.0022) were also detected. Such organic radicals were not observed in allyl alcohol epoxidations (Fig. 5.2; left panel). The rate of consumption of the A and B-type species varied with the type of substrate.

In the oxidation of cyclohexene, the **A**-type species were consumed 4.6 x 10^2 times faster (estimated from the EPR signal intensity as a function of time) than the **B**-type species. In the case of styrene, the **A** species were consumed 0.63 x 10^2 times faster than **B**. In allyl alcohol epoxidation, the **A**-type species are consumed twice faster. The higher reactivity of the **A**-type oxo-Ti species can be correlated with the reversible reduction-oxidation behavior of the corresponding Ti ions (Fig. 5.1). In cyclic voltammographs, a reversible redox couple was observed only for the **A**-type species. The **B**-type species showed only a reduction peak, the corresponding oxidation peak could not be detected. Hence, the facile reduction and oxidation behavior of the tetrapodal-Ti species, **A**-type, is responsible for their superior activity. The irreversible redox behavior of the tripodal Ti leads to weak activity.

5.3.4. Catalytic Activity and Selectivity

Oxidation of olefins containing allylic hydrogens can give rise to (1) epoxides, (2) allylic oxidation products (alcohol or ketone) or (3) cleavage of the double bond. In addition, the epoxide can undergo further acid-catalyzed isomerization (for example, styrene oxide to phenyl acetaldehyde) or hydration to diol (ethylene oxide to ethylene glycol).

5.3.4.1. Influence of Ti^{4+} Structure on the Oxidation of Cyclohexene

The product distribution in cyclohexene oxidation (Scheme 5.1) over different titanosilicate catalysts is listed in Table 5.1. Olefin conversion is higher over the mesoporous material Ti-MCM-41 and Ti-SBA-15 due to the greater ease of diffusion of

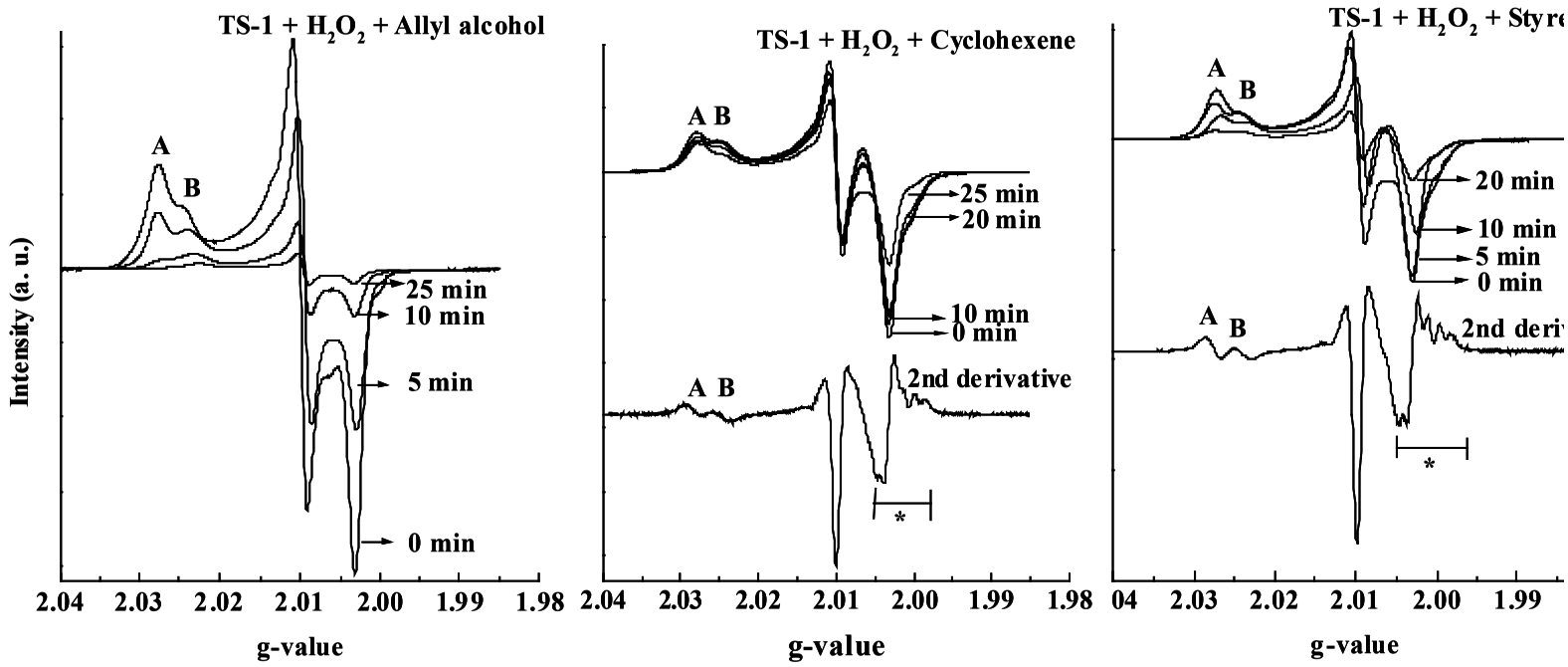

Fig. 5.2. Reactivity of Ti-oxo species on TS-1 + H_2O_2 system in substrate oxidation. Reactions were conducted at 333 K for a known period of time (0 – 25 min) and spectra recorded at 80 K. Asterisk (*) indicates signals due to substrate-based radicals. These could be seen more clearly in the 2nd derivative plots.

reactant molecules in their pores. However, the epoxide is favored only over TS-1. The large amount of diols formed over the mesoporous material is due to their relatively greater acidity and consequent hydration of the epoxide to the diols.

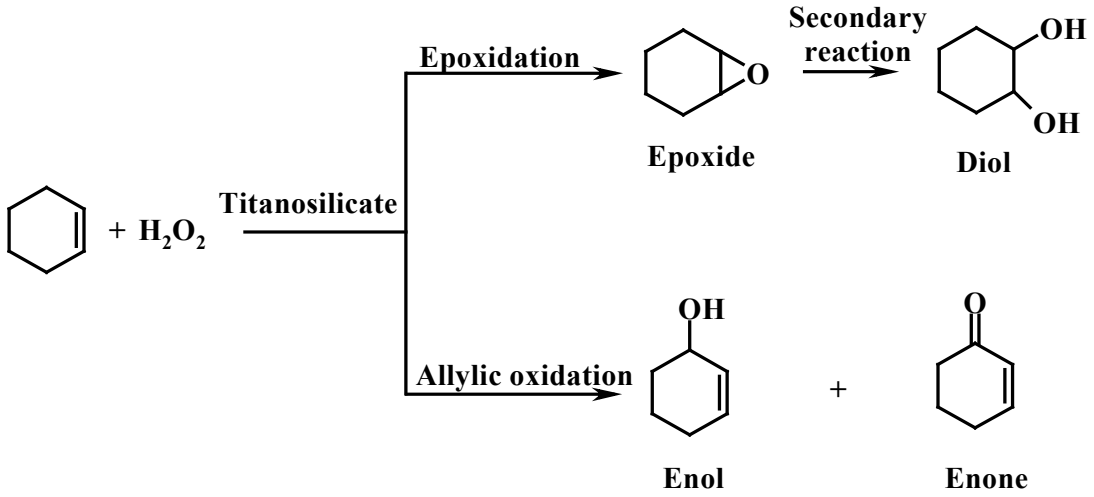

Scheme 5.1: Oxidation of cyclohexene

Table 5.1. Influence of Ti Structure: Oxidation of Cyclohexene with Aqueous H_2O_2[a]

Catalyst	Cyclohexene conv. mol%	TOF (h^{-1}) [b]	Product selectivity (mol %)			(Epoxide + diol) selectivity, %
			Epoxide	Diol	Allylic (-ol + -one)	
TS-1	18.6	10	55.6	28.7	15.7	84.3
Ti-MCM-41	32.4	17	12.9	60.3	26.8	73.2
Ti-SBA-15	52.5	25	12.0	62.0	26.0	74.0

[a]Reaction conditions: catalyst, 0.1 g; cyclohexene, 0.82 g (10 mmol); H_2O_2 (30% aqueous), 3.33 mmol; CH_3CN, 5 ml; temperature, 333 K; reaction time, 4 h.

[b]Turnover frequency (TOF, h^{-1}) = moles of cyclohexene converted (experimental) per mole of Ti per h.

5.3.4.2. Influence of Solvent

5.3.4.2.1. Oxidation of Cyclohexene

In the absence of solvents, cyclohexene conversion was significantly lower; –enol and –enone (from allylic oxidation) were the major products (Table 5.2). There was no epoxide/diol formation. The conversions were higher in the presence of aprotic solvents. Selectivity to epoxidation products (epoxide + diol) was higher in alcohol solvents. A similar trend was observed in acetonitrile-methanol (Table 5.2).

5.3.4.2.2. Oxidation of Styrene

Styrene oxide, phenyl acetaldehyde, benzaldehyde and benzoic acid were the products in styrene oxidation (Table 5.3). Secondary reactions of styrene oxide also yielded the diol and methylated diol products. A significant influence of solvent on the reactivity and product selectivity was noted in this case also (Table 5.3).

5.3.4.3. Oxidations in Presence of Radical Scavengers

Table 5.4 and Table 5.5 present the influence of hydroquinone, on product selectivities in the oxidation of cyclohexene and styrene over TS-1, respectively. In the absence of hydroquinone, oxidation occurs at both olefinic and allylic carbons (Scheme 1). Upon hydroquinone addition, the selectivity for epoxide increased to 100%. Allylic products were suppressed indicating that radical intermediates are probably involved in their formation. In the case of diols, poisoning of the acid sites responsible for the hydration of the epoxide to diols by hydroquinone is probably a reason for their absence in the products. A similar trend is also seen in the oxidation of styrene.

Table 5.6 shows the influence of various radical scavengers on the product selectivity in cyclohexene oxidation. The selectivity for the epoxidation products increased with different radical scavengers in the order: mannitol < catechol < thiourea < sodium acetate < sodium salicylate < *para*-benzoquinone < sodium formate < hydroquinone.

5.3.5. Reactive Oxo Radicals – EPR-Spin Trap Experiments

In view of the observation of Ti-oxo radicals on contact of TS-1 with H_2O_2 the role of radicals, if any, in the oxidation mechanism of TS-1, was investigated through EPR-spin trapping experiments with DMPO.

Table 5.2. Influence of Solvent: Oxidation of Cyclohexene with Aqueous H_2O_2 over TS-1[a]

Solvent	Cyclohexene conv. mol%	TOF (h^{-1})[b]	Product selectivity (mol%)				(Epoxide + diol) selectivity, %
			Epoxide	Diol	-enol	-enone	
No solvent	1.5	0.8	0	0	14.7	85.3	0
Acetonitrile	18.6	10.0	55.6	28.7	5.7	10.0	84.3
Acetone	19.2	9.9	5.9	69.3	9.7	15.1	75.2
Tert.-butanol	11.7	6.0	24.2	53.2	5.8	16.8	77.4
Methanol	14.7	7.6	0	88.7	0	11.3	88.7
Ethanol	9.9	5.1	0.2	90.6	0	9.2	90.8
Iso-propanol	9.6	4.9	2.3	88.7	0.2	8.8	91.0
Solvent mixture Acetonitrile:Methanol (vol:vol)							
66 : 34	16.8	8.6	24.4	58.3	4.1	13.2	82.4
50 : 50	16.5	8.5	18.1	64.3	4.6	13.0	82.7
34 : 66	15.3	7.9	7.6	79.9	2.7	9.8	87.5
25 : 75	15.0	7.7	4.1	85.9	1.5	8.5	88.0

[a]Reaction conditions: catalyst, 0.1 g; cyclohexene, 0.82 g (10 mmol); H_2O_2 (30% aqueous), 0.268 g (3.33 mmol); solvent, 5 ml; temperature, 333 K; reaction time, 4 h; cyclohexene/H_2O_2 (mol/mol) = 3. [b]Turnover frequency (TOF, h^{-1}) = moles of cyclohexene converted (experimental) per mole of Ti per hour.

Table 5.3. Influence of Solvent: Oxidation of Styrene with Aqueous H_2O_2 over TS-1

Solvent	Styrene conv. mol %	TOF (h^{-1})	Product selectivity (mol%)						(Styrene oxide + diols + phenyl acetaldehyde) selectivity, %
			Styrene oxide	Methylated diol	Diol	Phenyl acet-aldehyde	Benzal-dehyde	Others	
Methanol	39.9	8.9	35.9	46.0	1.1	0.3	13.8	2.9	83.3
Acetone	25.4	5.7	61.4	0.7	2.6	3.4	31.9	0.0	68.1
Methanol + Acetonitrile (1:1 v/v)	26.3	5.9	29.4	21.8	3.1	9.2	35.0	1.5	63.5

Reaction conditions: catalyst, 0.1 g; styrene, 8.63 mmol; styrene/H_2O_2 = 0.5 (mol/mol); solvent, 10 g; temperature, 333 K; reaction time, 8 h. Reaction was carried out in glass reactor. (TOF, h^{-1}) = moles of cyclohexene converted (experimental) per mole of Ti per hour.

Table 5.4. Influence of Hydroquinone Addition on the Epoxidation of Cyclohexene over TS-1.

Hydroquinone (mmol)	Cyclohexene conv. mol%	Product selectivity (mol%)		
		Epoxide	Diol	Allylic oxidation (-ol + -one)
Nil	18.6	55.6	28.7	15.7
0.018	15.3	100	0.0	0.0

Reaction conditions for epoxidation of cyclohexene: catalyst, 100 mg; cyclohexene, 10 mmol; HQ, 0 or 0.018 mmol; H_2O_2 (30% aqueous), 3.33 mmol; CH_3CN, 5 ml; temperature, 333 K; reaction time, 4 h.

Table 5.5. Influence of Hydroquinone Addition on the Epoxidation of Styrene over TS-1

Hydroquinone (mmol)	Styrene conversion (mol %)	Product selectivity (mol%)			
		Styrene oxide	Phenyl acetaldehyde	Benzaldehyde	Benzoic acid
0	16.4	37.8	12.2	49.3	0.7
0.009	11.5	45.5	12.9	39.8	1.8
0.018	7.9	59.0	12.8	27.2	1.0
0.027	8.0	62.4	13.2	23.3	1.1

Reaction conditions for epoxidation of styrene: TS-1, 100 mg; styrene, 8.63 mmol; H_2O_2 (30%, aqueous), 17.2 mmol; CH_3CN, 10 g; temperature, 333 K; reaction time, 8 h. Reaction was carried out in a rotating steel autoclave (Hiro Company, Japan model KH 02; 30 rpm).

Table 5.6. Oxidation of Cyclohexene in the Presence of Radical Scavengers

Radical scavenger	Cyclohexene conversion, %	Product selectivity, %				Epoxide + Diol selectivity, %
		Epoxide	Diol	-enol	-enone	
None	18.6	55.6	28.7	5.7	10.0	84.1
Mannitol	14.1	57.9	17.2	11.5	13.4	75.1
Catechol	14.4	62.5	20.1	11.0	6.4	82.6
Thiourea	9.9	43.9	42.3	6.7	7.1	86.2
Sodium acetate	26.4	73.1	14.8	2.3	9.8	87.9
Sodium salicylate	29.1	53.1	38.0	2.9	6.0	91.1
p-Benzoquinone	11.4	84.5	0	12.0	3.5	84.5
Hydroquinone	15.3	100	0	0	0	100
Sodium formate	26.1	94.3	3.8	0.3	1.6	98.1

Reaction conditions: catalyst (TS-1; 100 mg), cyclohexene (0.82 g), aq. H_2O_2 (30%, 0.268 g), acetonitrile (5 ml), radical scavenger (0.018 mmol in 0.1 ml water), temperature (333 K), reaction time (4 h); cyclohexene/H_2O_2 = 3 (mol/mol).

Upon reaction with various O-centered radicals (like $HO^{\bullet}$, $HOO^{\bullet}$ or $O_2^{-\bullet}$, generated through homolytic O-O cleavage), DMPO forms paramagnetic adduct complexes, which show characteristic EPR spectra differing significantly in their superhyperfine coupling constants (a_N and a_H) (Fig. 5.3). The superoxo and hydroperoxo-DMPO adducts (B) show similar EPR spectral pattern. The hydroxo-DMPO adduct (A), on the other hand, shows a completely different pattern (Fig. 5.4) (A: DMPO-OH: g = 2.0063, a_N = 14.9 G, a_H^{β} = 14.9 G. B: DMPO-OOH/$O_2^{-\bullet}$: g = 2.0063; a_N = 14.2 G, a_H^{β} = 11.2 G; a_H^{γ} = 1.25 G). The EPR spectrum of DMPO on contact with (H_2O_2 + TS-1) can, hence, be used to differentiate the oxo radicals formed in the H_2O_2-TS-1 system.

DMPO alone does not exhibit any EPR spectrum; radicals were also not detected in the absence of TS-1; the self-decomposition of H_2O_2 into O-centered radical species is negligible in the absence of TS-1. Contact of H_2O_2 with TS-1 gave

rise to the EPR spectrum of DMPO typical of $O_2^{-\bullet}$/ $HOO^{\bullet}$ radical adducts (compare Figs. 5.3 and Fig. 5.4). No radicals were observed in ethanol. The concentration of $O_2^{-\bullet}$ / $HOO^{\bullet}$ radicals (estimated using a weak-pitch standard supplied by Bruker) decreased in the following order: water-DMSO (3.3 x 10^{13} spins) > water-CH_3CN (1.2 x 10^{13} spins) > water alone (1.0 x 10^{13} spins) > water-C_2H_5OH (7.5 x 10^{11} spins). Solvents influence the identity of the radicals formed from H_2O_2 ($O_2^{-\bullet}$/$HOO^{\bullet}$ *vs* $HO^{\bullet}$, for example). Keeping in mind that higher epoxidation selectivities were observed in alcoholic solvents (Table 5.2), wherein the concentration of such O-centered radicals was minimal, an influence of such radicals on the formation of allylic oxidation products (enol and enone) in cyclohexene oxidation reactions may be inferred.

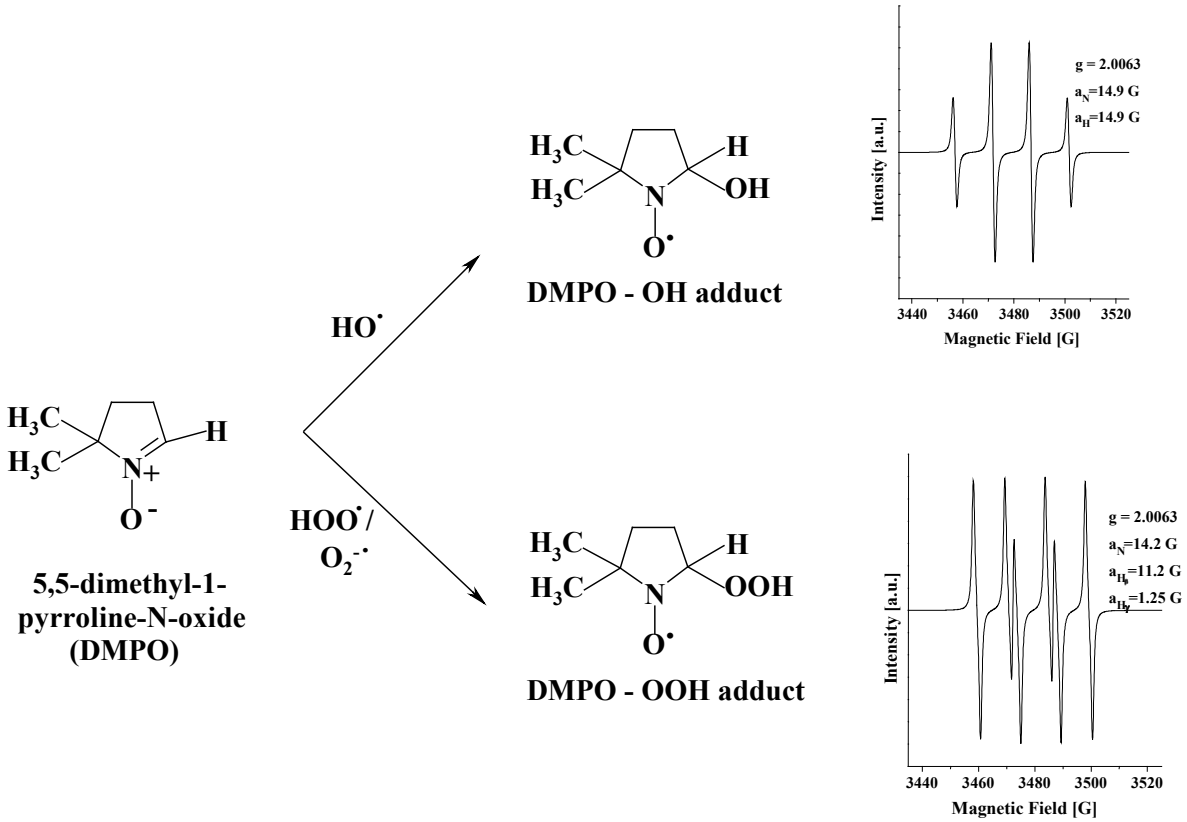

Fig. 5.3. Reaction of DMPO with O-centered radicals and the EPR spectra of the corresponding radical adducts.

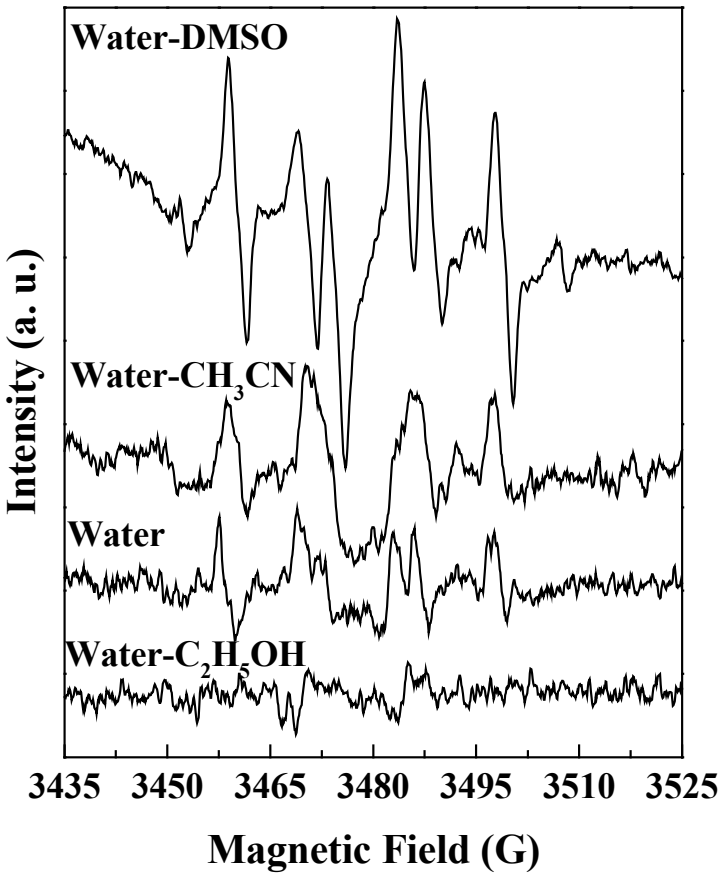

Fig. 5.4. EPR spectra (at 298 K; normalized intensity) of DMPO-oxygen centered radical adducts in TS-1 + H_2O_2 system – Influence solvents.

Radical-mediated reactions were suppressed in the presence of radical scavengers. The epoxidation tests were carried out in the presence of various radical scavengers. In the presence of a spin trap (DMPO), characteristic signals due to $O_2^{-\bullet}$ / $HOO^{\bullet}$ radical adducts were seen (Fig. 5.5). When a radical scavenger, hydroquinone, was added to this reaction mixture, the EPR pattern of DMPO-oxo radical was not seen. Instead, the quintet line pattern (indicated by asterisks; Fig. 5.5) due to the formation of semiquinone radicals was detected; the hydroquinone had preferentially reacted with the O-centered radicals and formed the semiquinone. When both hydroquinone and DMPO were added simultaneously to the reaction slurry, hydroquinone reacted faster and quenched the radicals even before DMPO, the spin

trap, could form the spin adducts. In this case, only the signals due to the semiquinone were observed.

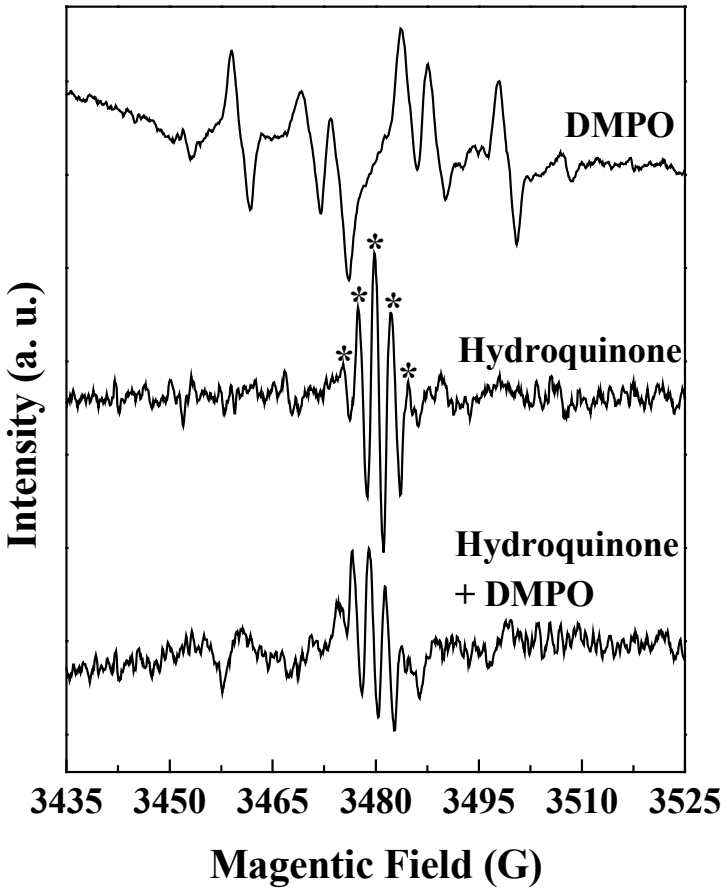

Fig. 5.5. EPR spectra (at 298 K) of (TS-1 + H_2O_2) contacted with DMPO, hydroquinone and DMPO + hydroquinone.

5.4. Conclusions

Various Ti-oxo radical species were generated on reaction of H_2O_2 with titanosilicate molecular sieves. The role of such radicals in the oxidation mechanism of TS-1 was investigated using EPR-spin traps, like 5,5-dimethyl-*1*-pyrroline-*N*-oxide (DMPO) and radical scavengers like hydroquinone. The EPR spectra of DMPO on contact with H_2O_2-TS-1 indicate that $O_2^{-\bullet}$ and $OOH^{\bullet}$ radicals are predominant. Their concentrations varied with the solvent. The oxo radicals influenced product selectivity in olefin epoxidation reactions. Addition of radical scavengers, like hydroquinone, suppressed the concentration of such radicals, and significantly enhanced the selectivity for the epoxide at the expense of the allylic oxidation

products. A novel method to control product selectivity in oxidations over titanosilicate molecular sieves is demonstrated.

5.5. References

[1] P. Ratnasamy, D. Srinivas, H. Knözinger, Adv. Catal. 48 (2004) 1.

[2] G.N. Vayssilov, Catal. Rev.-Sci. Eng. 39 (1997) 209.

[3] B. Notari, Adv. Catal. 41 (1996) 253.

[4] C. Lamberti, S. Bordiga, D. Arduino, A. Zecchina, F. Geobaldo, G. Spanó, F. Genoni, G. Petrini, A. Carati, F. Villain, G. Vlaic, J. Phys. Chem. B 102 (1998) 6382.

[5] V. Bolis, S. Bordiga, C. Lamberti, A. Zecchina, A. Carati, F. Rivetti, G. Spanò, G. Petrini, Langmuir 15 (1999) 5753.

[6] D. Gleeson, G. Sankar, C.R.A. Catlow, J.M. Thomas, G. Spanò, S. Bordiga, A. Zecchina, C. Lamberti, Phys. Chem. Chem. Phys. 2 (2000) 4812.

[7] J.M. Thomas, G. Sankar, Acc. Chem. Res. 34 (2001) 571.

[8] S. Bordiga, A. Damin, F. Bonino, G. Ricchiardi, A. Zecchina, R. Tagliapietra, C. Lamberti, Phys. Chem.Chem. Phys. 5 (2003) 4390.

[9] G. Tozzola, M.A. Mantegazza, G. Ranghino, G. Petrini, S. Bordiga, G. Ricchiardi, C. Lamberti, R. Zulian, A. Zecchina, J. Catal. 179 (1998) 64.

[10] G. Sankar, J. M. Thomas, C. R. A. Catlow, C. M. Barker, D. Gleeson, N. Kaltsoyannis, J. Phys. Chem. B 105 (2001) 9028.

[11] C. M. Barker, D. Gleeson, N. Kaltsoyannis, C. R. A. Catlow, G. Sankar, J. M. Thomas, Phys. Chem. Chem. Phys. 4 (2002) 1228.

[12] S. Bordiga, A. Damin, F. Bonino, G. Ricchiardi, C. Lamberti, A. Zecchina, Angew Chem. Int. Ed. 41 (2002) 4734.

[13] W. Lin, H. Frei, J. Am .Chem. Soc. 124 (2002) 9292.

[14] F. Corà, M. Alfredsson, C. M. Barker, R. G. Bell, M. D. Foster, I. Saadoune, A. Simperlar, C. R. A. Catlow, J. Solid State Chem. 176 (2003) 496.

[15] D.H. Wells, Jr, W. N. Delgass, K. T. Thomson, J. Am. Chem. Soc. 126 (2004) 2956.

[16] F. Bonino, A. Damin, G. Ricchiardi, M. Ricci, G. Spanò, R. D'Aloisio, A. Zecchina, C. Lamberti, C. Prestipino, S. Bordiga, J. Phys. Chem. B 108 (2004)

3573.

[17] F. Geobaldo, S. Bordiga, A. Zecchina, E. Giamello, G. Leofanti, G. Petrini, Catal. Lett. 16 (1992) 109.

[18] A. Tuel, Y. Ben Taârit, Appl. Catal. A: General 110 (1994) 137.

[19] Q. Zhao, X.-h. Bao, Y. Wang, L.-w. Lin, G. Li, X.-w. Guo, X.-s. Wang, J. Mol. Catal. A: Chemical 157 (2000) 265.

[20] K. Chaudhari, D. Srinivas, P. Ratnasamy, J. Catal. 203 (2001) 25.

[21] L. Bonoldi, C. Busetto, A. Congiu, G. Marra, G. Ranghino, M. Salvalaggio, G. Spanó, E. Giamello, Spectrochimica Acta 58A (2002) 1143.

[22] D. Srinivas, P. Manikandan, S.C. Laha, R. Kumar, P. Ratnasamy, J. Catal. 217 (2003) 160.

[23] R. Bal, K. Chaudhari, D. Srinivas, S. Sivasanker, P. Ratnasamy, J. Mol. Catal. A: Chemical 162 (2000) 199.

Chapter – 6

Superoxo-Vanadium Species in Vanadosilicate Molecular Sieves

6.1. Introduction

Vanadosilicate molecular sieves exhibit efficient catalytic activity in selective oxidation of hydrocarbons [1 - 12]. Interestingly, they catalyze the terminal, primary C-H bond oxidation of *n*-alkanes, which their titanium analogs cannot [13, 14]. Vanadosilicates also exhibit higher efficiency in the photocatalytic decomposition of NO [15, 16]. The type of oxygen species generated and the mode of O-O bond cleavage in the reactive oxygen intermediate influence the catalytic activity and product selectivity [1-12]. While there have been a large number of studies on the reactive oxygen species generated over Ti-silicates using a range of spectroscopic techniques [17 - 22], similar studies on V-silicates are scarce [23, 24]. In this chapter, *in situ* EPR spectroscopic evidence for the formation of reactive superoxo-vanadium(V) intermediates in microporous VS-1 and mesoporous V-MCM-41 molecular sieves is reported, for the first time. In the case of metal complexes in homogeneous solutions, the superoxo-vanadium species were found to be short-lived [25 - 28]. Stable species were, however, observed on silica-supported V_2O_5 on reduction in hydrogen followed by oxygen dosing [29 - 31]. In the present study, it is observed that the superoxo species, generated *in situ* in the EPR cells on contacting VS-1 or V-MCM-41 with H_2O_2 or *tert.*-butyl hydroperoxide (TBHP) are structurally different from those on silica-supported V_2O_5.

6.2. Experimental

The syntheses of vanadosilicate molecular sieves VS-1 and V-MCM-41 are described in Chapter 2. The samples were characterized by chemical analysis (AAS and XRF), XRD, N_2 adsorption measurements, FT-IR and diffuse reflectance UV-visible spectroscopy.

6.2.1. Sample Treatments

6.2.1.1. EPR

Reduction of Vanadosilicates with H_2. A known quantity of vanadosilicate sample was taken in EPR quartz tubes and reduced with the dry H_2 gas for a known period of time.

Vanadosilicates Contacted with Aq. H_2O_2 (HP). A known quantity of titanosilicate (40 mg) was taken in 4.5 mm o.d. Suprasil quartz EPR tubes. H_2O_2

(50%, 0.1 ml) was added to it in amounts adequate enough to wet the solid completely. In the experiments on solvent effects, the vanadosilicate samples were initially activated at 373 K in static-air, cooled to 298 K and then soaked in the desired solvent (0.4 ml). H_2O_2 was added and the EPR spectra were recorded.

6.2.1.2. Diffuse Reflectance UV-Visible

A known quantity of activated vanadosilicate (~ 2 g) was taken in a sample holder and to it, a known quantity of aqueous H_2O_2 (30%) was added till the solid became completely wet. Vanadosilicate sample which was not contacted with H_2O_2 was taken as the reference material.

6.2.2. Catalytic Activity – Oxidation of n-Hexane

The oxidation reactions were conducted in a closed 100 ml Teflon-lined steel autoclave. In a typical reaction 2.5 g of n-hexane, 1.3 g of aqueous H_2O_2 (30%) or 1.75 g of aqueous TBHP (70%) and 12.5 ml of solvent were taken. To that, vanadosilicate catalyst (0.4 g of VS-1 or 0.15 g of V-MCM-41) was added. The reaction was carried out at 373 K for 8 h in a rotating hydrothermal synthesis reactor (Hiro Co., Japan). At the end of the reaction, 12.5 ml of acetone was added to the reaction mixture and the catalyst was separated by centrifugation. The liquid portion was analyzed by gas chromatography (Varian 3400; CP-SIL8CB column; with a 30-m long and 0.53-mm i.d.) and products were identified, using standards and by GC-MS (Shimadzu QP-5000; with a 30-m long, 0.25-mm i.d. and 0.25 μm thick capillary column DB-1).

6.3. Results and Discussion

6.3.1. Characterization of Materials

6.3.1.1. XRD

The crystallinity (in the case of VS-1) and phase purity of vanadosilicates were confirmed from the XRD patterns (Fig. 6.1). The XRD pattern can be described based on an orthorhombic symmetry for VS-1 [32]. It may be noted that in the absence of V, the parent silicalite-1 sample shows a XRD pattern corresponding to a

monoclinic space group [33, 34]. The absence of splitting in the reflection at around 24.5º is a clear indication of a structural transition from a monoclinic to an orthorhombic symmetry as a consequence of V incorporation in the framework of silicalite-1 [33].

The low-angle (100) reflection and well resolved (110) and (200) reflections of V-MCM-41 indicate that V incorporation did not alter the long-range order in hexagonal symmetry of the mesoporous materials. For V-MCM-41 sample, the d spacing (d_{100}), estimated from the position of the low-angle peak is 3.8 nm. The unit cell parameter calculated using the equation $a = 2d_{100}/\sqrt{3}$ was 4.4 nm which is in good agreement with the values reported by others [35]. The absence of any additional peaks due to V_2O_5 indicates that all the vanadium in VS-1 and V-MCM-41 is present in a highly dispersed state. (Fig. 6.1).

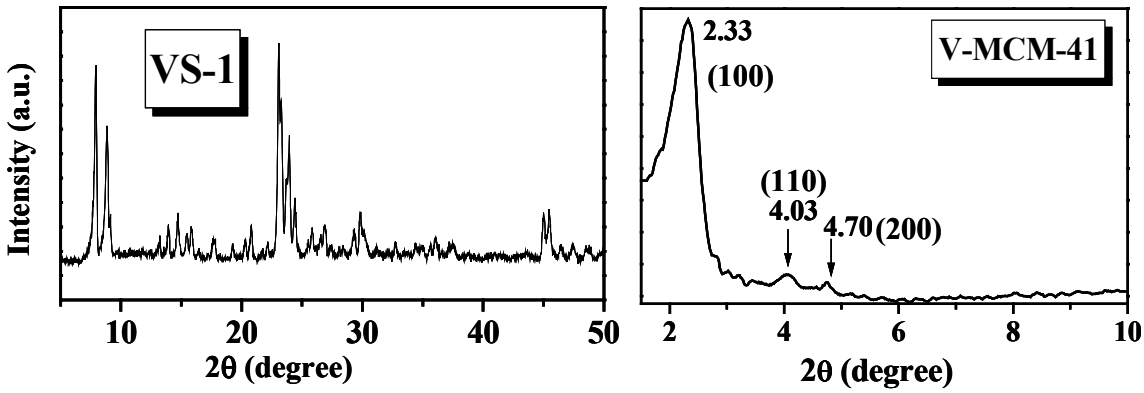

Fig. 6.1. XRD patterns of vanadosilicates. Reflections and corresponding 2θ values are indicated.

6.3.1.2. FT-IR

Silicalite-1 (a sample prepared with no vanadium) shows sharp characteristic IR peaks at 1080 and 595 cm^{-1}. A new feature was observed in VS-1 and V-MCM-41 at around 965 cm^{-1} (Fig. 6.2), which could be attributed to substituted vanadium species [32, 36]. Silicalite-1 also shows this feature. However, the intensity of it increased upon vanadium incorporation. It is known that presence of this band is an indication for incorporation of vanadium into the silicalite framework [32, 37]. In the case of VS-1, the band at 543 cm^{-1} indicates the formation of zeolitic structure.

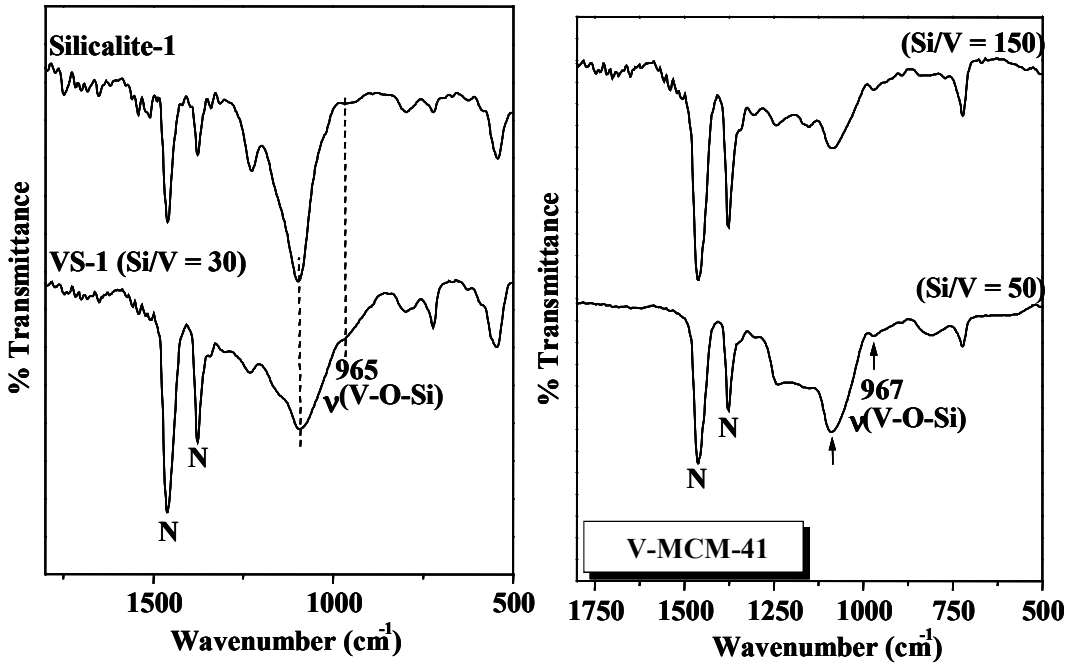

Fig. 6.2. FT-IR spectra in Nujol mull of silicalite-1, VS-1 and V-MCM-41. Characteristic bands are marked.

6.3.1.3. DRUV-Visible

At least four bands corresponding to the presence of four different types of vanadium species could be discerned from the diffuse reflectance spectrum of VS-1 recorded in the spectral range 200 – 500 nm [38] (Fig. 6.3). Absence of these bands in the spectrum of silicalite-1 indicates that they are arising from the incorporated vanadium species. The origin of this band is attributed to oxygen → metal charge transfer transition. V_2O_5 shows the charge transfer band at 475 nm. A blue shift of this band in the case of VS-1 is due to dispersion and tetra-coordination of vanadium. While the bands at 206 and 235 nm could be attributed to tetra-coordinated framework-substituted vanadium species, the band at 330 nm is possibly due to nano-particulate vanadium oxide species. The band at 275 nm is due to penta-coordinated vanadium structure. In V-MCM-41, vanadium is mainly present in a penta-coordinated state (243 – 250 nm) [38 - 40] and as a nano-particulate vanadium oxide. Absence of d-d transitions in calcined samples indicates that vanadium is present mostly in the +5 state.

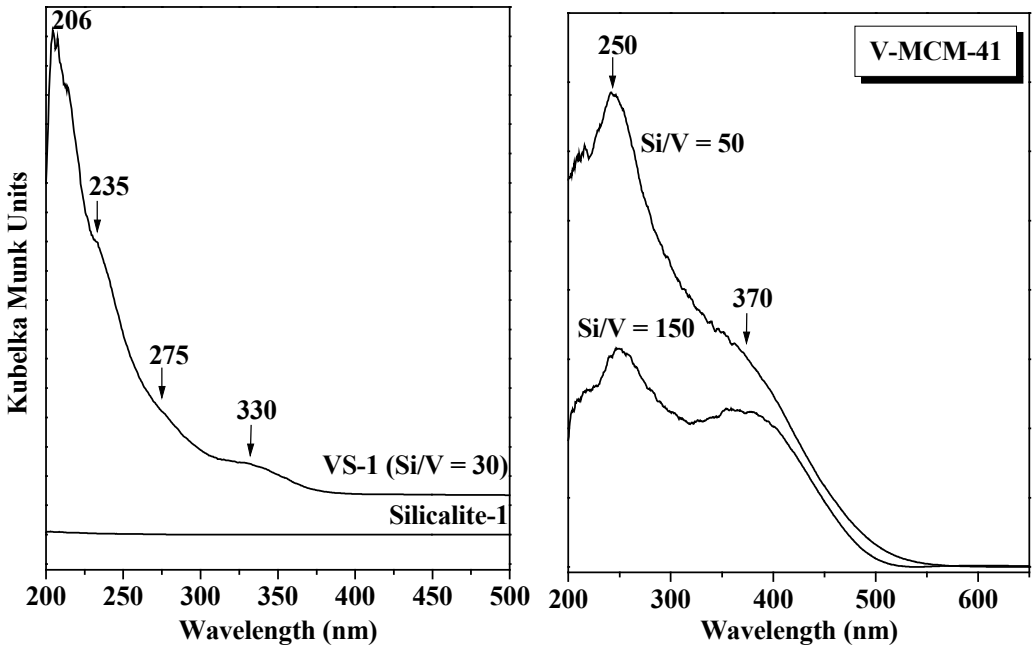

Fig. 6.3. DRUV-visible spectra of silicalite-1 and vanadosilicate samples. Peaks indicated correspond to the different types of vanadium species.

6.3.1.3. EPR

As-synthesized samples of VS-1 were paramagnetic and showed well-resolved EPR spectra (Fig. 6.4) typical of an isolated vanadium species, in a tetragonally distorted octahedral environment, with a +4 oxidation state. The parallel hyperfine features clearly reveal that there are at least two types of isolated vanadium ions (species I and II). The spin Hamiltonian parameters of these vanadium ions were determined by spectral simulation (species I: $g_{||}$ = 1.938, $g_{\perp}$ = 1.977, $A_{||}$ (^{51}V) = 188.0 G and $A_{\perp}$ (^{51}V) = 68.0 G. species II: $g_{||}$ = 1.938, $g_{\perp}$ = 1.970, $A_{||}$ (^{51}V) = 192.0 G and $A_{\perp}$ (^{51}V) = 68.0 G). Concentrations of species I and II (estimated by double integration of the 1st derivative simulated EPR spectrum) are in the ratio of 42:58. Upon calcination, VS-1 samples became EPR-silent, and the oxidation state of vanadium changed from +4 to +5 (d-d bands originally present in the as-synthesized samples have disappeared on calcination). These observations agree well with those reported by others [1, 32, 41].

Interestingly, in both the as-synthesized and calcined samples of V-MCM-41, the vanadium ions are in +5 oxidation state. The samples of V-MCM-41 were EPR-silent in the temperature range 298 – 77 K.

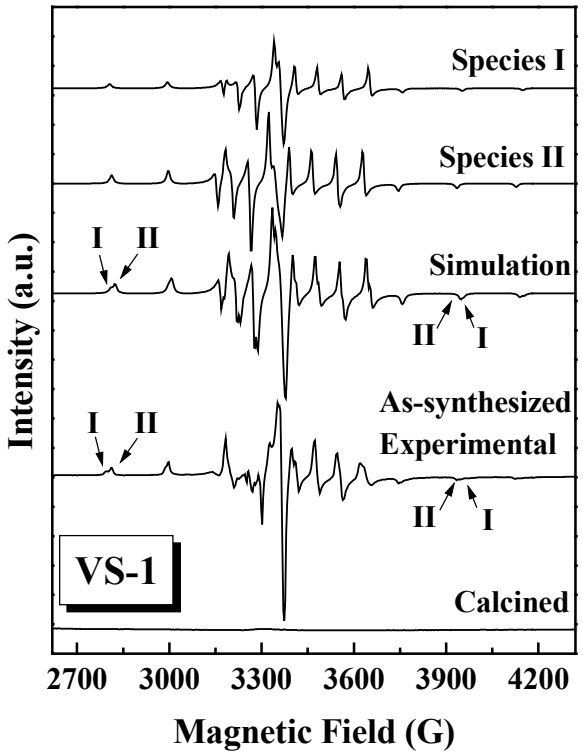

Fig. 6.4. EPR spectra of as-synthesized and calcined samples of VS-1. The deconvoluted and simulated plots are also shown.

6.3.2. Redox Behavior of Vanadium Species in Vanadosilicates

Reaction with dry hydrogen at elevated temperatures reduced vanadium in the calcined samples (VS-1 and V-MCM-41) from +5 to +4 oxidation state. When the reduction was conducted at 623 K, a V^{4+} species (type III species) characterized by spin Hamiltonian parameters: $g_{||}$ = 1.932, $g_{\perp}$ = 1.974, $A_{||}$ (^{51}V) = 197.0 G and $A_{\perp}$ (^{51}V) = 73.0 G was generated on VS-1. At higher temperatures (*c.a.*, 673 K and above), an additional species (type IV) characterized by $g_{||}$ = 1.930, $g_{\perp}$ = 1.974, $A_{||}$ (^{51}V) = 172 G and $A_{\perp}$ (^{51}V) = 72 G was also generated (Fig. 6.5). Concentrations of

type IV and III species are almost in the same ratio as that of species I and II in the as-synthesized samples (42:58) (Fig.6.4). The spin Hamiltonian parameters of the type III vanadium are considerably different from those of the type IV vanadium; the parallel hyperfine coupling constant ($A_{||}$ (^{51}V)) is lower for type IV than for type III species. These values are indicative of pseudo-tetrahedral coordination for vanadium in the type IV species and penta-coordinated geometry in the type III species. In other words, the type IV species corresponds to framework substituted vanadium ions and the type III are those located in the defect sites. Only the type III species were observed on V-MCM-41 even when the reduction was conducted above 673 K. Hence, V-MCM-41 contains the defect type vanadium species only. The reduction experiments reveal that the framework-substituted vanadium (type IV species) is more difficult to reduce than the defect-type vanadium (type III) species. The spin Hamiltonian parameters of different vanadium species are listed in Table 6.1.

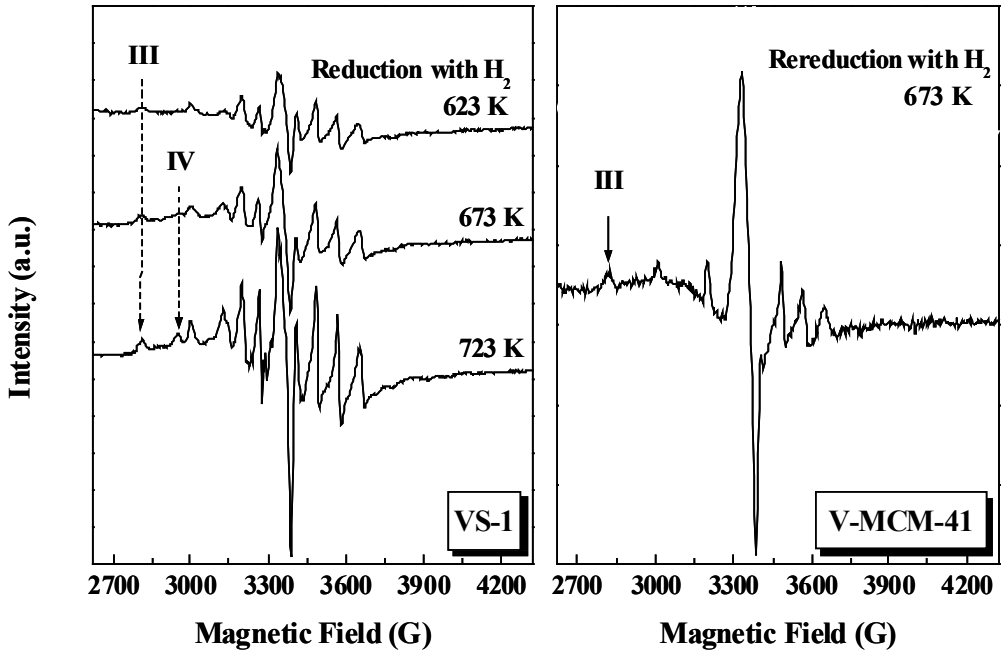

Fig. 6.5. EPR spectra of VS-1 and V-MCM-41 reduced with hydrogen at 623 – 673 K. Signals corresponding to type-III and IV vanadium species are indicated.

Table 6.1. EPR Spin Hamiltonian Parameters of V^{4+} Species in Vanadosilicates (Values Derived from Spectral Simulations)

Vanadosilicate	Treatment	Species	$g_{zz}/g_{\|\|}$	$g_{yy}, g_{xx}/g_{\perp}$	$A_{zz}/A_{\|\|}$ (G)	A_{yy}, A_{xx} / $A_{\perp}$ (G)
VS-1	-	I	1.938	1.977	188	68
as-synthesized		II	1.938	1.970	192	68
VS-1	Reaction	III	1.932	1.974	195	73
Calcined	with H_2	IV	1.930	1.974	172	73
V-MCM-41	Reaction	III	1.932	1.974	197	73
	with H_2					

6.3.3 Stability of Vanadosilicates

Stability of the catalyst is an important issue for its application in industrial catalysis. While VS-1 was stable over several weeks, V-MCM-41 was less stable. The vanadium content which was originally in +5 state in the calcined samples got converted to +4 state after several weeks. Not all vanadium could be converted back to the original +5 vanadium in the reduction / reoxidation experiments. Also in the reactions with H_2O_2, leaching of vanadium into solution was noted in V-MCM-41. Such a leaching was not observed in the case of VS-1. In other words, the silicate structure influences the stability of vanadium species in vanadosilicates.

6.3.4 Superoxo-Vanadium Species

Superoxo-vanadium(V) species were generated upon contacting vanadosilicates with H_2O_2, TBHP and H_2+O_2. The spin Hamiltonian parameters of the radicals are listed in Table 6.2.

Table 6. 2. EPR Spin Hamiltonian Parameters of $V^{5+}(O_2^{\bullet})$ in Vanadosilicates[a]

Vanadosilicate	Treatment	Species	$g_{zz}/g_{\|\|}$	g_{xx}, $g_{yy}/g_{\perp}$	A_{zz} (G)	A_{yy}, $A_{xx}/A_{\perp}$ (G)
VS-1	Aq. H_2O_2 30%	A	2.0203	2.0104, 2.0012	7.54	4.60, 1.1
VS-1	$H_2 + O_2$	A	2.0204	2.0100, 1.9935	9.38	Partly resolved
VS-1	TBHP-decane 50%	B	2.0313	2.0098, 2.0045	Nil	Nil
VS-1	Aq. TBHP 70%	B	2.0322	2.0098, 2.0035	Nil	Nil
V-MCM-41	Aq. H_2O_2 30%	A	2.0210	2.0102, 2.0012	6.90	4.53, 1.1
V-MCM-41	$H_2 + O_2$	A	2.0209	2.0100, 1.9934	9.15	Partly resolved
V-MCM-41	TBHP-decane 50%	B	2.0330	2.0100, 2.0043	Nil	Nil
		C	2.0235	2.0800, 2.0800	Nil	Nil
V-MCM-41	Aq. TBHP 70%	B	2.0330	2.0100, 2.0043	Nil	Nil
		C	2.0235	2.0800, 2.0800	Nil	Nil

[a]The spin Hamiltonian parameters were determined through spectral simulations.

Error in g-values is ± 0.0002 and A values is ± 0.03 G.

6.3.4.1. Generation of Superoxo-Vanadium Species on Contact with Aqueous H_2O_2

When contacted with 30% aqueous H_2O_2, the samples became paramagnetic and showed EPR spectra typical of a superoxide radical [42, 43] (hereafter referred to as type **A** species); (Fig. 6.6) with a well-resolved eight-line splitting pattern in both the g_{zz} and g_{yy} regions. These superhyperfine features reveal that the superoxide radical is coordinated to a vanadium center forming a 1:1 metal-superoxo complex ($V(O_2^{-\bullet})$ [25-31]. Vanadium superhyperfine features in g_{xx} region are not resolved. The rhombic g-anisotropy indicates that the $O_2^{-\bullet}$ ion is coordinated in an end-on fashion [42, 43].

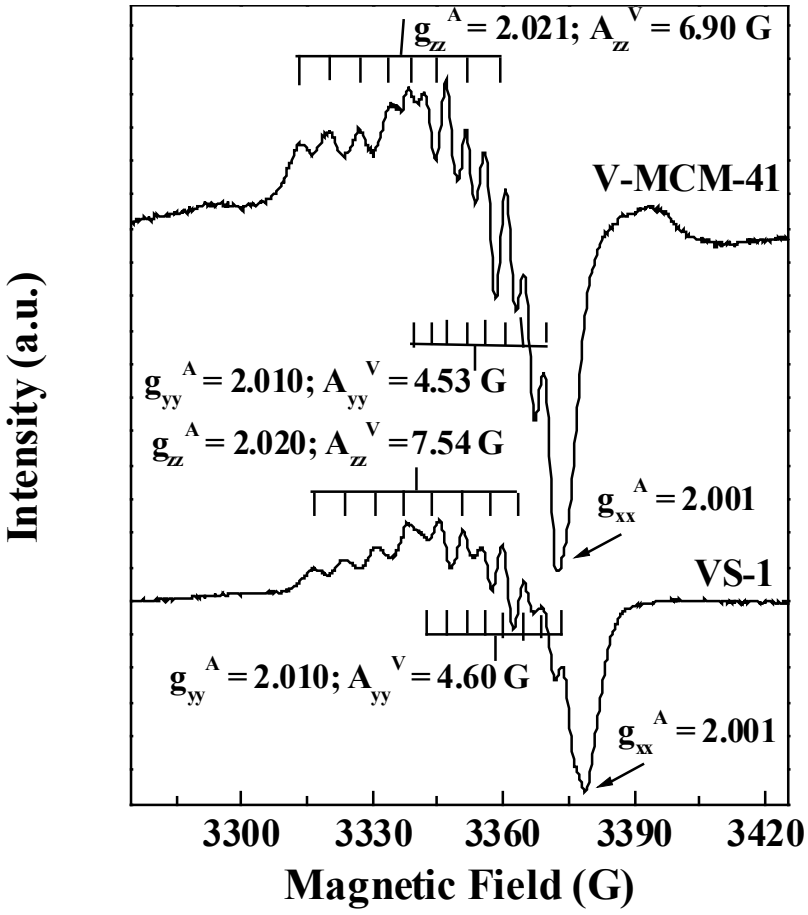

Fig. 6.6. EPR spectra superoxo-vanadium(V) species in vanadosilicates generated by contacting with (i) aq. H_2O_2 (30%). The vanadium hyperfine features are indicated. Spectra were recorded at 80 K and 9.45 GHz.

The nature of the silicate structure has a marked effect on the EPR spin Hamiltonian parameters of the superoxo-vanadium species (VS-1/H_2O_2: g_{zz} = 2.0203, g_{yy} = 2.0104, g_{xx} = 2.0012, A_{zz} = 7.54 G, A_{yy} = 4.60 G, A_{xx} = 1.1 G; V-MCM-41/H_2O_2: g_{zz} = 2.0210, g_{yy} = 2.0102, g_{xx} = 2.0012, A_{zz} = 6.90 G, A_{yy} = 4.53 G, A_{xx} = 1.1 G). The A_{zz} parameter is lower for the species generated over V-MCM-41 than on VS-1. The relative intensity of the signal is higher in the case of V-MCM-41 than in VS-1 (Fig. 6.6).

Solvents have a marked effect on the vanadium superhyperfine coupling constants (Fig. 6.7, Table 6.3). The A_{zz} value decreased in different solvents: water (7.54 G) > acetone (7.37 G) > methanol (7.0 G) > acetonitrile (6.8 G). The superoxide species generated with (H_2+O_2) on amorphous V_2O_5-SiO_2 showed resolved hyperfine features even in the g_{xx} region (g_{zz} = 2.023, g_{yy} = 2.011, g_{xx} = 2.004, A_{zz}^{V} = 9.7 G, A_{yy}^{V} = 6.8 G, A_{xx}^{V} = 5.9 G) [29 - 31], significantly different from those generated over vanadosilicates.

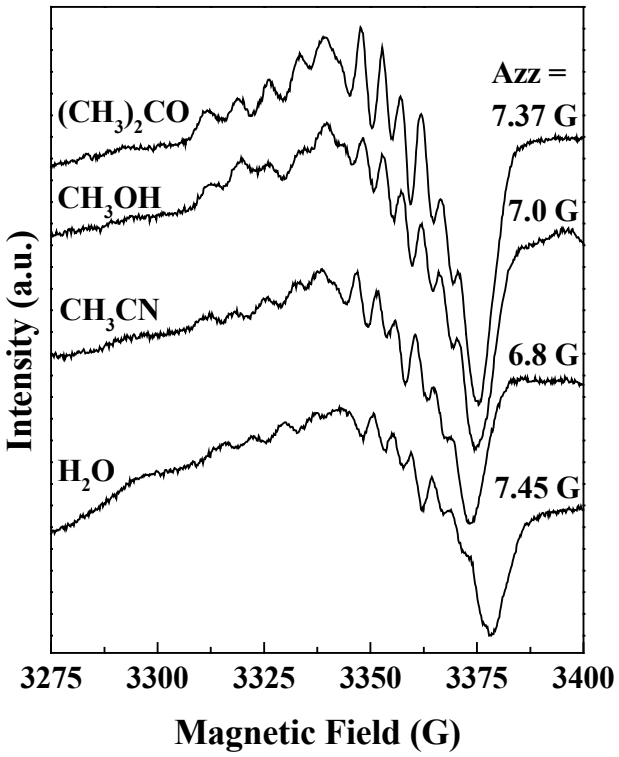

Fig. 6.7. Influence of solvent on superoxo-vanadium species in VS-1 generated on contact with aq. H_2O_2.

Table 6.3. EPR Spin Hamiltonian Parameters of $V^{5+}(O_2^{\bullet})$ (Type A species) Generated in VS-1 on Contact with Aq. H_2O_2 (30%) and Solvent

Solvent	$g_{zz}/g_{\|\|}$	g_{xx}, $g_{yy}/g_{\perp}$	A_{zz}^{V} (G)	A_{yy}^{V}, $A_{xx}^{V}/A_{\perp}$ (G)
Water	2.0206	2.0103, 2.0012	7.45	4.60, 1.1
Acetone	2.0217	2.0103, 2.0018	7.37	4.63, 1.1
Methanol	2.0216	2.0101, 2.0018	7.00	4.63, 1.1
Acetonitrile	2.0216	2.0103, 2.0018	6.80	4.63, 1.1

6.3.4.2. Generation of Superoxo-Vanadium Species on Contact with TBHP

When the vanadosilicates were contacted with 70% aqueous TBHP instead of H_2O_2, two different types of superoxo-vanadium species (hereafter referred to as type **B** and **C** species) were generated (Fig. 6.8).

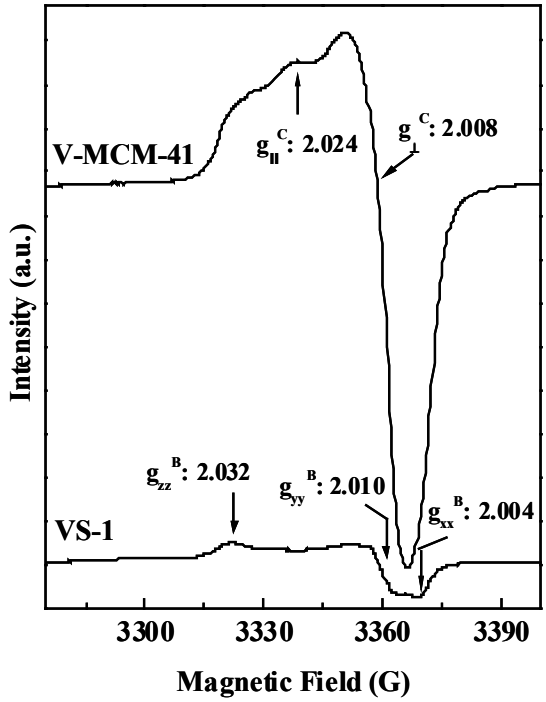

Fig. 6.8. EPR spectra superoxo-vanadium(V) species in vanadosilicates generated by contacting with TBHP (70% in aqueous). Spectra were recorded at 80 K and 9.45 GHz.

Unlike the type **A** species generated with H_2O_2, the type **B** and **C** species generated with TBHP did not show the characteristic, vanadium superhyperfine features (compare the spectra in Fig. 6.8 with those in Fig. 6.6). Only the **B** type

superoxide species were generated on VS-1 (g_{zz} = 2.0322, g_{yy} = 2.0098, g_{xx} = 2.0035). An additional superoxide species (**C**) was also generated on V-MCM-41 (species **B**: g_{zz} = 2.0330, g_{yy} = 2.010, g_{xx} = 2.0043 and species **C**: $g_{||}$ = 2.0235, $g_{\perp}$ = 2.0080) (Figure 6.8). While species **B** was characterized by rhombic g-anisotropy corresponding to an end-on coordinated superoxide ion, species **C** (generated only on V-MCM-41) was characterized by axial g-anisotropy corresponding to a side-on coordinated superoxide species [42, 43]. Species **B** and **C** differed in their $g_{zz/||}$ parameter. The $g_{zz/||}$ parameter of the species generated using TBHP (types **B** and **C**) was higher than those generated from H_2O_2 (type **A**). However, all these values are well within the range for a superoxide ion coordinated to a cation with +5 oxidation state [42, 43]. TBHP in an aqueous medium (70%) and in a non-aqueous medium (50%) gave rise to similar types of superoxide species.

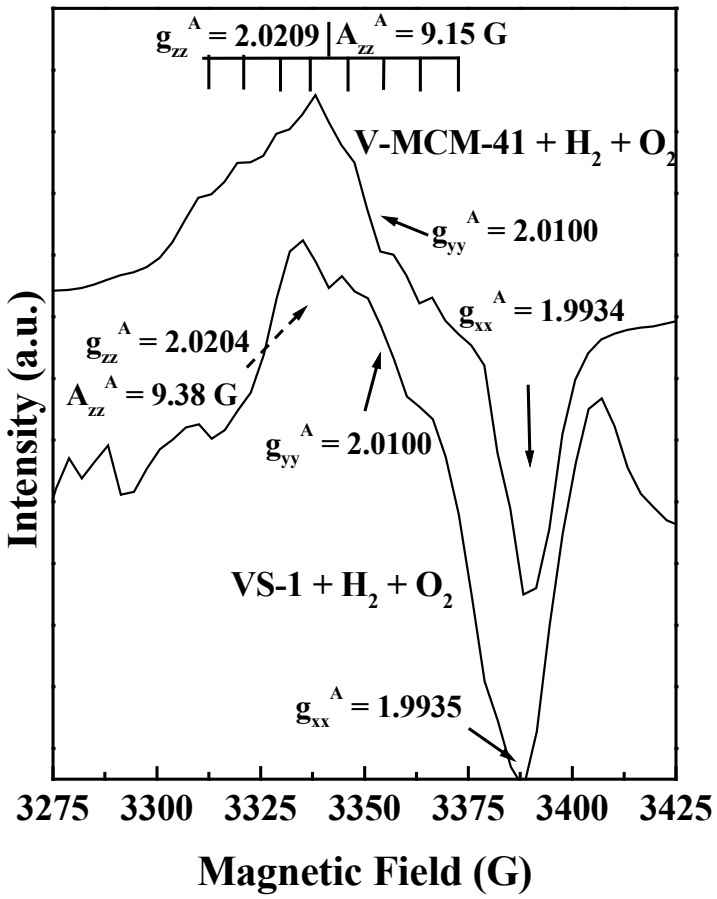

Figure 6.9. EPR spectra of the superoxo-vanadium species generated in vanadosilicates on contact with $H_2 + O_2$.

6.3.4.3. Generation of Superoxo-Vanadium Species on Contact with $H_2 + O_2$

Superoxo-vanadium species were generated also when the vanadosilicate samples were contacted with H_2 followed by O_2 (Fig. 3.9). The reduction with H_2 was conducted at 623 K for VS-1 and 673 K for V-MCM-41. Oxygen adsorption was done at 298 K. The oxo-vanadium species were similar to those generated contacting aqueous H_2O_2. However, the vanadium superhyperfine coupling constant is greater (9.15 G) than that observed for the species generated with aqueous H_2O_2 (7.54 G). Superhyperfine features are not observed in the g_{xx} region unlike in the case of V_2O_5 supported on silica [29 – 31].

6.3.4.4. Reactivity of Superoxo-Vanadium Species in Oxidation Reactions

When a known quantity of allyl alcohol or n-hexane was added, the superoxide signals decreased in intensity with time (Fig. 6.10). The signals disappeared after 20 min in the case of allyl alcohol; a longer time was needed for complete disappearance with *n*-hexane; Hence, the superoxo species generated on vanadosilicates on contact with H_2O_2 or TBHP are consumed by reaction with allyl alcohol or *n*-hexane to give the oxidation products.

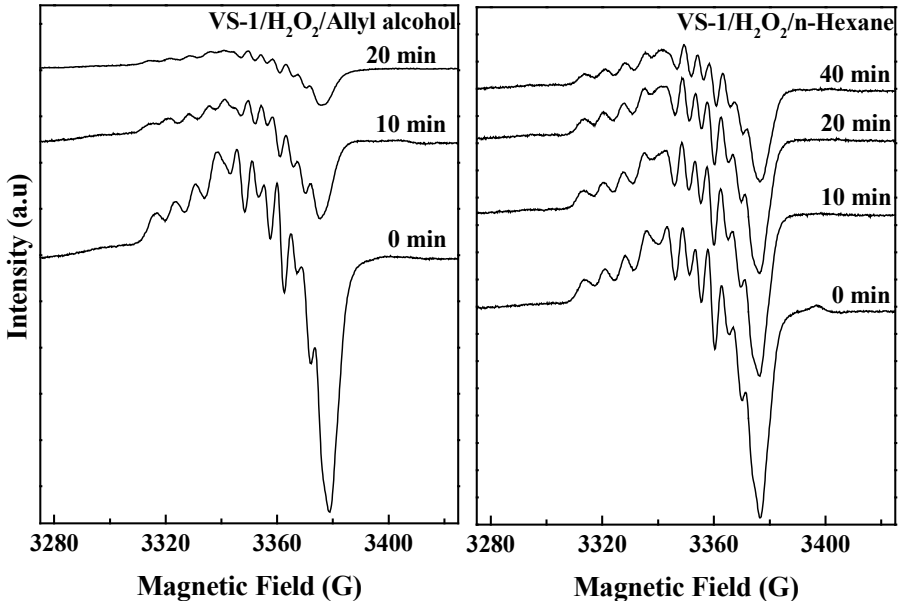

Fig. 6.10. EPR spectra of superoxo-vanadium(V) species during *in situ* oxidations with allyl alcohol and *n*-hexane for different periods of time at 323-333 K. The spectra were recorded at 80 K and 9.45 GHz.

DRUV-visible spectra of vanadosilicate samples contacted with H_2O_2 (aqueous) and TBHP (decane) were recorded taking the corresponding untreated vanadosilicates as reference material. A new asymmetric broad band was observed in the visible region (Fig. 6.11), the position of which is dependent on the silicate structure and oxidant. In the case of VS-1+aq. H_2O_2, this band appeared at 335 nm and for V-MCM-41 it shifted to 395 nm (curve not shown in figure). When TBHP in decane was used instead of aq. H_2O_2, this band appeared at 425 nm in the case of V-MCM-41 (Fig. 6.11 (b)). Based on the knowledge on peroxovanadium complexes the band at 425 nm observed in the case of V-MCM-41+TBHP system is attributed to η^2-peroxo to vanadium(V) charge transfer transition. Observation of this band at higher energy region in the case of the oxo species generated with H_2O_2 suggests that the type of oxo coordination in oxo-vanadium species is different from those generated using TBHP. The EPR spectral studies (discussed in the previous sections) indicated that the superoxo species is coordinate in an end-on fashion in the case of oxo-vanadium species generated contacting H_2O_2. Reaction with TBHP yielded a side-on coordinated superoxo-vanadium species. Hence, the DRUV-visible data provide supportive evidence that the type of oxo species generated is affected by the silicate structure and oxidant.

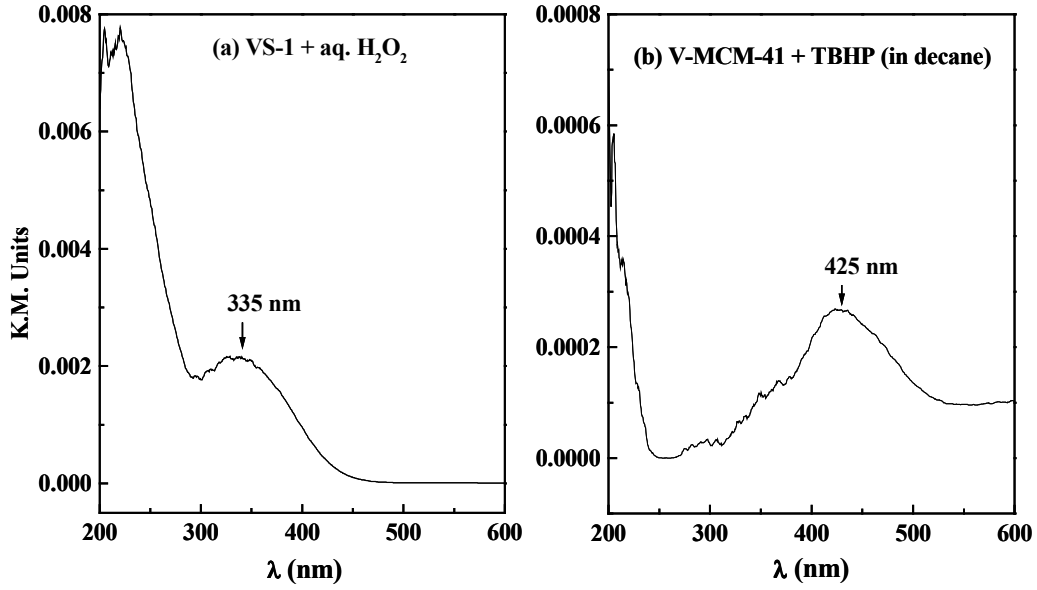

Fig. 6.11. DRUV-visible spectra: (a) VS-1 + aq. H_2O_2 and (b) V-MCM-41 + TBHP (in decane). The band corresponding to oxo-vanadium species is marked.

The vanadium superhyperfine coupling in the **A**-type species generated using H_2O_2 or (H_2 + O_2) arises due to a partial delocalization of electron density from the orbitals of superoxo oxygen to the vanadium orbitals. Such delocalization of electron density occurs only if the vanadium—($O_2^{-\bullet}$) bond (*i.e.*, the V—O bond) in vanado-superoxo species is covalent. The **B**- and **C**-type superoxo-vanadium species generated using TBHP did not show vanadium superhyperfine features (see Fig. 6.8), indicating that the unpaired electron is localized on the superoxo oxygen orbitals. Hence, the V—O bond of **B** and **C**-type species is ionic. Similar relations between superhyperfine coupling constants and the nature of bonding were observed also in the case of cobalt-dioxygen complexes [44]. It is known from the studies on titanosilicates and also from vanadosilicates [17] that the coordination number of vanadium increases on contact with H_2O_2 or TBHP from 4 to 5 or 6; $V(OSi)_3(OR)(O_2^{-\bullet})$-type oxo species have been proposed to form. Here, R= H and *tert*-butyl in the case of H_2O_2 and TBHP, respectively. The electron donating *tert*-butoxy group makes the vanadium center in the oxo-vanadium species rich in electron density, and hence, delocalization of electron density from superoxo oxygen to vanadium is not favored. As a consequence, the superoxo-vanadium species generated using TBHP possibly does not show superhyperfine coupling features in the EPR spectrum. A covalent V-O bond, wherein, part of the electron density on oxygen is delocalized onto the d-orbitals of V, leads to a lower amount of electron density on the superoxide ion. Since these electrons are being removed from the *antibonding* orbital of $O_2^{-\bullet}$, this strengthens the O-O bond, thereby, facilitating its heterolytic cleavage. An ionic V-O bond, on the contrary, weakens the O-O bond and leads to a homolytic O-O cleavage. The EPR spectroscopic studies reveal that the covalency of the V-O bond of superoxo-vanadium species in VS-1 is greater than that in V-MCM-41. In different solvents, it decreases in the following order: acetone > methanol > acetonitrile. Hence, it follows that the probability of a heterolytic O-O cleavage in oxidations over VS-1 should be greater than on V-MCM-41 and in the above solvents it should also decrease in the above order.

Table 6.4. Chemoselective Oxidation of *n*-hexane over V-silicates with Aq. H_2O_2 (30%)[a]

Vanado-silicate[b]	Oxidant	Solvent	C_6H_{14} conv.	TOF[c] (h^{-1})	Product selectivity (mol%)							Secondary / Primary
					Primary C-H bond oxidation			Secondary C-H bond oxidation				
			mol %		1-ol	-al	Acid	2-ol	2-one	3-ol	3-one	
VS-1	H_2O_2	$(CH_3)_2CO$	4.2	2	1.0	1.6	4.2	4.6	29.8	21.9	35.9	13.7
VS-1	H_2O_2	CH_3OH	6.0	3	1.4	2.0	5.8	5.6	30.0	26.5	28.7	9.9
VS-1	H_2O_2	CH_3CN	8.1	5	2.6	2.7	5.2	3.2	26.9	22.5	36.9	8.5
V-MCM-41	H_2O_2	CH_3CN	54.0	94	9.7	0.3	10.9	6.4	25.5	14.9	32.3	3.8
V-MCM-41	TBHP	CH_3CN	21.3	37	19.2	1.9	6.1	8.2	24.2	4.3	36.1	2.7

[a]*n*-Hexane = 2.5 g; *n*-hexane/oxidant = 3 (mol); solvent = 12.5 ml; VS-1 = 0.4 g; V-MCM-41 = 0.15 g; temperature = 373 K; time = 8 h. [b]Si/V output molar ratio (AAS): VS-1, 320; V-MCM-41, 350. [c]Turnover frequency (TOF) = moles of *n*-hexane converted per mole of vanadium per hour.

6.3.5. Catalytic Activity: Oxidation of *n*-Hexane over Vanadosilicates

In the oxidation of n-hexane the selectivity for secondary *vs* primary C-H bond oxidation is more over VS-1 than V-MCM-41 (Table 6.4) and this selectivity in the above solvents decreases in the order: acetone > methanol > acetonitrile [1]. With different oxidants, the primary C-H bond oxidation is more favored with TBHP (*vis-a-vis* H_2O_2) (Table 6.4).

These parallel variations of chemoselective primary C-H bond oxidation and the tendency for a homolytic O-O cleavage indicate that the primary C-H bond oxidation in *n*-alkanes is favored, probably, by a homolytic cleavage of the O-O bond in the *oxidant*. Oxidation of secondary C-H bonds can proceed by both the homo- and heterolytic O-O cleavage mechanisms.

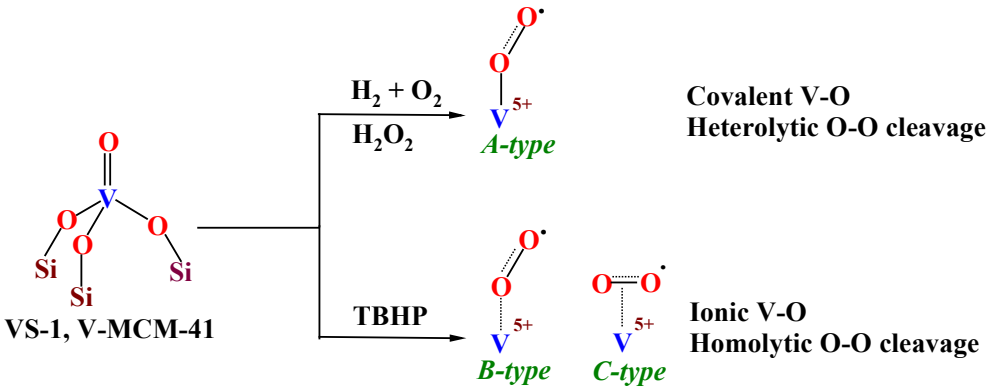

Scheme 6.1: Superoxo-vanadium (V) species generated in vanadosilicate molecular sieves contacted with ($H_2 + O_2$), H_2O_2 and TBHP.

6.4. Conclusions

EPR spectroscopic evidence was provided for the participation of oxygen radical ions in selective oxidations over vanadosilicate molecular sieves. In addition, the results indicate that the type of cleavage of the O-O bond in the oxidant (H_2O_2 or TBHP) influences the chemoselectivity of oxidation: A heterolytic cleavage leads to oxidation of secondary C-H bonds while the primary C-H bonds (in paraffins) are preferentially oxidized by a homolytic cleavage of the O-O bond. Scheme 6.1 summarizes the different types of superoxo-vanadium(V) species generated (types-A, B and C) in vanadosilicates upon contacting with oxidants like H_2O_2, ($H_2 + O_2$) or TBHP.

6.5. References

[1] P.R. Hari Prasad Rao, A.V. Ramaswamy, P. Ratnasamy, J. Catal. 137 (1992) 225.

[2] P.R. Hari Prasad Rao, A.A. Belhekar, S.G. Hedge, A.V. Ramaswamy, P. Ratnasamy, J. Catal. 141 (1993) 595.

[3] P.R.Hari Prasad Rao, A.V.Ramaswamy, P.Ratnasamy, J.Catal. 141 (1993) 604.

[4] K.R. Reddy, A.V. Ramaswamy, P. Ratnasamy, J. Catal. 143 (1993) 275.

[5] A.V. Ramaswamy, S. Sivasanker, Catal. Lett. 22 (1993).

[6] A.V. Ramaswamy, S. Sivasanker, P.Ratnasamy, Micropor. Mater. 2 (1994) 451

[7] P. Kumar, R. Kumar, B. Pandey, Synlett (1995) 289.

[8] A.P. Singh, T. Selvam, Appl. Catal. A: Gen. 143 (1996) 111

[9] A.P. Singh, T. Selvam, J. Mol. Catal. A: Chem. 113 (1996) 489.

[10] S. Kannan, T. Sen, S. Sivasanker, J. Catal. 170 (1997) 304.

[11] S.C. Laha, R. Kumar, Micropor. Mesopor. Mater. 53 (2002) 163.

[12] N.N. Trukhan, A.Y. Derevyankin, A.N. Shmakov, E.A. Paukshtis, O.A. Kholdeeva, V.N. Romannikov, Micropor. Mesopor. Mater. 44-45 (2001) 603.

[13] S.C. Laha, R. Kumar, Micropor. Mesopor. Mater. 53 (2002) 163.

[14] N.K. Mal, A.V. Ramaswamy, Appl. Catal A: Gen. 143 (1996) 75.

[15] M. Anpo, S.G. Zhang, S. Higashimoto, M. Matsuoka, H. Yamashita, J. Phys. Chem. B 103 (1999) 9295.

[16] S. Higashimoto, M. Matsuoka, S.G. Zhang, H. Yamashita, O. Kitao, H. Hidaka, M. Anpo, Micropor. Mesopor. Mater. 48 (2001) 329.

[17] P. Ratnasamy, D. Srinivas, K. Knözinger, Adv. Catal. 48 (2004) 1.

[18] J.M. Thomas, G. Sankar, Acc. Chem. Res. 34 (2001) 571.

[19] G. Sankar, J.M. Thomas, C.R.A. Catlow, C.M. Barker, D. Gleeson, N. Kaltsoyannis, J. Phys. Chem. B 105 (2001) 9028.

[20] W. Lin, H. Frei, J. Am. Chem. Soc. 124 (2002) 9292.

[21] S. Bordiga, A. Damin, F. Bonino, G. Ricchiardi, C. Lamberti, A. Zecchiana, Angew. Chem Int. Ed. 41 (2002) 4734.

[22] D. Srinivas, P. Manikandan, S.C. Laha, R. Kumar, P. Ratnasamy, J. Catal. 217 (2003) 217.

[23] T. Tatsumi, Y. Watanabe, Y. Himasawa, J. Tsuchiya, Res. Chem. Intermed. 24 (1998) 529.

[24] A.M. Gasymov, L.K. Przheval'skaya, V.A. Shvets, V.B. Kazanski, Kinet. Katal. 25 (1984) 358.

[25] H. Kelm, K.-J. Kruger, Angew. Chem. 113 (2001) 2406.

[26] R.C. Thompson, Inorg. Chem. 21 (1982) 859.

[27] J.P. Wilshire, D.T. Sawyer, J. Am. Chem. Soc. 100 (1978) 3972.

[28] H.B. Brooks, F. Sicilio, Inorg. Chim. 10 (1971) 2530.

[29] V.A. Shvets, M.E. Sarichev, V.B. Kasansky, J. Catal. 11 (1968) 378.

[30] V.A. Shvets, V.B. Kazansky, J. Catal. 25 (1972) 123.

[31] B.N. Shelimov, M. Che, J. Catal. 51 (1978) 143.

[32] G. Centi, P.F. Trifiro, A. Aboukais, C.F. Aissi, M. Guelton, J. Phys. Chem. 96 (1992) 2617.

[33] R. Millini, E.P. Massara, G. Perego, G. Bellussi, J. Catal. 133 (1992) 220, and 137 (1992) 497.

[34] R. Millini, G. Perego, Gazz. Chim. Ital. 126 (1996) 133.

[35] G. Grubert, J. Rathouský, G. Schulz-Ekloff, M. Wark, A. Zukal, Micropor. Mesopor. Mater. 22 (1998) 225.

[36] D. Lee, T. Liu, J. Sol-Gel Science Tech. 24 (2002) 69.

[37] J. Kornatowski, B. Wichterlová, J. Jirkovský, E. Löffler, W. Pilz, W. J. Chem. Soc., Faraday Trans. 92 (1996) 1067.

[38] S. Dzwigaj, M. Matsuoka, M. Anpo, M. Che, J. Phys. Chem. 104 (2000) 6012.

[39] T. Sen, R..Rajamohanan, S.Ganapathy, S. Sivasanker, J. Catal. 163 (1996) 354.

[40] T. Sen, V. Ramaswamy, S. Ganapathy, R. Rajamohanan, S. Sivasanker, J. Phys. Chem. 100 (1996) 3809.

[41] A. Tuel, Y. Ben Taârit, Appl. Catal. A: Gen. 102 (1993) 201.

[42] M. Anpo, M. Che, B. Fubini, E. Garrone, E. Giamello, M.C. Paganini, Topics, Catal. 8 (1999) 189.

[43] M. Che, A. Tench, J. Adv. Catal. 31 (1982) 77.

[44] R.D. Jones, D.A. Summerville, F. Basolo, Chem. Rev. 79 (1979) 139.

Chapter – 7

CuO-CeO_2-ZrO_2 and CuO-CeO_2-TiO_2 Composites: Active Sites and Catalytic Oxidations

7.1. Introduction

Ceria-based catalysts have been used for a variety of applications including automotive pollution control, fuel cell electrodes, hydrogen gas generation by hydrocarbon steam reforming, water-gas shift reaction, CO oxidation and several other oxidation reactions [1-5]. Incorporation of zirconia forming CeO_2-ZrO_2 solid solutions has imparted several advantages that include: (1) prevention of chain growth of ceria crystallites at high temperatures, (2) increased oxygen storage capacity (OSC) by improving the homogeneity of Ce and Zr atoms and the modification of the oxygen environment, (3) improved dispersion of supported noble metals and metal oxides, (4) increased resistance to sintering of metal ions, (5) enhanced tolerance to water vapor and sulfur compounds like SO_2, and (6) enhanced reactivities in water-gas shift and steam reforming reactions. However, the composition of ceria and zirconia is crucial determining the efficiency of the catalyst system. Having understood the superiority of zirconia incorporation it is attempted in this work to exploit CeO_2-ZrO_2-supported CuO catalysts as cheaper alternatives to the noble metal-based catalysts. Use of these catalysts and the influence of method of preparation and composition on selective oxidation of CO in hydrogen-rich fuels are explored. Studies are conducted also on CuO containing CeO_2-TiO_2 composites. The redox behavior and oxygen storage capacity of these materials were investigated. CuO-CeO_2-TiO_2 catalysts were evaluated for oxidative dehydrogenation of ethylbenzene to styrene.

The redox properties of Cu^{2+} ions play an important role in the catalytic activity for oxidation reactions. They depend on the dispersion and coordination of Cu^{2+} species, and the support on which the metal ions are dispersed. Larson et al. [6, 7]. found that catalysts using TiO_2 as carrier displayed a higher catalytic activity in CO oxidation than those supported on MoO_x, FeO_x and CoO_x. The activity of the catalyst at low temperature was superior to Pt/γ-Al_2O_3 catalysts [8]. Komova et al. [9] found that TiO_2-supported CuO could exist as Cu^{2+} ions, bulk CuO, chain stabilized Cu^{2+} ions, and two different oxide clusters with a structure similar to CuO. In contrast, Xu et al. [10] reported two types of Cu^{2+} ions - CuO phase and highly

dispersed Cu^{2+}, with significantly different reducibility on the anatase surface similar to CuO/ γ-Al_2O_3.

CuO-CeO_2 exhibits significant activity in the total oxidation of CO [11]. Even though, a large amount of structural studies on CuO-CeO_2-ZrO_2 system have been carried out [12 - 17], the influence of the size of cerium and zirconium oxides on dispersion, oxidation state, magnetic properties and catalytic activity, in PROX reactions, of copper catalysts supported on CeO_2-ZrO_2 is not understood completely. For example, what is the effect of CuO dispersion on the selectivity for CO oxidation (vis-à-vis H_2 and CH_4) in the presence of CO_2 and H_2O? In this study samples of CuO-CeO_2-ZrO_2 with varying concentrations of the individual components were prepared and characterized. The catalytic activity of these well-characterized samples in the selective oxidation of CO in a gas mixture with a composition similar to that present in typical PROX reactor effluents is also reported. The results are expected to throw further light on the influence of the structural characteristics of supported copper on their catalytic activity and selectivity in PROX and other oxidation reactions.

7.2. Experimental

The synthesis of materials is presented in Chapter 2. Catalytic activities of CuO-CeO_2-ZrO_2 materials were tested for preferential oxidation of CO to CO_2 in hydrogen-rich fuels. CuO-CeO_2-TiO_2 catalysts were investigated for the oxidative dehydrogenation of ethylbenzene to styrene. The content of CuO was varied in the range of 1 – 20%. For comparative studies, CuO supported on CeO_2, ZrO_2 and TiO_2 were also prepared and examined. The procedures for reactions are presented in Chapter 2.

7.2.1. Material Characterization

A Rigaku Geigerflex X-ray diffractometer with Ni-filtered Cu Kα radiation (λ = 1.5406 Å, 40 kV, 30 mA) was used to determine the crystallinity and phase purity of the samples. The XRD patterns were recorded in the 2θ range of 20-90°, with a scan speed of 2°/min. The average crystallite size was determined from the line widths of the XRD peaks corresponding to (111) reflection, using the Debye-Scherrer equation.

The specific surface area (S_{BET}) was estimated from the N_2 adsorption/desorption isotherms, measured at 77 K, using a Coulter 100 instrument.

Diffuse reflectance UV-visible (DRUV-visible) spectra were recorded on a Shimadzu UV-2550 spectrophotometer equipped with an integrating sphere attachment (ISR – 2200). Spectral grade $BaSO_4$ was the reference material.

In situ EPR measurements were done on a Bruker EMX spectrometer operating at X-band frequency ($\nu \approx 9.4$ GHz) and 100 kHz field modulation. The calcined sample (40 mg) was taken in a specially, designed quartz EPR cell (o.d. = 4 mm) fitted with greaseless stopcocks and having provision for adsorption/desorption of gases. Prior to EPR measurements, the samples were degassed at 773 K for 6 h (10^{-3} torr) and then treated with dry-hydrogen (20 ml/h) for 1 h at elevated temperatures. The spectra were recorded at both 298 and 77 K. No marked changes in spectral resolution were observed at lower temperatures.

Magnetic susceptibility measurements at 298 K (10 – 15 mg catalyst) were carried out with a Lewis-coil force magnetometer (Series 300, George Associates, USA) coupled with a high vacuum system (10^{-6} torr) with provision for *in situ* treatment in desired gases at elevated temperatures. Corrections for sample holder and ferromagnetic impurities, if any, were also made.

Temperature-programmed reduction (TPR) experiments were performed using a Micromeritics AutoChem 2910 instrument. A known amount (20 mg) of the sample was placed in a quartz reactor and treated with a O_2(22%)-He(78%) gas mixture at 773 K for 2 h. A gas mixture of H_2(5%)-Ar(95%) was then passed (30.22 ml/min) through the reactor. The temperature was raised to 1200 K at a heating rate of 10 K/min. A standard CuO powder was used to calibrate the amount of H_2 consumption.

X-ray photoelectron spectra (XPS) were acquired on a VG Microtech Multilab ESCA 3000 spectrometer with a non-monochromatized Mg Kα X-ray radiation ($h\nu$ = 1253.6 eV) on calcined, powder samples and after reduction at 573 K for 3 h. Base pressure in the analysis chamber was maintained at $3 - 6 \times 10^{-10}$ mbar. The energy resolution of the spectrometer was set at 0.8 eV at a pass energy of 20 eV. Binding energy (BE) was calibrated with respect to Au 4f 7/2 core level at 83.9 eV. The error in all the BE values reported is 0.1 eV.

7.3. Results and Discussion – $CuO-CeO_2-ZrO_2$ Composites

7.3.1. Structural and Textural Characterization

Fig. 7.1 shows the XRD patterns of CeO_2, CeO_2-ZrO_2, CuO(5%)-CeO_2(95%) and CuO(5%)-CeO_2(47.5%)-ZrO_2(47.5%). The reflections in the 2θ range of 28 – 80° indicate a distinct, cubic, fluorite structure [12 - 17]. In CeO_2-ZrO_2-based catalysts the reflections shifted to higher 2θ values compared to CeO_2 (shown by dotted lines in Fig. 7.1). The unit cell parameter (Table 7.1) of CeO_2-ZrO_2 is smaller (0.531 nm) than that of CeO_2 (0.548 nm) suggesting the formation of ceria-zirconia solid solutions [18]. The ZrO_2-based catalysts showed broad reflections and hence, the unit cell and average crystallite size parameters could not be determined with precision. No separate phase due to CuO or Cu_2O was detected, except in the samples with 10 wt% CuO. A majority of the total CuO is present at the surface of the support.

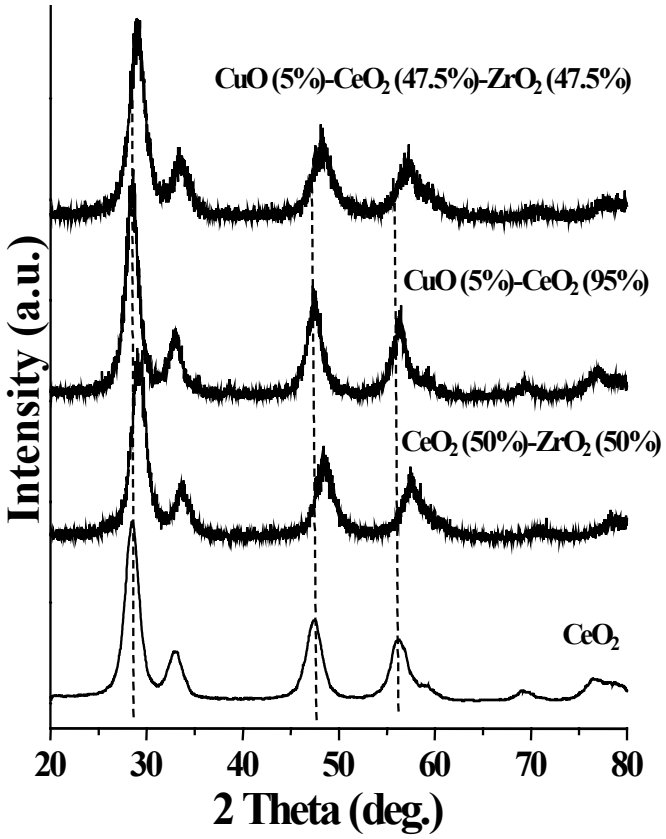

Fig. 7.1. XRD profiles of $CuO-CeO_2-ZrO_2$ samples.

Table 7.1. Structural Parameters (from XRD) and BET Surface Area of CuO-CeO_2-ZrO_2 Composites

Catalyst[a]	Unit cell parameter of the support oxide (nm)	Average crystallite size of support oxide (nm)	Unit cell parameter of CuO (nm)	Average crystallite size of CuO (nm)	S_{BET} (m^2/g)
CeO_2	0.548	4.9	-	-	150
CeO_2(50%)-ZrO_2(50%)	0.531	4.4	-	-	161
ZrO_2	-	-	-	-	172
CuO(1%)-CeO_2(99%)	0.547	6.6	-	-	117
CuO(5%)-CeO_2(95%)	0.545	7.8	-	-	129
CuO(10%)-CeO_2(90%)	0.542	8.4	0.438	4.1	124
CuO(1%)-CeO_2(49.5%)-ZrO_2(49.5%)	0.532	4.4	-	-	168
CuO(5%)-CeO_2(47.5%)-ZrO_2(47.5%)	0.533	4.2	-	-	148
CuO(10%)-CeO_2(45%)-ZrO_2(45%)	0.530	3.8	0.437	3.2	136
CuO(1%)-ZrO_2(99%)[b]	-	-	-	-	161
CuO(5%)-ZrO_2(95%)[b]	-	-	-	-	153
CuO(10%)-ZrO_2(90%)[b]	-	-	-	-	161

[a]Values in parentheses indicate composition in wt%. All the materials are prepared by co-precipitation route (method A),
[b]XRD peaks were broad.

The presence of zirconium decreased the crystallite size of ceria as well as CuO (Table 7.1). The crystallite size of ceria decreased from 8.4 (for CuO(10%)-CeO_2(90%)) to 3.8 nm (for CuO(10%)-CeO_2(45%)-ZrO_2(45%)). The corresponding decrease in the crystallite size of CuO was from 4.1 to 3.2 nm. When CuO was also present the crystallite size of ceria increased from 4.9 nm (for pure CeO_2) to 8.4 nm (for CuO(10%)-CeO_2(90%)).

S_{BET} values increased in the series: CeO_2 < CeO_2-ZrO_2 < ZrO_2 (Table 7.1). When CuO was also present, the CuO-CeO_2 samples showed a marked decrease in surface area (from 150 to 117 m^2/g). The decrease is not significant in CuO-CeO_2-ZrO_2 (Table 7.1). Zirconia incorporation in the support, hence, increases the surface area of the samples in agreement with the XRD results where formation of smaller crystallites is found in CeO_2-ZrO_2-based catalysts (Table 7.1; compare rows 7-9 with 4-6).

7.3.2. Redox Behavior

7.3.2.1. Temperature-Programmed Reduction

Pure ZrO_2 could not be reduced in H_2 in the temperature range 298 – 1200 K. CeO_2 showed two peaks at 658 and 794 K attributable to reduction of surface and bulk ceria compositions, respectively [16, 19]. In the presence of zirconia the reducibility of ceria increased and the reduction temperature decreased. In CeO_2-ZrO_2, the reduction of surface and bulk ceria occurred at 620 and 804 K, respectively.

Reduction of CuO supported on CeO_2, CeO_2-ZrO_2 and ZrO_2 started above 373 K [16, 17]. In pure CuO this occurred above 523 K. At least 2 to 3 reduction peaks were observed in the supported catalysts indicating the existence of different type of CuO species. CuO(5%)-ZrO_2(95%) showed overlapping reduction peaks at 465 K and 450 K (Fig. 7.2). These peaks in CuO(5%)-CeO_2(95%), appeared at lower temperatures, 445 and 425 K, respectively (Fig. 7.2). In CuO(5%)-CeO_2(47.5%)-ZrO_2(47.5%), they occurred at still lower temperatures, 435 and 398 K, respectively (Fig. 7.2). With different supports, the reducibility of CuO increased in the order: ZrO_2 < CeO_2 < CeO_2-ZrO_2. TPR of CuO supported on CeO_2 and ZrO_2 was investigated by several groups [20 – 22]. They observed CuO reduction peaks in the range 398 – 448 K and above 473 K. The former was attributed to that arising from

dispersed copper oxide clusters, strongly interacting with the support while the latter (above 473 K) from CuO particles. The TPR peaks for the catalysts (Fig. 7.2) reveal that the latter type of CuO particles is not present in the samples of present investigation and the CuO is mostly well dispersed.

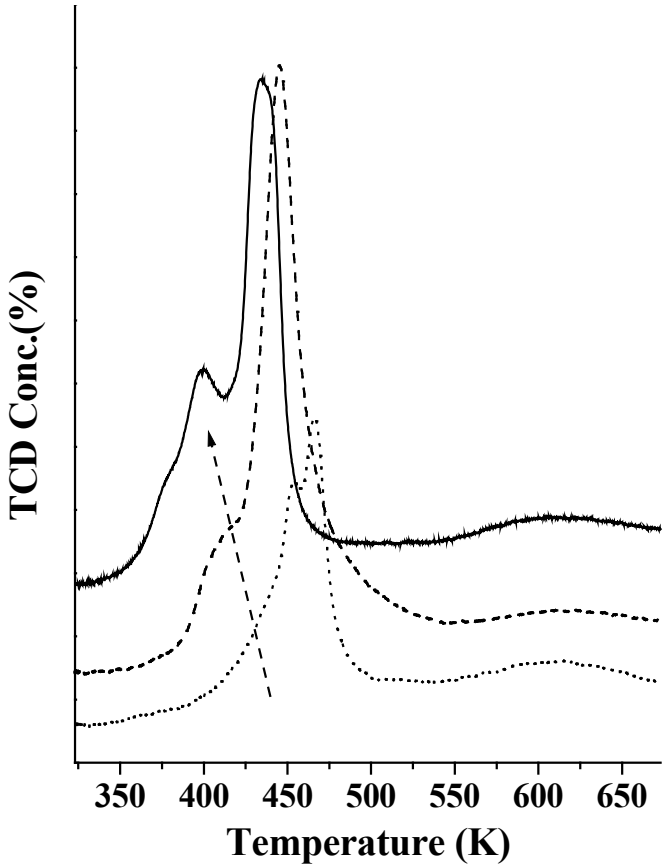

Fig. 7.2. TPR of CuO(5%)-ZrO_2(95%) (……), CuO(5%)-CeO_2(95%) (- - - - -) and CuO(5%)-CeO_2(47.5%)-ZrO_2(47.5%) (_____).

7.3.2.2. Electronic Spectroscopy

Both pure CeO_2 and CeO_2-ZrO_2 showed two UV bands at 257 and 338 nm attributable to $O^{2-} \rightarrow Ce^{4+}$ charge transfer (CT) transitions. The former is a specular reflectance band arising from the surface sites and the latter is a diffuse reflectance band arising from bulk ceria [23]. Pure ZrO_2 showed only one band at 215 nm. The extinction coefficients of these bands were different for different supports and decreased in the order: CeO_2 > CeO_2-ZrO_2 > ZrO_2. The intensity of the 338 nm band

in CeO_2-ZrO_2 (*vis-à-vis* pure CeO_2) increased due to substitution of Zr^{4+} in CeO_2 lattice and the consequent strain and lowering of symmetry at the site of cerium. These CT bands shifted to lower energy side (higher wavelength) when CuO was also present (Fig. 7.3, left panel). The shift is more noticeable in CuO-CeO_2 and CuO-ZrO_2 than in CuO-CeO_2-ZrO_2. In CuO(5%)-CeO_2(95%), these CT appeared at 267 and 345 nm (compared to 257 and 338 nm, respectively). In CuO(5%)-CeO_2(47.5%)-ZrO_2(47.5%), they appeared at 260 and 345 nm. In CuO(5%)-ZrO_2(95%), the 215 nm band shifted to 270 nm. These red shifts in the CT bands reveal an increase in the crystallite size of CeO_2 in the presence of CuO. These observations reinforce similar conclusions from the XRD data (Table 7.1).

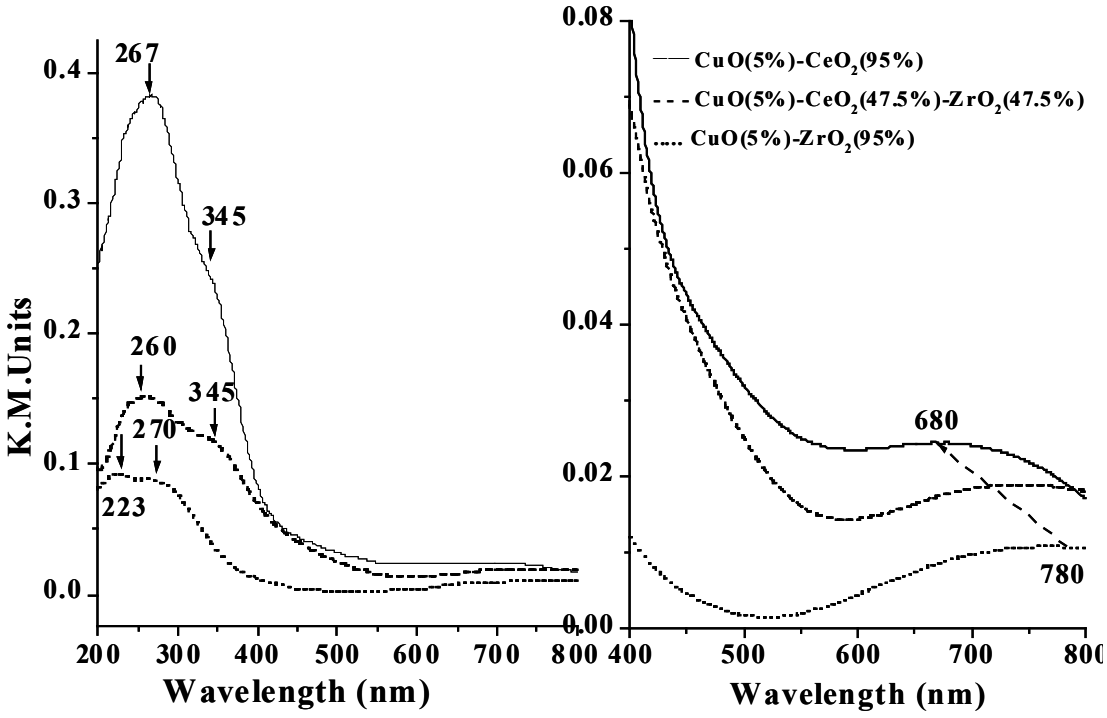

Fig. 7.3. DRUV-visible spectra showing the influence of support composition on the charge transfer (left) and d-d (right) transitions.

The CuO-containing catalysts showed a broad, d-d band in the visible region (Fig. 7.3, right panel). This band shifted from 780 (Cu^{2+} in six-fold coordination) to 680 nm (Cu^{2+} in four-fold coordination) with a change in the support from ZrO_2 to CeO_2-ZrO_2 to CeO_2 , respectively [24 - 26]. A similar shift (from 800 to 763 nm in

$CuO\text{-}ZrO_2$, 768 to 645 nm in $CuO\text{-}CeO_2\text{-}ZrO_2$ and 670 to 650 nm in $CuO\text{-}CeO_2$) was observed with an increase (from 1 to 10 wt%) in the CuO content indicating that the type of copper species in these catalysts is influenced by both the support and concentration.

7.3.2.3. EPR Spectroscopy

7.3.2.3.1. Redox Behavior of the Support

EPR spectra of CeO_2 reduced with dry hydrogen revealed the formation of two types of paramagnetic species, A, due to Ce^{3+} [27] ($g_{\perp}$ = 1.965 and $g_{||}$ = 1.940) and B, due to $O_2^{-\bullet}$ ions [28] (g_1 = 2.030, g_2 = 2.016 and g_3 = 2.011), the concentration of which depended on the reduction temperature (T_r) (Fig. 7.4, left panel).

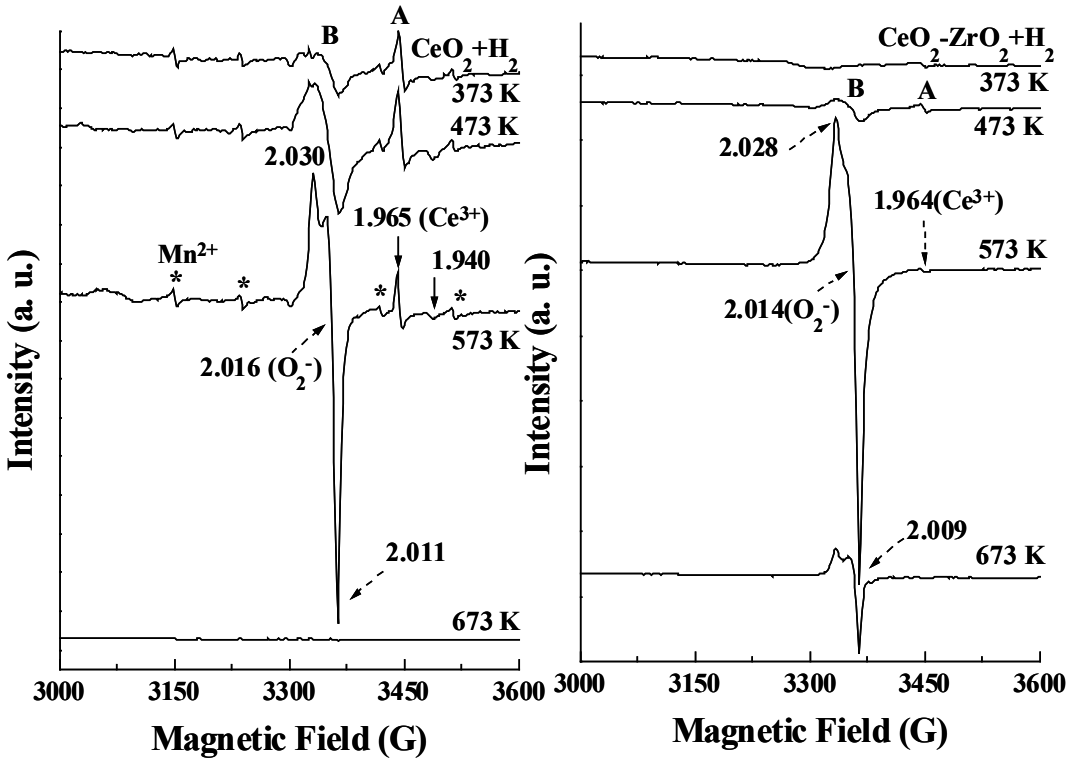

Fig. 7.4. EPR spectra (at 298 K) of Ce^{3+} (A) and $O_2^{-\bullet}$(B) ions generated on CeO_2 (left) and $CeO_2\text{-}ZrO_2$ (right) by reaction with H_2 at elevated temperatures

Intensity of A-signals reached a maximum at 573 K. Pure ZrO_2 did not form these paramagnetic species when reduced in hydrogen. $CeO_2\text{-}ZrO_2$ (Fig. 7.4, right panel) behaved in a manner similar to pure CeO_2. Upon reoxidation by exposure to

air at 298 K, the signals due to species A disappeared and of B decreased and broadened.

Species A and B could be generated, repeatedly, in several cycles indicating the facile redox behavior of CeO_2 and CeO_2-ZrO_2 supports. TPR had indicated that the reduction of ceria (not shown in figure) is facilitated in the presence of zirconia. The reduction of ceria occurred at 620 K in CeO_2-ZrO_2 compared to 658 K in CeO_2. Hence, higher amounts of Ce^{3+} are formed in reduced CeO_2-ZrO_2 composites than in pure CeO_2. Both EPR and TPR studies reveal that zirconium incorporation enhances the concentration of Ce^{3+}.

7.3.2.3.2. Redox Behavior of Supported Copper

At least four types of paramagnetic copper species (I – IV) could be identified in the EPR spectrum of CuO(1%)-CeO_2(99%) (Fig. 7.5(i), curve a).

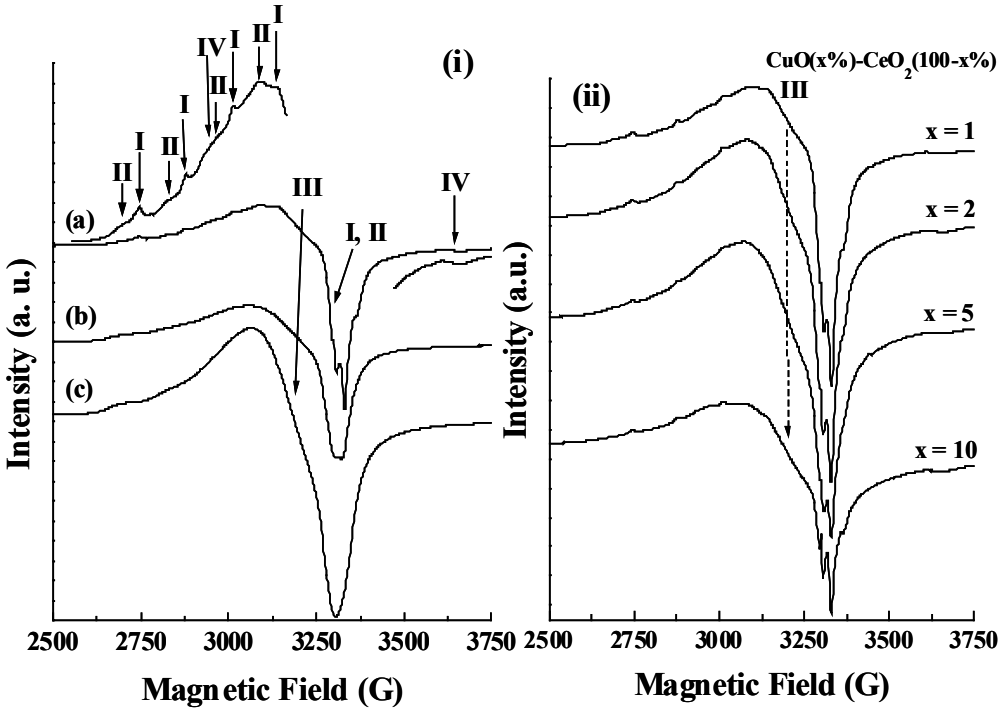

Fig. 7.5. Left: EPR spectra of CuO(1%) supported on (a) CeO_2, (b) CeO_2-ZrO_2 and (c) ZrO_2. Signals due to different Cu species (I, II, III and IV) are indicated by arrows. Right: Effect of CuO content on the EPR spectra of CuO(x%)-CeO_2(100-x%) catalysts

Types I and II correspond to isolated, monomeric Cu^{2+} species characterized by axial spectra with resolved Cu hyperfine features in the parallel and perpendicular

regions [12 - 14, 29, 30]. These species are different in their $g_{||}$ and $A_{||}$(Cu) values (Type I: $g_{||}$ = 2.300, $A_{||}$(Cu) = 126.4 G; Type II: $g_{||}$ = 2.339, $A_{||}$(Cu) = 124.8 G). Their $g_{\perp}$ (2.049) and $A_{\perp}$(Cu) (10.0 G) values are similar. The line width of species I is smaller than that of species II (curve a). The spin Hamiltonian parameters indicate that the geometry around Cu^{2+} is distorted octahedral. These species (I and II) are perhaps located in the lattice and surface sites of ceria crystallites, respectively [29]. The type III species characterized by a broad signal (line width = 210 G) centered at g_{av} = 2.10 is attributed to dipolar, interacting Cu^{2+} ions forming a nano-sized 2-dimensional structure [29]. The relative concentration of the type III species increased with copper content (Fig. 7.5(ii)). The visible band at 645 – 680 nm in the diffuse reflectance spectrum corresponds to this species. The type IV species showed two signals at 3017 and 3716 G corresponding to a single-quantum, perpendicular transitions of Cu^{2+}-Cu^{2+} dimers at the surface [30]. The exchange coupling constant (J) for these dimers (Type IV) was –52.5 cm^{-1} and Cu-Cu separation was 3.4 Å [30]. If the two copper ions of the dimer were to occupy adjacent Ce^{4+} locations in the fluorite lattice, their Cu-Cu separation would have been 5.41 Å. It was, hence, proposed that these interacting, Cu^{2+}-Cu^{2+} dimers in copper oxo species are at the surface of ceria [29, 30].

CuO(1%)-ZrO_2(99%), on the other hand, contained only two types of Cu^{2+} species *viz.*, isolated Cu^{2+} ions (II) and interacting Cu^{2+} ions (III) (Fig. 7.5(i), curve c). The spin Hamiltonian parameters of these species are different from CuO(1%)-CeO_2(99%) (Table 7.2). Unlike in CuO(1%)-CeO_2(99%) (Fig. 7.5(i), curve a), the perpendicular Cu-hyperfine features could not be resolved in CuO(1%)-ZrO_2(99%) (Fig. 7.5(i), curve c). The type III species of CuO-ZrO_2 showed a signal at g_{av} = 2.12.

CuO(1%)-CeO_2(49.5%)-ZrO_2(49.5%) showed spectra (Fig. 7.5(i), curve b) intermediate in shape to that of CuO(1%)-CeO_2(99%) and CuO(1%)-ZrO_2(99%). Cu species, types I, II and III were detected. Similar to CuO(1%)-CeO_2(99%), the type I species of CuO(1%)-CeO_2(49.5%)-ZrO_2(49.5%) showed resolved Cu-hyperfine features at parallel and perpendicular regions (Table 7.2). Signals of CuO(1%)-

Table 7.2. EPR Spin Hamiltonian Parameters (The Materials are Prepared by Precipitation Route (Method A)

Catalyst	Treatment	Assignment	Type	$g_{\|\|}$ or g_1	$g_\perp$ or g_2, g_3	$A_{\|\|}^{Cu}$ (G)	$A_\perp^{Cu}$ (G)
CeO_2	H_2 reduction	Ce^{3+}	A	1.940	1.965	-	-
		Ce^{4+}–$O_2^{-\cdot}$	B	2.030	2.011, 2.016	-	-
CeO_2(50%)-ZrO_2(50%)	H_2 reduction	Ce^{3+}	A	1.940	1.964	-	-
		Ce^{4+}–$O_2^{-\cdot}$	B	2.028	2.009, 2.014	-	-
CuO(1%)-CeO_2(99%)	-	Isolated Cu^{2+} in lattice site	I	2.300	2.049	126.4	10
	-	Isolated surface Cu^{2+}	II	2.339	2.049	124.8	Not resolved
		Interacting Cu^{2+}	III	2.10	2.10	Not resolved	Not resolved
		Isolated dimer	IV[a]				
CuO(1%)-ZrO_2(99%)		Isolated surface Cu^{2+}	II	2.336	2.063	130.0	Not resolved
		Interacting Cu^{2+}	III	2.12	2.12	Not resolved	Not resolved
CuO(1%)-CeO_2(49.5%)-ZrO_2(49.5%)	-	Isolated Cu^{2+} in lattice site	I	2.300	2.060	126.4	10
	-	Isolated surface Cu^{2+}	II	2.339	2.060	124.8	Not resolved
		Interacting Cu^{2+}	III	2.13	2.13	Not resolved	Not resolved

[a]The $g_\perp$ signals due to type IV were observed at 3017 and 3716 G; The $g_{\|\|}$ signals were weak and masked by types I –III.

CeO_2(49.5%)-ZrO_2(49.5%) were broader. Cu^{2+}-Cu^{2+} dimers (type IV) could not be detected. Thus, different types of CuO species were present in different amounts on CeO_2, ZrO_2 and CeO_2-ZrO_2.

The reducibility of CuO on various supports increased in the order: CuO-ZrO_2 < CuO-CeO_2 < CuO-CeO_2-ZrO_2 (Fig. 7.6). When Cu-CeO_2 and Cu-CeO_2-ZrO_2 were reduced at 573 K, almost all the copper was reduced. Reoxidation by exposing the samples to air regenerated the EPR spectrum of types I, II and IV species. Type III species could not be regenerated. The reduction-reoxidation of types I, II and IV species (isolated/dispersed copper) could be repeated several times. A similar observation was noted also on CeO_2-ZrO_2 supports. While 39.7% of total intensity could be regenerated upon reduction followed by reoxidation in CuO-CeO_2, it was only 31.4% in CuO-CeO_2-ZrO_2.

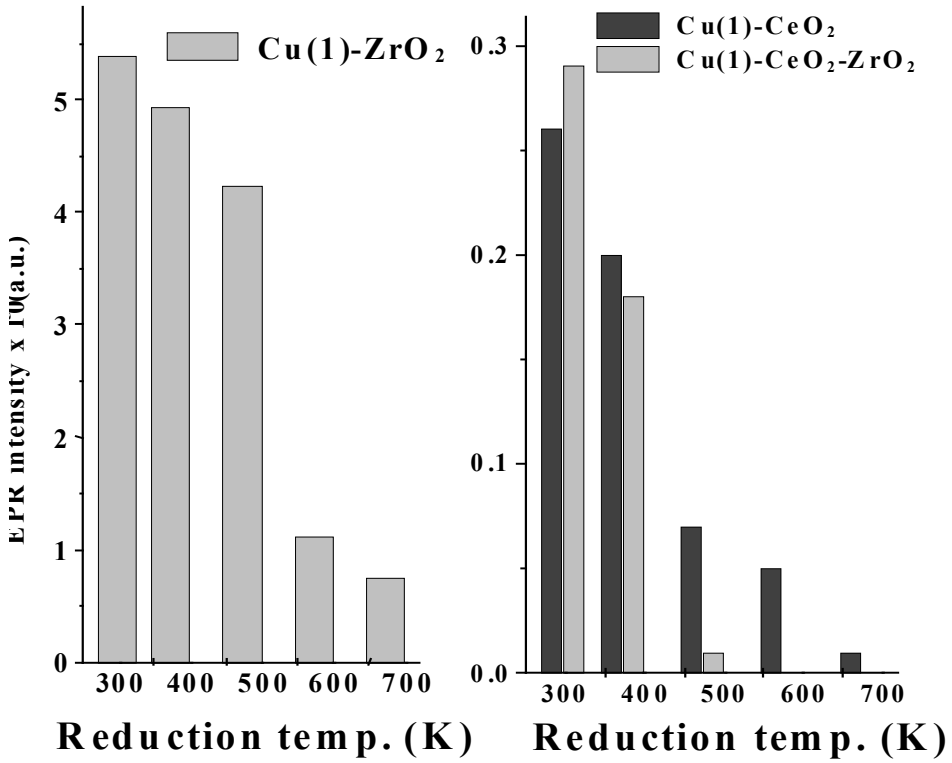

Fig. 7.6. Variation of Cu^{2+} signal intensity of CuO(1%)-CeO_2(99%), CuO(1%)-CeO_2(49.5%)-ZrO_2(49.5%) and CuO(1%)-ZrO_2(99%) as a function of reduction temperature.

Hence, the amount of reactive copper oxide that could be reduced and reoxidized is more on CeO_2 than on CeO_2-ZrO_2 support. The facile redox behavior and the abundance of the reactive copper species influence the CO oxidation activity of these catalysts (*vide supra*). In the absence of CuO, the supports CeO_2 and CeO_2-ZrO_2 generated Ce^{3+} ions and $O_2^{-\bullet}$ species. Such species were not detected in supported CuO catalysts.

7.3.2.4. Magnetic Susceptibility

Prior to magnetic susceptibility measurements the samples were first evacuated, then purged with He (5 – 10 ml/h) and again evacuated. Molar susceptibilities (χ_M) of ZrO_2, CeO_2-ZrO_2 and CeO_2 after diamagnetic correction are 0.026 $x10^{-3}$, 0.029 $x10^{-3}$ and 0.060 x 10^{-3} c.g.s. units, respectively. These values indicate weak paramagnetism. The Mn impurity and paramagnetic ions like Ce^{3+} and defect centers generated by evacuation/dehydroxylation are the probable causes for the weak paramagnetism of the evacuated samples. The variation in magnetic susceptibility (χ_M) of the samples with increasing CuO content is shown in Fig. 7.7.

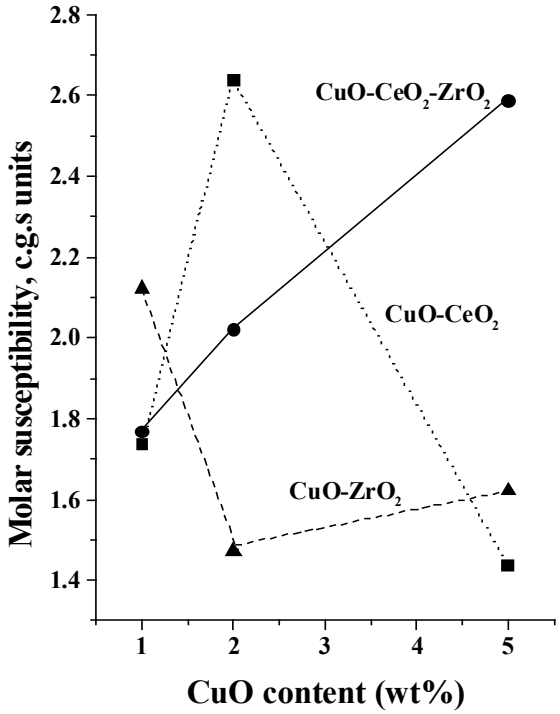

Fig. 7.7. Plot of molar magnetic susceptibility (χ_M) as a function of CuO content in CuO-CeO_2, CuO-CeO_2-ZrO_2 and CuO-ZrO_2.

The support influences the dispersion and magnetic state of copper significantly. From the linear increase in magnetic susceptibility, it may be concluded that the concentration of isolated, non-interacting Cu^{2+} ion increases with copper content in CeO_2-ZrO_2 (it may be recalled that Cu^{2+} is mainly responsible for the observed magnetic susceptibility). The presence of Cu^{1+} and *interacting* Cu^{2+} ions (at high concentrations) in CeO_2 and ZrO_2 probably account for their lower χ_M values at CuO content above 2 wt% (Fig. 7.7). In other words, in samples containing more than 2 wt% CuO, larger amounts of interacting Cu^{2+} ions/bulk CuO-like phases are formed on ZrO_2 and CeO_2 supports compared to CeO_2-ZrO_2. Apparently, CeO_2-ZrO_2 promotes a better and more stable dispersion of copper oxide. These results reinforce the conclusion from XRD (Table 7.1) that the average crystallite size of CuO on CeO_2-ZrO_2 is indeed smaller than that on CeO_2.

7.3.3. Preferential Oxidation of CO (PROX)

Catalytic activities of CuO supported on CeO_2, CeO_2-ZrO_2 and ZrO_2 at different reaction conditions (e.g., temperature, O_2/CO ratio, space velocity and time on stream) are presented in Tables 7.3 – 7.5 and Figures 7.8 – 7.10. PROX selectivity is defined as (oxygen consumed in CO oxidation) x 100 / (oxygen consumed in the oxidation of CO and H_2). At our reaction conditions oxidation of CH_4 was not observed. Oxygen conversion was more than 99.8%. The following conclusions are drawn:

1. CO oxidation increased with CuO content reaching a maximum at 5 wt% (Table 3; rows 1 – 4). CuO supported on CeO_2 exhibited superior activity than CuO-CeO_2-ZrO_2 and CuO-ZrO_2 (Table 7.3; compare rows 3, 5 and 6).
2. With a water-containing feed ($p(H_2O)$ = 200 torr), a decrease in the CO oxidation activity was observed. This decrease is more significant with ZrO_2-containing catalysts (Table 7.3, rows 5 and 6) and in the catalysts with a lower CuO-content (rows 1 and 2).
3. The adverse influence of H_2O on CO oxidation activity diminished above 423 K (Table 7.4).

Table 7.3. Preferential Oxidation of CO over CuO-CeO_2-ZrO_2 Catalysts

Catalyst	Feed without water					Feed with water[b]				
	CO		H_2		Sele.	CO		H_2		Sele.
	Comp. ppm	Conv. (%)	Comp. (v%)	Conv. (%)	(%)	Comp. ppm	Conv. (%)	Comp. (v%)	Conv. (%)	(%)
CuO(1%)-CeO_2(99%)	98	98.0	73.4	1.0	38.4	3070	37.3	73.1	1.4	14.6
CuO(2%)-CeO_2(98%)	82	98.3	73.4	1.0	38.5	1620	66.9	73.3	1.2	26.2
CuO(5%)-CeO_2(95%)	7	99.9	73.4	1.0	39.1	17	99.7	73.4	1.0	39.0
CuO(10%)-CeO_2(90%)	64	98.7	73.4	1.0	38.7	80	98.4	73.4	1.0	38.6
CuO(5%)-CeO_2(47.5%)-ZrO_2(47.5%)	89	98.2	73.4	1.0	38.5	495	89.9	73.4	1.0	35.2
CuO(5%)-ZrO_2(95%)	2950	39.8	73.1	1.4	15.6	3500	28.6	73.1	1.5	11.2

Reaction conditions: catalyst = 1.5 g, feed – H_2 (74.17%) + CO(0.49%) + CO_2(23.26%) + CH_4(2.08%); O_2/CO = 1.25, GHSV = 5000 h^{-1}; temperature = 423 K, run time = 4 h. Catalysts are prepared by co-precipitation route (method A).

[a]Selectivity of oxygen towards CO oxidation = (Oxygen consumed in CO oxidation) x 100/ (total oxygen consumed in CO + H_2 oxidation). [b]p(H_2O) – 200 torr.

Table 7.4. Effect of Temperature on the PROX Activity over $CuO(5\%)$-$CeO_2(47.5\%)$-$ZrO_2(47.5\%)$[a]

Temperature (K)	Feed without water					Feed with water[b]				
	CO		H_2		Sele. (%)	CO		H_2		Sele. (%)
	Comp. ppm	Conv. (%)	Comp. (v%)	Conv. (%)		Comp. ppm	Conv. (%)	Comp. (v%)	Conv. (%)	
373	2760	43.7	73.6	0.8	27.0	3610	26.3	73.6	0.8	18.5
398	775	84.1	73.5	0.9	38.1	2330	52.4	73.5	0.9	27.7
423	89	98.2	73.4	1.0	38.5	495	89.9	73.4	1.0	35.2
448	443	90.9	73.4	1.0	35.7	140	97.1	73.4	1.0	38.1
473	930	81.0	73.3	1.1	31.8	852	82.6	73.3	1.1	32.4

Reaction conditions: catalyst = 1.5 g, feed – H_2 (74.17%) + CO(0.49%) + CO_2(23.26%) + CH_4(2.08%); O_2/CO = 1.25, GHSV = 5000 h^{-1}. [a]Selectivity of oxygen towards CO oxidation = (Oxygen consumed in CO oxidation) x 100/ (total oxygen consumed in CO + H_2 oxidation). The catalyst was prepared by co-precipitation route (method A).
[b]$p(H_2O)$ – 200 torr.

4. The CO oxidation activity/selectivity increased with temperature reaching a maximum at 448-478 K (Table 7.4) due either to increased H_2 oxidation at higher temperatures and/or the growth of CuO particles above around 470 K [31].
5. The support has a marked effect on the catalytic activity (Fig. 7.8). With water-containing feed ($p(H_2O)$ = 200 torr), the CO oxidation activity decreased in the order: $CuO\text{-}CeO_2 > CuO\text{-}CeO_2\text{-}ZrO_2 > CuO\text{-}ZrO_2$. Copper-free supports also catalyzed the oxidation of CO and H_2. But their activities were considerably lower than the copper-containing catalysts. H_2 oxidation, takes place on both the metal and support.

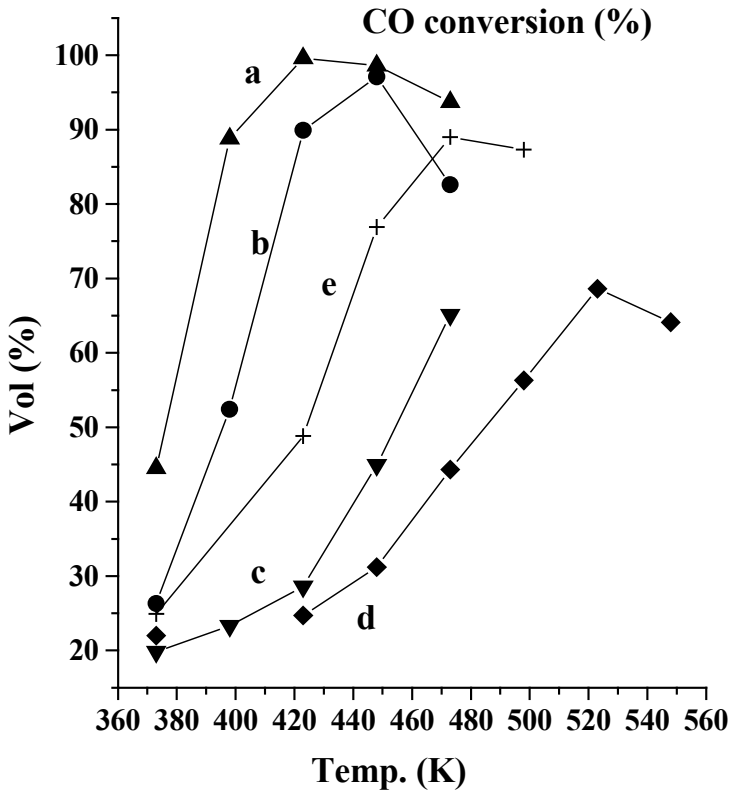

Fig. 7.8. Influence of support and temperature on the conversion of CO to CO_2. (Reaction conditions: catalyst =1.5 g, feed –(H_2(74.17%)+CO(0.49%)+ CO_2(23.26%)+CH_4(2.08 v%)) + water ($p(H_2O)$ = 200 torr), O_2/CO = 1.25, GHSV = 5000 h^{-1}; Run time = 4 h): 1- $CuO(5\%)\text{-}CeO_2(47.5\%)\text{-}ZrO_2(47.5\%)$; 2 – $CuO(5\%)\text{-}CeO_2(95\%)$; 3 – $CuO(5\%)\text{-}ZrO_2(95\%)$; 4 – CeO_2; 5 – $CeO_2(50\%)\text{-}ZrO_2(50\%)$.

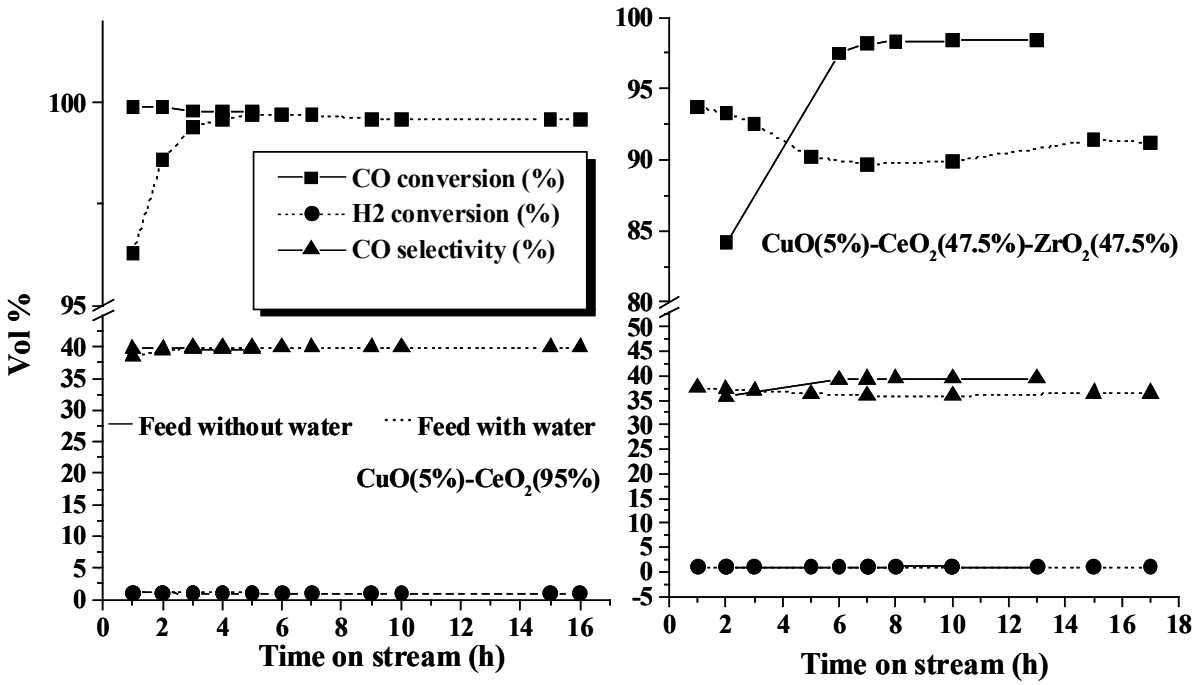

Fig. 7.9. Influence of time on stream and water in feed on CO and H_2 conversions and CO selectivity. (Reaction conditions: catalyst = 1.5 g, feed – (H_2(74.17%)+CO(0.49%)+CO_2(23.26%)+CH_4(2.08 v%)) + water (p(H_2O) = 200 torr), O_2/CO = 1.25, GHSV = 5000 h^{-1}). Catalyst: CuO(5%)-CeO_2(95%) (left panel); CuO(5%)-CeO_2(47.5%)-ZrO_2(47.5%) (right panel).

6. CuO-CeO_2 and CuO-CeO_2-ZrO_2 samples exhibited a stable activity in long-term (18 h) experiments (Fig. 7.9).
7. At high space velocities, in the presence of water in the feed, while the H_2 conversion was not affected, the CO conversion and PROX selectivity were decreased (Fig. 7.10, left panel). As expected the PROX *selectivity* was high (94.9%) at a low value of O_2/CO.
8. CO oxidation increased with an increase in O_2/CO ratio. Almost complete conversion of CO to CO_2 was observed beyond a O_2/CO ratio of 1.25 (Fig. 7.10; right panel).

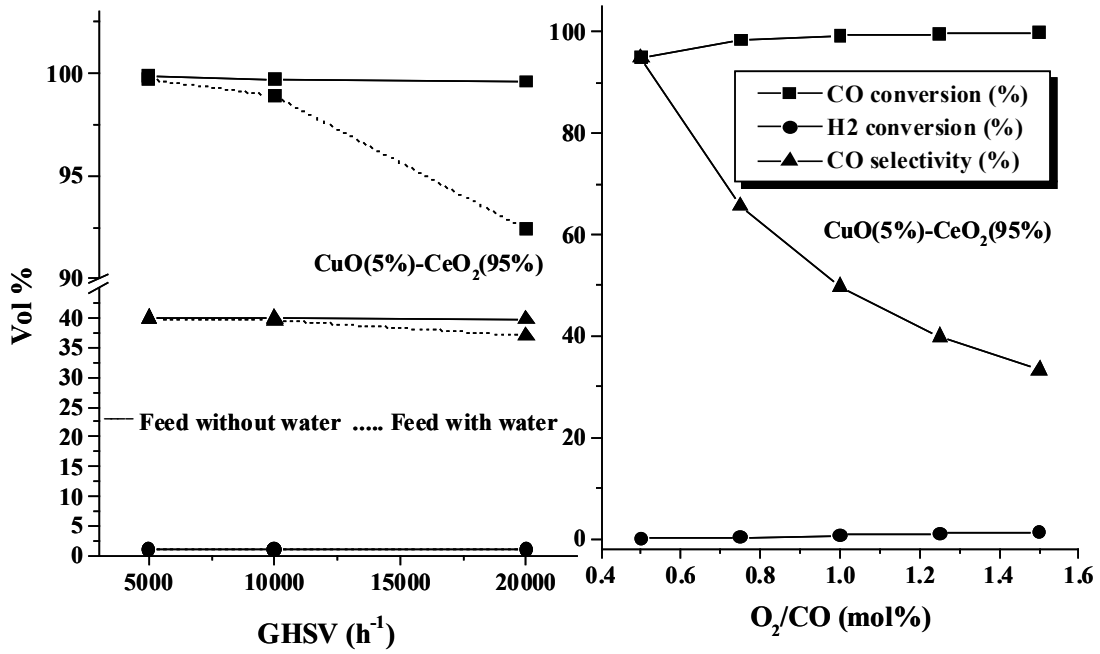

Fig. 7.10. Effect of space velocity (GHSV; left panel) and O_2/CO (right panel) on the PROX activity/selectivity. (Reaction conditions: catalyst (CuO(5%)-CeO_2(95%) =1.5 g, feed –(H_2(74.17%)+CO(0.49%)+CO_2(23.26%)+CH_4(2.08 v%)) + water (p(H_2O) = 200 torr), Run time = 4 h).

9. Table 7.5 illustrates the PROX activity for a feed consisting of the effluent from a fuel processor (steam reformer-cum-high temperature (HTS)-cum-low temperature water gas shift (LTS) reactors combination). Indian LPG (liquefied petroleum gas), comprising mostly of C_3 and C_4 hydrocarbons (both saturates and olefins), was the feed to the steam reformer. 40%NiO-30%CeO_2-30%ZrO_2 was the steam reforming catalyst operating at 923 K, GHSV = 20,000 h^{-1} and steam/carbon = 3.0 [32]. Both the HTS (Fe-Cr oxides) and LTS (CuO-ZnO-Al_2O_3) catalysts were commercial samples from Süd-Chemie (India) operated at conditions recommended by the catalyst manufacturer. With this realistic feed, CuO-CeO_2-ZrO_2 exhibited higher PROX *selectivity* than CuO-CeO_2 and CuO-ZrO_2. Long-term experiments with this feed (27 h) also confirmed the stability of this catalyst even in the presence of realistic amounts of CO_2 and H_2O. The CO content in the effluent from the PROX reactor was consistently below 10 ppm for CuO-CeO_2 and 50 ppm for CuO-CeO_2-ZrO_2.

Table 7.5. Preferential Oxidation of CO in the Effluent from LTS on $CuO-CeO_2-ZrO_2$

Catalyst	Conversion of CO (%)	Conversion of H_2 (%)	Selectivity[a]
$CuO(5\%)-CeO_2(95\%)$	99.95	2.8	20.3
$CuO(5\%)-CeO_2(47.5\%)-ZrO_2(47.5\%)$	99.5	0.8	47.0
$CuO(5\%)-ZrO_2(95\%)$	53.0	0.8	32.1

Reaction conditions: Average feed composition – (5000 ppm CO+20% CO_2+70%H_2+balance H_2O+CH_4); GHSV = 20,000 h^{-1}, catalyst = 1.5 g, O_2/CO = 1.25, temperature = 423 K.

[a]Selectivity of oxygen towards CO oxidation = (Oxygen consumed in CO oxidation) x 100/ (total oxygen consumed in CO + H_2 oxidation).

Both the PROX activity and selectivity of the CuO are significantly affected by interactions with the underlying support. Bera et al. [33] attributed the promoting effect of CeO_2 in the $CuO-CeO_2-ZrO_2$ system for CO oxidation to the lowering of the redox potentials of the Cu^{2+}/Cu^{1+} and Cu^{1+}/Cu^0 couples in a CeO_2 matrix in relation to CuO and $CuO-ZrO_2$. In agreement with the present results (TPR and EPR), they also observed that the Cu species in a $CuO-CeO_2$ matrix require less energy for reduction and reoxidition than in the case of pure CuO and $CuO-ZrO_2$. The oxidation of CO on metals is known to obey a single site Langmuir–Hinshelwood kinetic model [34] where CO and O_2 compete for the same sites. In the case of a metal-reducible oxide system (like our reduced $Cu-CeO_2-ZrO_2$), it may be expected that while CO may adsorb on copper sites, O_2 (and H_2 and H_2O) may adsorb on both the metal (Cu) and support (CeO_2-ZrO_2) (Fig. 7.8). The availability of additional surface oxygen and the consequent higher activity of $CuO-CeO_2$ and $CuO-CeO_2-ZrO_2$ in CO oxidation are, thus, understandable.

Both the XRD and magnetic susceptibility data indicate that the dispersion of supported CuO decreases in the series $CeO_2-ZrO_2 > CeO_2 > ZrO_2$. EPR and magnetic susceptibility data indicate that while a small amount of copper is incorporated in the CeO_2/ZrO_2, fluorite lattice (forming a solid solution), most of it is present on the

surface as isolated, monomeric copper as well as dimeric copper oxo species containing magnetically interacting copper ions, nano-sized copper oxide clusters and a bulk, CuO-like phase. While the isolated and dispersed CuO species exhibit reversible reduction-oxidation behavior, the bulk CuO-like phase exhibits irreversible reduction behavior. The amount of reducible and reoxidizable CuO content is more on CeO_2 (39.7%) than on CeO_2-ZrO_2 catalysts (31.4%) (EPR). The concentration of the bulk-like CuO phase decreases in the series ZrO_2 > CeO_2 > CeO_2-ZrO_2. The PROX *selectivity* of these samples correlated with the concentration of the *dispersed* nano-sized CuO species.

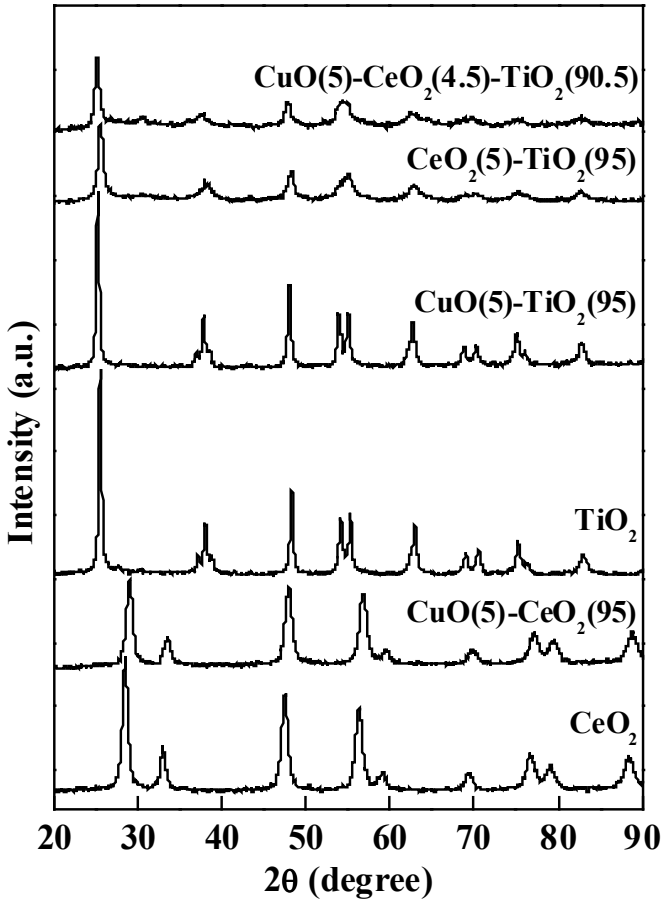

Fig. 7.11. XRD profiles of CuO-CeO_2-TiO_2 composites.

7.4. Results and Discussion – $CuO-CeO_2-TiO_2$ Composites

7.4.1. Structural and Textural Characterization

Fig. 7.11 shows the XRD pattern of representative CeO_2-TiO_2 composites. All the materials dealt in this section are prepared by alcoholysis / sol-gel route (method B). In the case of CeO_2-rich supports for example CeO_2, CeO_2(95 mol%)-TiO_2(5 mol%) and CeO_2(50 mol%)-TiO_2(50 mol%), the XRD pattern correspond to that of a distinct, cubic, fluorite structure [35]. Unit cell parameter of the support oxide decreased from 0.541 nm to 0.536 nm as a consequence of TiO_2 incorporation. No separate TiO_2 phase was detected. These observations indicate that a solid solution of CeO_2-TiO_2 phase is formed. A similar observation was noted also in the case of CeO_2-ZrO_2 mixed oxide composites investigated in Section 7.3. Even if a separate TiO_2 phase existed, it must have been present in an XRD-amorphous form.

TiO_2-rich supports (TiO_2 and CeO_2(5 mol%)-TiO_2(95 mol%)), on the other hand, showed XRD pattern attributable to tetragonal, anatase-like structures [10]. Presence of CuO affected the unit cell parameters (a and c) only marginally (Table 7.6). No separate CuO or Cu_2O phase was detected, except in the samples CuO(10 mol%)- CeO_2(90 mol%). Separate copper oxide phase could not be found even at 20 mol% loading in $CuO-TiO_2$. Hence, CuO is present in a highly dispersed form in these materials. The dispersion is rather higher on TiO_2 than on CeO_2. A similar observation was found also in the case of $CuO-CeO_2-ZrO_2$ oxides (Section 7.3). One of the roles of TiO_2 is, thus, to form a dispersed CuO phase in $CuO-CeO_2-TiO_2$ composites.

CeO_2 prepared *via* alcoholysis route (method B) yielded larger crystallites (10.4 nm) that that prepared *via* precipitation route (method A; 4.9 nm) (Tables 7.1 and 7.6). In other words, the method of preparation influenced the crystallinity. When TiO_2 was present, the crystallite site of CeO_2 decreased markedly (Table 7.6). CeO_2 incorporation affected the crystallite size of TiO_2 in a similar manner. Also the crystallite size of the support was similarly affected due to the presence of CuO. In other words, while the pure oxidic supports form larger crystallites, mixed oxides, in general, yielded smaller crystallites. It is interesting to note that while the presence of

CuO increased the crystallite size of CeO_2 in the samples prepared by co-precipitation route (method A, Table 7.1) a reverse affect was observed in the samples prepared by alcoholysis route (method B, Table 7.6).

Table 7.6. Structural Parameters and Surface Areas of CuO-CeO_2-TiO_2

System[a]	Unit cell parameter of the support oxide (nm)[b]	Avg. crystallite size of the support oxide (nm)	S_{BET} (m^2/g)
CeO_2	0.541	10.4	56
CeO_2(5%)-TiO_2(95%)	0.377, 0.242	11.4	70
TiO_2	0.377, 0.249	21.2	11
CuO(1%)-CeO_2(99%)	0.541	11.0	
CuO(5%)-CeO_2(95%)	0.533	8.3	67
CuO(10%)-CeO_2(90%)	0.544	8.6	35
CuO(1%)-CeO_2(4.95%)-TiO_2(94.05%)	0.378, 0.244	12.2	72
CuO(2%)-CeO_2(4.90%)-TiO_2(93.10%)	0.377, 0.231	10.9	73
CuO(3%)-CeO_2(4.85%)-TiO_2(92.15%)	0.378, 0.251	11.2	66
CuO(5%)-CeO_2(4.75%)-TiO_2(90.25%)	0.378, 0.247	12.8	
CuO(10%)-CeO_2(4.50%)-TiO_2(85.50%)	0.378, 0.254	4.8	166
CuO(20%)-CeO_2(4%)-TiO_2(76%)	0.381, 0.249	8.3	
CuO(5%)-CeO_2(9.5%)-TiO_2(85.5%)	XRD amorphous		172
CuO(5%)-CeO_2(47.5%)-TiO_2(47.5%)	0.536	6.5	124
CuO(5%)-CeO_2(90.25%)-TiO_2(4.75%)	0.539	8.6	130
CuO(1%)-TiO_2(99%)	0.374, 2.350	21.5	14
CuO(5%)-TiO_2(95%)	0.378, 0.254	20.3	18
CuO(10%)-TiO_2(90%)	0.375, 0.241	8.3	35
CuO(20%)-TiO_2(80%)	0.375, 0.242	9.8	34

[a]All the materials are prepared by alcoholysis route (method B). Values in parentheses are mol%.
[b]For CeO_2-rich materials the value correspond to cubic cell parameter (a) and for TiO_2-rich materials the values represent the tetragonal cell parameters (a & c).

S_{BET} of the support (determined from nitrogen adsorption-desorption measurements) increased in the order: TiO_2 < CeO_2 < CeO_2-TiO_2. Loading of CuO influenced S_{BET} values (Table 7.6).

7.4.2. Electronic Spectroscopy

Both CeO_2 and TiO_2 showed two UV bands at 240 and 265 nm attributable to $O^{2-} \rightarrow Ce^{4+}$ and $O^{2-} \rightarrow Ti^{4+}$ charge transfer (CT) transitions. The former is due to specular reflectance. The later one arising from bulk is shifted to the lower energy side upon CuO loading [23].

The CuO containing catalysts showed a broad d-d band in the visible region (Fig. 7.12, right panel). This band shifted from ~ 850 (Cu^{2+} in six-fold coordination) to 680 nm (Cu^{2+} in four-fold coordination) with a change in the support from TiO_2 to CeO_2-TiO_2 and CeO_2, respectively. A similar shift (from 800 to 763 nm in CuO-TiO_2, 768 to 645 nm in CuO-CeO_2-TiO_2 and 670 to 650 nm in CuO-CeO_2) was observed with an increase (from 1 to 20 wt%) in the CuO content indicating that the type of copper species in these catalysts is influenced by both the support and CuO concentration. Similar observations were found also in the case of CuO-CeO_2-ZrO_2 systems (Section 7.3.2.2).

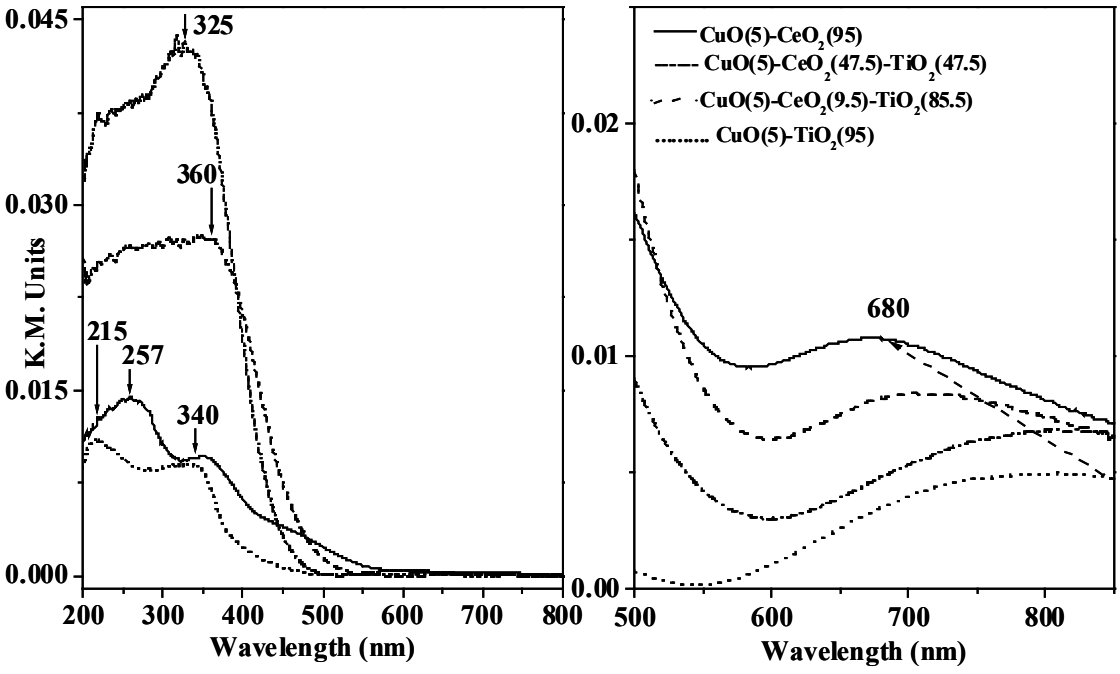

Fig. 7.12. DRUV-visible spectra showing the influence of support composition on the charge transfer (left) and d-d (right) transitions.

7.4.3. EPR Spectroscopy – Redox Behavior

Pure TiO_2 could not be reduced even at 673 K. At least four types of paramagnetic Cu species (I, I', D and III) could be identified in the EPR spectrum (Fig. 7.13) of CuO-CeO_2-TiO_2 samples. Types I and I' correspond to isolated, monomeric, Cu^{2+} species characterized by axial spectra with resolved Cu hyperfine features in the parallel and perpendicular regions. These species differed in their parallel g and A-values (Type I: g_{II} = 2.300, A_{II} = 133 G; Type I': g_{II} = 2.426, A_{II} = 76.1 G). Their $g_{\perp}$ (2.049) and $A_{\perp}$ (10.0 G) values were similar (Table 7.7). The linewidth of species I is higher than that of species I'.

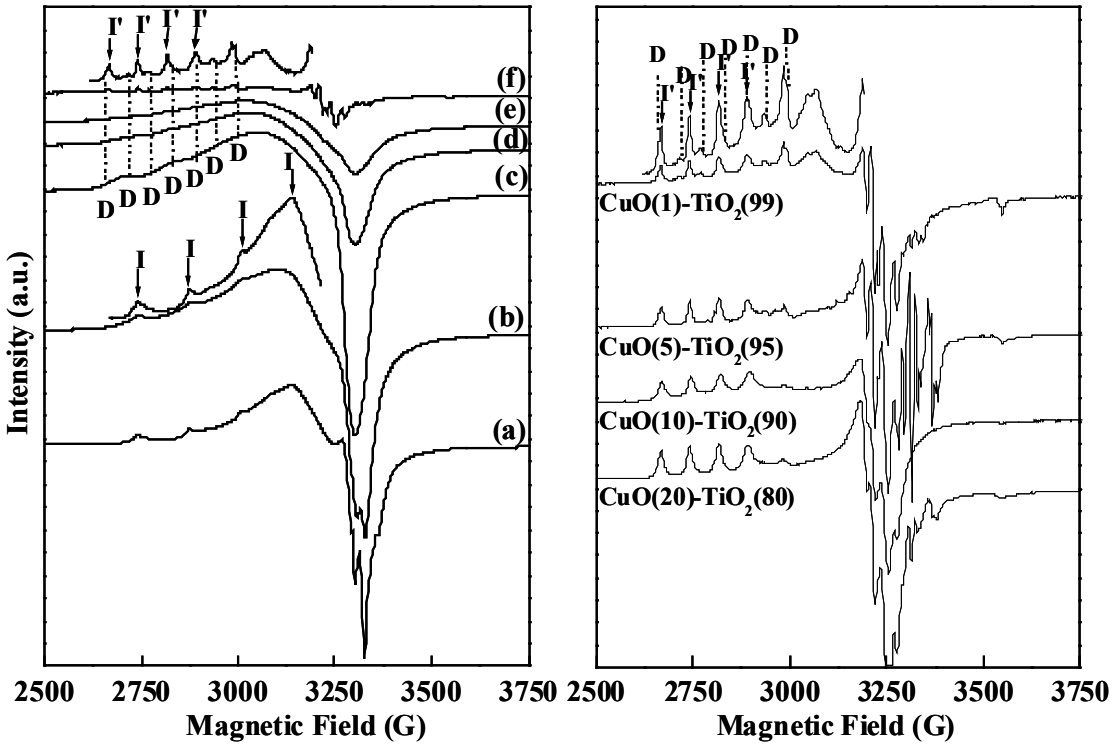

Fig. 7.13. Left: EPR spectra of CuO(1%) supported on (a) CeO_2, (b) CeO_2(50)-TiO_2(50), (c) CeO_2(20)-TiO_2(80), (d) CeO_2(10)-TiO_2(90), (e) CeO_2(5)-TiO_2(95) and (f) TiO_2. Signals due to different Cu species (I, I' and D) are indicated. Right: Effect of CuO content on the EPR spectra of CuO-TiO_2.

A dimeric Cu^{2+}(D) species characterized by the seven hyperfine features were predominantly observed in case of CuO(1%)-TiO_2(99%) samples. The dimeric Cu^{2+} species (D) were not observed at higher loading of CuO (*i.e.* beyond 5 mol%) on TiO_2. However, both I' and D-type Cu^{2+} species were absent in the case of CuO-CeO_2-TiO_2 systems. In case of CeO_2 and CeO_2-TiO_2 supports, an additional species (type-III) was observed. The type-III species characterized by a broad signal (linewidth = 140 G) centered at g_{av} = 2.10 is attributed to dipolar, interacting Cu^{2+} ions forming a nano-sized 2-dimensional structure.

In case of TiO_2 support, it is observed that, even at high loading of CuO (20 mol%), the Cu-species are mainly of type-I'. Interacting, cluster-type Cu^{2+} species were found on TiO_2 support. The EPR signal (type-I & I') intensity did not increase linearly with CuO content indicating the presence of EPR-inactive Cu-cluster phase on TiO_2 supports. This could be seen more clearly when the spectra of 1% CuO on different supports is compared (Fig. 7.13).

The signal intensity is higher in CeO_2-supported CuO than on CeO_2-TiO_2 support. Although well-resolved hyperfine features were observed, the over signal intensity of CuO(1%) is the lowest on TiO_2 support (Fig. 7.13, Left). This suggest that the content of paramagnetic Cu on different supports decreases in the order: CuO-CeO_2 > CuO-CeO_2-TiO_2 > CuO-TiO_2. Hence, at 1% CuO loading the Cu species are present as isolated Cu^{2+} ions and as non-paramagnetic nano-cluster species on TiO_2 supports. However, only the former-type and weakly interacting CuO-type species are present on CeO_2. With increasing CuO loading (1 to 20 mol%) the concentration of weakly interacting CuO-type species increased on CeO_2 supports. However, on TiO_2 support, resolved EPR signals corresponding to monomeric Cu^{2+} species were detected even at 20 mol% CuO loading but their concentration was not significantly different from that found in the samples loaded with 1 mol% CuO on TiO_2 This suggests that with increasing CuO content, on TiO_2 supports, possibly more amounts of non-paramagnetic, strongly interacting copper species are formed.

Table 7.7. EPR Spin Hamiltonian Parameters of CuO-CeO_2-TiO_2

Catalyst	Assignment	Type	$g_{\|}$ or g_1	$g_{\perp}$ or g_2, g_3	$A_{\|}$ (Cu) G	$A_{\perp}$ (Cu) G
CuO(1%)-CeO_2(99%)	Isolated Cu^{2+}	I	2.300	2.047	133	10
CuO(1%)-TiO_2 (99%)	Isolated Cu^{2+}	I'	2.427		73.8	
	Dimeric Cu^{2+}	D	2.388		56.1	
CuO(1%)-CeO_2(4.95%)-TiO_2(94.05%)	Isolated Cu^{2+}	I'	2.426	2.046	76.1	N.R.
CuO(1%)-CeO_2(49.5%)-TiO_2(49.5%)	Isolated Cu^{2+}	I	2.293	2.046	133	N.R.
	Interactive Cu^{2+}	III	2.11	2.11	N.R.	N.R.
CuO(1%)-CeO_2(9.9%)-TiO_2(89.1%)	Isolated Cu^{2+}	I'	2.423	2.049	N.R.	N.R.
	Interacting Cu^{2+}	III	2.12	2.12	N.R.	N.R.

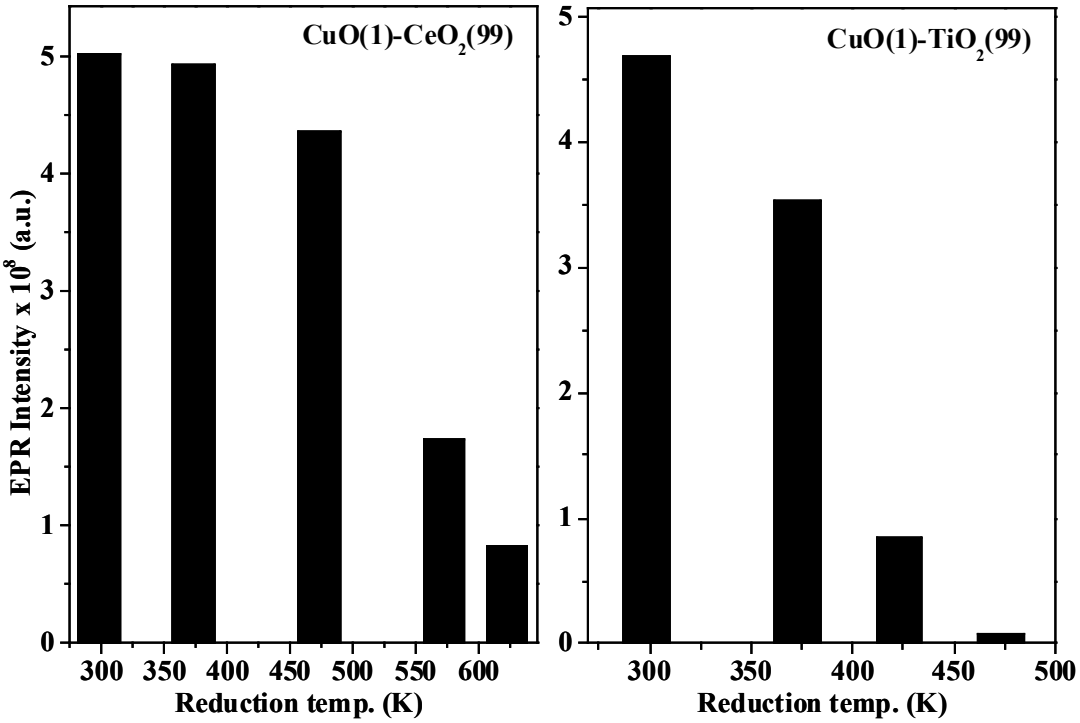

Fig. 7.14. EPR signal intensity of CuO(1%)-CeO_2(99%) and CuO(1%)-TiO_2(99%) as a function of reduction temperature.

The reducibility of CuO with hydrogen on different supports increased in the order CeO_2 < TiO_2 as shown in the Fig. 7.14. In other words, the support influences the copper ion reducibility. This is in agreement with the hyperfine coupling constant of copper on different supports. While the parallel Cu hyperfine coupling constant is about 133 G for CuO-CeO_2, that for CuO-TiO_2 is only 73 G (Table 7.7). Hyperfine coupling constant arises due to interaction of electron spin with the nuclear spin of the paramagnetic ions (Cu^{2+} in this case). The lower magnitude of hyperfine coupling constant in the case of CuO-TiO_2 indicates that the unpaired electron is delocalized more on to the ligand orbitals. In other words, the copper ions on TiO_2 are in an electron deficient state. Hence, their reduction is more facile that the copper ions on CeO_2 which are relatively richer in electron density.

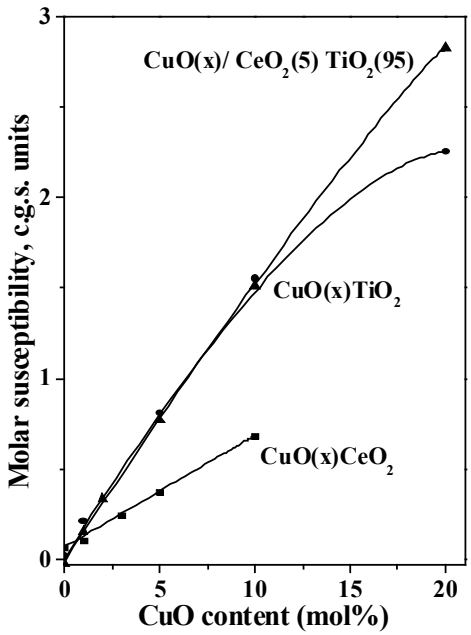

Fig. 7.15. Plot of molar magnetic susceptibility (χ_M) as a function of CuO content in CuO-CeO_2, CuO-CeO_2-TiO_2 and CuO-TiO_2.

7.4.4. Magnetic Susceptibility

The magnetic susceptibility (χ_M) of the samples increased almost linearly with increase in CuO content as shown in Fig. 7.15. For different supports, χ_M values decreased in the order: CuO-CeO_2-TiO_2 > CuO-TiO_2 > CuO-CeO_2. In other words, the mixed oxide support enhanced the dispersion of copper compared CeO_2 and TiO_2.

A similar observation was found also in the case of CuO-CeO_2-ZrO_2 systems (Section 7.3.2.4).

7.4.5. XPS

The XPS studies (Fig. 7.16) revealed that the oxidation state of copper is +2 in all the samples investigated in this section. A plot of surface Cu *vs.* total CuO content (Fig. 7.17) indicates that in the case of CeO_2 support the surface available copper is more than that on TiO_2.

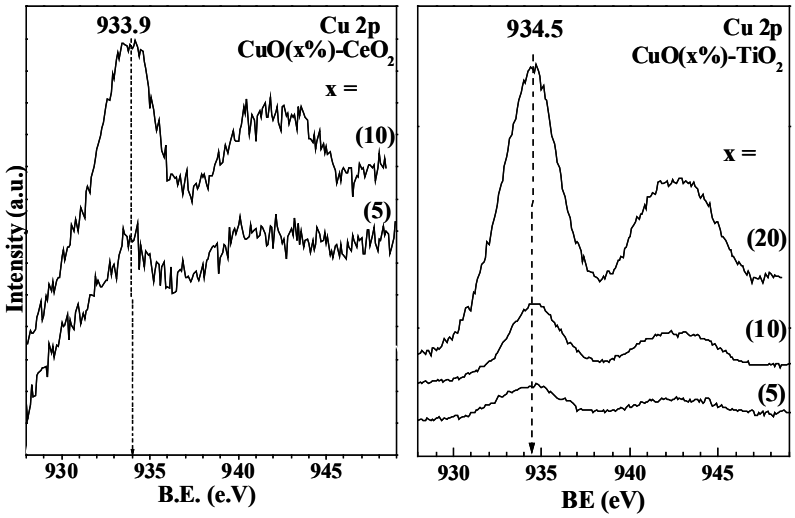

Fig. 7.16. XPS of CuO-CeO_2 and CuO-TiO_2 prepared by alcoholysis route (method B). The amount of copper content (in mol%) present in the catalyst is indicated.

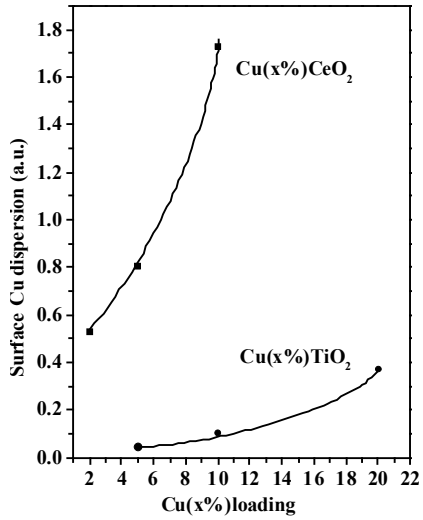

Fig. 7.17. Surface Cu^{2+} on CeO_2 and TiO_2 (from XPS).

The characterization studies reveal that TiO_2 incorporation in CeO_2 promotes the dispersion and enhances the reducibility of CuO species. A similar observation was found also in the case of CeO_2-ZrO_2 supported CuO. A comparative studiy (compared Figs. 7.6 and 7.14) indicates the reducibility of copper is much easier in the presence of TiO_2 than in the presence of ZrO_2 in the support composition. The facilitated reducibility will have consequences on the reactivity of supported CuO.

7.4.6. Decomposition of H_2O_2

Decomposition of H_2O_2 is catalyzed by metals and metal ions. The rate of decomposition, however, depends on the nature, oxidation state and electronic properties of metal ion. The catalytic activities of CuO-CeO_2-TiO_2 catalysts for H_2O_2 decomposition are reported in Table 7.8. Support has a definite influence on the rate of H_2O_2 decomposition. The rate of H_2O_2 decomposition is higher on CuO(5%)-TiO_2 (95%) than on CuO(5%)-CeO_2(95%), CuO(5%)-CeO_2(47.5%)-TiO_2(47.5%) and CuO(5%)-CeO_2(90.25%)-TiO_2(4.75%). This indicates that more amounts of active, surface copper species are available on TiO_2 than on CeO_2 and CeO_2-TiO_2 composites. Cu^{2+} ions on TiO_2 exhibited lower hyperfine coupling constants in the EPR spectrum. The low hyperfine coupling constant indicates that the unpaired electron density on copper is lower in the case of CuO present on TiO_2 than on CeO_2 and CeO_2-TiO_2 supports. In agreement with the EPR results, XPS shows higher binding energy for Cu on TiO_2 (934.5 eV) than on CeO_2 (933.9 eV) (Fig. 7.16). The electron deficient copper on TiO_2 support is obviously more active in H_2O_2 decomposition than the copper on CeO_2 and CeO_2-TiO_2 supports. It may be noted that TiO_2 alone is not active for H_2O_2 decomposition. However, when CuO is present, it exhibited very high catalytic activity (Table 7.8). On the contrary, the support CeO_2 showed activity for H_2O_2 decomposition (Table 7.8). This is because ceria is an easily reducible oxide than titania and hence, can decompose H_2O_2. Unlike in the case of CuO-TiO_2 systems, supporting CuO on CeO_2 did not improve the catalytic activity markedly for H_2O_2 decomposition (Table 7.8). Thus, the H_2O_2 decomposition studies clearly indicate that the support oxide plays a crucial role determining the catalytic activity of supported metal oxide.

Table 7.8. Decomposition of Hydrogen Peroxide over CuO-CeO_2-TiO_2 Catalysts

Catalyst	H_2O_2 decomposition rate constant ($k \times 10^5$, sec^{-1})				Activation energy (E_a, $kJ.mol^{-1}$)
	306 K	312 K	318 K	323 K	
CuO(5%)/TiO_2 (95%)	26.9	54.8	99.6	133.9	86.2
CuO(5%)-CeO_2(47.4%)-TiO_2(47.5%)	4.7	9.6	18.4	29.2	90.2
CuO(5%)-CeO_2(90.25%)-TiO_2(4.75%)	2.6	4.0	7.8	11.9	70.7
CuO(5%)-CeO_2(95%)	9.8	16.4	24.9	31.7	62.1
CeO_2	6.3	12.2	18.2	22.6	68.2
TiO_2	0.4	0.4	0.4	0.4	5058.0

Pure TiO_2 did not decompose H_2O_2.
Reaction conditions: Catalyst, 0.1 g; aq. H_2O_2 (16%); 1.2 g, water, 50 ml; H_2O_2 decomposition followed by titration with $KMnO_4$ (0.1 N). Catalysts were prepared by alcoholysis route (method B).

7.4.7. Oxidative Dehydrogenation of Ethylbenzene with N_2O

Styrene (more than 20 million tones per annum) is industrially manufactured by dehydrogenation of ethylbenzene (EB) at 823 – 923 K, using potassium-promoted iron(III) oxide catalyst and an excess amount of superheated steam as a diluant and heat carrier [36, 37]. This process wastes a large amount of latent heat of vaporizing water. Oxidative dehydrogenation of EB is an alternative, attractive route as the reaction can be conducted at lower temperatures [38, 39]. Presently, catalyst stability and styrene yield are the bottlenecks in the oxydehydrogenation process. Mixed oxides, phosphates and activated carbon materials have shown promising results in recent times [40, 41]. There have been reports on the promotional effect of CO_2 on styrene yield [42 - 44]. The catalysts reported are active only at temperatures above 823 K. The reaction with CO_2 forms CO by-product.

Nitrous oxide (N_2O) with long average lifetime of about 150 years in the atmosphere is 300 times more strongly influencing "greenhouse effect" gas than CO_2. Hence, concerted efforts to control its levels in the atmosphere either by developing alternative "green" technologies that do not generate N_2O as by-product [45] or to

catalytically decompose N_2O into N_2 and O_2 [46 - 48] or utilize it as an oxidant in the synthesis of value-added chemicals [49 - 51] are of great importance. In this study it is found, for the first time, that when the oxidative dehydrogenation reaction was conducted over CuO-CeO_2-ZrO_2 catalysts, using N_2O as an oxidant, EB conversion and styrene selectivity comparable to that of the commercial process are obtained at much lower temperatures (673 K). The process is energy saving and doesn't generate toxic effluents like CO. Most importantly, the process effectively utilizes the atmospheric "greenhouse effect" gas (N_2O) in the production of a value-added commodity chemical *viz.*, styrene.

Table 7.9. Catalytic Activity: Oxidative Dehydrogenation of Ethylbenzene with N_2O as Oxidant

Catalyst	Method of Catalyst Preparation	EB conv. mol%	Selectivity (%)		
			Styrene	Benzene	Toluene
CuO(5%)-CeO_2(95%)[a]	A: Co-precipitation	56.6	79.0	15.1	5.9
CuO(5%)-CeO_2(95%)[b]	B: Alcoholysis	56.0	77.1	17.6	5.0
CuO(5%)-ZrO_2(95%)[a]	A: Co-precipitation	46.5	90.7	5.0	4.3
CuO(5%)-TiO_2(95%)[b]	B: Alcoholysis	20.0	90.0	9.0	1.0
CuO(5%)-CeO_2(47.5%)-ZrO_2(47.5%)[a]	A: Co-precipitation	60.1	86.2	10.6	3.2
CuO(5%)-CeO_2(47.5%)-TiO_2(47.5%)[b]	B: Alcoholysis	49.0	86.8	12.2	1.0
CuO(5%)-CeO_2(9.5%)-TiO_2(85.5%)	B: Alcoholysis	33.0	90.0	9.5	0.5

[a]Reaction conditions: catalyst, 1.5 g; temperature, 673 K; N_2O, 50 ml/min; EB, 2 g/h; WHSV = 1 h^{-1}.

[b]Reaction conditions: catalyst, 1.0 g; temperature, 648 K; N_2O, 50 ml/min; EB, 2.3 g/h; WHSV = 2 h^{-1}.

Catalytic activities of CuO-CeO_2-ZrO_2 and CuO-CeO_2-TiO_2 catalysts are presented in Table 7.9. CuO(5%)-CeO_2(95%) prepared by co-precipitation and alcoholysis routes exhibited similar catalytic activity. The activity of CuO on

different supports decreased in the order: CuO(5%)-CeO_2(95%) > CuO(5%)-ZrO_2(95%) > CuO(5%)-TiO_2(95%). Styrene monomer selectivity, however, increased in the reverse order. A maximum of about 90% styrene selectivity at a ethylbenzene (EB) conversion level of 20 – 46.5% was obtained over TiO_2 and ZrO_2 supports. Dealkylated products - toluene and benzene formed in minor quanties. Zirconia offered high styrene selectivity and ceria enhanced the catalytic activity. CuO supported on CeO_2-ZrO_2 composites exhibited enhanced activities than that on CeO_2-TiO_2 composites. Among various catalyst compositions, CuO(5%)-CeO_2(47.5%)-ZrO_2(47.5%) showed the highest activity and styrene yield (Table 7.9).

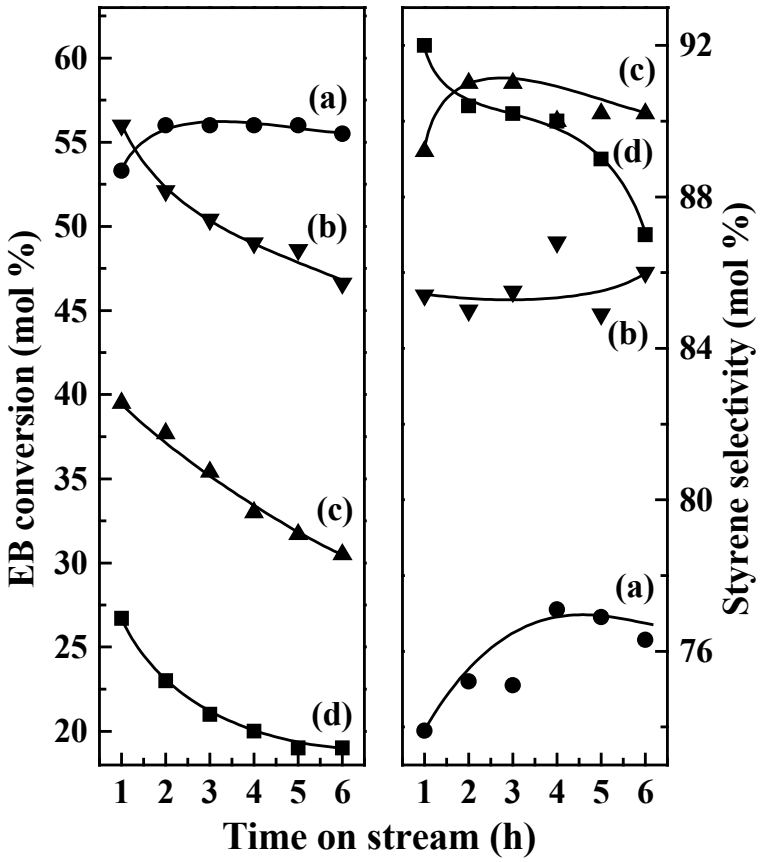

Fig. 7.18. Time on stream studies – oxidative dehydrogenation of ethylbenzene (EB). Catalyst: (a) CuO(5%)-CeO_2(95%), (b) CuO(5%)-CeO_2(47.5%)-TiO_2(47.5%), (c) CuO(5%)-CeO_2(9.5%)-TiO_2(85.5%), (d) CuO(5%)-TiO_2(95%).

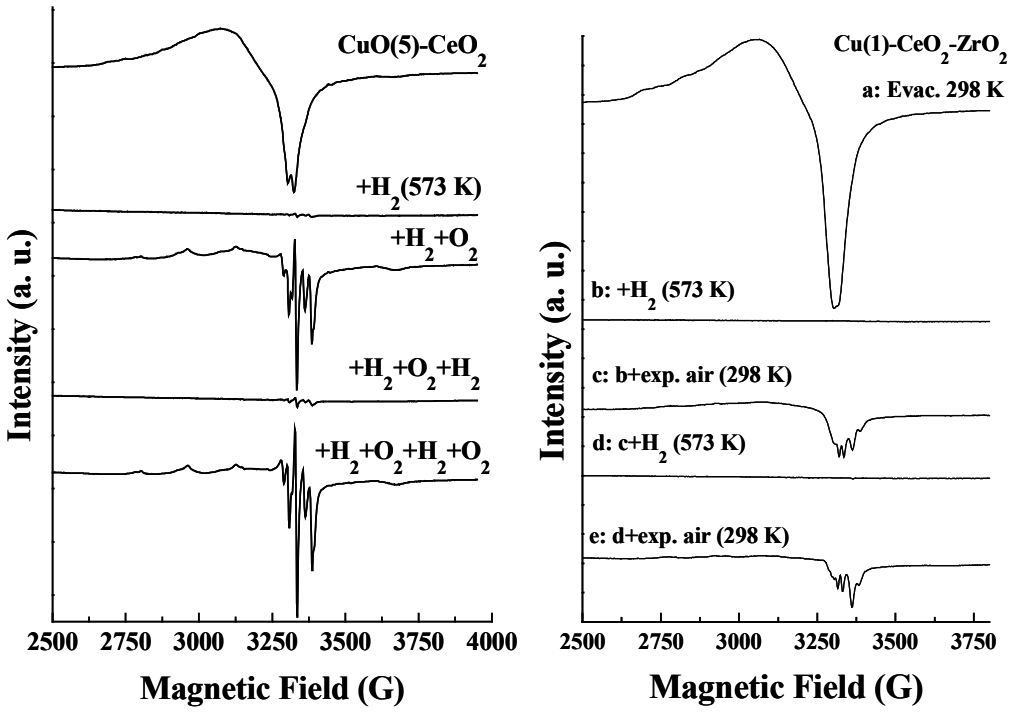

Fig. 7.19. Reversible reduction and reoxidation behavior of CuO on CeO_2 (left) and CeO_2-ZrO_2 (right) supports.

Time on stream (TOS) studies revealed that while the CuO(5%) supported on TiO_2 containing compositions deactivated with time, the CeO_2 supported catalysts showed stable activity for, at least up to, 6 h. Interestingly, the activity and selectivity over CuO(5%)-CeO_2(95%) increased with the reaction time (Fig. 7.18). CuO on CeO_2-ZrO_2 which exhibited the highest activity among different catalysts investigated in this work also showed similar stable catalytic activity during time on stream studies. ZrO_2 incorporation into the CeO_2 lattice enhanced the oxygen storage-release capacity (OSC). Such an enhancement was not observed when TiO_2 was present in CeO_2 lattice. Further, the hyperfine coupling constants in EPR indicated that copper on CeO_2-ZrO_2 compositions is relatively in a more reduced state than the copper ions on CeO_2-TiO_2 compositions. This is also clearly evident from the hydrogen reduction studies that CuO on TiO_2 is more easily reducible than that on CeO_2/ZrO_2 (compare Figs.7.6 and 7.14). Additionaly, CuO on CeO_2 and CeO_2-ZrO_2 supports exhibited

reversible reduction and oxidation behavior. Such a facile reversible redox behavior was not observed in the case of CuO-TiO_2 and CuO-CeO_2-TiO_2 catalysts. Hence, the spectroscopic and catalytic activity studies reveal that oxygen storage-release capacity of the support oxide, dispersed copper species that are relatively in a reduced state with rich unpaired electron density in the metal orbitals and facile reversible reduction-oxidation behavior of the metal species are the crucial factors determining the reactivity of CuO catalysts in preferential CO oxidation and oxidative dehydrogenation of ethylbenzene.

7.5. Conclusions

In this study**,** the influence of composition and preparation procedure in the CeO_2-ZrO_2 and CeO_2-TiO_2 system on the structure, reduction behavior and catalytic activity of supported CuO in the preferential oxidation of CO in the presence of excess H_2 was investigated. The CO oxidation activity/selectivity of CuO on different supports increased in the order: CuO-ZrO_2 < CuO-CeO_2-ZrO_2 ≤ CuO-CeO_2. A catalyst of composition containing 5%CuO exhibited stable activity in long-term experiments, using as feed the effluent from an actual steam reformer-cum-water gas shift reactor combination generating hydrogen from commercial liquefied petroleum gas. Water has negligible effect on the CO oxidation activity of CeO_2-based catalysts. The CuO-CeO_2-ZrO_2 catalysts exhibited efficient activity also for oxidative dehydrogenation of ethylbenzene with N_2O as oxidant. When TiO_2 was present in the support, the catalysts deactivated during time-on stream experiments. TiO_2 containing CuO catalysts exhibited inferior activity than the ZrO_2 containing catalysts. The studies revealed that (1) oxygen storage-release capacity of the support oxide, (2) dispersed copper species that are relatively in a reduced state with rich unpaired electron density in the metal orbitals and (3) facile reversible reduction-oxidation behavior of the metal species are the crucial factors determining the reactivity of CeO_2-ZrO_2 and CeO_2-TiO_2-based CuO catalysts.

7.5. References

[1] D.L. Trimm, Z. Ilsen Önsan, Catal. Rev. Sci. Tech. 43 (2001) 31.

[2] T.V. Choudhary, D.W. Goodman, Catal. Today 77 (2002) 65.

[3] J.R. Rostrup-Nielson, T. Rostrup-Nielson, CATTECH 6 (2002) 150.

[4] M.J. Kahlich, H.A. Gasteiger, R.J. Behm, J. Catal. 171 (1997) 93.

[5] H. Igarashi, H. Uchida, M. Suzuki, Y. Sasaki, M.Watanabe, Appl. Catal. A: Gen. 159 (1997) 159.

[6] P.O. Larsson, A. Andersson, L.R. Wallenberg, J. Catal. 163 (1996) 279.

[7] P.O. Larsson, A. Andersson, J. Catal. 179 (1998) 172.

[8] J. Xiaoyuan, D. Guanghui, L. Liping, C. Yingxu, Z. Xiaoming, J. Mol. Catal. A: Chem. 218 (2004) 187.

[9] O.V. Komova, A.V. Shimakov, V.A. Rogov, J. Mol. Catal. A Chem. 161 (2000) 191.

[10] B. Xu, D. Li, Y. Chen, Chem. Soc. Faraday Trans. 94 (1998) 1905.

[11] G. Avgouropoulos, T. Ioannides, H.K. Matralis, J. Batista, S. Hocevar, Catal. Lett. 73 (2001) 33.

[12] A. Martínez-Arias, M. Fernández-García, J. Soria, J.C. Conesa, J. Catal. 182 (1999) 367.

[13] A. Martínez-Arias, M. Fernández-García, O. Gálvez, J.M. Coronado, J.A. Anderson, J.C. Conesa, J. Soria, G. Munuera, J. Catal. 195 (2000) 207.

[14] A. Martínez-Arias, M. Fernández-García, A.B. Hungría, A. Iglesias-Juez, O. Gálvez, J.A. Anderson, J.C. Conesa, J. Soria, G. Munuera, J. Catal. 214 (2003) 261.

[15] J. Xiaoyuan, L. Guanglie, Z. Renxian, M. Jianxin, C. Yu, Z. Xiaoming, Appl. Surf. Sci. 173 (2001) 208.

[16] M.-F. Luo, Y.-J. Zhong, X.-X. Yuan, X.-M. Zheng, Appl. Catal. A: General 162 (1997) 121.

[17] G. Avgouropoulos, T. Ioannides, Appl. Catal. A: General 244 (2003) 155.

[18] A. Martínez-Arias, M. Fernández-García, V. Ballesteros, L.N. Salamanca, J.C. Conesa, C. Otero, J. Soria, Langmuir 15 (1999) 4796.

[19] H. Vidal, J. Kašpar, M. Pijolat, G. Colon, S. Bernal, A. Cordón, V. Perrichon, F.

Fally, Appl. Catal. B. Environmental 27 (2000) 49.

[20] W. Liu, M. Flytzani-Stephanopoulos, Chem. Eng. J. 64 (1996) 283.

[21] L. Kundakovic, M. Flytzani-Stephanopoulos, Appl. Catal. A: General 171 (1998) 13.

[22] G. Wrobel, C. Lamonier, A. Bennani, A. D'Huysser, A. Aboukais, J. Chem. Soc. Faraday Trans. 92 (1996) 2001.

[23] A. Bensalem, F. Bozon-Verduraz, M. Delamar, G. Bugli, Appl. Catal. A: General 121 (1995) 81.

[24] H. Praliaud, S. Mikhailenko, Z. Chajar, M. Primet, Appl. Catal. B. Environmental 16 (1998) 359.

[25] S. Velu, K. Suzuki, M. Okazaki, M.P. Kapoor, T. Osaki, F. Ohashi, J. Catal. 194 (2000) 373.

[26] P.I. Paulose, G. Jose, V. Thomas, G. Jose, N.V. Unnikrishnan, M.K.R. Warrier, Bull. Mater. Sci. 25 (2002) 69.

[27] J.L.G. Fierro, J. Soria, J. Sanz, J.M. Rojo, J. Solid State Chem. 66 (1987) 154.

[28] M. Che, J.F.J. Kibblewhite, A.J. Tench, M. Dufaux and C. Naccache, J. Chem. Soc. Faraday Trans. I 69 (1973) 857.

[29] P.G. Harrison, I.K. Ball, W. Azelee, W. Daniell, D. Goldfarb, Chem. Mater. 12 (2000) 3715.

[30] A. Aboukais, A. Bennani, C.F. Aïssi, G. Wrobel, M. Guelton, J.C. Vedrine, J. Chem. Soc. Faraday Trans. 88 (1992) 615.

[31] M.M. Gunter, T. Ressler, R.E. Jentoft, B. Bems, J. Catal. 203 (2001) 133.

[32] P. Ratnasamy, D.Srinivas, H.S.Soni, A.J. Chandwadkar, H.S. Potdar, C.S.Gopinath, B.S.Rao, Stud. Surf. Sci. Catal. 135 (2001) 1270.

[33] P. Bera, S. Mitra, S. Sampath, M.S. Hegde, Chem. Commun.(2001) 927.

[34] R.J. Farrauto, C. Bartholomew, Introduction to Industrial Catalytic Processes, Chapman & Hall, London, UK, Ch. 1, 38, 39 (1997).

[35] P. Fornasiero, G. Balducci, R.Di. Monte, J. Kašpar, V. Sergo, G. Gubitosa, A. Ferrero, M. Graziani, J. Catal. 164 (1996) 173.

[36] E. H. Lee, Catal. Rev., 8 (1973) 285.

[37] G. Mestl, N. I. Maksimova, N. Keller, V. V. Roddatis, R. Schlögl, Angew. Chem.

Int. Eng. Ed. 40 (2001) 2066.

[38] S. Geisler, I. Vauthey, D. Farusseng, H. Zanthoff, M. Muhler, Catal. Today 81 (2003) 413.

[39] F. Cavani, F. Trifirò, Appl. Catal. A: General 133 (1995) 219

[40] P. Ingallina, L. Carluccio, C. Perego, G. Del Piero, F. Assandri, Eur. Pat. Appln., 1,160,011 (2001).

[41] N. Keller, N. I. Maksimova, V. V. Roddatis, M. Schur, G. Mestl, Y. V. Butenko, V. L. Kuznetsov, R. Schlögl, Angew. Chem. Int. Ed. 41 (2002) 1885.

[42] Y. Sakurai, T. Suzaki, K. Nakagawa, N.-o. Ikenaga, H. Aota, T. Suzuki, J. Catal. 209 (2002) 16.

[43] N.-o. Ikenaga, T. Tsuruda, K. Senma, T. Yamaguchi, Y. Sakurai, T. Suzuki, T. Ind. Eng. Chem. Res. 39 (2000) 1228.

[44] N. Mimura, I. Takahara, M. Saito, Y. Sasaki,K. Murata, Catal. Lett. 78 (2002) 125.

[45] J. M. Thomas, R. Raja, G. Sankar, R. G. Bell, D. W. Lewis, Pure & Appl. Chem. 73 (2001) 1087.

[46] T. Nobukawa, S.-i. Tanaka, S.-i. Ito, K. Tomishige, S. Kameoka, K. Kunimori, Catal. Lett. 83 (2002) 5.

[47] G. Centi, L. Dall'Olio, S. Perathoner, J. Catal. 192 (2000) 224.

[48] S. Imamura, R. Hamada, Y. Saito, K. Hashimoto, H. Jindai, J. Mol. Catal. A: Chemical 139 (1999) 55.

[49] E. Suzuki, K. Nakashiro, Y. Ono, Chem. Lett. (1988) 953.

[50] L. Mendelovici and J. H. Lunsford, J. Catal. 94 (1985) 37.

[51] J. M. López Nieto, A. Dejoz, M. I. Vazquez, W. O'Leary, J. Cunningham, Catal. Today 40 (1998) 215.

Chapter – 8
Summary and Overall Conclusions

Design and development of efficient, solid catalysts for chemoselective hydrocarbon oxidations with molecular oxygen or H_2O_2, at mild conditions, are of paramount importance in catalysis research. Although, titanium silicalite-1 (TS-1) has been found to be a highly efficient oxidation catalyst, its application to larger substrate molecules of pharmaceutical interest is restricted due to its microporous structure. The Ti in large and mesoporous titanosilicate molecular sieves is, however, not as active as that in TS-1. Several other factors including method of catalyst preparation, solvent, oxidant, temperature etc., influence the catalytic activity and selectivity of titanosilicate molecular sieves. Vanadosilicates, wherein vanadium is substituted for Si in silicate framework, exhibited chemoselectivities different from those of analogous titanosilicates. In this thesis, a detailed understanding of the causes for the differences in activities of titano- and vanadosilicate molecular has been investigated employing spectroscopic and magnetic susceptibility techniques. Different types of reactive oxo-Ti/V species (hydroperoxo, peroxo and superoxo, for example) were generated contacting Ti/V-molecular sieves with H_2O_2, urea-H_2O_2 adducts or H_2+O_2. The concentrations of the oxo-Ti species varied with the framework structure of the metallosilicates. Further, the mode of O-O bond cleavage (homo *vs* heterolytic cleavage) which influences the product selectivity was found to depend on the molecular and electronic structure of Ti and V species and the type of oxidant used. A systematic correlation of these oxo species with chemoselectivity in hydrocarbon oxidation reactions over different micro and mesoporous titano- and vanado-silicate molecular sieves has provided deeper understanding of the mechanism and factors affecting the chemoselective oxidations. Fine-tuning the support structure and active Ti sites by impregnating small quantities of alkali/alkaline earth ions or noble metal ions afforded generation of more reactive oxo species, which in turn improved the chemoselectivity. Addition of small quantities of radical scavengers like hydroquinone also resulted in similar effects. The studies revealed that by a proper fine-tuning of the catalyst and reaction system it would be possible to develop more efficient chemoselective metallosilicate catalyst.

Recently, base metal-supported CeO_2 catalysts are being widely investigated for applications in hydrogen generation by hydrocarbon steam reforming. Presence of

oxides like zirconia and titania in the support influenced the catalytic oxidation activity/selectivity. In this thesis a detailed investigation of the influence of ZrO_2 and TiO_2 incorporation in CeO_2 matrix on oxygen storage capacity (OSC), metal ion dispersion and redox properties of copper have been made. Catalytic activities of the CuO_2-CeO_2-ZrO_2 and CuO-CeO_2-TiO_2 composites for preferential CO oxidation (PROX) and oxidative dehydrogenation of ethylbenzene have been investigated. The studies revealed that the support and its composition exhibit a profound influence on metal speciation and catalytic activity. Details of the conclusions made from different chapters are presented below.

In situ EPR spectroscopic studies (Chapter-3) revealed two types of superoxo-Ti species (A and B) in TS-1 contacted with aqueous H_2O_2 or urea-H_2O_2 adducts with the A-type being more preponderant than B. Mainly, the type-B species was detected in mesoporous Ti-MCM-41 and Ti-SBA-15. Both these oxo-Ti species arise from the framework substituted Ti ions only. The A-type species are those arising from Ti ions having tetrapodal $Ti(OSi)_4$ structure while the B-type are those arising from Ti ions having tripodal $Ti(OH)(OSi)_3$ structure. Variable temperature EPR studies revealed that the oxo-Ti species undergo interconversion between superoxo and hydroperoxo/peroxo-Ti. This interconversion is more facile in the case of A-type than B-type oxo-Ti species. Noble metal (Pd or Pt)-impregnation modified the Ti structure (Chapter 3). The noble metal-modified Ti^{4+} could be reduced even at 323 K while the unpromoted Ti^{4+} ions required 773 K for reduction in dry-hydrogen. More interestingly, similar kind of superoxo-Ti species could be generated in Pd-TS-1 samples contacting with H_2+O_2 mixtures instead of aqueous H_2O_2 (Chapter-3). Further, upon noble metal impregnation, the A-type were generated in more amounts than the B-type oxo-Ti. Structure-activity correlations revealed that while the A-type oxo-species are responsible for selective epoxidations, the B-type superoxo-Ti species lead to non-selective products. In other words, the study revealed that the type of the oxo-Ti species generated determines the product selectivity. Noble-metal impregnation facilitated formation of A-type oxo-Ti species that are responsible for selective epoxidations. The oxo-species were also monitored by DRUV-visible spectroscopy and magnetic susceptibility techniques.

Addition of a small amount of alkali or alkaline earth ion during oxidation reactions enhances the chemoselectivity in epoxidations (allyl alcohol, allyl chloride and styrene) over TS-1 and Ti-MCM-41 molecular sieves (Chapter-4). Variation of pH from acidic to alkaline conditions and modification with alkali or alkaline earth metal ions affected the oxo-Ti species formed on titanosilicates. The A-types species formed in more amounts than the B-type in basic pH when TS-1 was modified with alkali and alkaline earth ions. Structure-activity studies revealed that the epoxide selectivity correlates with the hydroperoxo species concentration. The role of alkali and alkaline earth metal ions was not only to suppress the acidity generated during oxidation reactions (which can lead to hydrolysis of epoxides) but, to modify the structure and electronic properties of oxo-Ti species. Thus, the study reveals that alkali metal modification modifies the Ti structure and enhances chemoselectivity in epoxidations.

The mode of O-O bond cleavage (homolysis *vs* heterolysis) in oxo-Ti species generated over TS-1 contacting with H_2O_2 was studied in Chapter-5. Cyclohexene is a sensitive probe for the study of O-O bond cleavage and hence, catalytic activity studies for epoxidation of cyclohexene were investigated. While the heterolytic cleavage (generating ionic intermediates) produces epoxides, homolytic cleavage (generating radical species) yields allylic oxidation products (cyclohexenol and cyclohexenone). Silicate structure and solvent influenced the product selectivity. The O-centered radicals ($HO^{\bullet}$, $HOO^{\bullet}$ and $O_2^{-\bullet}$) generated *via* homolytic O-O bond cleavage are highly short lived. Their life-time was enhanced by forming adducts with spin-traps such as DMPO. EPR spectroscopy identified the formation of such radicals and the influence of solvent on their generation. Addition of a small amount of a radical quencher (hydroquinone, for example) suppressed the radical mediated reactions and enhanced cyclohexene epoxide selectivity. Thus, the studies revealed that the mode of O-O bond cleavage in the oxo-species is of paramount importance and the structure of Ti can influence the cleavage. In Chapters 3 and 4, it was found that noble metal or alkali / alkaline earth ion impregnation enhances chemoselectivity of TS-1. In Chapter-5, it was noted that suppression of radical mediated reactions by addition of a small quantity of radical quenchers also improves the chemoselectivity.

EPR spectroscopy of reactive superoxo-vanadium(V) species in vanadosilicate molecular sieves (microporous VS-1 and mesoporous V-MCM-41) generated on contact with H_2O_2, *tert.*-butyl hydroperoxide (TBHP) or (H_2+O_2) is reported in Chapter-6. By suitable choice of the silicate structure, solvent and oxidant it was possible to control the vanadium—($O_2^{-\bullet}$) bond (i.e., the V—O bond) covalency, the mode of O-O cleavage (in the superoxo species) and thereby, chemoselectivity in the oxidation of *n*-hexane: Oxidation by TBHP over V-MCM-41, for example, yielded 27.2% of (*n*-hexanol + *n*-hexanal + *n*-hexanoic acid), among the highest chemoselectivity for oxidation of the terminal $–CH_3$ in a linear paraffin, reported to date. Over these vanadosilicates, oxidation of the primary C-H bond occurs only *via* a homolytic O-O bond cleavage; the secondary C-H bond oxidations may proceed *via* both the homo- and heterolytic O-O cleavage mechanisms.

Chapter – 7 reported studies on CuO-CeO_2-ZrO_2 and CuO-CeO_2-TiO_2 composites. The influence of support composition on (1) oxygen storage capacity and (2) metal ion dispersion and reducibility was investigated. The activity of the catalysts in preferential CO oxidation and oxidative dehydrogenation of ethyl benzene was studied. The mixed oxide composite influenced the catalytic activity. CuO(5%) supported on CeO_2(50%)-ZrO_2(50%) exhibited the highest activity and selectivity. Structure-activity correlations have been investigated.

By and large, the thesis reports the factors influencing chemoselectivity in oxidation reactions over metallosilicates and ceria-based mixed metal oxides. The study reveals that the chemoselectivity can be enhanced by suitably modifying the support composition. The work contributes to a deeper understanding of selective oxidation reactions and toward developing active and selective heterogeneous oxidation catalysts.

LIST OF RESEARCH PUBLICATIONS

1. Reactive oxygen species in epoxidation reactions over titanosilicate molecular sieves
   Vasudev N. Shetti, P. Manikandan, D. Srinivas, P. Ratnasamy
   J. Catal. 216 (Nos. 1-2) (2003) 461 – 467.

2. Enhancement of chemoselectivity in epoxidation reactions over TS-1 catalysts by alkali and alkaline metal ions
   Vasedev N. Shetti, D. Srinivas, P. Ratnasamy
   J. Mol. Catal. A: Chemical 210 (Nos. 1 – 2) (2004) 171 – 179.

3. Influence of the support on the preferential oxidation of CO in hydrogen-rich stream reformats over the CuO-CeO_2-ZrO_2 system
   P. Ratnasamy, D. Srinivas, C.V.V. Satyanarayana, P. Manikandan, R.S. Senthil Kumaran, M. Sachin, **Vasudev N. Shetti**
   J. Catal. 221 (No. 2) (2004) 455 – 465.

4. Ti-oxo radicals and product selectivity in olefin oxidations over titanosilicate molecular sieves
   Vasudev N. Shetti, D. Srinivas, P. Ratnasamy
   Zeitschrift für Physikalische Chemie 219 (2005) 905 - 920.

5. Chemoselective alkane oxidation by superoxo-vanadium(V) in vanadosilicate molecular sieves
   Vasudev N. Shetti, M. Jansi Rani, D. Srinivas, Paul Ratnasamy
   J. Phys. Chem. B 110 (2006) 677-679.